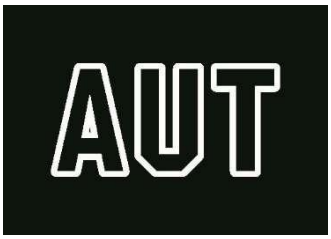

School of Science

Self-assembly in the design of Cooperative Catalysts for Organic Synthesis

Pablo Solís Muñana

A thesis submitted to

Auckland University of Technology

in fulfilment of the requirements for the degree of

Doctor of Philosophy

2021

Abstract (English)

Catalysis is, without a doubt, one of the most powerful approaches for accelerating chemical reactions and the facilitation of new reaction pathways. Recently, catalyst systems that involve the active participation of multiple catalytic units have generated intense interest among chemists due to improved efficiencies and access to novel reactivities. Examples of catalysts that utilise multiple, simultaneous activation sites include enzymes, which in general can catalyse reactions with much higher efficiencies than synthetic catalysts. Furthermore, for reactions involving multiple catalytic units, their efficiency can be improved when the required catalytic units are brought together into proximity. The direct covalent linking of catalytic units is the most common strategy to bring requisite catalytic units together. While this approach can be used to produce well-defined catalytic pockets, it also presents inconveniences from a synthetic point of view, and its non-modularity can complicate the optimisation of the catalyst.

In this thesis, an alternative, modular approach for bringing catalyst units into proximity is presented, based on the introduction of hydrophobic interactions to induce self-assembly. In a proof-of-concept study, we synthesised amphiphilic catalysts containing the Zn^{2+}-binding ligand 1,4,7-triazacyclononane attached to a C_{16}-hydrocarbon chain (C_{16}TACN). This amphiphilic ligand self-assembled in aqueous buffer to form vesicular structures, allowing the formation of catalytic pockets that catalysed the transphosphorylation of hydroxypropyl *p*-nitrophenyl phosphate (HPNPP). We demonstrated that our vesicular system could accelerate the reaction three orders of magnitude faster than the control molecule and that this rate acceleration could be attributed to the ability of neighbouring catalytic units to act cooperatively. Remarkably, the formation of the assembled catalyst was observed to be promoted by the presence of the HPNPP substrate, in analogy to many natural systems.

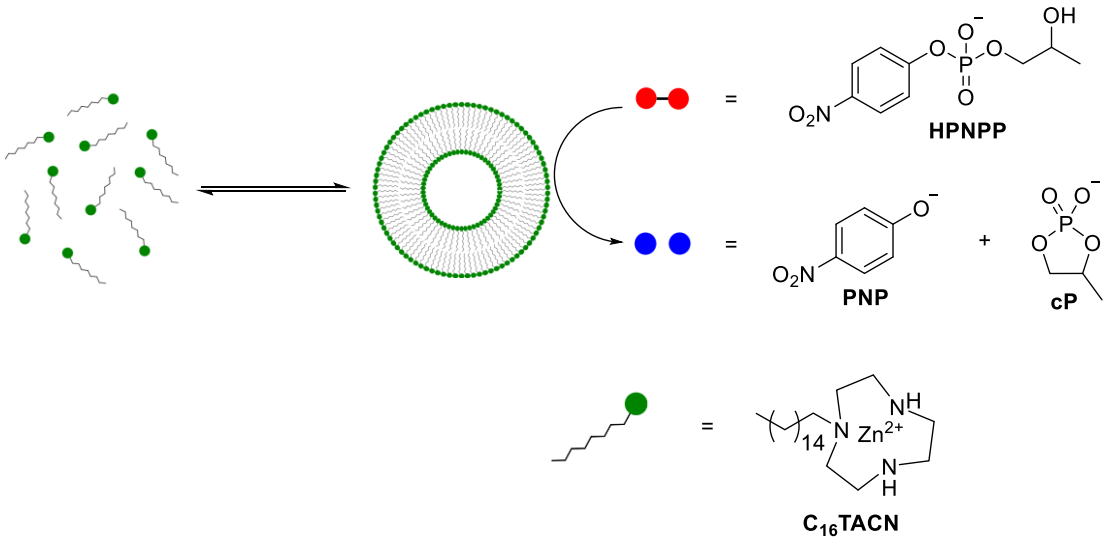

To demonstrate that introduction of hydrophobic interactions could be advantageous for the design of catalysts for synthetically useful reactions, we applied these concepts to a catalyst designed for the hydrolytic kinetic resolution (HKR) of terminal epoxides. Jacobsen's HKR of epoxides requires the simultaneous interaction of two catalytic units in the transition state of the rate-determining step, and thus benefits from preorganisation that brings the catalyst units together. We designed a (salen)Co complex functionalised with hydrocarbon chains to increase its hydrophobicity and its propensity to self-assemble. We demonstrated that our functionalised catalyst could perform the HKR 10 times faster than the commercially available complex. This is due to two effects: enhanced cooperativity due to self-assembly in homogenous conditions, and increased homogenisation between the phases under biphasic conditions. The novel complex can be utilised in industrially relevant neat conditions, without the addition of organic solvents.

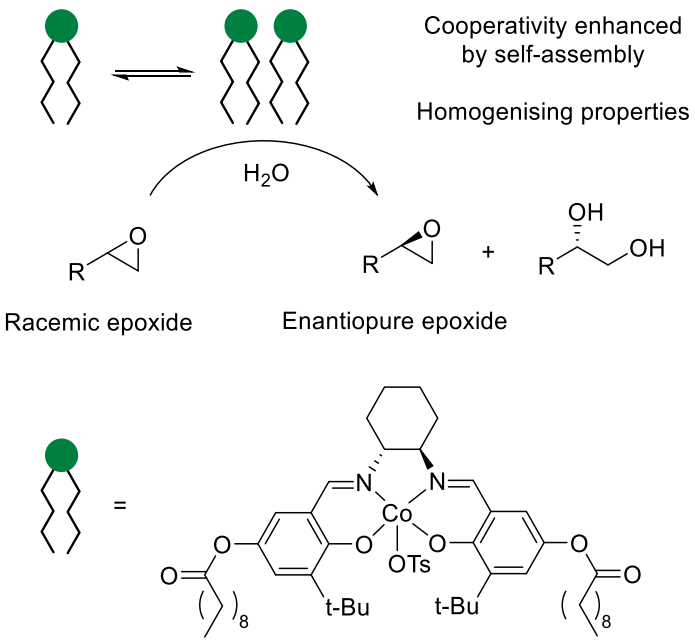

Abstract (Català)

La catàlisi és, sens dubte, un dels enfocaments més potents per accelerar les reaccions químiques i facilitar les noves vies de reacció. Recentment, els sistemes catalítics que impliquen la participació activa de múltiples unitats catalítiques han generat un interès intens entre els químics a causa de la millora de l'eficiència i l'accés a noves reactivitats. Alguns exemples de catalitzadors que utilitzen múltiples llocs d'activació simultània són els enzims, que en general poden catalitzar reaccions amb eficiències molt més altes que els catalitzadors sintètics. A més, per a reaccions que impliquen múltiples unitats catalítiques, l'eficiència es pot millorar quan les unitats catalítiques necessàries s'uneixen a la proximitat. L'enllaç covalent directe de les unitats catalítiques és l'estratègia més comuna per reunir les unitats catalítiques necessàries. Tot i que aquest enfocament es pot utilitzar per produir bosses catalítiques ben definides, també presenta inconvenients des del punt de vista sintètic i la seva nul·la modularitat pot complicar l'optimització del catalitzador.

En aquesta tesi es presenta un enfocament alternatiu i modular per apropar les unitats catalitzadores, basat en la introducció d'interaccions hidrofòbiques per induir l'autoensamblatge. En un estudi de prova de concepte, vam sintetitzar catalitzadors amfifílics que contenen el lligand vinculant a Zn^{2+} 1,4,7-triazaciclonona unit a una cadena d'hidrocarburs C_{16} (C_{16}TACN). Aquest lligand amfifílic es va autoensamblar en solució tampó per formar estructures vesiculars, permetent la formació de bosses catalítiques que van catalitzar la transfosforilació del fosfat de *p*-nitrofenil hidroxipropil (HPNPP). Vam demostrar que el nostre sistema vesicular podia accelerar la reacció tres ordres de magnituds més ràpidament que la molècula de control i que aquesta velocitat d'acceleració es podria atribuir a la capacitat de les unitats catalítiques veïnes d'actuar de forma cooperativa. Remarcablement, es va observar que la formació del catalitzador reunit era promoguda per la presència del substrat de la reacció.

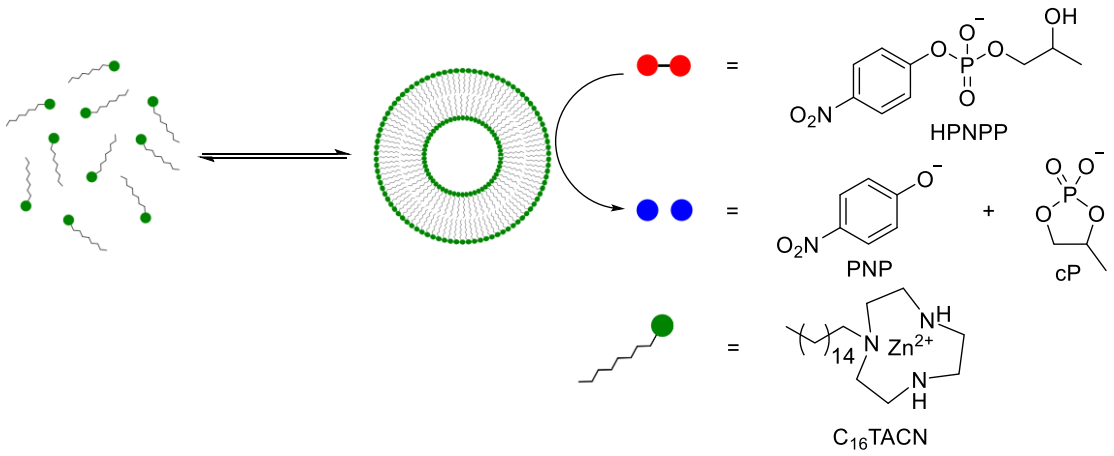

Per demostrar que la introducció d'interaccions hidrofòbiques podria ser avantatjosa per al disseny de catalitzadors per a reaccions útils sintèticament, hem aplicat aquests conceptes a catalitzadors per a la resolució cinètica hidrolítica (HKR) dels epòxids terminals. L'HKR d'epòxids de Jacobsen requereix dues unitats catalítiques l'estat de transició del pas determinant de la taxa i, per tant, es beneficia de la preorganització que uneix les unitats catalitzadores. Hem dissenyat un catalitzador de (salen)Co funcionalitzat amb cadenes d'hidrocarburs per augmentar la seva hidrofobicitat i la seva propensió a muntar-se a si mateix. Vam demostrar que el nostre catalitzador funcionalitzat podia realitzar l'HKR 10 vegades més ràpid que la molècula de control disponible en el comerç. Això es deu a una combinació de dos efectes: una cooperativitat millorada a causa de l'autoassemblatge en condicions homogènies i una major homogeneïtzació entre les fases en condicions bifàsiques. Aquesta reacció es pot realitzar en condicions netes industrialment rellevants, en una barreja bifàsica d'epòxid i aigua, sense la necessitat d'afegir un dissolvent addicional.

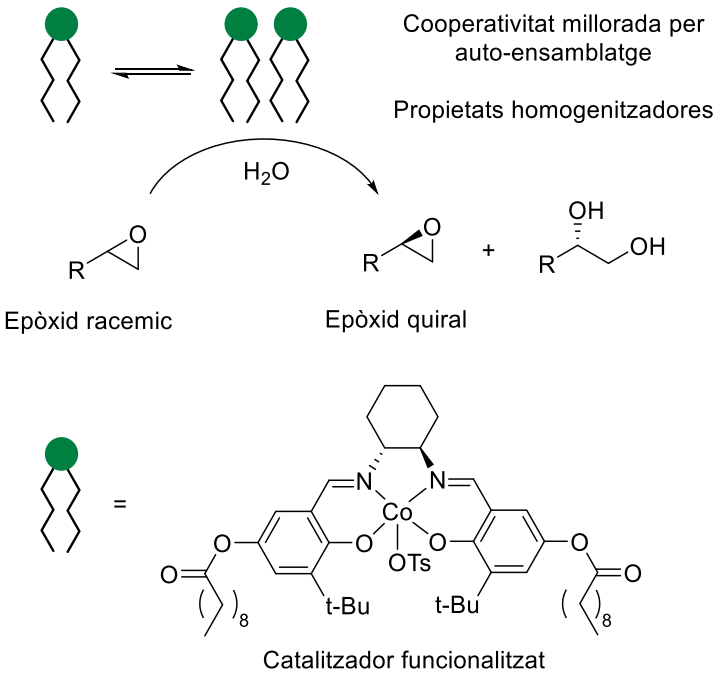

Abstract (Castellano)

La catálisis es, sin duda, uno de los enfoques más potentes para acelerar las reacciones químicas y facilitar las nuevas vías de reacción. Recientemente, los sistemas catalíticos que implican la participación activa de múltiples unidades catalíticas han generado un interés intenso entre los químicos debido a la mejora de la eficiencia y el acceso a nuevas reactividades. Algunos ejemplos de catalizadores que utilizan múltiples puntos de activación simultánea son las enzimas, que en general pueden catalizar reacciones con eficiencias mucho más altas que los catalizadores sintéticos. Además, para reacciones que implican múltiples unidades catalíticas, la eficiencia se puede mejorar cuando las unidades catalíticas necesarias unen a la proximidad. El enlace covalente directo de las unidades catalíticas es la estrategia más común para reunir las unidades catalíticas necesarias. Aunque este enfoque se puede utilizar para producir bolsas catalíticas bien definidas, también presenta inconvenientes desde el punto de vista sintético y su nula modularidad puede complicar la optimización del catalizador.

En esta tesis se presenta un enfoque alternativo y modular para acercar las unidades catalizadoras, basado en la introducción de interacciones hidrofóbicas para inducir el autoensamblaje. En un estudio de prueba de concepto, hicimos sintetizar catalizadores amfifílicos que contienen el ligando vinculante a Zn^{2+} 1,4,7-triazaciclonona unido a una cadena de hidrocarburos C_{16} (C_{16}TACN). Este ligando amfifílicos se autoensambla en solución tampón para formar estructuras vesiculares, permitiendo la formación de bolsas catalíticas que catalizaron la transfosforilación del fosfato de *p*-nitrofenil hidroxipropil (HPNPP). Demostramos que nuestro sistema vesicular podía acelerar la reacción tres órdenes de magnitudes más rápidamente que la molécula de control y que esta velocidad de aceleración se podría atribuir a la capacidad de las unidades catalíticas vecinas de actuar de forma cooperativa. Remarcablemente, se observó que la formación del catalizador reunido era promovida por la presencia del sustrato de la reacción.

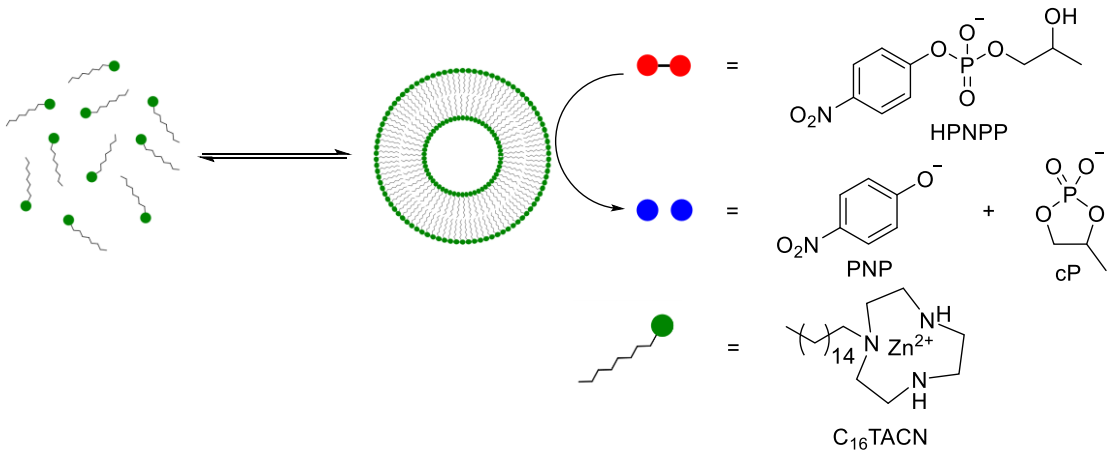

Para demostrar que la introducción de interacciones hidrofóbicas podría ser ventajosa para el diseño de catalizadores para reacciones útiles sintéticamente, hemos aplicado estos conceptos a catalizadores para la resolución cinética hidrolítica (HKR) de los epóxidos terminales. El HKR de epóxidos de Jacobsen requiere dos unidades catalíticas el estado de transición del paso determinante de la tasa y, por tanto, se beneficia de la preorganització que une las unidades catalizadoras. Hemos diseñado un catalizador de (salen)Co funcionalizado con cadenas de hidrocarburos para aumentar su hidrofobicidad y su propensión a montarse a sí mismo. Demostramos que nuestro catalizador funcionalizado podía realizar la HKR 10 veces más rápido que la molécula de control disponible en el comercio. Esto se debe a una combinación de dos efectos: una cooperatividad mejorada debido al autoensamblaje en condiciones homogéneas y una mayor homogeneización entre las fases en condiciones bifásicas. Esta reacción se puede realizar en condiciones limpias industrialmente relevantes, en una mezcla bifásica de epóxido y agua, sin la necesidad de añadir un disolvente adicional.

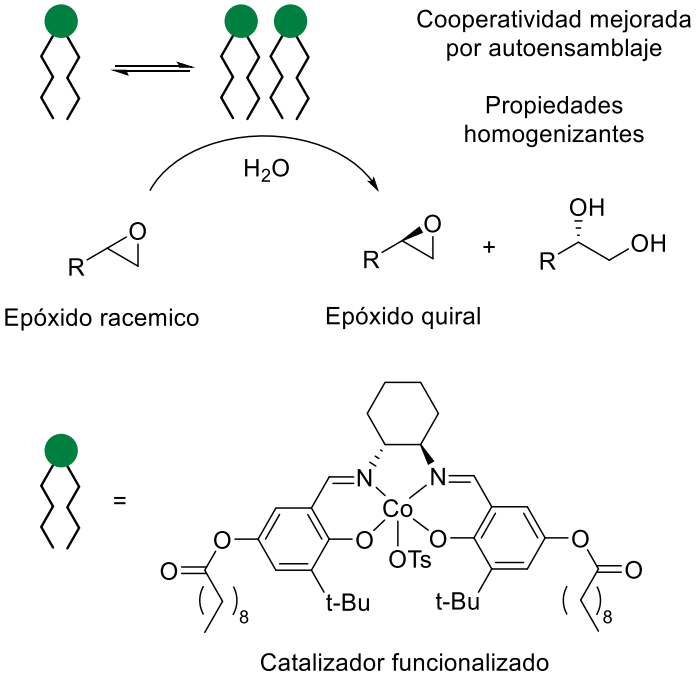

A mi familia, especialmente a mis abuelos Ismael y Antonia.

Acknowledgments

First of all, I am infinitely grateful to my supervisor Dr Jack L.-Y. Chen for the opportunity to study my PhD under his supervision. The endless support he shows to his students eases the journey and creates a magnificent work environment to do research. I want to thank him for his guidance; his comments and tips always got me in the right direction. Thanks also for his trust; he has always been opened to listen to anything I wanted to say. Also, for the encouragement and patience when I felt lost or less enthusiastic, and finally for the friendship built along all these years. I want to thank Professor Leonard Prins and his team for allowing me to do two month-long stays in his group and to collaborate for a publication, also for the help and advice he provided to me – I learned a lot during that time. Also, thanks to Professor Gregory G. Warr for his valuable help and suggestions with SANS and SAXS, and Cassandra Fleming for making the lab a better place.

I would also like to thank the members of Chen group, especially to Chloe Ren who helped me become familiar with the workspace and made me feel welcome, and also for the great chats about our research. I am grateful too to Joanne Salam and Bronte Carr for their time and energy that contributed to the research. Gracias también Andrés Tiban por los buenos ratos en el laboratorio compartiendo vitrina y tomando algo. All of them are wonderful co-workers and friends.

I wish to thank other friends that I made at Auckland University of Technology during my PhD. Emily Griffiths, for being so welcoming with me since day one, for her help regarding any admin issue, and most importantly for becoming a great friend, thanks also to Tom Doyle for the great times. Thanks to Cameron Waghorn and Franko Schrumpf for all the laughs and good times both in the lab and at Vesbar, they are outstanding inorganic chemists, and soon also PhDs . I finalment gràcies Dra. Sandra Grau Bartual pels consells i debats sobre ciència, pero principalment per les birres, i per ser una gran amiga que m'ha ajudat sempre que ha pogut.

A few other people I met during my career also have to be mentioned here for their impact in my journey as a scientist. Gràcies a les companyes i companys de la Universitat Rovira i Virgili, especialmente a Aitor Linares Capataz por haber sido, y seguir siendo un gran amigo que siempre está ahí; també gràcies a les companyes que van acompanyar-me durant tota la carrera i la cafeteria de la facultat, amb els quals l'amistat encara perdura: la Dra. Alba Maceira Torrents, a l'Alex Asensio Turné, al Dr. Cristian Marro Bellot, a la Gemma Rius Painous, en Martí Àvila Llopis, la Patricia Celades Altés i a en Roger Puigpinós Morros. Gràcies a les companyes i companys de Repsol Química, especialmente a José Manuel Navarro García i a en Xavier Cornudella Rius per tot el que em van ensenyar, i per fer-me sentir valorat com a treballador. Gràcies també a les companyes i companys d'Esteve Química, especialment a l'Alba Llera Tejero, la Mireia Lopez Lopez i als i les analistes del laboratori de procés per ensenyar-me a fer servir molts instruments analítics i sobretot per les bones estones al laboratori. Estic molt agraït

també amb els companys i companyes del màster a la Universitat de Barcelona, especialment a l'Èric Cots Fargas, i a en Sergi Ordeix per ser uns grans amics i companys amb els que he passat molts bons moments. Gràcies a el Profesor Josep Bonjoch i al Dr. Ben Bradshaw per la seva supervisió durant el treball de final de màster i la seva ajuda durant el màster i posteriorment. També vull agrair en especial a la Dra. Mar Saladrigas Rodríguez, que va ajudar-me dins i fora el laboratori durant el màster i ràpidament es va convertir en una gran amiga.

I would like to thank Auckland University of Technology for allowing me to do my PhD in its facilities and for the funding. Thanks also to the New Zealand Institute of Chemistry letting me be one of their representing students and for organising such interesting talks and conferences. Also, thanks to the MacDiarmid Institute for letting me be part of their institute and for the COVID-19 extension funding provided.

Gracias también a todos los amigos a los que aún no he podido mencionar por vuestro apoyo, compañía y amistad, sobre todo gracias a Mateo Bernal Manero, Daniel Maestre Andrés y Enric Morán Gutiérrez.

Muy especialmente quiero agradecer a mi familia el apoyo que me han dado apoyo de todas las maneras posibles, especialmente a mi madre, mi padre, mi hermana y mis abuelos, por cuidarme estando cerca o lejos de ellos, sin vuestro apoyo no hubiese podido embarcarme en este viaje.

Finalment, gràcies Virginia per les teves correccions de l'anglès en aquesta tesi, per sobre tot pel teu suport, la teva paciència durant tot aquest temps i per estimar-me tant i tan bé.

Thank you all! Gràcies a totes i tots! ¡Gracias a todas i todos!

Table of contents

Chapter two: Proof of concept; self-assembly of cooperative catalysts for the cleavage of RNA and DNA model molecules

Chapter three: Utilising hydrophobic interactions to develop more efficient catalysts for the hydrolytic kinetic resolution of terminal epoxides

Abbreviations

δ	chemical shift
λ_{em}	em emission wavelength
λ_{ex}	ex excitation wavelength
ΔG	Gibbs free energy
µ	micro
ACP	assembled catalytic pairs
Ar	aryl
ATP	adenosine triphosphate
AuNP	gold nanoparticle
Boc	*tert*-butyloxycarbonyl
BPNPP	bis(*p*-nitrophenyl) phosphate
CAC	critical aggregation concentration
CAPS	*N*-cyclohexyl-3-aminopropanesulfonic acid
CHES	*N*-cyclohexyl-2-aminoethanesulfonic acid
cP	cyclic phosphate
DCM	dichloromethane
DIPEA	*N*,*N*-diisopropylethylamine
DLS	dynamic light scattering
DMAP	4-dimethylaminepyridine
DNA	deoxyribonucleic acid
DNPB	dinitrophenyl butanoate
E_a	activation energy
e.e	enantiomeric excess
EDC	*N*-(3-dimethylaminopropyl)-*N*′-ethylcarbodiimide
eq.	equivalent
Et al.	et alia

FMOC	fluorenyl methoxycarbonyl
h	hour(s)
HCl	hydrochloric acid
HEPES	4-(2-hydroxyethyl)-1-piperazineethanesulfonic acid
HKR	hydrolytic kinetic resolution
HOMO	highest occupied molecular orbital
HPNPP	hydroxypropyl *para*-nitrophenyl phosphate
HRMS	high resolution mass spectrometry
Hz	hertz
Ic	interconnection
Ig	integration
IR	infrared
J	coupling constant
K_2	dimerisation constant
K_{asso}	association constant
K_{eq}	equilibrium constant
k_{obs}	observed constant
LUMO	lowest unoccupied molecular orbital
m	multiplet
Me	methyl
MeCN	acetonitrile
MeOH	methanol
min	minute(s)
mmole	millimole(s)
NMR	nuclear magnetic resonance
p	*para*
Ph	phenyl

PMA	phosphomolybdic acid
PNP	*para*-nitrophenolate
PNPP	*para*-nitrophenyl phosphate
ppm	parts per million
r.t.	room temperature
RNA	ribonucleic acid
s	second(s)
SEPHCHC	2-succinyl-5-enolpyruvyl-6-hydroxy-3-cyclohexene-1-carboxylate
SHCHC	(1*R*,6*R*)-2-succinyl-6-hydroxy-2,4-cyclohexadiene-1-carboxylate
T	temperature
TACN	1,4,7-triazacyclononane
TBME	*tert*-butyl methyl ether
TEM	transition electronic microscope
TEM	transmission electron microscopy
THF	tetrahydrofuran
TLC	thin layer chromatography
TMS	trimethylsilyl or tetramethylsilane
Ts	tosyl
TS	transition state
UV	ultraviolet
v/v	volume to volume ratio
Vol	volume

List of Figures

List of Tables

Attestation of Authorship

I hereby declare that this submission is my own work and that, to the best of my knowledge and belief, it contains no material previously published or written by another person (except where explicitly defined in the acknowledgements), nor material which to a substantial extent has been submitted for the award of any other degree or diploma of a university or other institution of higher learning.

Pablo Solís Muñana

Chapter One

Introduction

1.1. Introduction to catalysis

Catalysis is used to accelerate chemical reactions and allows access to novel chemical reactivity. A catalyst is a substance that increases the reaction rate and which can perform multiple reaction cycles without being consumed and it reduces the overall activation energy. This reduction in avtivation energy is done by lowering the energy of the transition state of the rate-limiting step, or by opening up new mechanistic pathways. Catalysis affects the kinetics of a reaction, not its thermodynamics, and therefore the total change in free energy for a catalysed reaction is the same as that of the non-catalysed one (Figure **1**).[2]

Importantly, catalysis plays a central role in the production of numerous chemical products in our modern, industrialised society. In the chemical industry, 70% of all chemical products are synthesised using catalysis.[1]

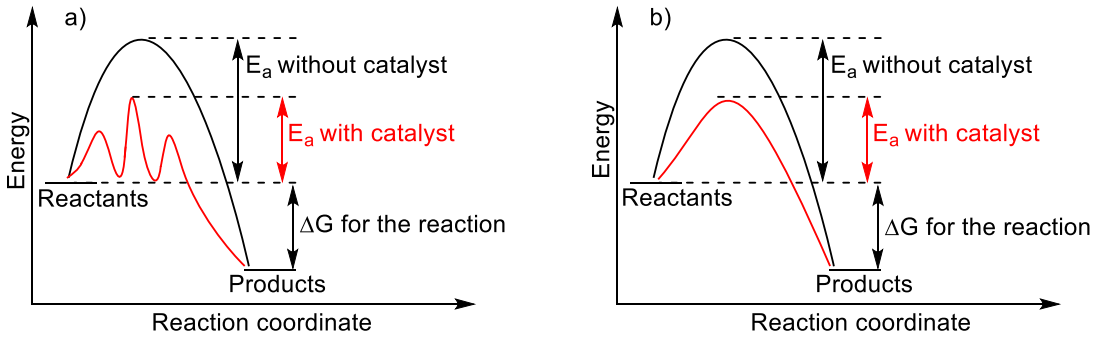

Figure 1. Two examples of the energy profile of an exothermic reaction, the uncatalysed reaction is shown in black and the reaction utilising catalysis shown in red. a) Catalysis allows a new reaction pathway with a lower activation energy. b) Catalysis decreases the energy of the transition state, the reaction mechanism remains the same.

Depending on the phase in which the catalyst is found with respect to the reactants, catalysis can be divided into two major types: homogeneous and heterogeneous. In homogeneous catalysis, the catalyst and the reactants are found in the same phase, while in heterogeneous catalysis, the catalyst and the reactants are found in different phases.[3] In the following example, Rosebrugh, Grubbs and co-workers used homogeneous catalysis to perform ring-closing metathesis reactions, where both the catalyst and the starting material are soluble in dichloroethane. In this example, the researchers used soluble Ru carbene complex **1.1** for the synthesis of macrocycles, achieving good yield and excellent selectivity for the *Z* isomer of lactone **1.2** (**Figure 2**).[4] Ring-closing metathesis is extensively used in organic synthesis to form unsaturated rings, a reaction challenging to achieve without catalysis.

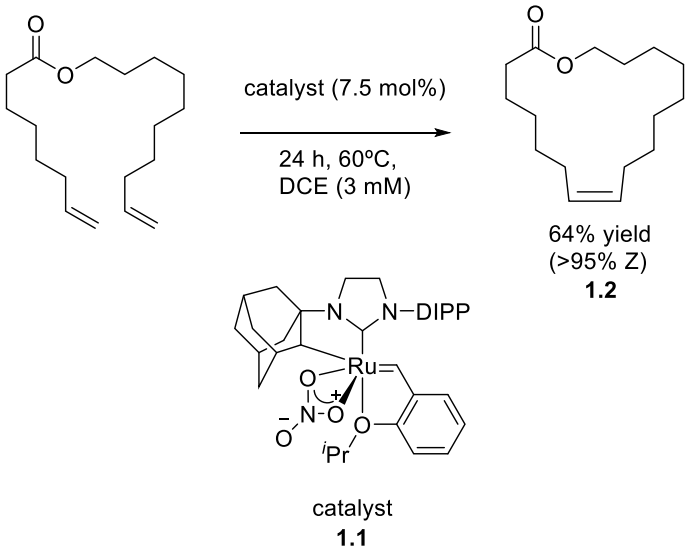

Figure 2. A ring-closing metathesis reaction utilising homogeneous catalysis.[4]

An example of a hydrogenation reaction, this time utilising heterogeneous catalysis, is shown in **Figure 3**. The rhodium-platinum oxide catalyst **1.4** hydrogenates acetophenone (**1.3**) to yield the saturated alcohol **1.5.**[5] Industrially, the most commonly employed heterogeneous catalysts are for hydrogenation reactions.

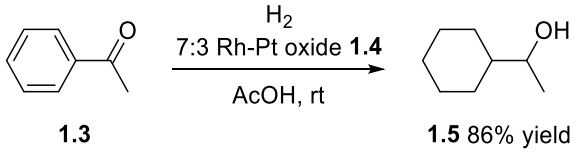

Figure 3. Acetophenone hydrogenation utilising heterogeneous catalysis.[5]

Homogeneous and heterogeneous catalysis each have their specific advantages and disadvantages. With homogeneous catalysis, the catalytic sites and reaction mechanisms are generally well defined, diffusion problems are uncommon, and they typically show higher activities and selectivities. However, catalyst recovery can be difficult, and the stability and, therefore, turnover number of the catalyst are generally lower than heterogeneous catalysts. On the other hand, heterogeneous catalysts generally have longer lifetimes, the products of the reaction can be easily separated from the catalyst, and it is much easier to re-use the recovered catalyst. However, mechanistic understanding of the catalytic activity is generally poor, there can be issues with diffusion, and the selectivity and activity are usually lower than for homogeneous catalysis.[6]

Enzymatic catalysis combines some advantages from homogeneous and occasionally also some from heterogeneous catalysis. Due to their complexity and dynamic nature, enzymes present a series of properties that allow them to achieve yields and reaction rates that are rarely superseded by synthetic systems.[7–10]

1.2. Multi-Catalysis

Catalysis in traditional synthesis generally relies on the activation of a single reagent by a single catalytic unit. While such catalyst systems have been very successful, there has been a recent drive towards the use of multiple catalysts within a single reaction system, in part inspired by biological systems. This strategy is widely used by enzymes and has been referred to as multi-catalysis,[11] where more than one catalytic unit is involved in the activation of a chemical process. For example, the serine-histidine-aspartate triad is known for its nucleophilic catalysis in enzymatic systems. In this system, three functional groups work together cooperatively and are responsible for several chemical transformations, including the 2,5-elimination of pyruvate from 2-succinyl-5-enolpyruvyl-6-hydroxy-3-cyclohexene-1-carboxylate (**1.6**), converting it into the molecule (1*R*,6*R*)-2-succinyl-6-hydroxy-2,4-cyclohexadiene-1-carboxylate (**1.7**) (**Figure 4**).[12,13]

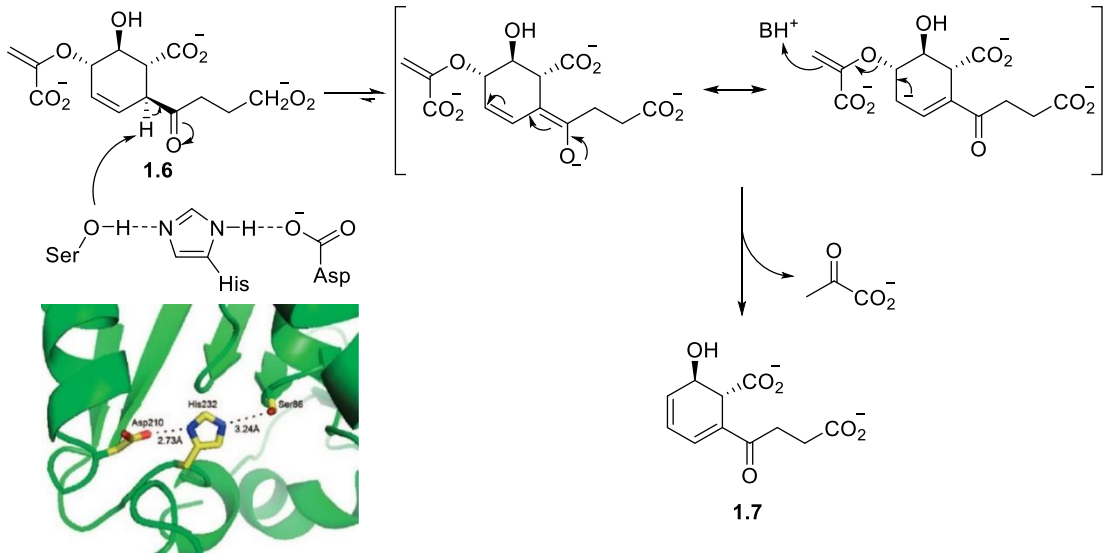

Figure 4. Proposed mechanism of the 2,5-elimination of pyruvate utilising the Ser-His-Asp triad in *E.coli*. [12]

Synthetic chemists have reproduced numerous multi-catalyst systems to enhance reaction efficiencies, successfully demonstrating that these systems can be used to reduce reaction times, obtain higher yields, increase selectivity, and open up new reaction pathways.[11,14] Multi-catalysis is a broad term and encompasses various strategies, including multifunctional catalysis, cascade

catalysis, multiple-activation catalysis, and synergistic catalysis. While these categories may sound similar, there are key differences in the location of the two (or more) catalytic units, whether the catalytic units act on a single substrate or multiple substrates and whether the activation is concurrent or sequential.

1.2.1. Multifunctional catalysis

In multifunctional catalysis, one or more reagents are activated by different functional groups within the same catalytic complex. Usually, in this kind of catalysis, the different catalytic units are joined together covalently. In general, by combining the action of two or more catalytic units, multifunctional catalysis is able to decrease the activation energy for a chemical reaction more than traditional catalysis, achieving enhanced efficiencies.[15] Nevertheless, the optimisation of these catalysts can be challenging. As the various catalytic units are connected covalently, any intention in performing a change in the design of the catalyst requires a re-synthesis and a re-optimisation of the whole catalyst. Covalent bonding can also introduce potentially undesirable conformational rigidity to the system, for example, fixing the orientation of functional groups in an unsatisfactory conformation.[16]

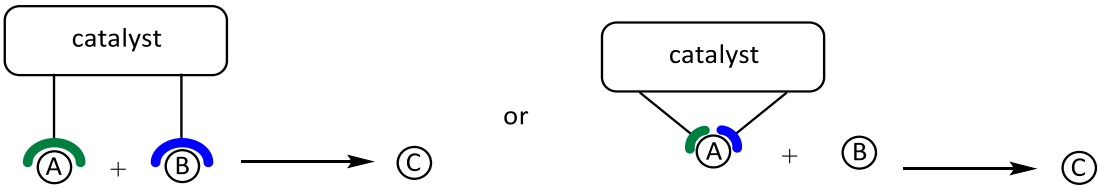

Figure 5. Schematic representation of multifunctional catalysis.

One example of a multifunctional catalytic system is presented by Lin *et al*. and shows a Lewis acid and a Lewis base joined covalently, forming the catalyst **1.8**.[17] It catalyses a [2+2] cycloaddition to form the four-membered lactone **1.11**. The Lewis acid, a Co(II) complex, activates aldehyde **1.9**, increasing its electrophilicity. The Lewis base, a tertiary amine, converts ketene **1.10** into a transient chiral nucleophilic ammonium enolate, which reacts with the activated aldehyde **1.9** to afford the desired *β*-lactone **1.11** (**Figure 6**).

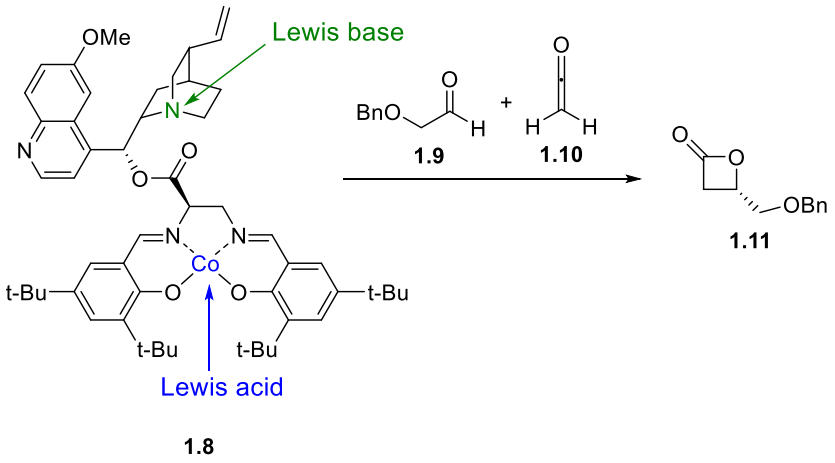

Figure 6. Lactone formation using a multifunctional catalyst.[17]

Another example by Liao *et al*. uses a multifunctional catalyst system to access chiral tetrahydroquinolines (**1.13**).[18] The bifunctional catalyst **1.12** activates the electrophile **1.14** by the combined interaction of three basic sites: an oxygen from the phosphoramide moiety and the oxygens from the triflate moiety, as well as an acidic proton from the phosphoramide moiety (**Figure 7**).

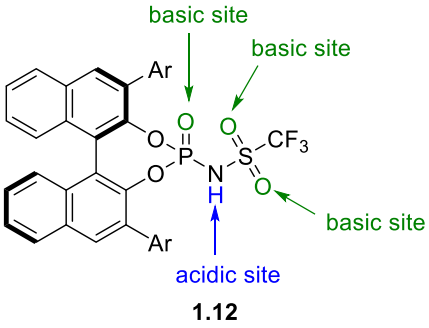

Figure 7. A multifunctional catalyst presented by Liao *et al.*[18]

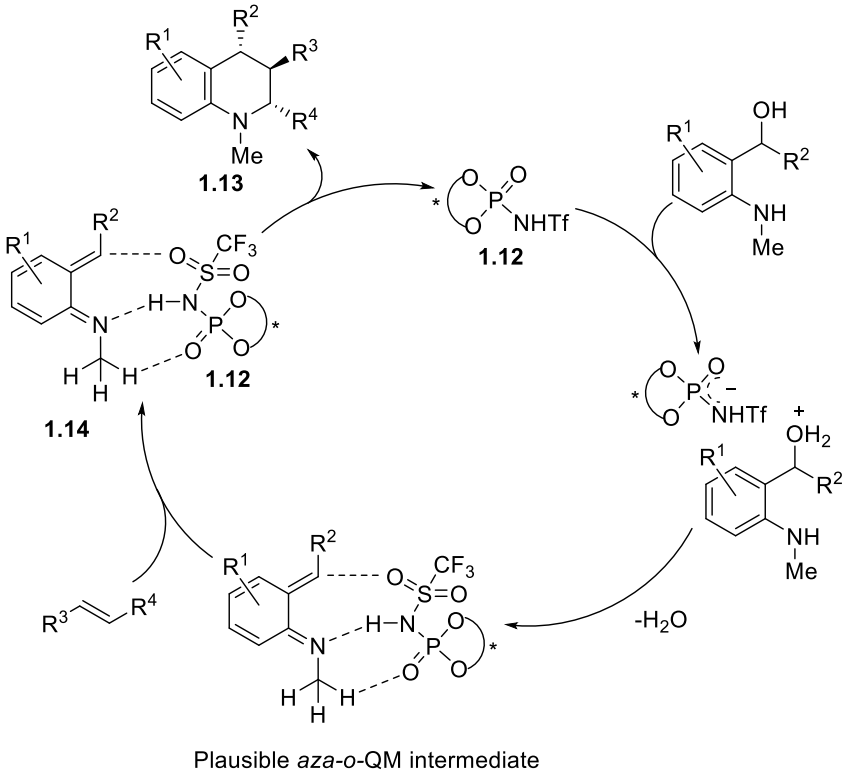

Figure 8. Proposed catalytic cycle involving the multifunctional catalyst **1.12** to synthesise tetrahydroquinolines **1.13**.[18]

1.2.2. Cascade catalysis

Cascade catalysis is another example of multi-catalysis where two or more catalytic units are involved in two or more chemical reactions that occur in a sequential manner (**Figure 9**). The utilisation of this kind of catalysis allows one to perform multiple steps of a reaction sequence in the same flask in a "one-pot" manner. This approach usually reduces the amount of effort, time, and work-ups for a synthesis, and as a consequence, this approach has great importance from the perspective of green chemistry.[19] However, it is worth mentioning that cascade catalysis does not reduce the overall activation energy of the chemical transformations compared to each of the catalytic reactions performed separately.

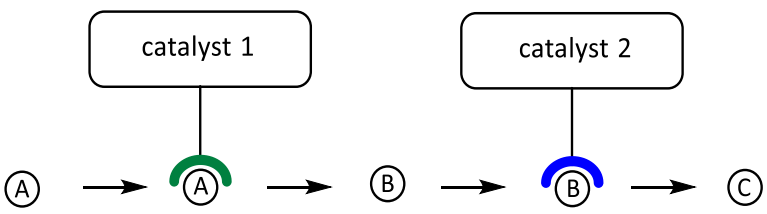

Figure 9. Schematic representation of cascade catalysis.

An example of this cascade approach presented by Belot *et al*. shows two sequential catalytic reactions conducted in a one-pot fashion.[20] The first reaction is an organocatalytic Michael addition, and the second one is a gold-catalysed cyclisation. The stereo-controlled Michael addition is catalysed by Hayashi-Jørgensen's catalyst (**1.17**), which reacts with aldehyde **1.15** to form an asymmetric, nucleophilic enamine. This intermediate reacts stereospecifically with the Michael acceptor **1.16**, forming the functionalised aldehyde **1.18**. The aldehyde then reacts intramolecularly with the triple bond, forming a cyclised product in a stereospecific manner. In this final step, the triple bond is electrophilically activated by the gold catalyst **1.19**. Both reactions were studied separately before being combined in the one-pot approach. Combining both reactions in a one-pot fashion saves energy and resources by removing a work-up and a purification (**Figure 10**).

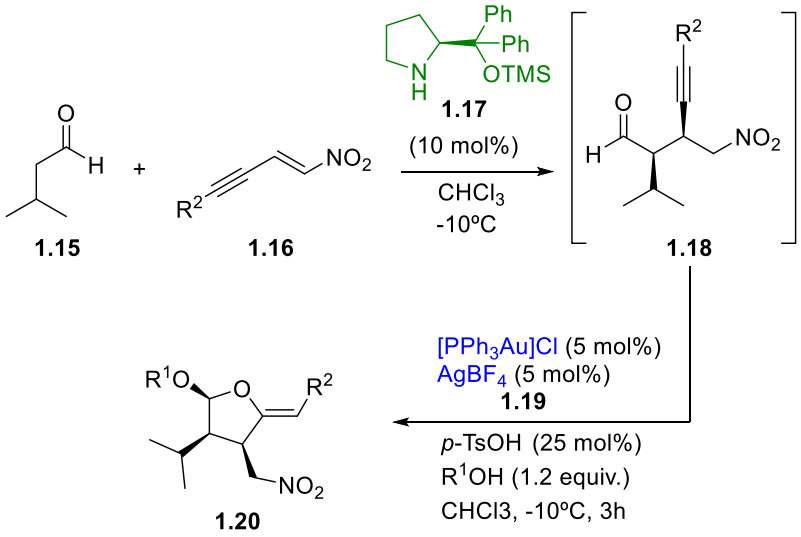

Figure 10. A one-pot organocatalytic Michael addition/gold-catalysed tandem cyclisation.[20]

Another example of cascade catalysis by Chung and co-workers uses three catalytic cascade reactions to synthesise fenestrane **1.24** from enyne **1.21** (**Figure 11**). The first reaction utilises cobalt nanoparticles (**1.25**) to catalyse a Pauson-Khand reaction that transforms the enyne into the bicyclic, conjugated ketone **1.22**. The second step uses Pd(II) catalyst **1.26** to catalyse an allylic alkylation, and introduces an alkyne to form intermediate **1.23**. The third step involves the same catalyst as the first step, cobalt nanoparticles, to drive another Pauson-Khand reaction. This cascade achieved the synthesis of fenestrane in a one-pot manner and good yield over the three-step sequence.[21]

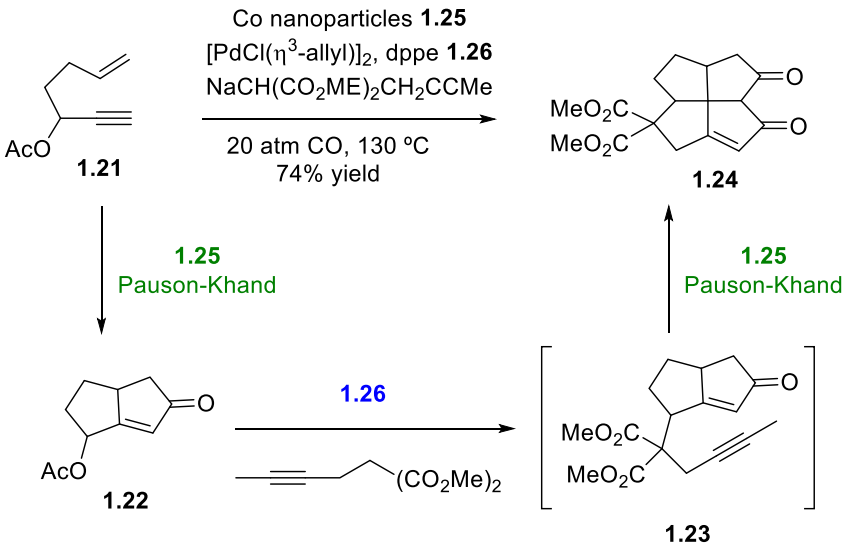

Figure 11. One-pot synthesis of a fenestrane from an enyne utilising three catalytic cascade reactions.[21]

1.2.3. Multiple-activation catalysis

In multiple-activation catalysis, several catalytic units activate the same reagent for a chemical reaction, and those catalytic units are from independent chemical entities. The activation of a single reagent by multiple catalytic units can result in a pronounced rise in its reactivity. This way of activation allows the reagent to react with substrates with which would not normally react.[22] In contrast to multifunctional catalysis, the catalyst units involved in multiple-activation systems are commonly found on different chemical entities rather than being covalently joined together and thus can be optimised individually. There is, however, an entropic price to pay to bring the catalytic units into proximity. In most cases, this means higher concentrations of the catalyst units are required for these systems.

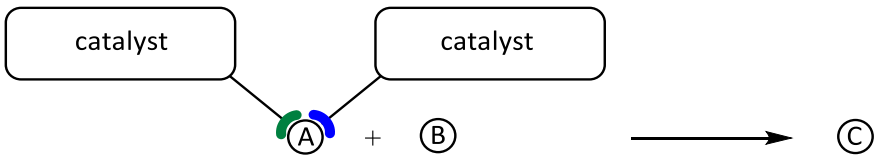

Figure 12. Schematic representation of multiple-activation catalysis.

A fascinating example by Jacobsen and co-workers accomplishes an asymmetric Povarov reaction that utilises two catalytic units acting simultaneously (**Figure 13**). In the proposed transition state, both catalysts activate the same molecule, and both catalysts are held together by

hydrogen bonding. The functionalised asymmetric urea **1.30** activates imine **1.27** with a sulfoxide group and binds to triflate **1.31** by hydrogen bonding from the urea group. Triflate **1.31** activates imine **1.27**, which, once activated, reacts with 2,3-dihydrofuran (**1.28**) to form the polycycle **1.29**.[22]

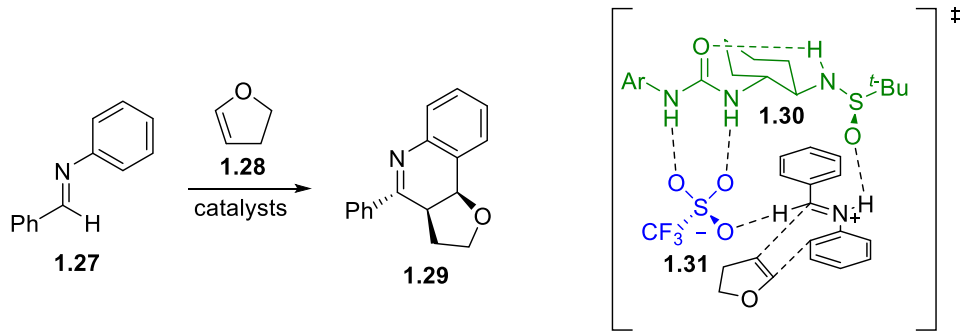

Figure 13. An asymmetric multiple activation catalyst system for a Povarov reaction. Reaction scheme (left), and proposed transition-state (right).[22]

The following example by Shi shows a multiple-activation system used to accelerate a Baylis-Hillman reaction. L-Proline (**1.35**) and imidazole (**1.34**) are the catalysts used to activate the starting material aromatic aldehyde **1.32** and α,β-unsaturated ketone **1.33**. In the proposed catalytic cycle, the reaction starts with the condensation between L-proline and the α,β-unsaturated ketone. The activated iminium intermediate next participates in a 1,4-nucleophilic attack with imidazole as the nucleophile, resulting in the formation of an enamine intermediate. This multiple-activation allows an aldol reaction to occur between the enamine and the aromatic aldehyde, forming a new chiral centre. Finally, an elimination occurs to release the imidazole and L-proline is lost following hydrolysis to obtain the final product **1.36**. Both catalysts activate the α,β-unsaturated ketone in the reaction. It is also worth mentioning that this specific reaction does not proceed with just one of the catalysts present in the reaction media, both are needed to convert the reactants to products (**Figure 14**).[23]

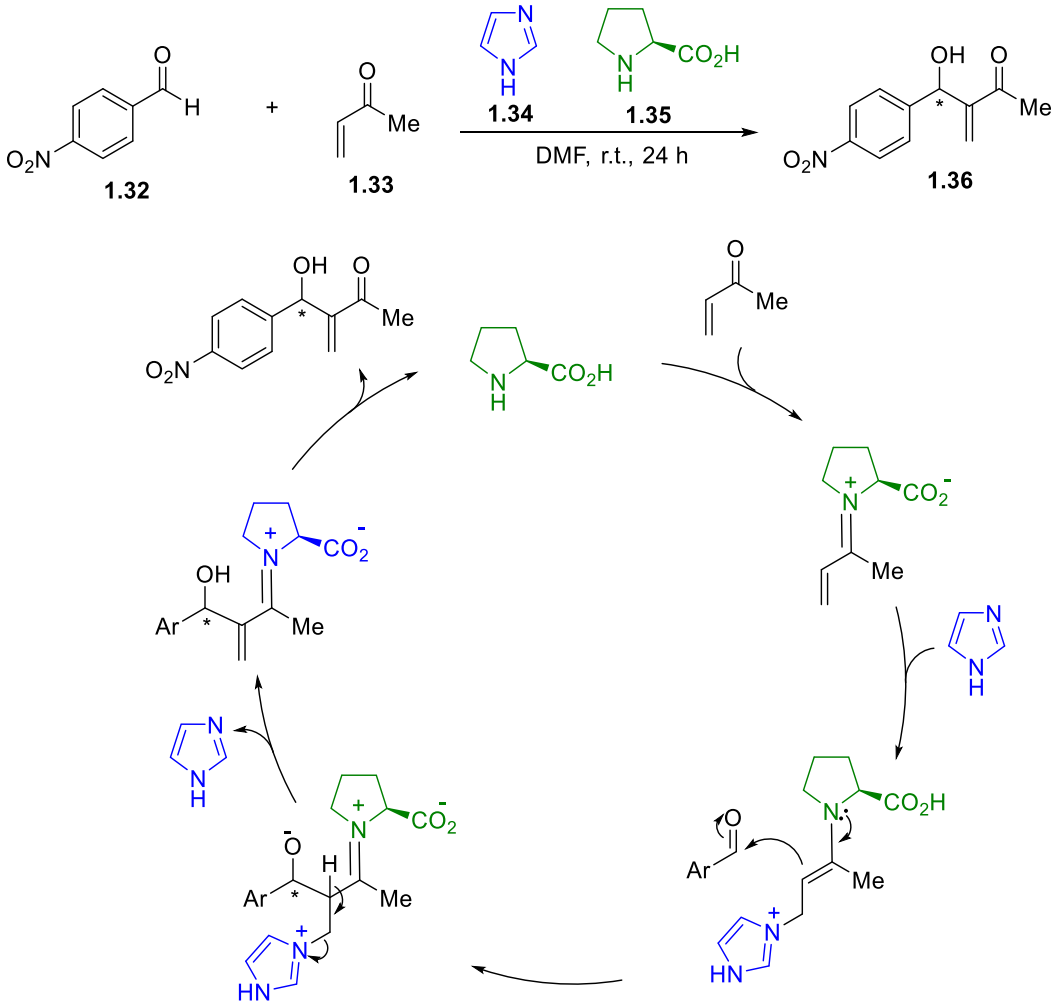

Figure 14. Multiple-activation catalysis combining Lewis base catalysis and iminium activation for the acceleration of the Baylis-Hillman reaction.[23]

1.2.4. Synergistic catalysis

Synergistic catalysis describes situations where various reagents are activated simultaneously but independently by different catalytic units to accelerate a single chemical transformation. In contrast with multi-functional catalysis, in this kind of catalysis, the catalytic units are independent molecules. By utilising synergistic catalysis, chemical species that would not react with each other in un-catalysed conditions can interact and create new bonds, broadening the number of possible chemical reactions and approaches immensely.[11] With this kind of catalysis, as in the case of multiple-activation catalysis, the various catalytic units are not directly joined together, and there is an entropic price to pay to bring them close together to react.

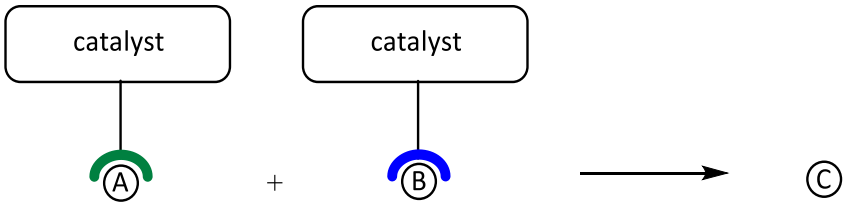

Figure 15. Schematic representation of synergistic catalysis.

Trost and Luan showed an example of synergistic catalysis where a chemical transformation proceeds via the convergence of a vanadium-catalysed propargylic rearrangement and a palladium-catalysed allylic alkylation (**Figure 16**). The vanadium catalyst **1.39** reacts with the propargylic alcohol **1.37** to generate the vanadium-allenoate intermediate **1.42**. This intermediate reacts with another activated intermediate, a π-allyl palladium complex **1.43**, to give the desired alpha allylated α,β-unsaturated ketone **1.41**.[24]

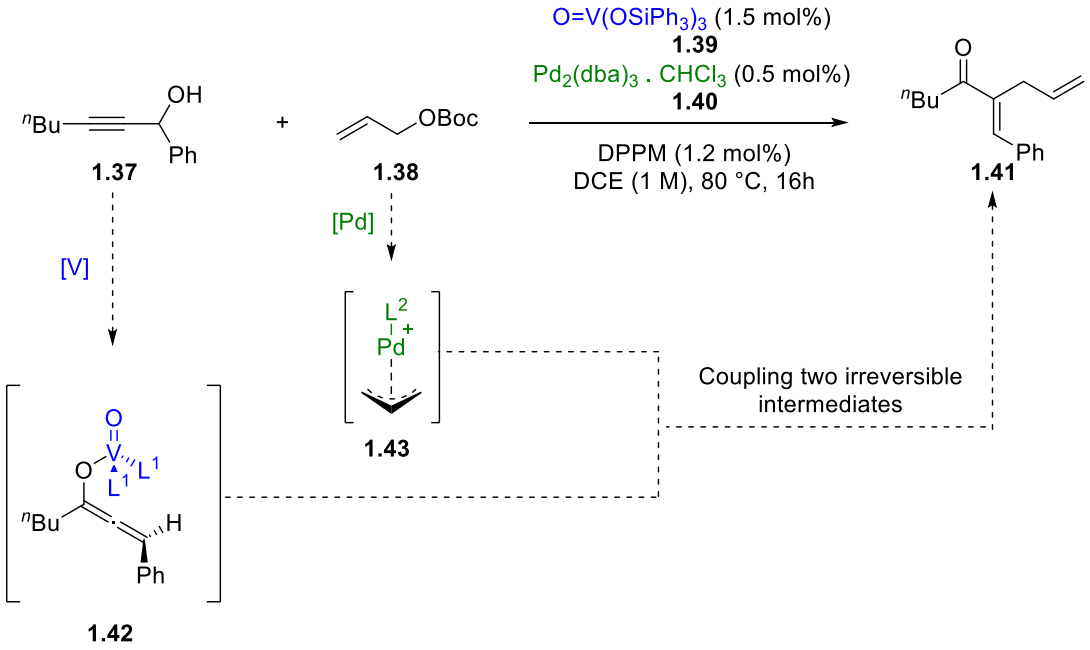

Figure 16. Synergistic catalysis via the convergence of vanadium catalysis and palladium catalysis.[24]

When more than one catalyst unit is involved in reducing the activation energy (E_a) of the rate-determining step (multi-functional catalysis, multiple activation catalysis and synergistic catalysis), we consider that the catalytic units act in a cooperative manner.

1.3. Cooperativity and cooperative catalysis

Cooperativity describes how two or more interactions combine to give behaviour that is not equal to the sum of the individual interactions acting separately.[25] This behaviour leads to what are known as 'emergent' properties – collective functionality not seen in the individual components, and which is a key feature of systems chemistry. A classic example of cooperativity is seen in many enzymes with multiple binding sites. The binding of a ligand to a binding site can increase the affinity of additional binding sites (positive cooperativity) or decrease their affinity (negative cooperativity). An archetypical example of positive cooperativity is the binding of oxygen to haemoglobin. Once an oxygen molecule binds haemoglobin in one of its four coordination sites, the affinity for oxygen of the other three sites increases (**Figure 17**).[25,26]

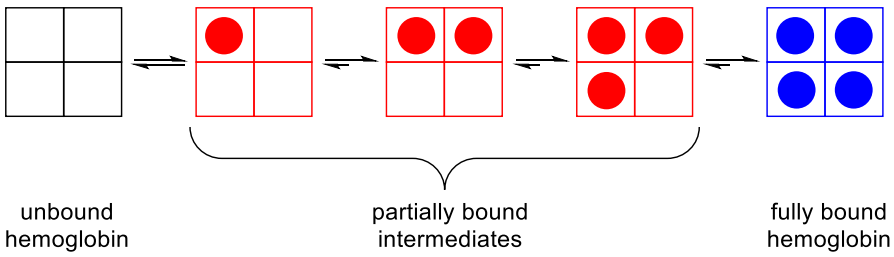

Figure 17. Representation of positive cooperativity in the binding of haemoglobin.[25]

The concept of cooperative catalysis has evolved and advanced rapidly over the past two decades.[14] Novel systems have been introduced to activate substrate(s) with various catalysts to accomplish higher efficiencies than traditional catalysts in terms of reaction rates, yields, regioselectivity, diastereoselectivity, and enantioselectivity. As briefly mentioned above, we define cooperative catalysis as examples of catalysis that decreases the E_a of the rate-determining step of a reaction and which utilises more than one catalytic unit in the activation of one or more substrates. Cooperative catalysis includes multifunctional catalysis, multiple activation catalysis, and synergistic catalysis.

1.3.1. Theoretical aspects of cooperative catalysis

Traditional catalysis decreases the gap between the HOMO (highest occupied molecular orbital) and the LUMO (lowest unoccupied molecular orbital) of two reacting species by either increasing the energy of the HOMO or by lowering the energy of the LUMO (**Figure 18**, a). When employing synergistic catalysis, and with most multifunctional catalysis systems, the energies of both the HOMO and the LUMO are altered to diminish the gap between them, resulting in an

even smaller activation energy and even more effective reaction acceleration. (**Figure 18**, c).[11] In the case of multiple activation catalysis, only one reagent is activated, and the catalysts either increase the energy of the HOMO or reduce the energy of the LUMO of the activated reagent. However, this difference is more pronounced than with mono-activated catalysis (**Figure 18**, b)). With cascade catalysis, multiple reactions are being performed sequentially, but just one catalytic unit is involved per reaction, and therefore, there is no greater activation of the HOMO or LUMO in each step just by adding multiple catalysts.

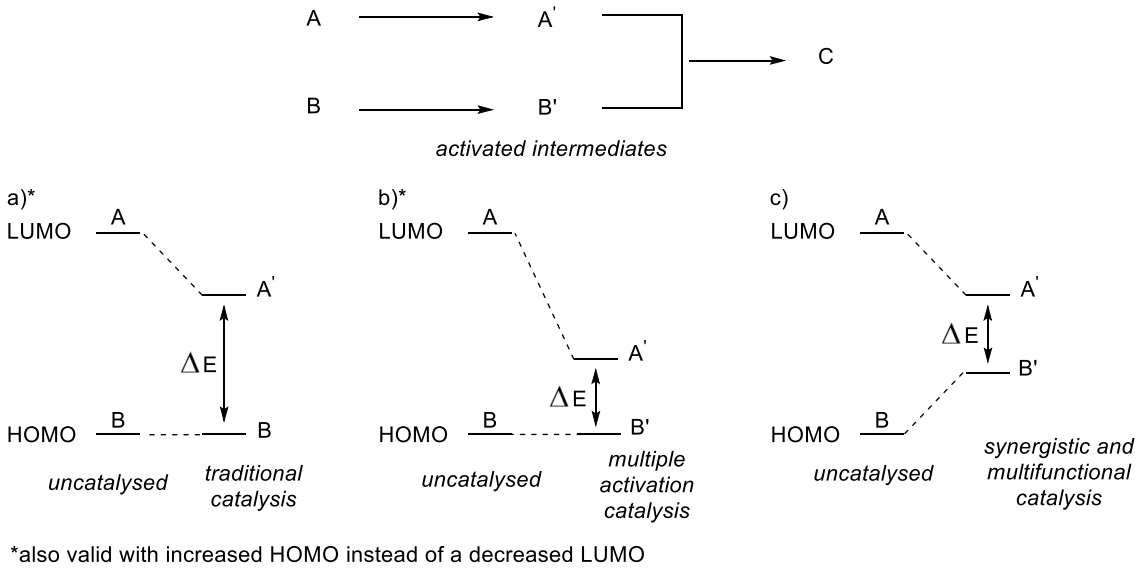

Figure 18. a) ΔE seen with traditional catalysis, b) ΔE seen with multiple activation catalysis, c) ΔE seen with synergistic or multifunctional catalysis.[11]

In an example of synergistic catalysis by Ibrahem and Córdova, two catalysts were added to the system, one decreasing the LUMO of one reactant and the other increasing the HOMO of the second. The reaction studied was the α-allylic alkylation of aldehydes and ketones. The catalytic cycle starts with the condensation of pyrrolidine (**1.44**) and an aldehyde or ketone (**1.45**) to form enamine **1.46**. This enamine formation increases the nucleophilicity of the α position, or in other words, the HOMO of the reagent has increased. In a parallel way, Pd(0) catalyst **1.48** adds oxidatively to allyl acetate (**1.59**), forming π-allylpalladium (II) complex **1.47**. This oxidative addition is needed to increase the electrophilicity of the allylic group, or to rephrase it, the LUMO of the second reagent has been decreased. Once both these reagents are activated, they react to generate the α-allyl iminium cation **1.50** that, after hydrolysis, releases the α-allyl carbonyl compound **1.51**.[27]

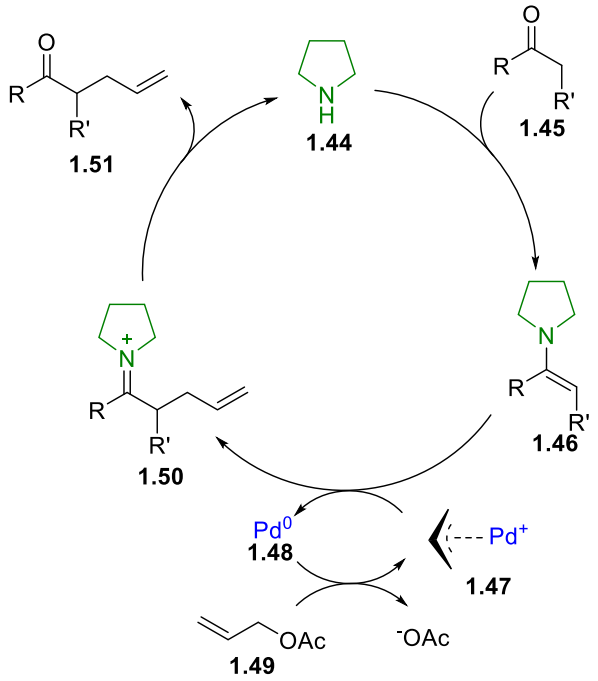

Figure 19. α-Allylation of aldehydes and ketones utilising organocatalysis and palladium catalysis acting synergistically.[27]

When the two required catalysts are added separately in solution, an entropic barrier of bringing multiple catalytic units together needs to be overcome for effective cooperativity to occur. To overcome this entropic cost, several design strategies have been investigated. In the next section, we will explore the advantages and potential of these different strategies for increasing the efficiency of cooperative catalysis.

1.3.2. Methods to enhance cooperative catalysis

1.3.2.1. Covalent bonding between catalytic units

The catalytic units required for cooperative catalysis can be brought together by direct covalent bonding. Examples where two or more of the same catalytic units have been brought together by covalent bonding can be seen in the formation of dimers,[28–30] oligomers,[31,32] dendrimers,[33,34] and attachment onto molecular scaffolds such as calixarenes.[35] There are also various examples where different catalytic units are brought together in space by direct covalent linkage.[36,37]

A study by Matsunaga *et al.*[38] (**Figure 20**) illustrates how the covalently-linked heterobimetallic catalyst **1.54** can be used to perform an asymmetric ring-opening reaction. The linked catalyst provided a higher efficiency than the non-linked counterparts, achieving up to 72% yield and 91%

e.e. of the chiral monosubstituted diol **1.55**. In this example, the gallium moiety activates the oxygen of epoxide **1.52**, increasing its electrophilicity, whereas the lithium stabilises the phenolic alkoxide **1.53**.

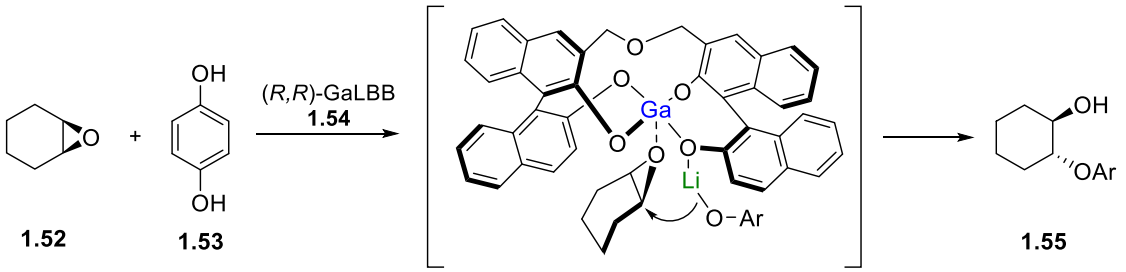

Figure 20. Covalently linked, heterobimetallic catalyst for ring-opening reactions.[38]

An example by Okino *et al.* (**Figure 21**) described a chiral, covalently linked, bifunctional organocatalyst **1.58** for the Michael addition of malonates **1.57** to nitroolefins **1.56**.[39] A thiourea moiety acts as a Lewis acid, whereas a tertiary amine acts as a Lewis base, providing good yields and enantioselectivities. Test reactions involving the thiourea and tertiary amine components added separately in solution resulted in poor yields. Enantiomeric excesses were not tested for this comparison, as the catalysts used for that experiment were not chiral.

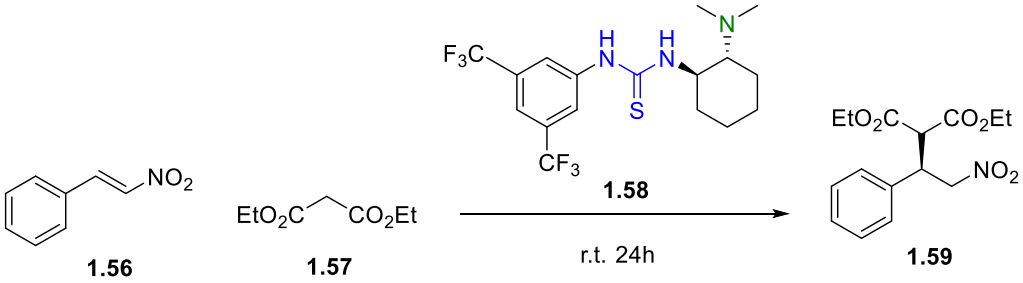

Figure 21. Enantioselective Michael reaction of diethyl malonate to a nitroolefin catalysed by a bifunctional organocatalyst.[39]

Even though covalent bonding is an efficient method for overcoming the entropic barrier in cooperative catalysis, it is not an optimal solution for the discovery of cooperative catalysts, their optimisation it is not as modular as treating the catalysts separately. If one catalyst unit needs to be optimised, the entire catalyst would need to be re-synthesised and re-examined for its catalytic properties.

1.3.2.2. Catalytic units supported on surfaces

A modular approach to constructing efficient cooperative catalysis can be performed by anchoring the catalytic units onto a surface. Examples of surfaces where catalytic units can be anchored onto to achieve an enhancement in reaction rate include metal nanoparticles,[40–42] silica,[43–45] and polymers.[46] An advantage of some of these supported catalysts is the facile recycling of the catalyst, even though the extra step required for immobilisation to bring these catalytic units close together can be considered as another synthetic step, and purification processes are often required to obtain the active catalyst.

The functionalised biomimetic nanoparticle **1.60** by Zheng *et al.* (**Figure 22**) demonstrates how cooperativity was achieved between functionalised aspartate and histidine residues, both anchored onto iron oxide nanoparticles.[47] The reaction was shown to be cooperative and useful for the cleavage of phosphate esters **1.61** and esters **1.62** under mild conditions. The catalyst could also be recovered easily by taking advantage of the magnetic properties of the nanoparticle.

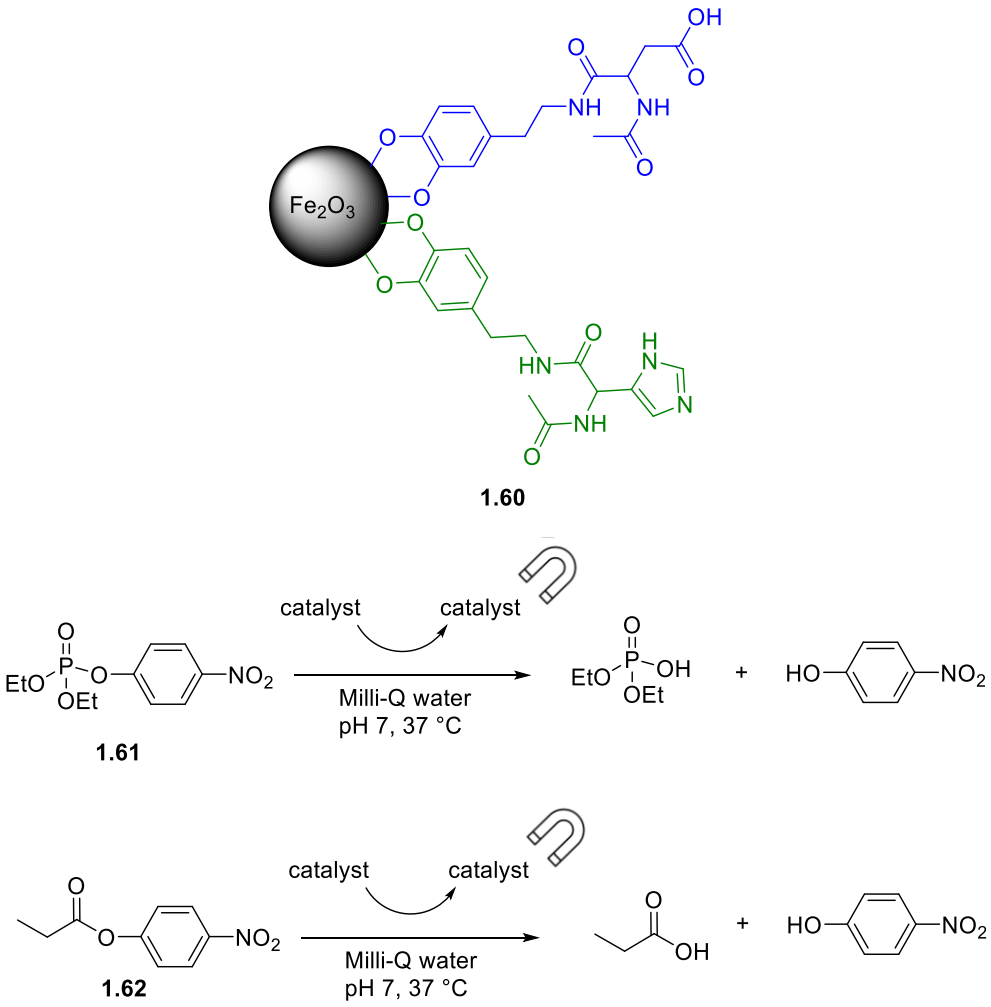

Figure 22. A magnetic, biomimetic nanocatalyst for the cleavage of phosphoesters and esters.[47]

Scrimin and co-workers presented an example of the functionalised gold-nanoparticle **1.63** for the cleavage of bis(*p*-nitrophenyl) phosphate, a model compound for DNA (**Figure 23**).[48] The activation mode involves two positively charged Zn^{2+} ions, with each metal ion coordinated to a cyclic polyamine. These ligands are anchored onto a gold nanoparticle (AuNP), which induces proximity between the active sites. The Zn^{2+} ions act to activate the phosphate ester, making it more susceptible to a nucleophilic attack. The same ions also stabilise a hydroxide anion, which attacks and hydrolyses the phosphate ester, mimicking the enzymatic cleavage of DNA molecules.

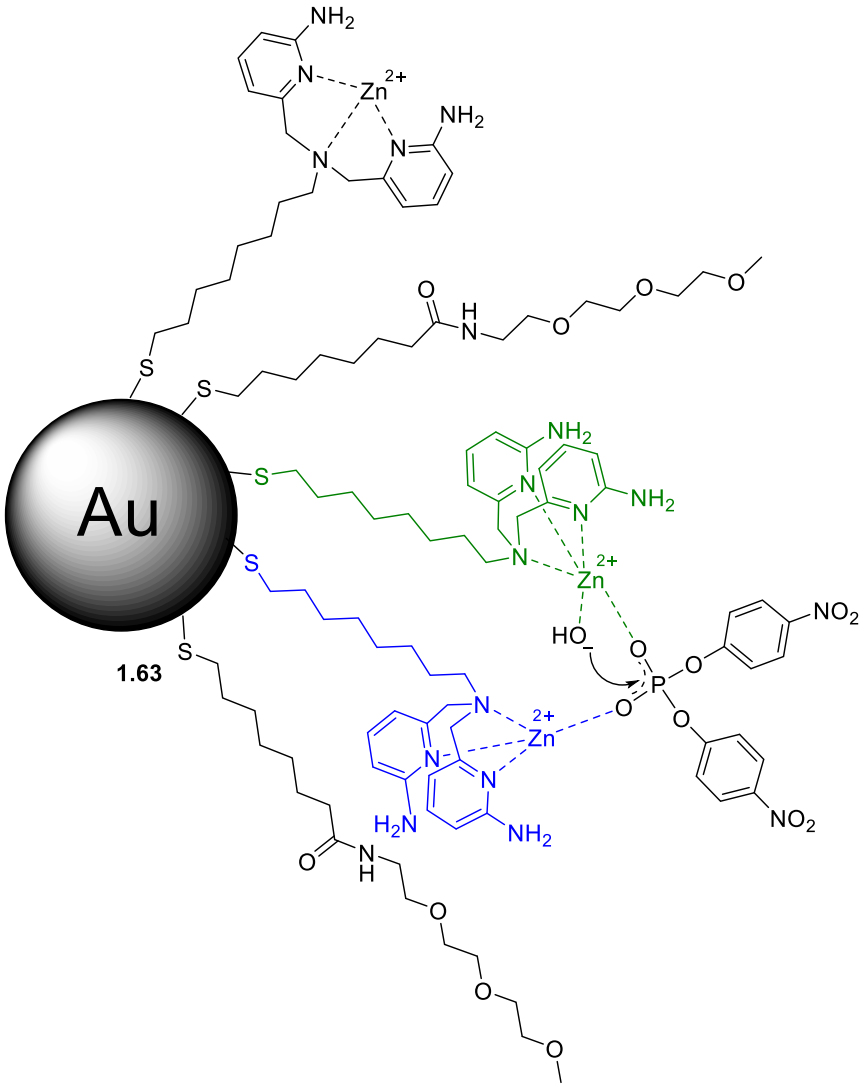

Figure 23. Functionalised gold nanoparticles for the transphosphorylation of a DNA model compound.[48]

Cordova and co-workers have described an example of multifunctional catalysis where different catalytic units are anchored onto a SiO_2 surface (**Figure 24**).[49] One catalytic unit consists of a chiral, functionalised Hayashi-Jørgensen's organocatalyst **1.64**. The second catalytic unit is

formed by coordinated palladium complex **1.65**. The first step of the reaction involves just the Hayashi-Jørgensen moiety and catalyses a stereospecific Michael addition. The second step of the reaction is based on a carbocyclisation reaction where both catalytic units are involved.

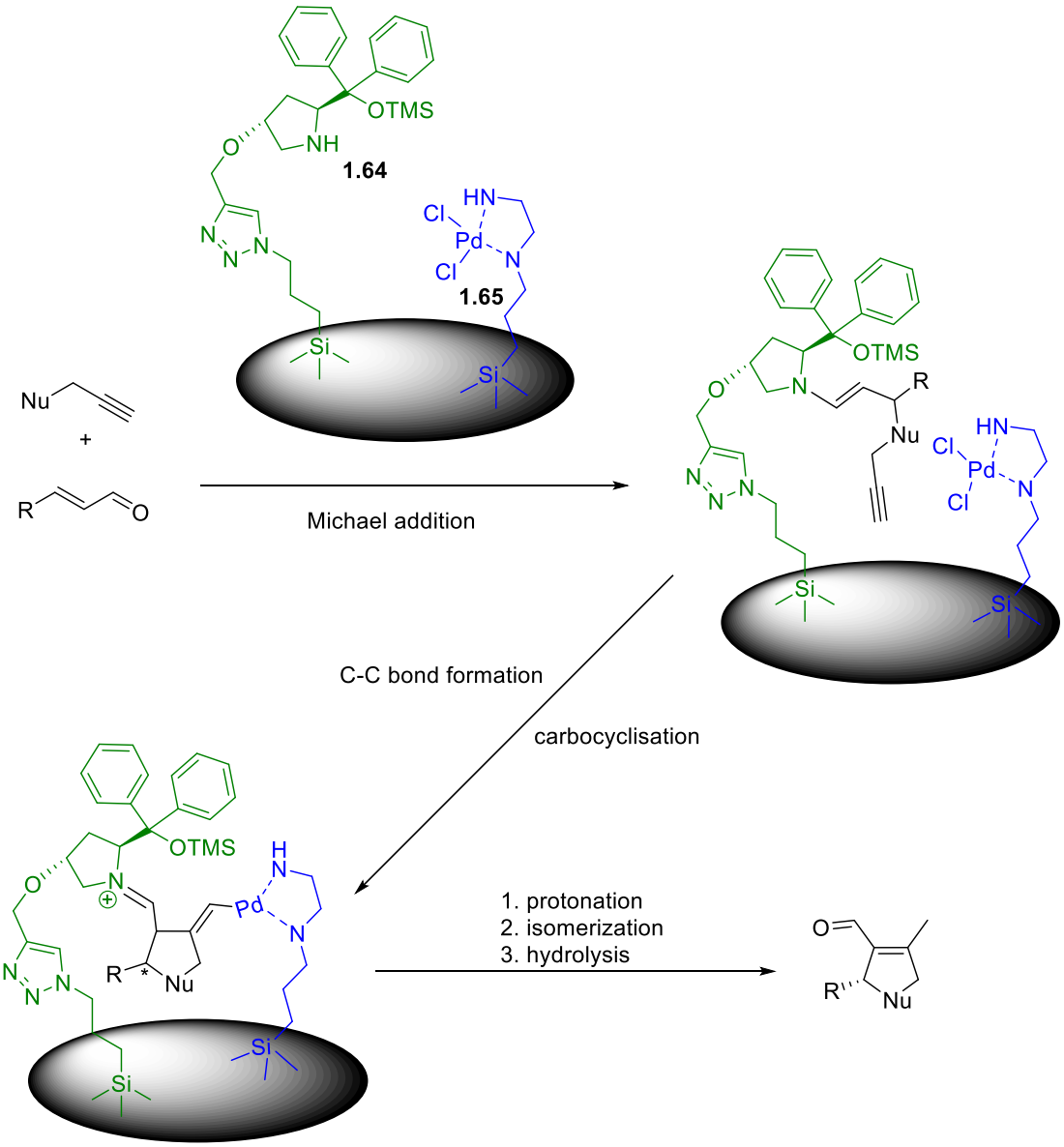

Figure 24. Enantioselective heterogeneous synergistic catalysis for an asymmetric cascade transformation.[49]

1.3.2.3. Hydrogen bonding in self-assembled catalytic units

An even more flexible approach to accomplish cooperativity can be found when the catalytic units are self-assembled. By using this strategy, the catalytic units can be modified individually, and they do not need to be anchored onto a solid surface. This approach avoids extra synthetic and purification steps, making the synthesis of the catalyst more straightforward.

An appealing example of the self-assembly of cooperative catalysts has been presented by Guo *et al.*[50] In this example, two macrocyclic catalytic units (**1.66**) self-assemble using hydrogen bonding (**Figure 25**). The reaction studied was the decarboxylative Mannich reaction of cyclic aldimine **1.67** with β-ketoacid **1.68**, and the rate of the reaction was shown to be second order with respect to the catalyst. Interestingly, the self-assembly process is induced by the presence of the substrate, which results in its chemical transformation by catalysis (**Figure 26**).

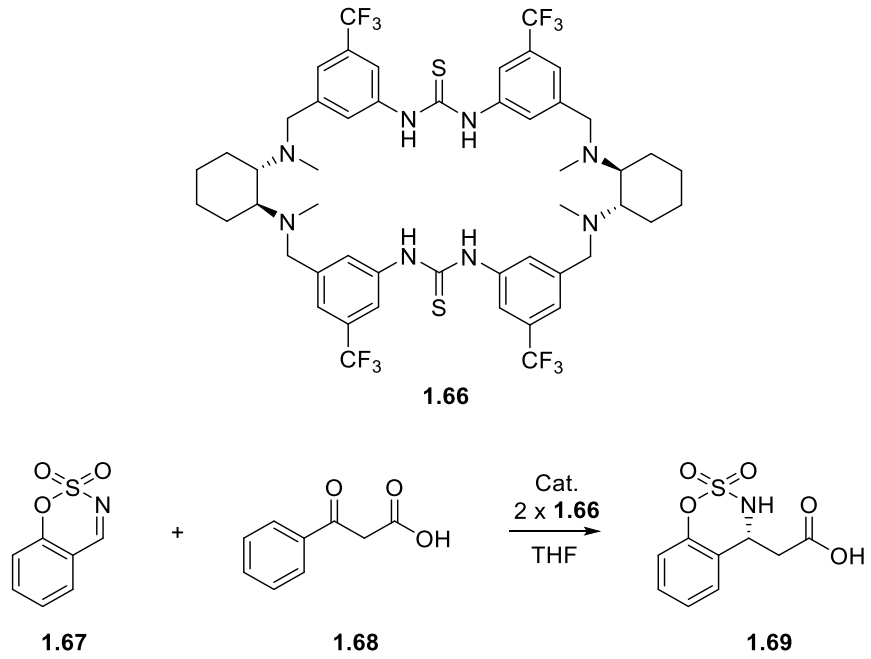

Figure 25. Structure of the tetraamino-bis-thiourea chiral macrocycles and its use in the catalysis of a decarboxylative Mannich reaction.[50]

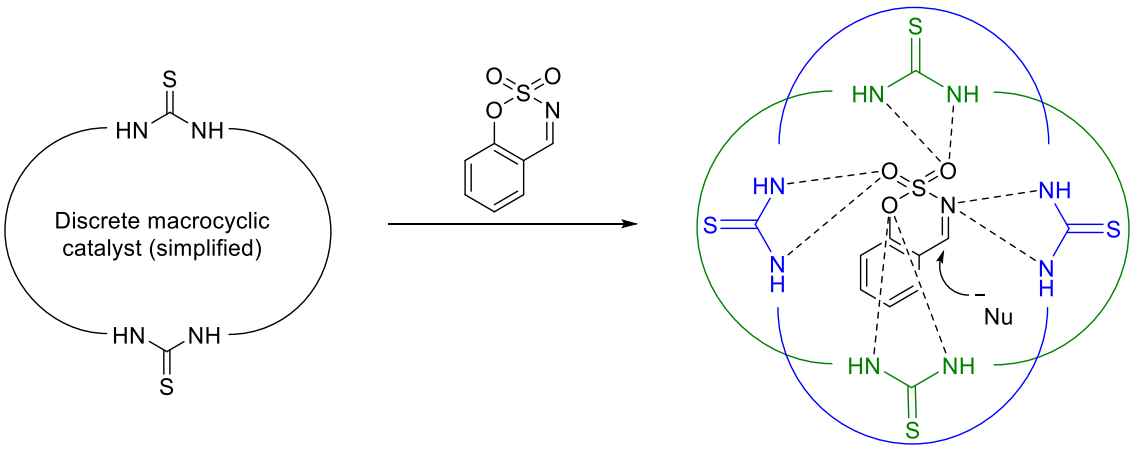

Figure 26. The substrate-induced dimerisation of a chiral macrocyclic catalyst by hydrogen bonding.[50]

Wärnmark and co-workers designed cooperative pairs of catalytic units that self-assembled by hydrogen bonding.[51] They studied the nucleophilic ring-opening reaction of meso epoxide **1.72** by trimethylsilyl azide (**1.73**) (**Figure 27**) and utilised (salen)Cr moieties **1.70** and **1.71** as catalytic units. The reaction displays a second-order dependence with respect to the catalyst,[52] and the reaction showed higher catalytic activity when utilising the hydrogen-bonded dimeric version of the catalyst than when utilising a monomeric version of the catalyst. However, the enantioselectivities of the final product **1.74** were lower than the ones observed when utilising the classic monomeric version of the catalyst.

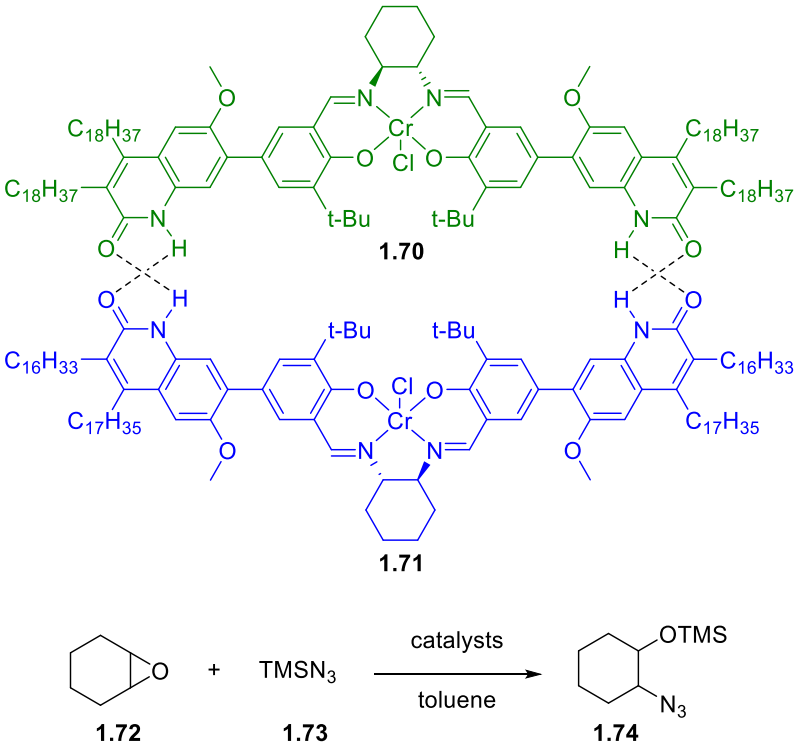

Figure 27. Catalytic pair self-assembled by hydrogen bonding and used in the nucleophilic ring-opening of meso epoxides.[51]

Hong and co-workers presented another example utilising hydrogen bonding to improve catalytic efficiency.[53] This system presented (salen)Co(II) catalytic units (**1.75**), which were functionalised to allow dimerisation by hydrogen bonding. They studied the nitro-aldol reaction utilising aromatic aldehydes **1.76** and nitromethane (**1.77**). The reaction was performed in dichloromethane and in the presence of a tertiary amine base (**Figure 28**). Both the yield and the enantiomeric excess of the final product **1.78** were improved when using the dimeric catalysts compared to the non-functionalised version of the catalyst.

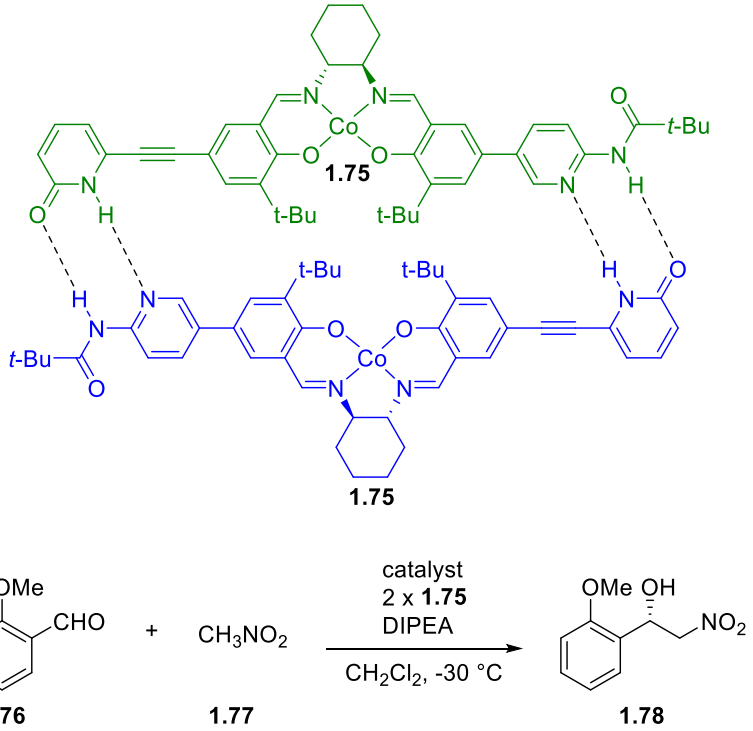

Figure 28. Hydrogen bonding self-assembled dinuclear (salen)Co(II) catalyst for the nitro-aldol reaction.[53]

The same group later used a hydrogen-bonded self-assembled (salen)Co(III) version of these catalysts for the hydrolytic kinetic resolution of terminal epoxides, showing enhanced catalytic activities with the dimeric catalyst over the monomeric control.[54] This example is explained in further detail in the third chapter of this thesis, where we look more closely at the hydrolytic kinetic resolution of epoxides.

1.3.2.4. Ionic pair self-assembled catalytic units

Xia *et al.* presented an example utilising ionic pairs for the self-assembly of the catalytic units. The reaction studied was an enantioselective oxa-Michael-Mannich reaction between a range of salicylic aldehydes (**1.82**) and cyclohexenones (**1.80**).[55] The catalysts are a functionalised pyrrolidine (**1.79**) and a primary amino acid (**1.81**). Two catalytic cycles converge in a key step to form the polycyclic final product **1.83**. One catalytic cycle is based on the condensation of the aromatic aldehyde with the amine of the amino acid, forming an imine. The other catalytic cycle is based on the condensation between the cyclohexenone with the functionalised pyrrolidine, forming an iminium ion. Then both intermediates converge, with protonation of the aromatic

nitrogen atom by the primary amino acid, creating an ionic pair that brings the intermediates close together, enhancing the cooperative reaction (**Figure 29**).

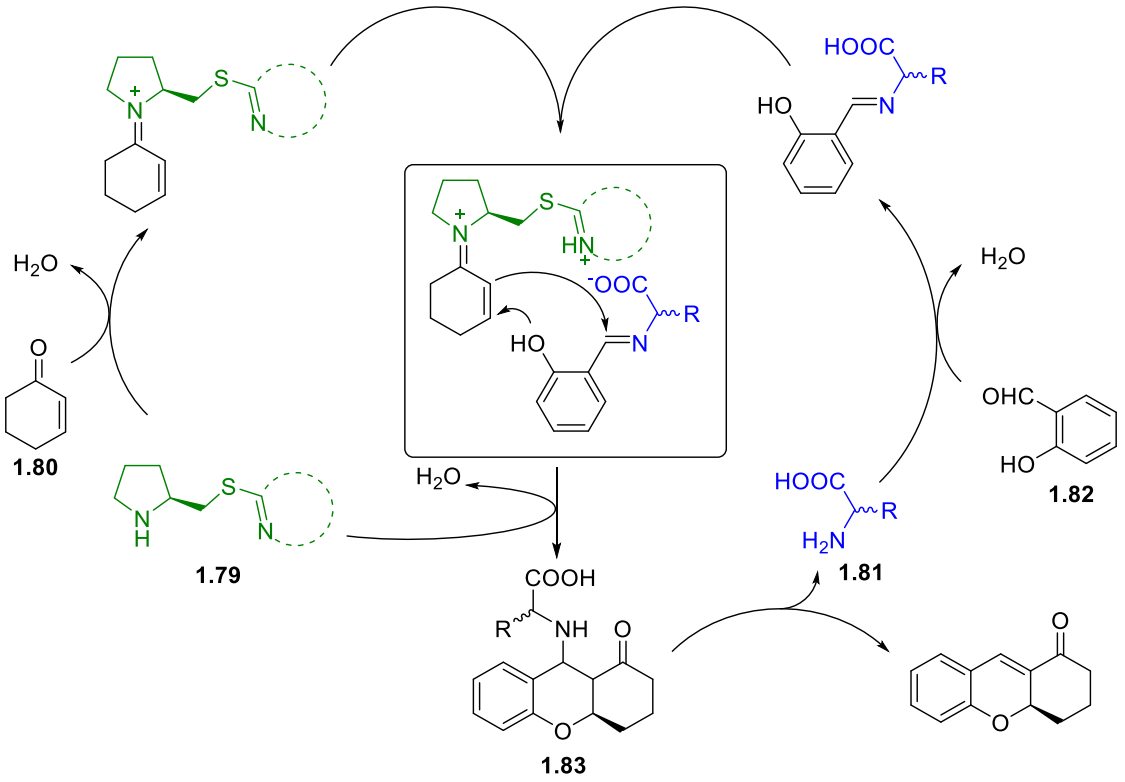

Figure 29. Catalytic ionic pair assemblies in an enantioselective oxa-Michael-Mannich reaction. [55]

The use of dynamic systems such as supramolecular ones present several advantages, including modularity and being more synthetically accessible. Utilising self-assembly also allows the design of systems that can respond to the surrounding environment or stimuli, as in the example presented by Wang *et.al.*[50] where the system responded to the presence of substrate, promoting dimerisation of the catalyst.

1.4. Supramolecular chemistry

Defined by J.-M. Lehn in a Nobel lecture in 1987 as "*the chemistry of the intermolecular bond, covering the structures and functions of the entities formed by the association of two or more chemical species"*,[56] supramolecular chemistry studies non-covalent interactions between individual chemical entities. The first person to postulate the existence of intermolecular interactions was Van der Waals in 1873.[57] In 1890, Fischer introduced the "lock and key"

analogy for the enzyme-substrate interaction as an early concept for molecular recognition and host-guest chemistry, another idea reliant on intermolecular interactions (**Figure 30**).[58]

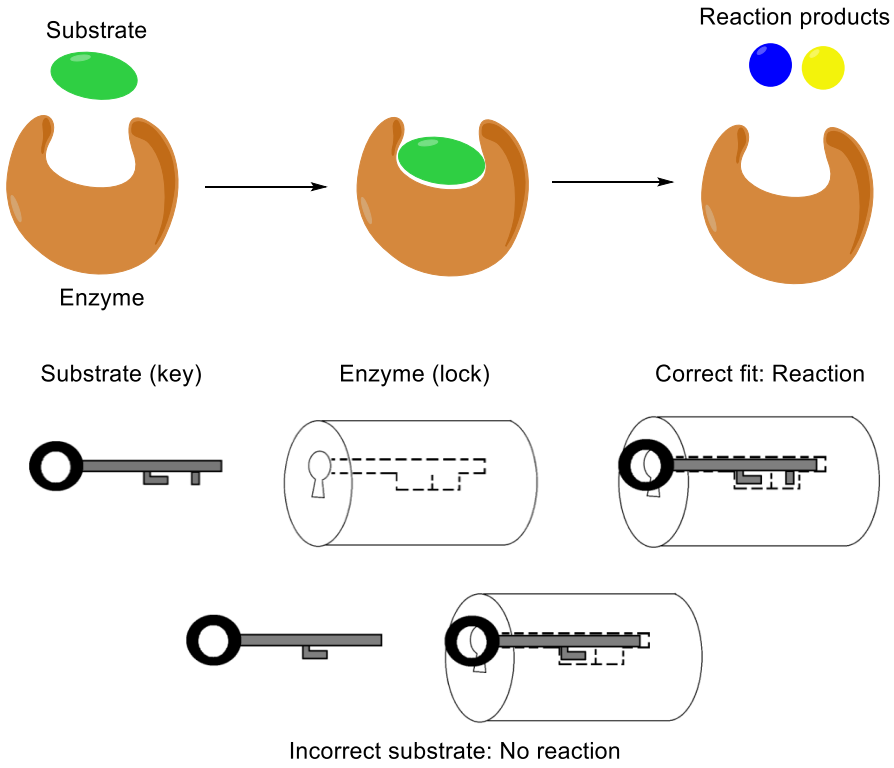

Figure 30. Lock and key analogy for enzymatic substrate selectivity.[58]

Correct interpretations of hydrogen bonding played a vital role in the elucidation of the double-helix shape of the DNA molecule in 1968.[59] Around the same time, self-assembled structures based on non-covalent interactions like micelles and microemulsions were studied and elucidated by chemists. Furthermore, in the 1960s, Pedersen synthesised the first macrocyclic crown ethers **1.84** (**Figure 31**).[60] This achievement was a breakthrough in the field, as it was one of the first examples of the utility and potential of synthetic supramolecular systems.

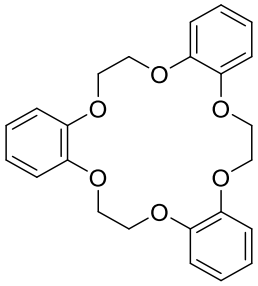

1.84

Figure 31. Example of a crown ether synthesised by Pedersen.[60]

In 1987, Lehn, Cram and Pedersen were awarded the Nobel Prize for their work in selective host-guest complexes. In the 1990s, molecular machinery starts to be developed by researchers like Stoddart,[61] who earned the Nobel Prize in 2016 for the design and synthesis of molecular machines alongside Feringa and Sauvage. Sauvage described the synthesis of catenanes and molecular knots,[62] Feringa worked on developing molecular motors,[63] and Stoddart described the synthesis of rotaxanes.[64]

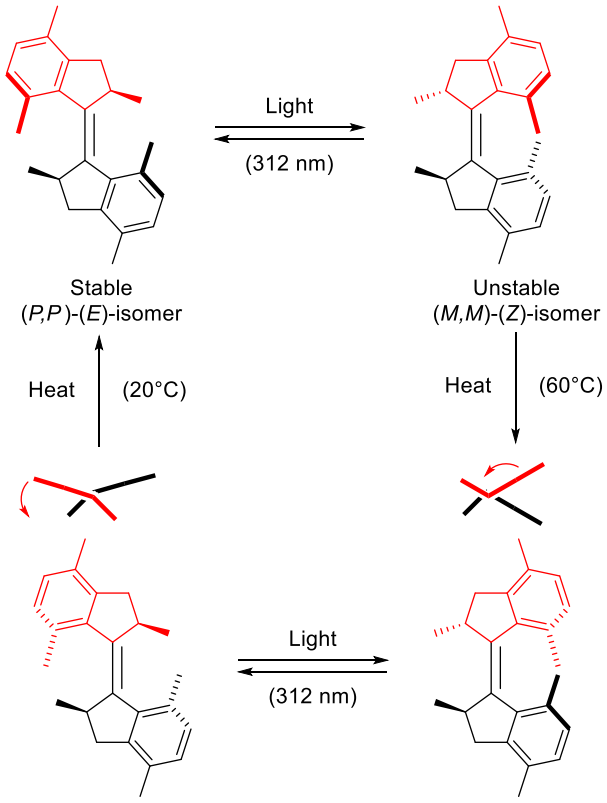

Figure 32. Feringa and co-workers' molecular rotor [65]

Currently, supramolecular chemistry is still a "hot" and rapidly evolving subject, fundamental in the development of nanotechnology, new materials, catalysis, drug delivery, and plays a critical role in the study of non-equilibrium systems and how supramolecular forces are involved in self-organisation and the origin of life.[66]

1.4.1. Self-organisation

Self-organisation refers to processes where the organisation or order of a (generally open) system increases without being guided by an external agent. Examples of self-organisation can be found in a wide variety of systems. For example, at the atomic level, self-organisation phenomena are responsible for properties such as spontaneous magnetisation. At the molecular level, we can find self-organisation with, for example, processes such as micelle formation. In biology, we can observe self-organisation when cells order themselves to form tissues. Social systems are also relevant forms of self-organisation. For example, humans divide tasks and share wealth to advance and create fairer environments to live in.

From a chemist's point of view, self-organisation may occur as part of thermodynamic equilibrium systems, kinetically trapped systems, or non-equilibrium systems (**Figure 33**).[67] In the first two cases, where structures are formed from components at thermal equilibrium or in a kinetically trapped state, the structures formed are stable over time. In non-equilibrium self-assembly, the structures require a constant input of energy to maintain a high energy state. This requirement for the input on energy and the dynamic nature of these systems allows the introduction of time-dependent, dissipative processes.[68,69]

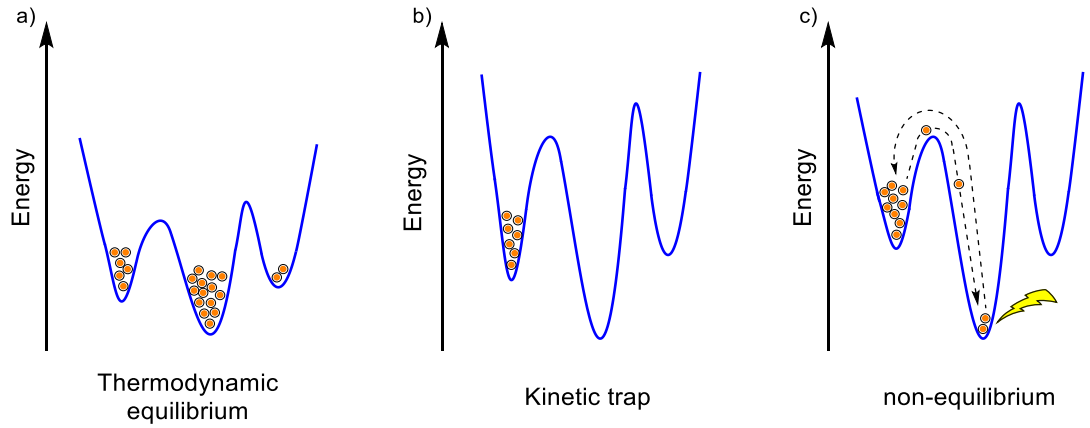

Figure 33. Schematic representation of the Gibbs free energy diagrams of: a) system at a thermodynamic equilibrium; b) system at kinetic trap; c) non-equilibrium system, where energy is utilised to achieve an out-of-equilibrium, dissipative state.[69].

The properties of a system that arise collectively from interactions among the system's components are defined as emergent properties. For instance, a single heart cell is not able to pump blood, but all the heart cells that combine to form the heart, and which then act together collectively, can. Emergent properties can appear from self-organisation and lead to complexity. Complexity and emergent properties can be found in all levels of organized systems, from sub-atomic to atomic, atomic to molecular, molecular to supramolecular and supramolecular to cellular levels. Beyond that, it can be seen from cells to tissues, tissues to organs, organs to organisms, organisms to societies, and societies to ecosystems (**Figure 34**).

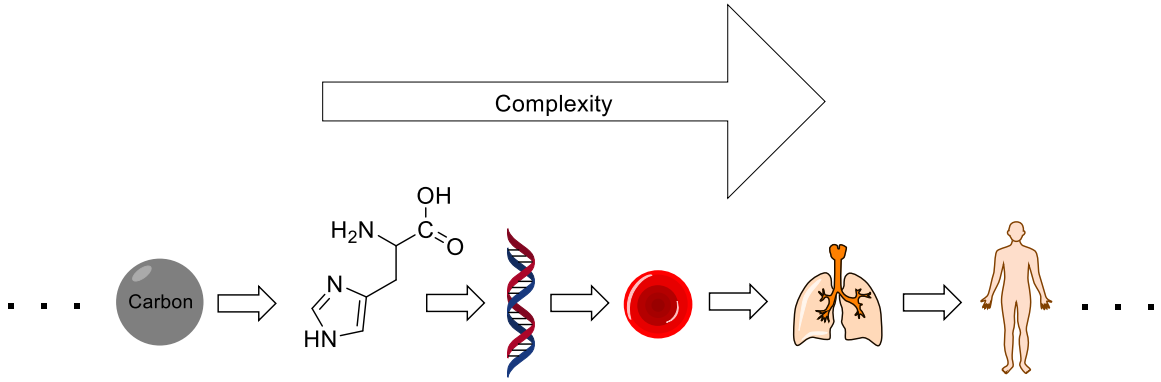

Figure 34. Towards complexity.

An important emergent property of chemistry and non-equilibrium systems is life itself. It is generally accepted that living beings must possess the ability to replicate, utilise energy and chemical resources through metabolism, and be compartmentalised as individual entities; it is not so clear, however, how these properties were integrated into the transition from non-living matter to living matter (and where the frontier was established between these two). Most theories consider that the key trigger could be the development of a system capable of self-replication. One possible scenario is the incorporation of metabolic processes into a self-replicating system. Two recent examples that utilise system chemistry approaches have demonstrated how this scenario may have been possible. The first example by Monreal Santiago, Otto *et al.* show how a synthetic self-replicator can employ a photoactive co-factor to form a photocatalytic structure and harness light energy to increase its replication rate.[70] The second example by Ottelé, Mayer, Otto *et al.* demonstrates how the self-replicator can spontaneously acquire catalytic properties in an example of proto-metabolism.[71] Both studies are based on a self-replicating system emerging from a dynamic library of disulfide-based macrocycles in equilibrium, and for both studies, the building block is a peptide sequence that terminates in a benzene-1,3-dithiol moiety (**1.85**). The building blocks combine to form a mixture of trimeric and tetrameric based macrocycles under oxidative conditions. Also, small amounts of hexamer are formed, and these self-assemble into

fibres. These fibres have the ability to exponentially grow if mechanically agitated and are the self-replicator of interest (**Figure 35**).

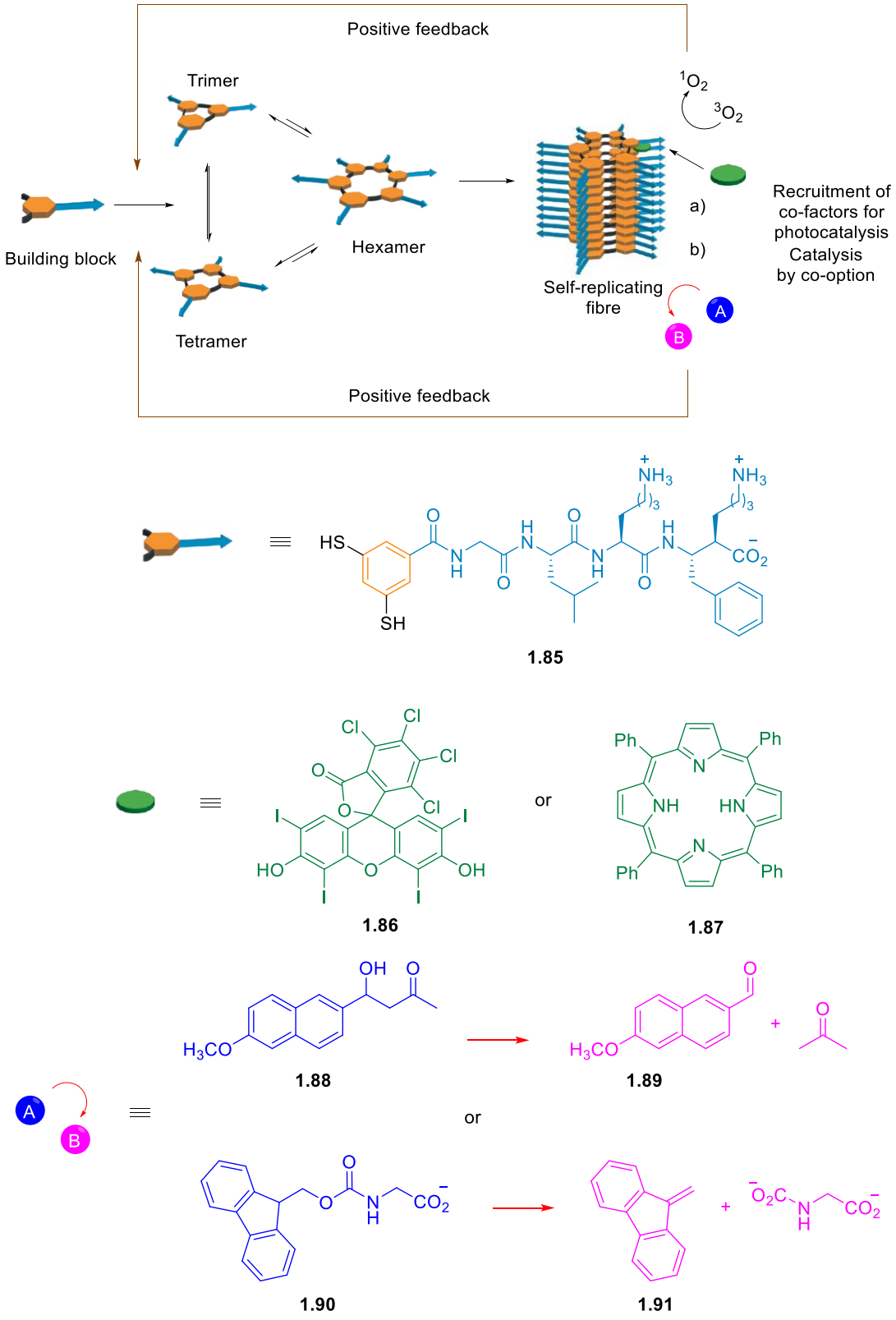

Figure 35. Schematic representation of the formation of a self-replicator capable of protometabolism and legend. [70–72]

In the first study (**Figure 35a**), it is shown how a self-replicator can harness energy from the environment and utilise that energy to enhance its ability to replicate. Co-factor recruitment processes accomplish this, and some organic dyes known to promote the formation of singlet oxygen ($^1O_2$) were investigated. These oxidative state allows the oxidation of the building block's thiols to disulphides, forming trimers and tetramers, the precursors of the self-assembling hexamer. Rose Bengal (**1.86**) was one of the co-factors studied, and its structure allows it to interact with the fibres made from the hexamer by forming a supramolecular J-aggregate (a type of dye whose absorption band shift to a longer wavelength when it self-assembles). A new red-shifted band in the absorbance of Rose-Bengal allowed irradiation of the fibre-Rose Bengal structure in a selective manner utilising yellow light. This property promoted the generation of singlet oxygen, which increased the concentration of trimers and tetramers, and promoted fibre growth resulting in a positive feedback loop. Tetraphenylporphyrin (**1.87**) could be used as an alternative co-factor. This dye is known to be poorly soluble in water, but its better solubility in the presence of the fibre resulted in the promotion of the formation of single oxygen. It is important to remark that the fibres formed from the hexamers solubilises tetraphenylporphyrin (**1.87**) more efficiently than the trimers or the tetramers. This example illustrates how a simple mechanism such as enhancing solubility can result in the recruitment of co-factors by a replicator.[70]

The second study (**Figure 35, b)**) explains how the ability to catalyse chemical reactions can emerge spontaneously from the self-replicator, this being an essential characteristic of metabolism. The reaction studied was the retro-aldol reaction of the β-hydroxyketone 'methodol' (**1.88**). The formation of the fibre creates binding pockets for the hydrophobic substrate to bind. The self-assembly of the building blocks also brings the lysine residues together, lowering the apparent pK_a. The enhanced nucleophilicity of the lysine residues accelerates the retro-aldol reaction. Notably, the emergence of catalytic activity could be correlated with fibre formation since the effect is more significant than the effect with the monomeric building blocks or the mixture of trimers and tetramers. The team also studied the catalytic cleavage of FMOC-glycine (**1.90**), utilising the enhanced Brønsted basicity of the lysine residues once self-assembly occurs. Deprotonation of the acidic proton of the FMOC causes its fragmentation and the formation of an alkene, dibenzofulvene (**1.91**). The formation of this alkene accelerated the oxidation of the building block, forming the trimer and tetramer mixture that provide positive feedback of the self-replication process. The structures formed were selected for their ability to replicate instead of for their catalytic activity. This publication demonstrated how a self-replicator is able to spontaneously acquire catalytic activity, an essential step for a replicator to potentially achieve metabolism.

1.4.2. Supramolecular self-assembly

From a chemistry perspective, self-assembly refers to the process by which larger species spontaneously form from smaller components.[73] It should be noted that self-assembly is not just an attribute of a supramolecular system; it is also present in other chemical systems such as the growth of crystals and more, biological systems and other kinds of systems.

Self-assembled molecular systems that use weak, non-covalent forces open up the possibility of forming structures that are in equilibrium with the non-assembled form, since the interactions involved are generally reversible. In particular, in this thesis, we are interested in the hydrophobic effect; this is the tendency of non-polar molecules to form aggregates in the presence of water.[3,74] Amphiphiles are perfect candidates to study these systems and effects, as they can interact with each other non-covalently, making larger supramolecular assemblies.

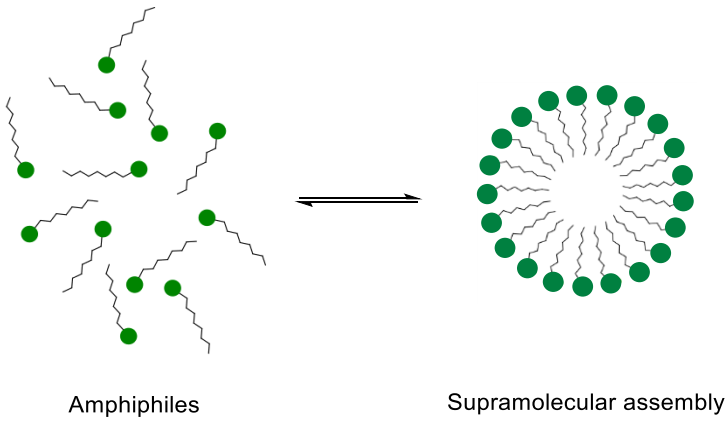

Figure 36. Representation of the self-assembly of amphiphiles.

Amphiphiles denote compounds that contain moieties that have an affinity for both water and oils. They are made of a hydrophilic part, usually called the head group, and a hydrophobic fragment frequently called the tail. This dual behaviour makes amphiphiles behave very peculiarly in the presence of water, as they generally self-assemble above specific concentrations creating aggregates that are in equilibrium within the non-aggregated amphiphiles. Some examples of supramolecular self-assemblies formed by amphiphiles include micelles, vesicles, Langmuir monolayers and liquid crystal phases.[75]

1.4.3. Supramolecular catalysis

Enzymatic catalytic systems have been the biggest inspiration for supramolecular catalytic systems. [9,10,76] Whereas enzymatic systems are far more complex than supramolecular systems, by designing simpler systems, one can estimate the relative importance of different structural factors in an enzymatic catalyst. Simpler systems are also synthetically more accessible and will generally tolerate a much wider range of reaction conditions than enzymes. Ultimately, the development of supramolecular systems that are able to replicate the efficiencies observed in enzymatic catalytic is one of the key goals of supramolecular catalysis research.

Different biomimetic supramolecular systems have been developed over the years. An example that utilises cooperative catalysis is presented by Salvio *et al.* and demonstrated how guanidinium and a Cu^{2+} anchored onto the calixarene moiety **1.92** cooperatively catalysed the transphosphorylation of an RNA model molecule. One of the roles of the *cone*-calix[4]arene moiety is to allow the precise allocation of both catalytic units in space,[77] achieving excellent catalytic rates for the transphosphorylation reaction compared to the non-supported molecules.

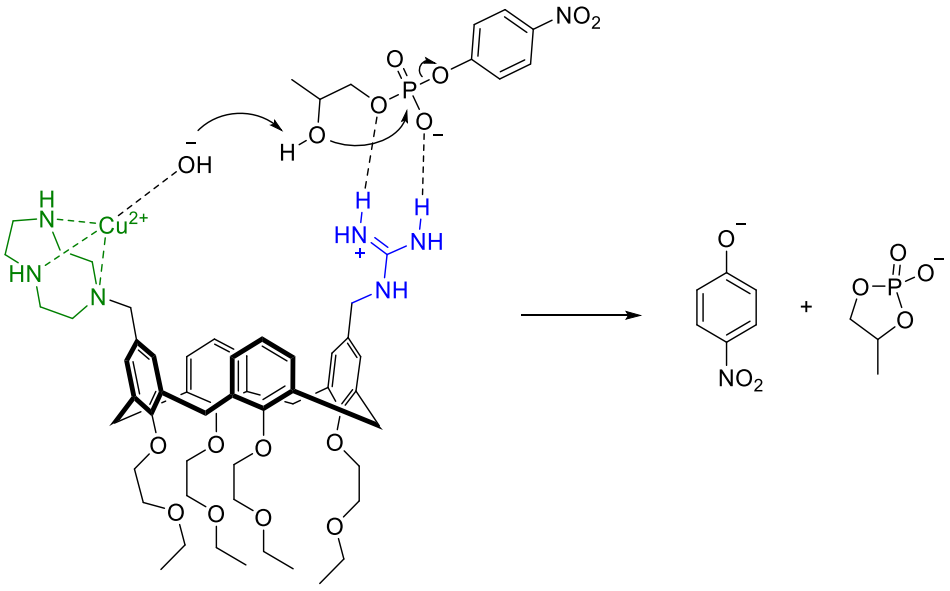

1.92

Figure 37. RNA model molecule transphosphorylation by *cone*-calix[4]arene Cu^{2+}/ guanidinium supported catalyst.

Another biomimetic example by Cram and co-workers presents a chiral acyl transfer catalyst that contains crown ether **1.93**. The stereospecificity of the catalytical reaction can be rationalised by a predicted complementary fit of guest to host. The host-guest binding involving the ammonium

ion from the guest **1.94** resembles the transacylation reactions performed by the enzyme trypsin (**Figure 38**).[78]

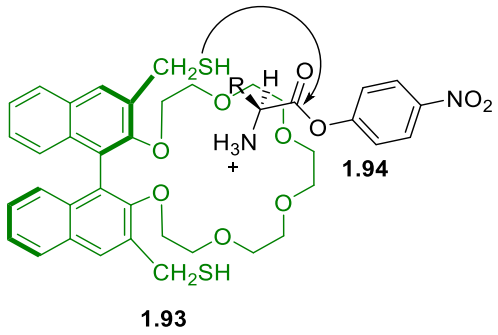

Figure 38: Cram's crown ether transacylation catalyst.[78]

In 1998, Sanders pointed out that even though supramolecular catalysis is a well-developed field, there are very few examples of practically useful supramolecular catalysts.[79] He suggested that this failure may come from the delicate and quite unpredictable balance between the need for rigidity and the need for conformational flexibility. Taking enzymes as an example of a perfected catalytic model, Sanders affirmed that its efficiency is achieved by intermolecular interactions that guide the trapped substrates very precisely along the reaction pathway towards the transition state and beyond. His reflections on ways to improve these catalytic systems were condensed in the following sentence: *"... in the search for effective catalysis the fear of entropy in flexible systems has taken us too far in the direction of rigidity and pre-organization"*.[79] From this, it could be interpreted that there has not been enough research into tactically positioning catalytic functionalities using dynamic approaches rather than relying on pre-organisation.

1.5. Aims of this thesis

The principal objective of this thesis is to demonstrate that cooperative catalysts can be formed by utilising hydrophobic interactions to induce the self-assembly of the required catalytic units. Apart from the initial proof of concept study, we aim to demonstrate that this concept can be applied to synthetically useful systems. We are interested in multi-catalytic systems that involve multiple catalytic units in the rate determining step. This includes multiple activation catalysis, synergistic catalysis, and multifunctional catalysis. Cascade catalysis systems will not be an area of focus, as for this system, bringing catalytic units closer in space will not affect the activation energy of the rate determining step.

The potential advantages of using self-assembly to achieving cooperativity relies on its high modularity – the catalytic units can be synthesised and optimised separately before being

assembled. Another novel aspect of this method for achieving cooperativity is its dynamism and reversibility; the use of weak reversible forces allows the system to be dynamic, and other features can be explored, such as the study of emergent properties. The features of modularity and reversibility could be combined to design combinatorial systems for the development of novel cooperative catalysts, where a library of functionalised catalytic units could be prepared, and a "mix and match" strategy could be utilised to obtain rapid information about the efficiency of different catalyst units acting cooperatively for a specific transformation. This could save time, money, and chemical resources in the development of new cooperative catalysts. Finally, the ultimate aim is to gain a better understanding and a new perspective for the of design cooperative catalysis, and to demonstrate that these concepts are practically useful.

Chapter Two

Proof of concept; self-assembly of cooperative catalysts for the cleavage of RNA and DNA model molecules

2.1. HPNPP cleavage as a model system for cooperative catalysis

In this chapter, we investigated the validity of the initial hypothesis: cooperative catalytic reactions can be improved by bringing the required catalytic units close in proximity by utilising hydrophobic effects. To test this hypothesis, we studied the cleavage of hydroxypropyl *p*-nitrophenyl phosphate (**2.1**, HPNPP), a model substrate for RNA cleavage. The intramolecular cleavage of HPNPP results in the formation of *p*-nitrophenolate (**2.2**) and a cyclic phosphate (**2.3**) (**Figure 39**).

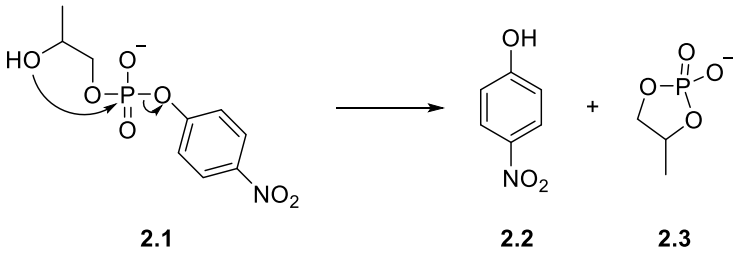

Figure 39: Intramolecular cleavage of HPNPP.

It is known that this reaction is second order with respect to the catalyst as two cationic *zinc* atoms need to be in close proximity to catalyse this reaction with high efficiency. It is proposed that one of the metal ions activates the substrate as a Lewis acid, and the other metal ion stabilises the nucleophile. This system has been extensively studied and represents a "simple" biomimetic reaction that requires the cooperation of multiple functional groups for efficient catalysis. Numerous strategies have been used by various research groups to induce cooperativity and these are discussed below.

2.1.1. Covalent attachment onto a molecular scaffold

An early example of cooperative catalysis utilising multiple zinc cations is presented by Molenveld, Reinhoudt and co-workers and utilises the calixarene scaffold **2.4** (**Figure 40**).[80] In this example, the functionalised calixarene catalysed the cyclisation of HPNPP at pH 7, 25°C. The likely mode of action involves the synergistic operation of the two zinc centres. One zinc ion acts as a Lewis acid activating the phosphate group, while the second activates the nucleophilic hydroxyl group. The calixarene also plays an essential role as a molecular scaffold that organises the two zinc groups' spatial arrangement, thereby facilitating substrate binding. The rate obtained for the dinuclear catalyst was 50 times faster than the monomeric version of the catalyst.

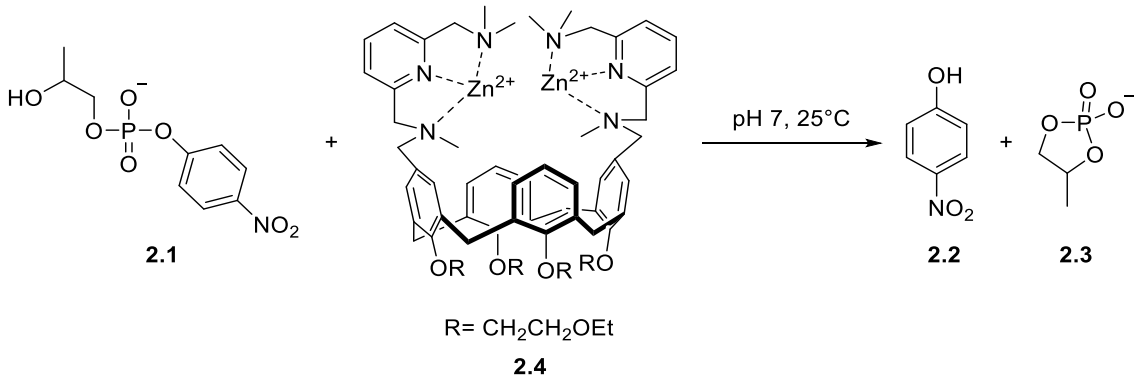

Figure 40: Calix[4]arene-based dinuclear phosphoesterase mimic.[80]

2.1.2. Incorporation into a dendrimer

Scrimin and co-workers developed catalyst **2.5** by functionalizing (poly(propylene imine)) dendrimers with Zn^{2+}-1,4,7-triazacyclononane complexes, as shown in **Figure 41**.[33] The rates of transphosphorylation of HPNPP by these metallo-dendrimers increased with the degree of functionalization, reaching a maximum when Zn^{2+} chelates were attached to each primary amine on the initial dendrimer structure (n = 16). The cleavage mechanism has been demonstrated to involve cooperation between two complexed Zn^{2+} ions on the dendrimer's surface.

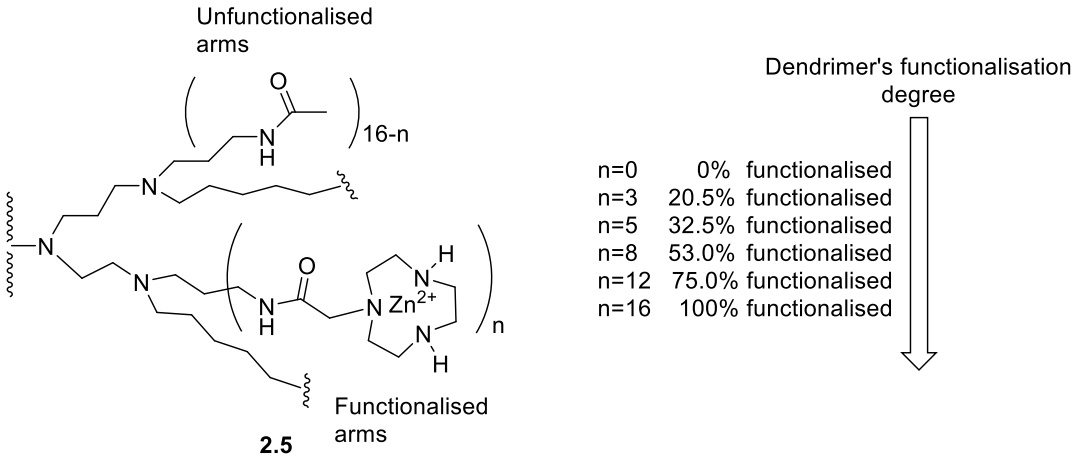

Figure 41. Structure of 1,4,7-triazacyclononane (TACN) functionalised dendrimers.[33]

2.1.3. Immobilisation onto nanoparticles

The same research group synthesised functionalised gold nanoparticles (AuNPs) **2.6**, which incorporate 1,4,7-triazacyclononane (TACN) units onto their surface to perform the cleavage of HPNPP. [40] In the last few years, they improved the system further by controlling the polarity of ligands on the nanoparticle.[81]

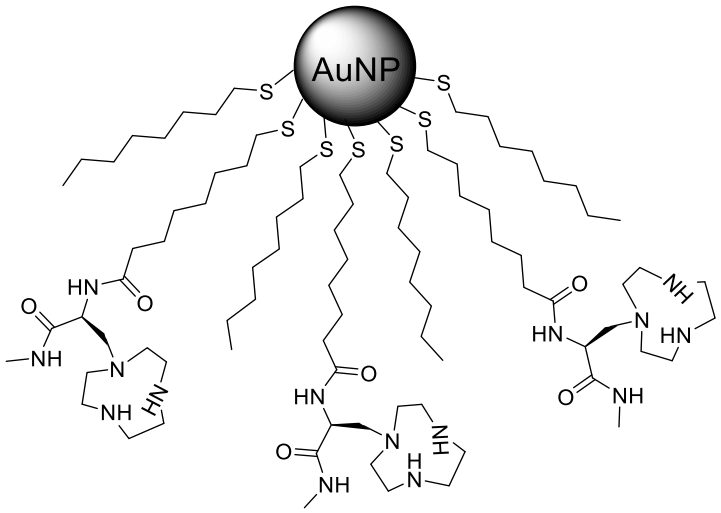

2.6

Figure 42. Structure 1,4,7-triazacyclononane functionalised gold nanoparticle.[40]

The authors were able to obtain evidence of cooperativity by measuring the reaction rate as Zn^{2+} ions were titrated into a solution of the TACN-functionalised AuNPs (**Figure 43**). The reaction rate increases with the addition of Zn^{2+} ions, but this increase is low at low concentrations. This effect is likely due to the low probability of finding neighbouring Zn^{2+} ions. Adding more Zn^{2+} to the media allows the reaction to go faster, since the probability of various Zn^{2+} ions to stay nearby increases. Then, when all the catalytic sites are full or nearly full, the addition of extra Zn^{2+} does not result in a dramatic increase in the reaction rate. All this results in a sigmoidal profile, as observed in **Figure 43**. The sigmoidal profile observed is characteristic of cooperative systems. This is a relevant experiment that supports strongly that multiple Zn^{2+} act cooperatively for the cleavage of HPNPP.

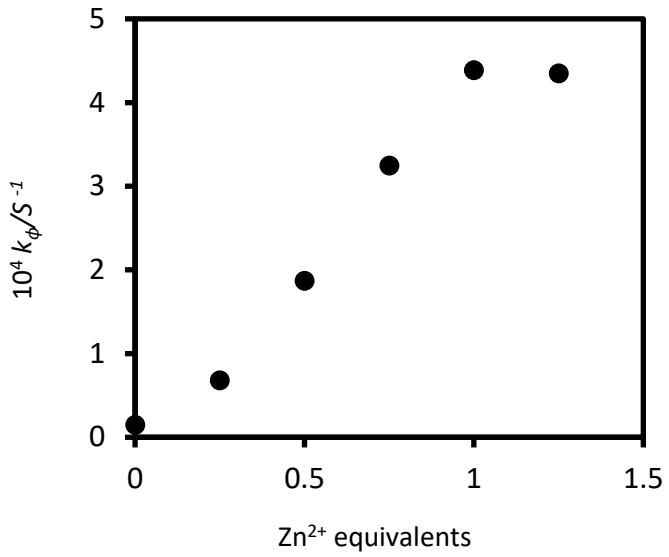

Figure 43. Dependence of the rate constant for the cleavage of HPNPP by a functionalised gold nanoparticle **2.6** on the equivalents of Zn^{2+} ions.[40]

2.2. Aim of the chapter

This chapter aims to demonstrate that hydrophobic interactions can drive cooperative catalysis. The use of these interactions presents advantages over covalently linked ones, such as the modularity of the system and the possibility to exploit the reversibility of the assembly to control the catalysis. It can also present advantages over similar systems that use hydrogen bonding to achieve the assembled state, since the addition of hydrocarbon chains to the catalytic unit is generally more straightforward than the addition of more reactive hydrogen donors and hydrogen acceptors. The higher reactivity of the functionality added could present undesirable reaction pathways during catalysis, which is less of an issue when utilising inert hydrocarbon chains.

A second objective is to demonstrate that the self-assembled state can be promoted by the substrate of the catalysis. Despite literature suggesting micelles to be too dynamic to achieve cooperative catalysis,[40] we decided to explore their potential reversible self-assembly and use it to promote cooperative catalysis. Our objective was to find a substrate not only able to promote aggregation, but one that, once the assembled state is established, can be cleaved by the assembled catalytic units (**Figure 44**). Since amphiphiles were used, we rationalised the need for a substrate that decreased the critical aggregation concentration (CAC) of the system when present. As we will see in this chapter, additives can also be used to promote amphiphilic assembly, opening the possibility of controlling aggregation externally.[82,83]

To summarise, the aim was to develop a system where hydrophobic interactions could be used to drive the self-assembly of a cooperative catalyst. Secondly, we wanted to exploit the reversible

nature of this self-assembly to design a dynamic system, where the substrate could induce the formation of the cooperative catalyst. Our system of interest would be the cleavage of the phosphate ester HPNPP using amphiphiles containing Zn^{2+} ions.

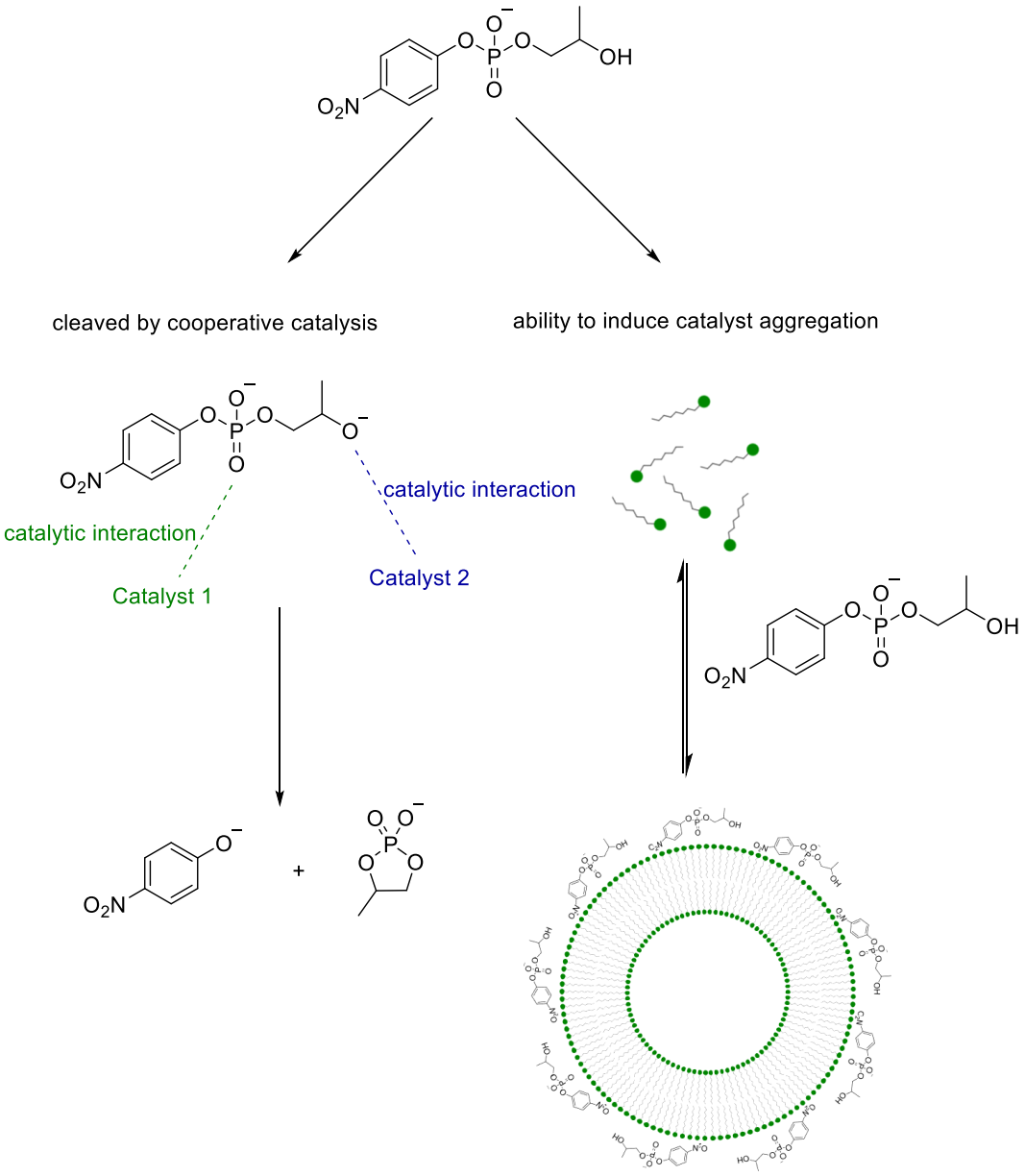

Figure 44. Desired properties of the chosen substrate.

2.3. HPNPP as the model substrate

As we have seen above, phosphate ester cleavage has been intensely studied by a large number of groups.[84–87] These systems can be studied in water and have been used to demonstrate cooperativity in many different systems, including covalently-linked, dendritic or nanoparticle systems. Specifically, we rationalised that HPNPP, which is negatively charged at pH 7, could be used for promoting aggregation of cationic amphiphiles and possibly be cleaved by the proximity of two catalytically active amphiphiles containing positively charged Zn^{2+}. Therefore, HPNPP seemed a promising substrate, with the potential combination of both the capacity of decreasing the CAC of an amphiphilic system and the ability to be cleaved by the amphiphiles by cooperative catalysis (**Figure 44**).

The amphiphilic catalysts chosen needed to present the capacity to cleave HPNPP when close in proximity. Since the reaction studied was a phosphate ester cleavage, and numerous examples in the literature suggested that this kind of reaction could be performed using multiple metallic centres, we decided to use Zn^{2+} as the active site of the catalyst, known to be an efficient choice to execute this transformation.[40,84,86,88–90] The positively charged Zn^{2+} forms part of the polar part of the amphiphile.

The catalytic role of the first Zn^{2+} in this cooperative catalytic reaction is activating the phosphate electrophile, lowering its LUMO by acting as a Lewis acid. However, various studies seem to not agree on the exact role of the second Zn^{2+} ion in this mechanism. On the one hand, some studies propose that this second Zn^{2+} also activates the phosphate, which would result in an even lower LUMO.[91,92] In that case, this second Zn^{2+} would also be acting as a Lewis acid. On the other hand, other studies propose that this second Zn^{2+} helps with the formation and stabilization of the negative charge on the hydroxyl group.[29,87] However, where there is consensus is that this reaction is much more efficient when there are two metallic centres in close proximity and can act cooperatively.[33,40,87,91,93]

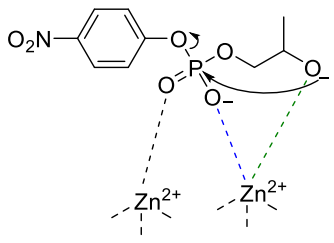

Figure 45. The role of Zn^{2+} in HPNPP cleavage.

2.3.1. Synthesis of the catalyst and substrate

Prins and co-workers demonstrated that the addition of small oligoanions could regulate the aggregation behaviour of amphiphiles.[82,83] Amphiphilic C_{16}TACN·Zn^{2+} (**2.7**) (**Figure 46**), containing Zn^{2+}-binding 1,4,7-triazacyclononane (TACN) headgroups were observed to form stabilised vesicular aggregates in the presence of ATP (**2.9**). This study relied on the ability of charged counterions to effectively stabilise the micellar and vesicular aggregation of surfactants containing charged head groups.[94,95] Such counterions have been shown to dramatically decrease the critical aggregation concentration (CAC) of amphiphiles in solution.[94]

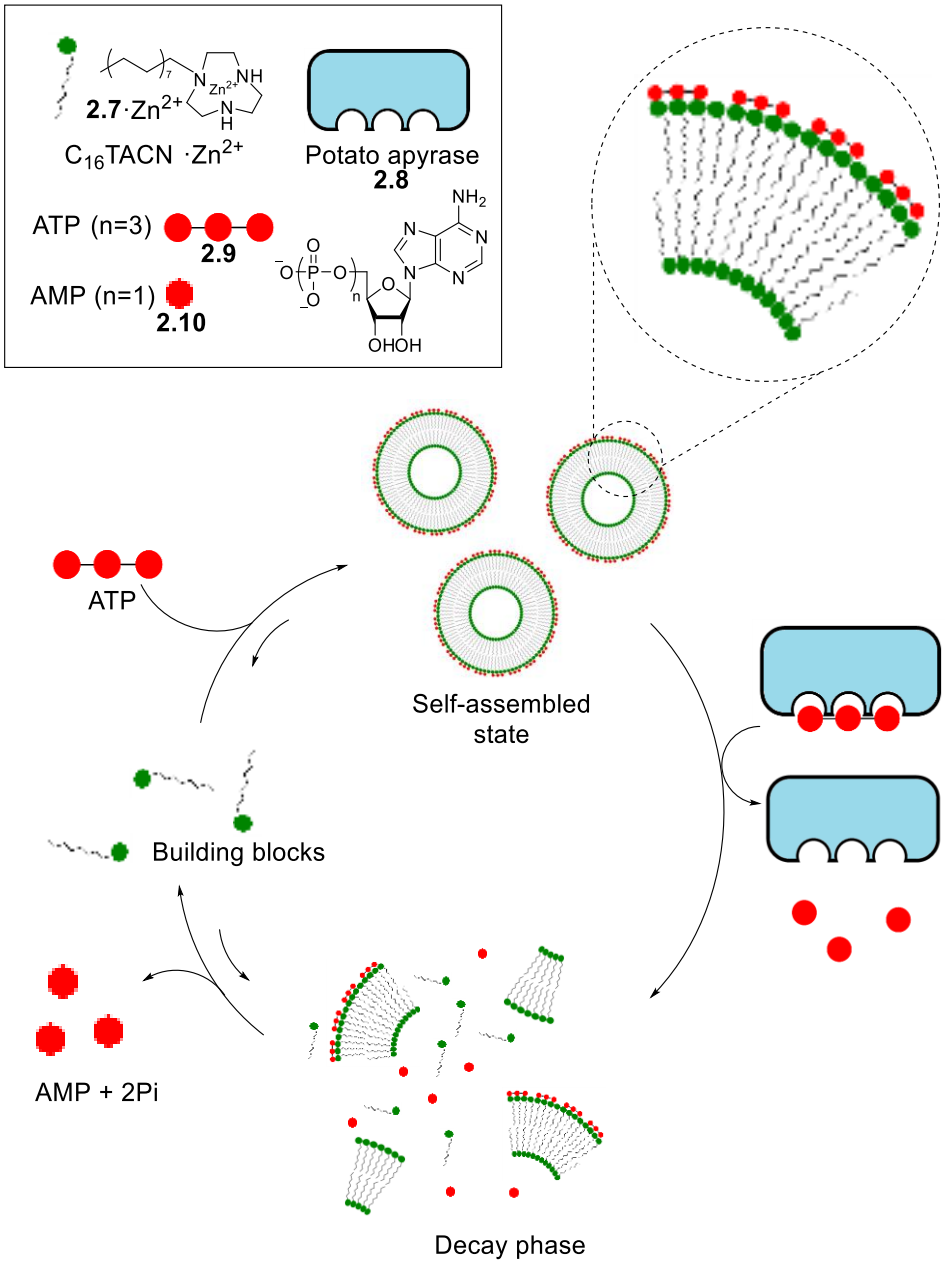

Figure 46. ATP driven dissipative self-assembly of vesicular nanoreactors.[82]

Inspired by this and other examples,[28,33,40,77] we decided to use a 1,4,7-triazacyclononane as a coordinating moiety for both its functionality and simplicity. The idea was to functionalise TACN with a hydrocarbon chain to create an amphiphilic molecule. For the system to be effective, the hydrophobic tail needed to be non-polar enough to be able to form aggregates, so we decided to synthesise a number of ligands with different chain lengths, including the $C_{16}TACN{\cdot}Zn^{2+}$ **2.7** catalytic units that Prins *et al.* used for the example previously described (**Figure 46**).[82]

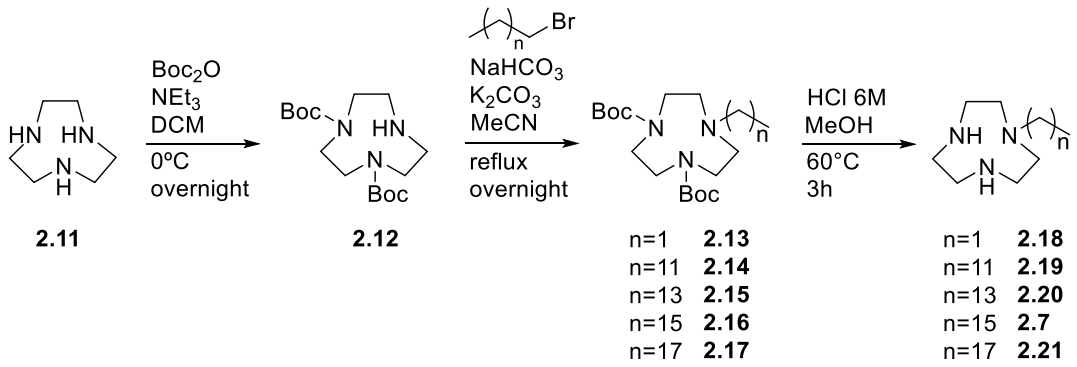

Figure 47. Synthetic route to achieve the desired ligands starting from 1,4,7-triazacyclononane.

Starting the synthesis from commercially available 1,4,7-triazacyclononane (TACN, **2.11**), the molecule was protected with a *tert*-butyloxycarbonyl (Boc) group in two out of the three nitrogens present to obtain **2.12**.[96] Next, the product from the protecting step was alkylated at the non-protected nitrogen with a hydrophobic hydrocarbon chain. The alkylated molecule was then deprotected to obtain the hydrochloride salt of the desired amphiphilic ligand (**Figure 47**). The final Zn^{2+} complexes were generated in situ before running kinetic experiments, and as we will see later, the confirmation of catalysis indicated effective complexation of the Zn^{2+} cations to the ligands.

As mentioned before, the non-polar hydrocarbon chains needed to provide enough kinetic stability to the aggregates, so they would remain together in space for enough time to perform the transphosphorylation reaction. Therefore, it was decided to use the long-chain 1-bromohexadecane and 1-bromooctadecane in the alkylation step to obtain 1-hexadecyl-1,4,7-triazonane (**2.7**) and 1-octadecyl-1,4,7-triazonane (**2.21**), respectively. The reaction between the ligands C_nTACN and zinc nitrate ($ZnNO_2$) yielded the catalytic units $C_nTACN{\cdot}Zn^{2+}$. $C_{18}TACN{\cdot}Zn^{2+}$ (**2.21**$\cdot Zn^{2+}$) was found to be not very soluble in the required experimental conditions, and as a result, $C_{16}TACN{\cdot}Zn^{2+}$ (**2.7**$\cdot Zn^{2+}$) was chosen as the primary catalyst of interest.

Control ligands were also synthesised from 1-bromoethane, 1-bromooctane, 1-bromododecane and 1-bromotetradecane to obtain 1-ethyl-1,4,7-triazonane (**2.18**), 1-dodecyl-1,4,7-triazonane

(**2.19**) and 1-tetradecyl-1,4,7-triazonane (**2.20**) respectively. The addition of $ZnNO_2$ to each of these ligands yielded the $C_nTACN{\cdot}Zn^{2+}$ control catalysts.

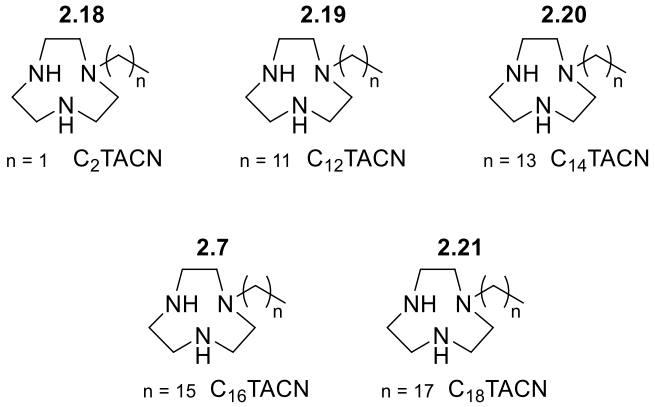

Figure 48. Synthesised TACN ligands.

The substrate, hydroxypropyl *p*-nitrophenyl phosphate (HPNPP), was synthesised following a reported procedure utilising disodium *p*-nitrophenyl phosphate, epoxypropane and an exchange of the cation for barium (**Figure 49**).[97] After achieving the synthesis of the required catalysts and the substrate, attention turned towards the analysis of the properties of the designed supramolecular system.

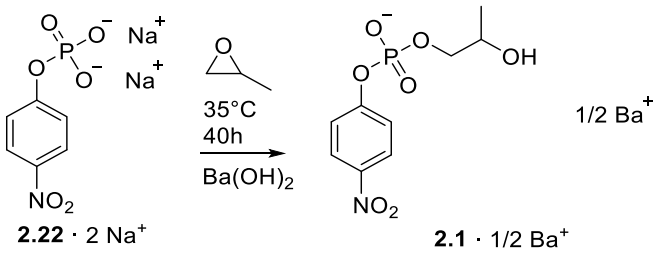

Figure 49. HPNPP synthesis.

2.3.2. Determination of CAC and structural data.

The critical aggregation concentration (CAC) refers to the concentration of an amphiphile that, when surpassed, results in a shift towards the aggregated form of the equilibrium between unaggregated and aggregated species. This is an important physical parameter of amphiphiles, and for this chapter, it was important to determine the CAC of our monomer in different conditions in order to determine the effect of aggregation on catalysis.

The CAC was first calculated for **2.7**·Zn^{2+} in different concentrations of HPNPP. First, the CAC of **2.7**·Zn^{2+} was measured in the absence of substrate by titrating increasing amounts of the amphiphile to an aqueous solution buffered at pH 7.0, and containing Nile red (**2.23**, **Figure 50**) as a non-polar probe (5 μM, λ_{ex} = 570 nm, λ_{em} = 643 nm). This probe is not soluble in water, but it is solubilised in the non-polar region of micellar and vesicular assemblies, leading to a change in the emission fluorescence intensity after the CAC is reached. By determining the intersection between the lines of best fit obtained before the change in slope, and the line of best fit obtained after the change in slope, an accurate value for the CAC can be obtained.[98]

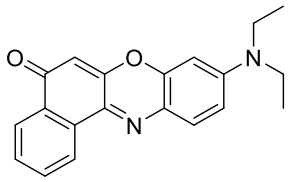

2.23

Figure 50. Molecular structure of Nile red.

The critical aggregation concentration for **2.7**·Zn^{2+} in the absence of HPNPP was measured to be close to 93 μM, a value in close agreement with previous studies (**Figure 51**).[82]

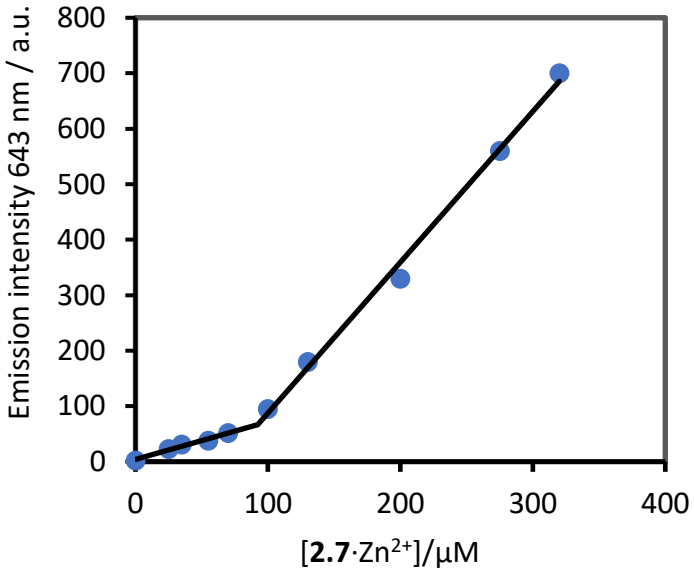

Figure 51. Critical aggregation concentration determination for **2.7**·Zn^{2+} in the absence of HPNPP. pH 7.0, [HEPES buffer] = 5mM. Nile Red (2 μM, λ_{ex} = 570 nm, λ_{em} = 643 nm). The trend lines are the linear fit to the first three and last four data points.

The CAC was then calculated at different concentrations of HPNPP utilising the same fluorescence technique. A significant decrease in CAC can be observed at increasing concentrations of HPNPP (**Figure 52**), supporting the hypothesis that HPNPP can be used as a counterion to induce aggregation of cationic amphiphiles, which increases the thermodynamic stability of the formed assemblies.

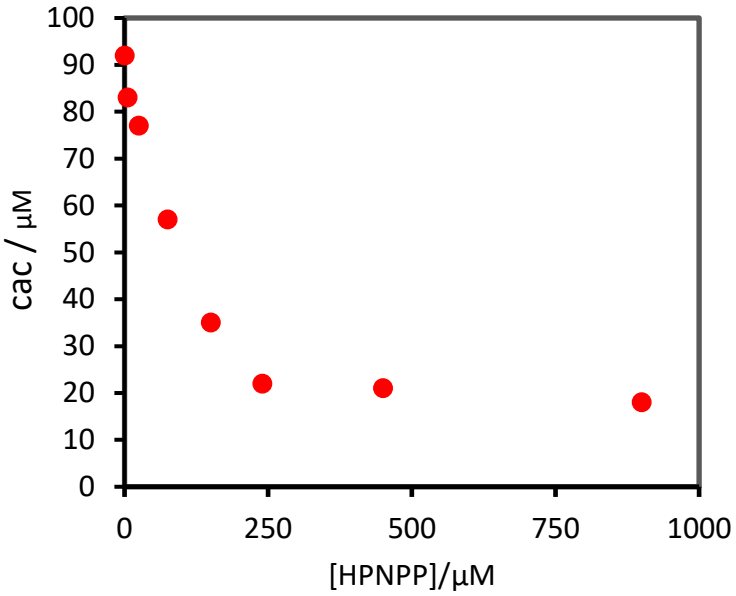

Figure 52. CAC values for **2.7**·Zn^{2+} at different HPNPP conc.; pH 7.0; [HEPES buffer] = 5mM, using Nile red as a fluorescence probe (2 μM, λ_{ex} = 570 nm, λ_{em} = 643 nm).

The amount of Nile red used in the experiments was 2 μM, and there was a possibility that this amount of Nile red may also induce the formation of assemblies. We attempted to use lower concentrations of Nile red, but found that sensitivity was lost, and the data was found to be unreliable. We compared the CAC of the system when utilising 2 μM and 5 μM of Nile red, and found that the profiles of the curves can vary but that the CACs determined under both conditions were found to be within experimental error (**Figure 53**). Since the data matched closely when using 2 μM or 5 μM of Nile red, we believe that the Nile red used in the experiments does not significantly impact the self-assembly of the amphiphiles.

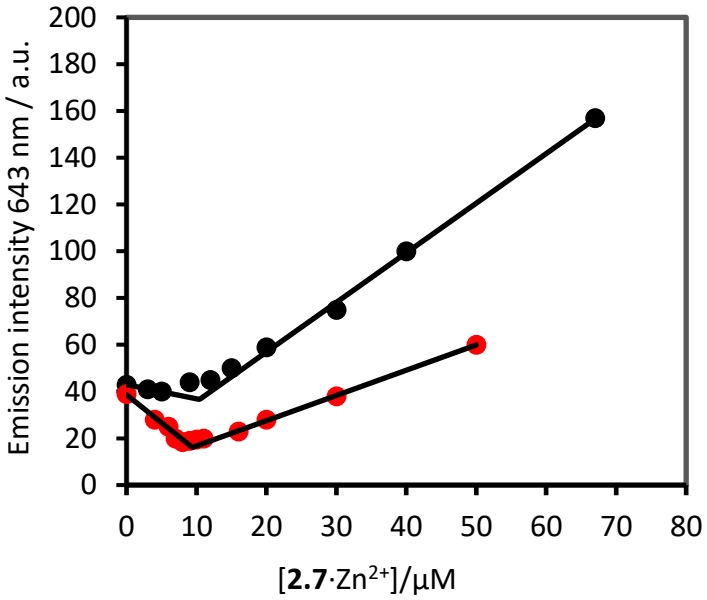

Figure 53. Emission intensity profiles for Nile red (λ_{ex} = 570 nm, λ_{em} = 643 nm) at 2 μM and 5 μM at increasing **2.7**·Zn^{2+} concentrations in the presence of 500 μM HPNPP.

The formation of assemblies above the CAC was also supported by dynamic light scattering (DLS) experiments (**Figure 54**). In short, dynamic light scattering is a technique used to determine the size and size distribution of particles in solution by irradiating the sample in solution or suspension with light. The scattering of the light gives information about the size of the particles in solution. The observation of larger aggregates in the presence of HPNPP (24 ± 15 nm) suggests that the substrate plays a role in the formation and the size of the assemblies (**Figure 54**).

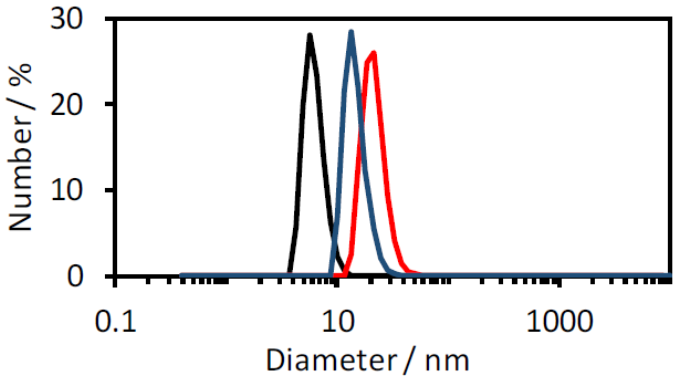

Figure 54. Hydrodynamic diameter of assemblies measured with dynamic light scattering. Black line: [**2.7**·Zn^{2+}] = 200 µM, [HPNPP] = 0 µM, Red line: [**2.7**·Zn^{2+}] = 75 µM, [HPNPP] = 250 µM, measurement performed just after addition of HPNPP. Blue line: [**2.7**·Zn^{2+}] = 75 µM, [HPNPP] = 250 µM, measurement performed after 48 hours of reaction. All experiments were performed in aqueous buffer solution (HEPES, 10 mM, pH 7.0) at 25 ℃.

Objects of a similar size were also observed by (cryo) transmission electronic microscope (TEM/cryoTEM) (**Figure 55**). With traditional TEM, uranyl acetate was needed as a stain to observe the self-assembled structures. With cryoTEM, the samples are cooled to cryogenic temperatures, and it allows the sample to be observed without the need for staining and without utilising charged grids that might affect the aggregation. With both methods, circular hollow structures in the range of 20-40 nm were observed, supporting the fact that HPNPP promotes the formation of vesicular assemblies. Confocal microscopy was used to observe the formation of vesicular structures upon the addition of HPNPP in real time. From a solution with no initial fluorescence, we were able to observe the formation of fluorescent structures upon the addition of HPNPP.

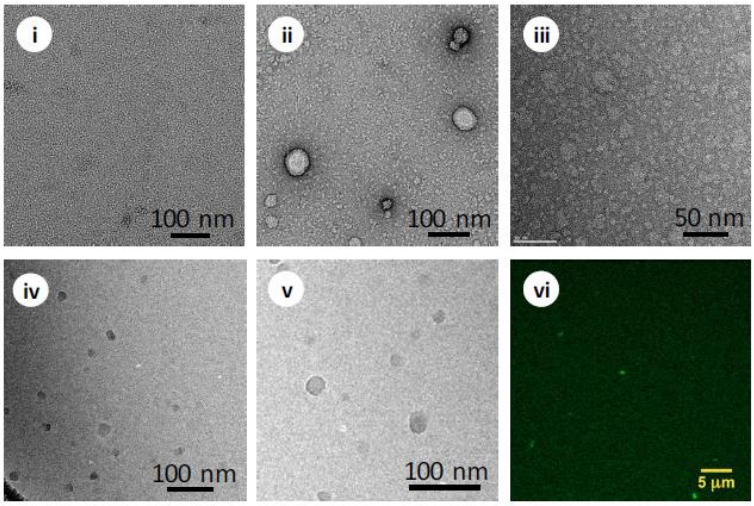

Figure 55. Representative transmission electron microscopy (TEM) images of: (i) [**2.7**·Zn^{2+}] = 50 µM in the absence of substrate HPNPP. (ii) vesicles with [**2.7**·Zn^{2+}] = 50 µM in the presence of HPNPP (250 µM) (iii) structures formed with [**2.7**·Zn^{2+}] = 50 µM in the presence of waste. (iv) and (v) representative cryoTEM images with [**2.7**·Zn^{2+}] = 50 µM and [HPNPP] = 250 µM. (vi) representative image of vesicles with confocal microscopy for samples prepared with [**2.7**·Zn^{2+}] = 75 µM, [HPNPP] 250 µM and [coumarin 153] = 1 µM. All experiments were performed in aqueous buffer solution (HEPES, 10 mM, pH 7.0) at 25 °C, and standard TEM images were stained with 1% uranyl acetate solution.

2.3.3. Catalytic properties of the system

Satisfied that the formation of aggregates was promoted by the substrate HPNPP, we studied the catalytic activity of the formed assemblies. A cyclic phosphate (cP, **2.3**) and *para*-nitrophenolate (PNP **2.2**) are the products of HPNPP hydrolysis (**Figure 56**), conveniently allowing the reaction to be followed spectrophotometrically due to the absorption of *para*-nitrophenolate in the visible region (405 nm).

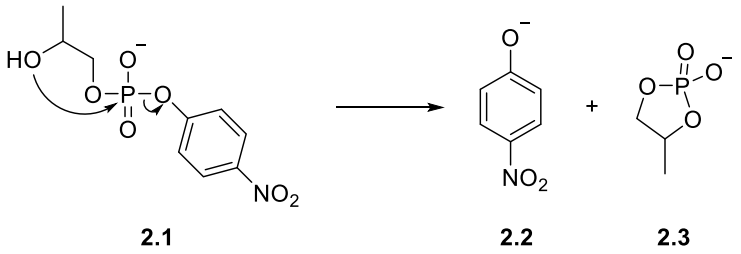

Figure 56. Transphosphorylation of HPNPP.

Figure 57 shows the initial rate for the hydrolysis of HPNPP (62 μM) at different concentrations of **2.7**·Zn^{2+} in aqueous buffer ([HEPES] = 10 mM, pH 7). At low concentrations of **2.7**·Zn^{2+} (0 – 50 mM), the initial hydrolysis rates were observed to be slow. At concentrations above 50 mM, however, the initial rates increased significantly, with the reaction rate being directly proportional to the surfactant concentration. Several relevant conclusions can be obtained from this experiment. Firstly, the point where the trend lines from the three first points and the four last points converge is at 54 μM, and this matches the critical aggregation concentration determined for these conditions using Nile red (~55 μM, **Figure 58**, **Figure 52**). This indicates that self-assembly is an important factor in facilitating catalysis.

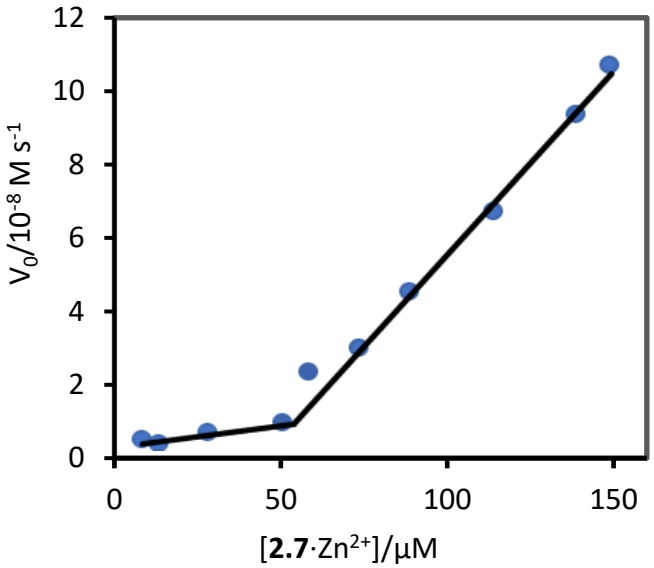

Figure 57. Initial rate of HPNPP hydrolysis at increasing **2.7**·Zn^{2+} concentrations ([HPNPP] = 62 μM), ([HEPES] = 10 mM, pH 7, 40 °C), the trend lines are the linear fit to the first three and last four data points.

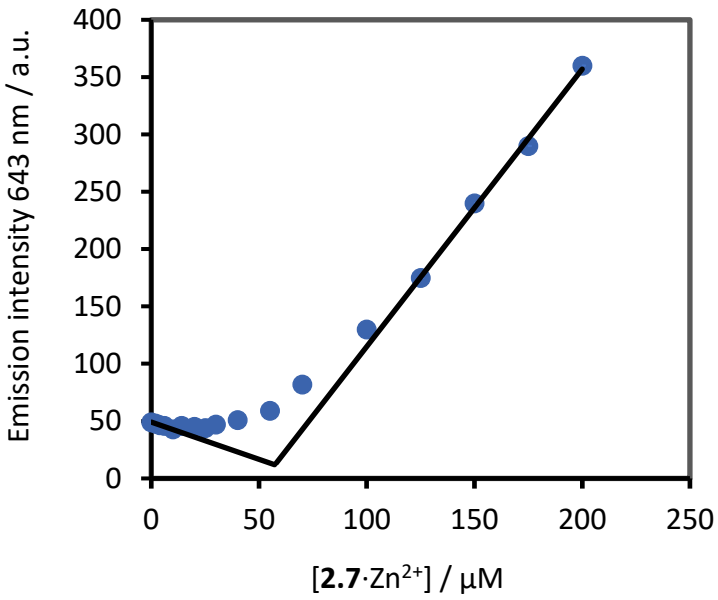

Figure 58. Critical aggregation concentration determination for **2.7**·Zn^{2+} ([HPNPP] = 62 µM), ([HEPES] = 10 mM, pH 7, 40 °C) Nile Red (2 µM, λ_{ex} = 570 nm, λ_{em} = 643 nm), the trend lines are the linear fit to the first three and last four data points.

Comparison of the slopes below and above the CAC shows that the assemblies have significantly higher catalytic activity compared to the monomeric surfactant (**Figure 57** and **Figure 58**). The significant rate enhancement was also confirmed by complementary experiments described in the following section.

Even though this reaction is well known to be second order with respect to the catalyst, from **Figure 57**, we observe a first-order-like dependence on the catalyst concentration after the CAC is reached. This can be explained in the following treatment. Considering that our system consists of an equilibrium between monomeric and aggregated states, this equilibrium can be represented by the following expression, where **n** is the number of monomers present in the aggregate:

$$\mathbf{n}\ \text{monomer} \rightleftharpoons \text{aggregate} \qquad \textbf{Equation 1}$$

As we know that two catalytic units are needed for this reaction, we can assume that assembled catalytic pairs (ACP) — or dimers — are the actual catalytic species. We can consider the vesicular structure as made up of multiple ACPs. Expressing the aggregate as multiple ACPs gives us the following expression:

$$\mathbf{n}\ \text{monomer} \rightleftharpoons \tfrac{\mathbf{n}}{2}\ \text{ACP} \equiv 2\ \text{monomer} \rightleftharpoons \text{ACP} \qquad \textbf{Equation 2}$$

The equilibrium constant between the two species would be:

$$K_{eq.} = [ACP] / [monomer]^2 \quad \textbf{Equation 3}$$

Then since the catalytic pairs are the active species, the rate equation would be:

$$Rate \propto k[ACP] \quad \textbf{Equation 4}$$

And the total catalyst can be expressed as the sum of the monomers and aggregates/dimers.

$$[cat\ (total)] = \mathbf{n}[aggregate] + [monomer] = \mathbf{2}[ACP] + [monomer] \quad \textbf{Equation 5}$$

When K_{eq} is small: [monomer] > > [ACP]

$$Rate \propto k[ACP] = kK_{eq.}([monomer])^{\mathbf{2}} = kK_{eq}\,([cat(total)]\text{-}\mathbf{2}[ACP])^{\mathbf{2}} \approx kK_{eq.}([cat(total)])^{\mathbf{2}} = k_{obs}\,([cat(total)])^{\mathbf{2}} \quad \textbf{Equation 6}$$

This would show the rate dependence is a squared function with respect to the total amount of catalyst added, typically observed in second-order systems where the catalysts are not directly joined together.

But when K_{eq} is large: [ACP] > > [monomer] then $\mathbf{2}[ACP] \approx [cat(total)]$

And the rate expression becomes:

$$Rate \propto k[ACP] \approx k\mathbf{1/2}[cat(total)] = k_{obs}[cat(total)] \quad \textbf{Equation 7}$$

This would show a linear rate dependence with respect to the total amount of catalyst added, and the rate would be observed as a first-order-like dependence with respect to the catalyst once the critical aggregation concentration is reached. Since this last case is what is observed in our system, we can conclude that after a certain concentration is reached (CAC), the concentration of ACPs is much higher than the concentration of non-assembled monomers.

Evidence of catalysis was also found using ^{31}P-NMR spectroscopy. To an NMR tube containing 75 μM of **2.7**·Zn^{2+} at pH 7 ([HEPES buffer] = 10 mM), HPNPP was added (1.0 mM), and the changes in the ^{31}P NMR spectra were tracked as a function of time. The intensity of the signal due to HPNPP (-5.69 ppm) decreases, while a new signal at 17.14 ppm originating from the cyclic phosphate waste product appears (**Figure 59**).

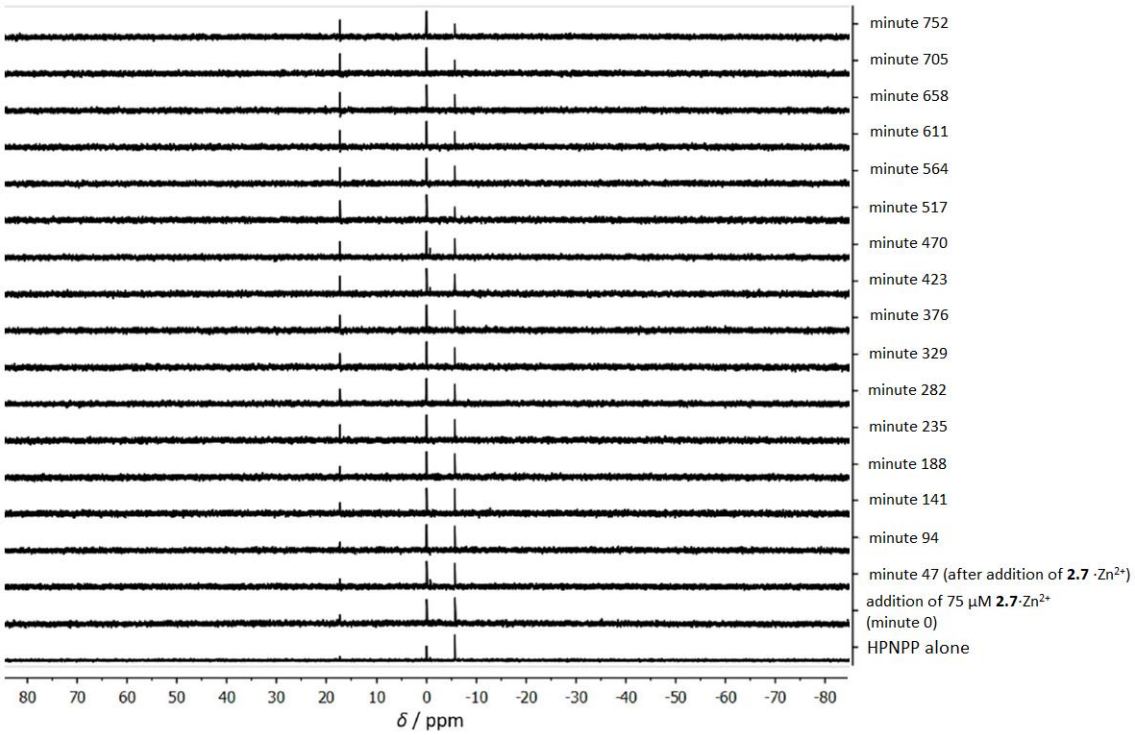

Figure 59. ^{31}P-NMR spectrum (9:1 H_2O:D_2O, 202 MHz, 303 K) starting from the bottom: 1 mM HPNPP alone, then spectra just after the addition of 75 µM **2.7**·Zn^{2+} following by spectra taken at equal intervals of 47 min up to 13 h. The signal at 0 ppm originates from the coaxial reference (K_2HPO_4 in HEPES buffer at pH 7).

The strong rate acceleration observed upon the formation of self-assemblies suggest that a cooperative mechanism in the rate-determining step is likely, similar to catalytic nanoparticles containing the same TACN· Zn^{2+} complex. However, this observation also could be explained by other effects, such concentration effects commonly observed is traditional micellar catalysis.[99]

Micellar catalysis uses the formation of micellar aggregates to accelerate chemical reactions. In traditional micellar catalysis, the rate acceleration is believed to be due to concentration effects when non-polar reactants are solubilised into the non-polar internal medium of the micelles. This can allow certain chemical transformations to be performed in the absence of organic solvents.[100],[101] Lipshutz's research group, which focuses on micellar catalysis for organic transformations, has demonstrated that it is possible to perform multiple reactions in aqueous micellar systems that would normally require an organic solvent.[102,103] For instance, they have reported good results when performing Sonogashira couplings in aqueous micellar media utilising TPGS-750-M/H_2O as a surfactant (**Figure 60**).[102]

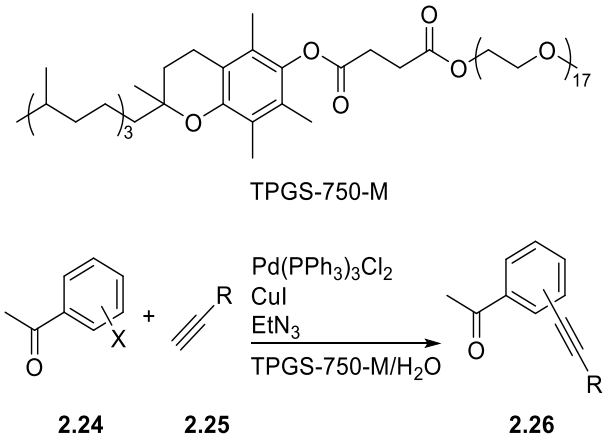

Figure 60. Sonogashira coupling performed in aqueous micellar media.[102]

To demonstrate that the rate acceleration observed in our system is not due simply to a concentration effect, an experiment was performed where the initial rate of the transphosphorylation was monitored at varying concentrations of the cation Zn^{2+}. A fixed concentration of the catalyst **2.7** was used for this experiment, as all other parameters were also fixed ([HEPES buffer] = 5 mM, pH 7, [**2.7**] = 50 µM, [HPNPP] = 500 µM, 40 °C) (**Figure 61**).

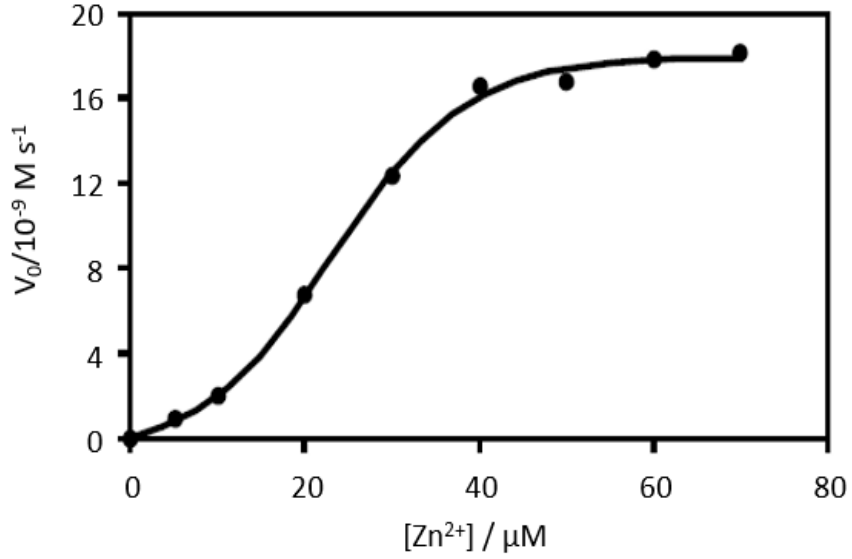

Figure 61. Initial rate of HPNPP hydrolysis at a fixed concentration of **2.7** and varying Zn^{2+} concentrations ([HEPES buffer] = 5 mM, [**2.7**] = 50 µM, [HPNPP] = 500µM, 40 °C).

In this experiment, we observed that at low concentrations of Zn^{2+}, the initial rates for the reaction were slow, even though the concentration of **2.7** was above the CAC for those conditions. The

explanation for this effect is that when there are numerous TACN moieties to be coordinated onto, the Zn^{2+} are unlikely to be allocated near neighbouring Zn^{2+} cations. This precludes cooperativity between catalytic units as they are not close to each other under these conditions, and therefore a slow rate is observed. At higher concentrations of Zn^{2+} cations the probability of finding neighbouring Zn^{2+} cations increases. Consequently, cooperativity emerges, and the rate of the reaction increases with the increasing concentration of Zn^{2+}. At even higher concentrations of Zn^{2+}, saturation is reached as no other coordinating positions are available, and no more catalytic units can be formed. This results in a plateau in the observed reaction rate.

The observed sigmoidal profile is characteristic of cooperative catalysis by metal centres[40],[104] and supports the hypothesis that the rate increase is due to cooperativity within catalytic units and not concentration or solvation effects. For this experiment to be suitable and relevant, we must demonstrate that aggregates are present at all conditions of the experiment. The CAC of **2.7** was therefore measured in the presence of 500 μM HPNPP and in the absence of Zn^{2+} in HEPES buffer 5 mM (**Figure 62**).

In **Figure 62**, when measuring the fluorescence emission intensity at increasing concentration of the ligand, it can be observed that a change in slope occurs at a concentration of 13 μM. This is again due to a change in the fluorescence of Nile red when the CAC is reached. This confirms the presence of aggregates at the conditions of the above experiment, as we were working at 50 μM, which is much higher than the CAC. A solvation or concentration-effect explanation for the rates can be dismissed because aggregates are still present at low concentrations of Zn^{2+}, and the rate is significantly low until enough concentration of Zn^{2+} is added. Subsequently, the best explanation for the observed effects is that the rate increase is due to cooperativity between neighbouring Zn^{2+} cations, brought together by self-assembly.

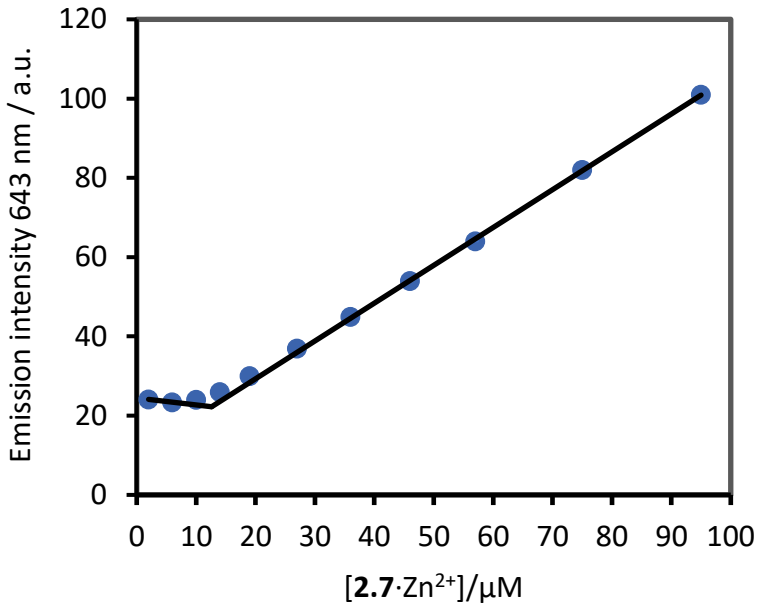

Figure 62. Emission intensity profiles for Nile Red (5 μM, λ_{ex} = 570 nm, λ_{em} = 643 nm) at increasing **2.7**·Zn^{2+} concentrations, in the presence of 500 μM HPNPP in the absence of Zn^{2+}; the dotted lines are the linear fit to the first two and last five data points, indicating a CAC of 13 μM.

The observation of cooperative catalysis by **2.7**·Zn^{2+} assemblies was not an obvious result. Analogous surfactants with shorter chains were previously reported by Scrimin and co-workers showing low catalytic activity – this was attributed to the highly dynamic nature of the aggregates, with a suspected quick exchange of the amphiphiles between the assemblies and the bulk solution.[40] To study the effect of the length of the hydrophobic chain on catalytic activity, the catalytic activity of a number of analogues were performed (**2.18**·Zn^{2+}, **2.19**·Zn^{2+}, **2.20**·Zn^{2+}, **2.7**·Zn^{2+}, **2.21**·Zn^{2+}) as is has been shown that the kinetic stability of surfactant-based assemblies is enhanced by increasing the length of the hydrocarbon chain.[105] **Figure 63** shows the transphosphorylation activity at different catalyst concentrations and equimolar Zn^{2+} in a buffered solution containing excess HPNPP (500 μM). As expected, an increase in catalytic activity was observed by increasing the concentration of the catalyst·Zn^{2+} complex. Drastic differences in reactivity were observed with the different analogues. For example, reaction rate utilising **2.21**·Zn^{2+} is roughly double that of the rate of reaction with **2.7**·Zn^{2+} at 100 μM, which is over a magnitude higher than that of **2.20**·Zn^{2+} (note the logarithmic scale on both axes). At the same concentration, the activities of **2.19**·Zn^{2+} or **2.18**·Zn^{2+} were negligible.

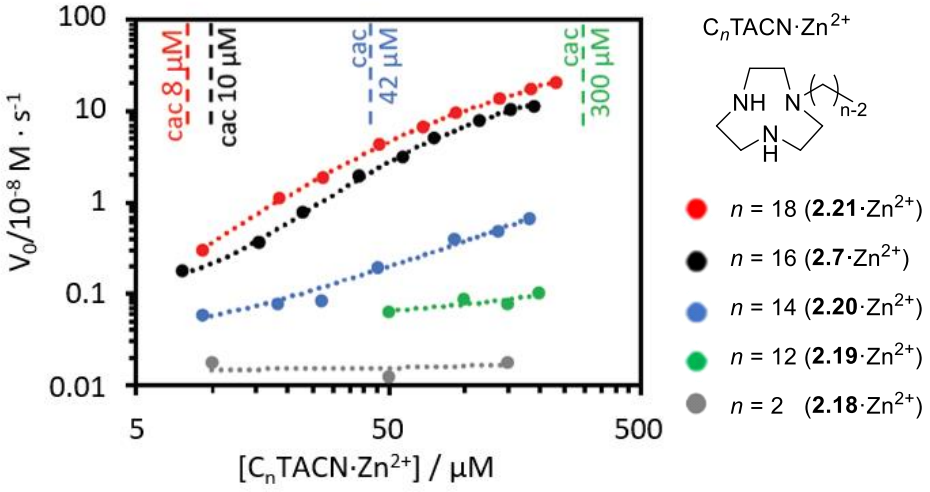

Figure 63. Initial rate of HPNPP transphosphorylation at increasing $C_nTACN·Zn^{2+}$ concentrations (n = 2 to 18, see legend).

The CAC of **2.19**·Zn^{2+}, **2.20**·Zn^{2+}, **2.7**·Zn^{2+} and **2.21**·Zn^{2+} in the presence of 500 µM HPNPP was determined next by the cumulative addition of $C_nTACN·Zn^{2+}$ to a solution containing HEPES buffer (5 mM) and Nile red (2 µM). The fluorescence emission intensity was measured at 643 nm, while exciting at 570 nm. Lower CAC values were obtained with an increase in the hydrocarbon chain length (**Figure 64**).

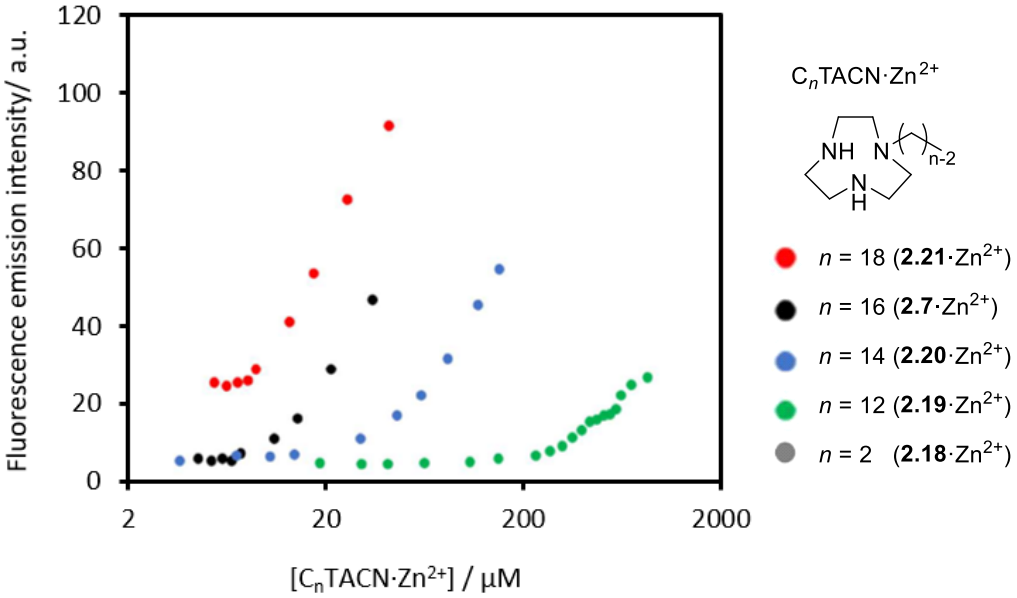

Figure 64. Emission intensity profiles, pH 7.0, [HEPES buffer] = 5 mM, 40 °C. Nile Red (2 µM, λ_{ex} = 570 nm, λ_{em} = 643 nm) at increasing $C_nTACN·Zn^{2+}$ concentrations (see legend for details), in the presence of 500 µM HPNPP at 25°C.

Notably, a comparison of the rise of the catalytic activity with the critical aggregation concentration value for **2.20**·Zn^{2+} in the presence of 500 μM of HPNPP (42 μM) reaffirms that assembly of the catalytic units is an essential prerequisite for effective catalysis (**Figure 63**, **Figure 64**). Reduced catalytic activity for **2.18**·Zn^{2+} and **2.19**·Zn^{2+} is in agreement with the fact that these amphiphiles do not aggregate at the concentration range studied, as shown in **Figure 63**.

One could expect to observe similar catalytic activity between two ligands (e.g. **2.7**·Zn^{2+} and **2.21**·Zn^{2+}) once aggregates are formed, as the effective concentration of the assembled catalytic pairs should be the same. However, we can see that this was not the case, and that the catalytic activity of **2.21**·Zn^{2+} is significantly higher than the rate for **2.7**·Zn^{2+} under the same reaction conditions. To examine the origins of this difference in reaction rate, we decided to compare the transphosphorylation rate for **2.7**·Zn^{2+} and **2.21**·Zn^{2+} at different substrate concentrations.

Figure 65 shows the initial rate of reaction plotted against HPNPP concentration. Fitting of the curve to Michaelis-Menten kinetics yielded similar V_{max}[i] values for **2.21**·Zn^{2+} ($7.8 \pm 0.3 \times 10^{-8}$ mol s^{-1}) and **2.7**·Zn^{2+} ($7.2 \pm 0.6 \times 10^{-8}$ mol s^{-1}), indicating that there are no intrinsic differences in the catalytic pocket in the assemblies[106]. This can be expected as we do not anticipate any major differences between the catalytic pockets formed from **2.21**·Zn^{2+} and **2.7**·Zn^{2+}. In contrast, the different K_M[ii] values obtained indicate differences in the affinity of the catalysts to the substrate[106] (K_M **2.21**·Zn^{2+} = 0.53 ± 0.06 mM and K_M = **2.7**·Zn^{2+} 1.0 ± 0.1 mM). The lower K_M observed with **2.21**·Zn^{2+} suggests that the complex formed between the catalytic pair and the substrate is formed more readily than with **2.7**·Zn^{2+}.

[i] V_{max} refers to the maximum initial rate achieved by the system when varying the amount of substrate.
[ii] K_M refers to the substrate concentration when the reaction rate is equal to half of the V_{max} value.

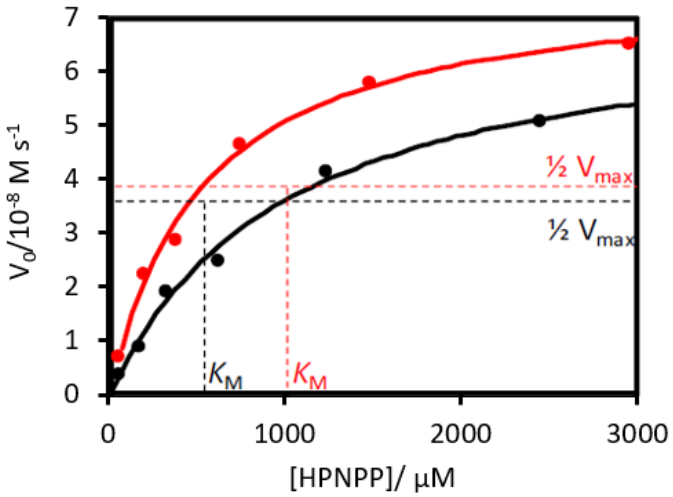

Figure 65. Initial rate of HPNPP hydrolysis at increasing HPNPP concentrations, and a fixed concentration of $C_nTACN{\cdot}Zn^{2+}$ ([$C_nTACN{\cdot}Zn^{2+}$] = 50 µM, [HEPES buffer] = 50 mM), the solid line shows fitting according to Michaelis-Menten kinetics. Experiments were performed in aqueous buffer at pH 7, at 40 °C. Red circles are for **2.21**·Zn^{2+}, black circles are for **2.7**·Zn^{2+}.

These experiments were performed to demonstrate the Michaelis-Menten characteristics of this system and required the addition of increasing concentrations of the substrate HPNPP in order to approach V_{max}. Because the concentration of substrate HPNPP needed was so high (up to 3 mM), we required higher concentrations of buffer to ensure that the buffer capacity was not breached, thus for used [HEPES buffer] = 50 mM. It is worth emphasising that in this particular system, an increase in the substrate concentration increases the amount of catalyst present by shifting the equilibrium between the non-assembled and the assembled states. The observation that the critical aggregation concentration is inversely correlated to the hydrophobicity of the amphiphiles implies that, for a more hydrophobic catalyst, a higher amount of assembled catalytic pairs are present than in the with less hydrophobic catalysts (the same molar concentration of catalyst molecules). This fact suggests that the aggregated or "active" state is increasingly more populated with longer hydrophobic chains, and it would explain the higher rates observed when employing the most hydrophobic surfactants, and subsequently, the difference in K_M values.

The ability of the system to cleave successive additions of the substrate is shown in **Figure 66**. We first added 125 µM HPNPP to a buffered solution containing 50 µM of **2.7**·$Zn^{2+,}$ and after 48 h, the reaction was considered complete as a further increase in absorption was detected. To the same solution, further aliquots of HPNPP were added up to 3 times. It can be observed that the rate of the reaction decreased dramatically with each successive addition. However, the

observation that the system presents catalytic activity after each addition indicates that the waste products for the transphosphorylation reaction do not permanently inhibit the catalytic sites. The raw kinetic data for this refuelling experiment is shown in the **Appendix**.

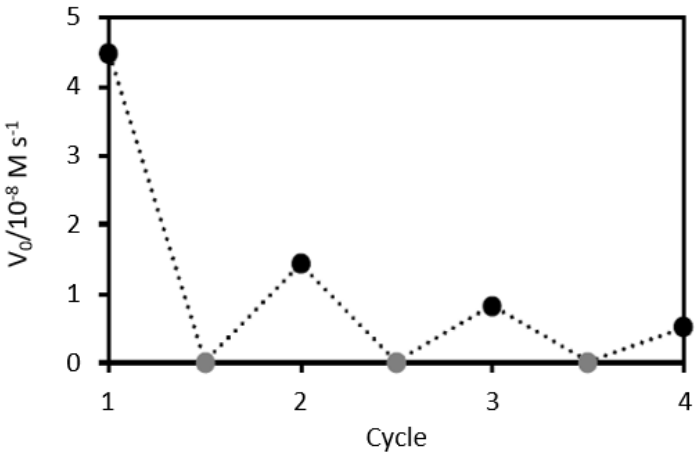

Figure 66. Initial rates of HPNPP hydrolysis after successive additions of HPNPP (125 μM each addition) in the presence [HEPES buffer] = 5 mM and [**2.7**·Zn^{2+}] = 50 μM at 40 °C. black data points represent the rate directly after each addition; grey data points represent the rate after 48 hours before the addition of the new batch of fuel.

2.3.4. Self-assembly properties after reaction completion

The behaviour of the assemblies following HPNPP hydrolysis was studied by examining the samples after 48 h, when almost all the substrate was converted into products. DLS and TEM experimental data showed the presence of assemblies similar in size to the ones in the presence of HPNPP (**Figure 54**, **Figure 55**). CAC measurements in the presence of waste products (cP and PNP) were conducted, and we were able to demonstrate that the waste products are also able to stabilise the formation of aggregates (**Figure 67**).

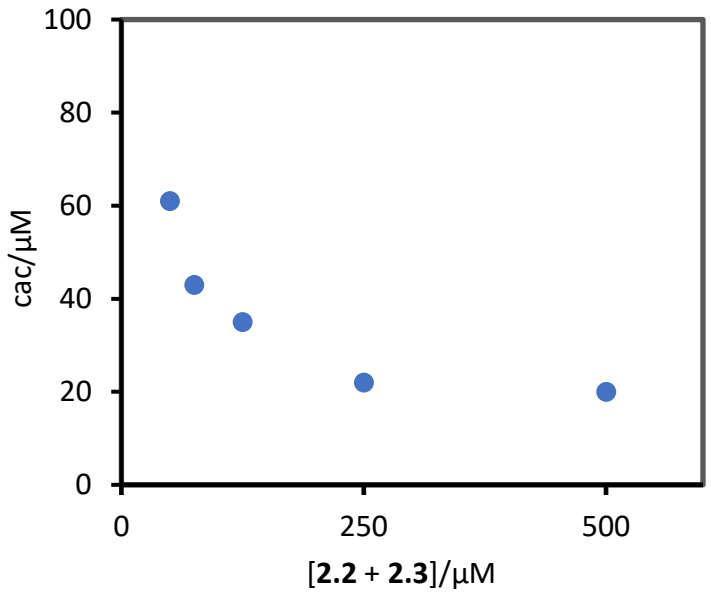

Figure 67. CAC of the system in the presence of PNP and cP at different PNP and cP concentrations; pH 7.0; [HEPES buffer] = 5 mM, Nile Red (2 μM, λ_{ex} = 570 nm, λ_{em} = 643 nm).

These experiments suggested that the waste products have a similar affinity for the assemblies as the substrate HPNPP. Disappointingly, this implies that the system does not spontaneously dissipate upon substrate consumption and form the individual non-assembled catalysts. Nevertheless, this state is still a responsive one, as shown by refuelling experiments (**Figure 66**). As we have seen, the catalytic activity can be reactivated by adding new batches of the substrate after its consumption, showing that the binding is reversible and that the catalyst does not become irreversibly inhibited by the accumulated products of the reaction. The catalytic activity is reduced with each subsequent addition of substrate; this happens because the presence of waste products compete with the substrate for binding to the catalytic sites.

2.3.5. Substrate-induced self-assembly

This system has been shown to be responsive to the presence of a substrate (HPNPP) that templates the formation of the active catalyst by promoting the self-assembly of the catalytic units. Once assembled, these catalytic units catalyse the hydrolysis of the substrate by cooperative catalysis (**Figure 68**).[107]

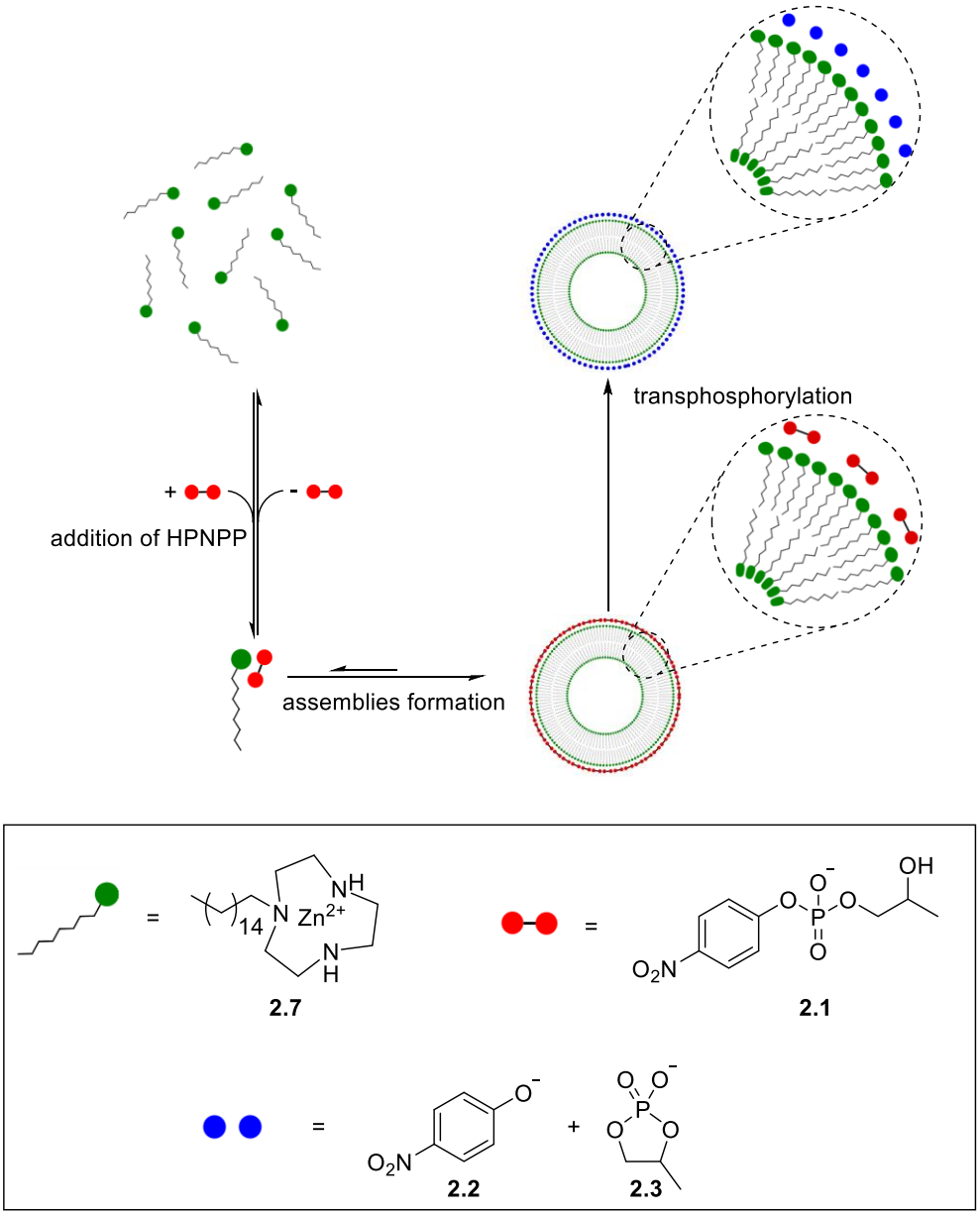

Figure 68. Substrate-induced self-assembly of cooperative catalysts.

2.4. BPNPP – a DNA model substrate

While our system was an important example of a dynamic system where the substrate induced the formation of the catalyst, we wanted to investigate ways to form a truly dissipative system that operated out-of-equilibrium. This would require a substrate that would form products that cannot stabilise the formation of the catalyst, resulting in dissipation and reformation of the catalytic monomers. In an attempt to achieve this, we investigated the properties of the DNA

model substrate bis(*p*-nitrophenyl) phosphate (**2.27**, BPNPP) (**Figure 69**). We had reasons to believe that this substrate could be cleaved by our cooperative catalytic system as literature has shown that this substrate can be cleaved by the cooperative action of two metal centres, similarly as for HPNPP (**Figure 70**).[28,93,108,109]

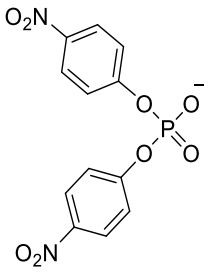

2.27

Figure 69. Molecular structure of BPNPP.

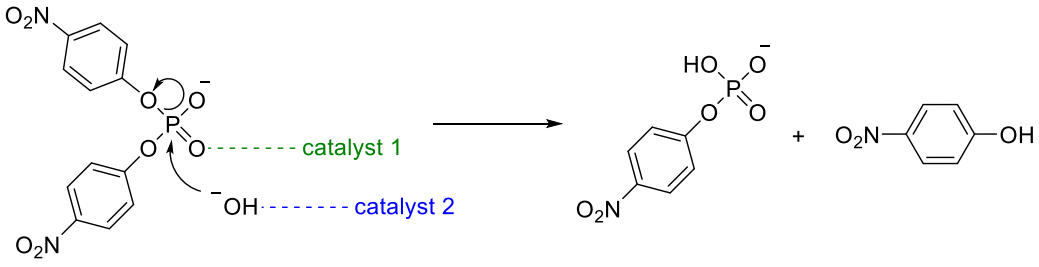

2.27 **2.22** **2.2**

Figure 70. BPNPP cleavage by cooperative catalysis.

BPNPP cleavage, however, is more challenging than HPNPP. While HPNPP is a model molecule for RNA, BPNPP (**2.7**) is a model molecule for the much less reactive DNA. One of the reasons why RNA is chemically less stable than DNA is the presence of a hydroxyl group in the 2' position (marked in **Figure 71**). The presence of this hydroxyl group allows RNA to be cleaved intramolecularly, whereas DNA cleavage requires an external nucleophile, which is less favoured entropically (**Figure 71**).[110] In addition, RNA and HPNPP form stable 5-member cyclic phosphates, while that is not the case with DNA and BPNPP. That makes DNA cleavage more challenging to perform than RNA cleavage. Once BPNPP is hydrolysed, it yields *para*-nitrophenyl phosphate (PNPP, **2.22**) and *para*-nitrophenolate (PNP **2.2**), which can be conveniently followed by UV-Vis spectrophotometry.

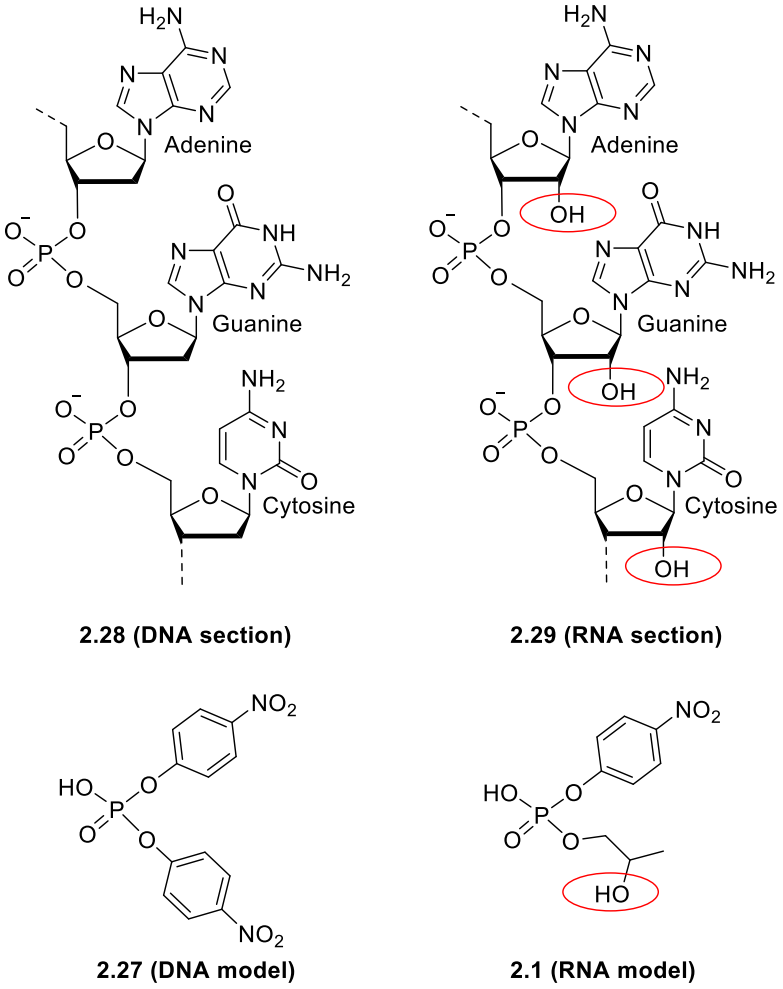

Figure 71. A DNA molecule section with three nucleotides (above, left), an RNA molecule section with three nucleotides shown (above, right), the DNA model BPNPP (below, left), the RNA model HPNPP (below, right).

2.4.1. Preliminary experiments

BPNPP is commercially available and was purchased from Sigma-Aldrich. The identical catalytically active amphiphiles used for HPNPP cleavage were also used for BPNPP, utilising **2.7**·Zn^{2+} and **2.21**·Zn^{2+} as the primary catalysts and **2.18**·Zn^{2+}, **2.19**·Zn^{2+}, **2.20**·Zn^{2+} as the control catalysts.

After performing some literature review and finding a similar system,[28] we decided to carry preliminary experiments at pH 10 utilising *N*-cyclohexyl-2-aminoethanesulfonic acid (CHES) as the buffering agent. In the example by Breslow and co-workers, a bifunctional catalyst **2.30** containing two coordinated Zn^{2+} (**Figure 72**) cooperatively cleaved BPNPP, achieving its maximum efficiency when working at pH 10.

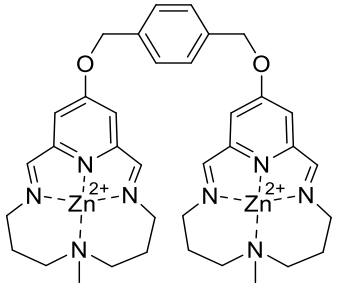

2.30

Figure 72: Breslow's cooperative catalyst for the cleavage of BPNPP.

In our preliminary experiments in the absence of catalyst, we observed that the rate of cleavage of BPNPP was slow even at a pH as high as 10. This was also observed qualitatively by the lack of an immediate yellow colour following BPNPP addition, in contrast to what is seen with HPNPP, where the yellow colour appeared rapidly after the substrate addition. When we tested the ability of our catalytic system using **2.21**·Zn^{2+} in aqueous buffered solutions to cleave BPNPP, we observed a rapid increase in absorbance at 430 nm. However, upon closer observation, we noticed that the increase in absorbance was across the whole range from 250 nm to 550 nm (**Figure 73**) and the typical yellow colour formed from the release of PNP was not observed.

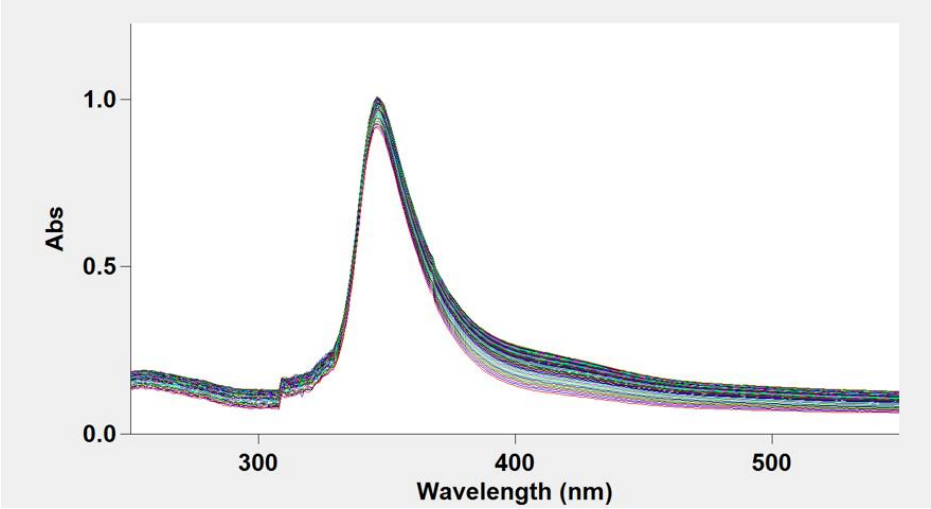

Figure 73. Absorbance UV-Vis spectra from 250 nm to 550 nm, spectral lines were registered every 1 minute. First line starts at the bottom and the absorbance increases every minute. [**2.21**] = 20 μM, [Zn^{2+}] = 20 μM, [BPNPP] = 500 μM, [CHES] = 10 mM, pH 10.

These results suggested that the initial fast absorbance increase observed for this system is not from BPNPP hydrolysis and the formation of PNP. The increase in absorption across the whole spectral range suggested that the presumed absorption may be due to the formation of vesicles from the amphiphiles, resulting in increased scattering as light passed through the sample. An overnight experiment was then conducted where the spectral data was taken every 40 minutes and revealed that after the initial rapid increase in absorbance in the whole spectrum, the rate from PNP production could be distinguished as a new peak at 430 nm. The same experiment was carried out utilising **2.21** without Zn^{2+} and **2.18**·Zn^{2+} as control experiments, it can be extracted that hydrolysis only occurs for **2.21** +Zn^{2+} (**Figure 74**).

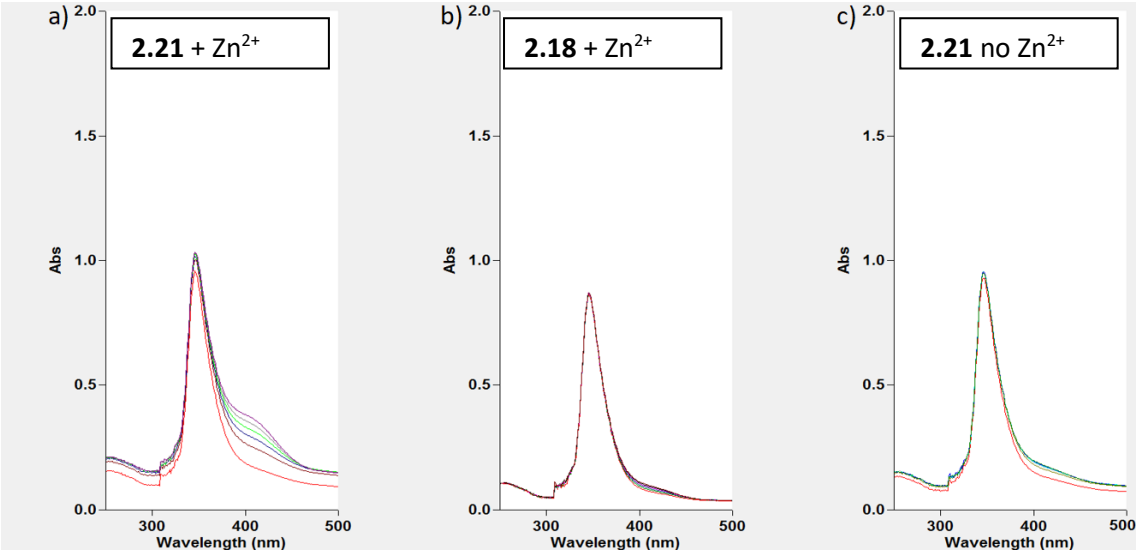

Figure 74. Absorbance UV-Vis spectra from 250 nm to 500 nm, spectral lines were registered every 40 minutes for each spectrum. The first spectral lines start at the bottom. a) [**2.21**] = 20 µM, [Zn^{2+}] = 20 µM, [BPNPP] = 500 µM, [CHES] = 10 mM, pH 10. b) [**2.18**] = 20 µM, [Zn^{2+}] = 20 µM, [BPNPP] = 500 µM, [CHES] = 10 mM, pH 10. c) [**2.21**] = 20 µM, [Zn^{2+}] = 0 µM, [BPNPP] = 500 µM, [CHES] = 10 mM, pH 10.

From the experiment shown in **Figure 74**, it can be concluded that the hydrolysis reaction is taking place only in the presence of **2.21**·Zn^{2+}, generating a distinctive new peak at 430 nm (**Figure 74, a**). The reaction did not occur when Zn^{2+} was not present (**Figure 74, c**), indicating that its role in the chemical transformation is essential. When utilising the shorter chain catalytic units **2.18**·Zn^{2+} (which does not aggregate at these conditions), the reaction rate was substantially slower, supporting the hypothesis that self-assembly of the catalytic units to form catalytic pairs is essential for this reaction (**Figure 74, b**). It can also be concluded that the initial rate cannot be measured accurately during the first two hours of the reaction; luckily, the reaction proceeds slowly enough to not achieve a significant conversion in the first two hours (less than 10%); therefore, the initial rate can be taken from data points following the first two hours.

2.4.2. pH Testing experiments

Satisfied that the preliminary experiments were positive for a possible self-assembled cooperative catalytic system, we proceeded to compare the rate of the reaction at different pH values. The rate of the hydrolysis is faster at higher pH solutions, but the background reaction (hydrolysis by hydroxide in solution without the need for the addition of catalysts) also increases at higher pH values. To determine the optimum pH at which to work at, we calculated the rate of BPNPP hydrolysis at different pH values and subtracted the background reaction (**Figure 75**). From the plot below, we can see that the maximum rate is achieved at pH 10, in agreement with previous literature reports.[28]

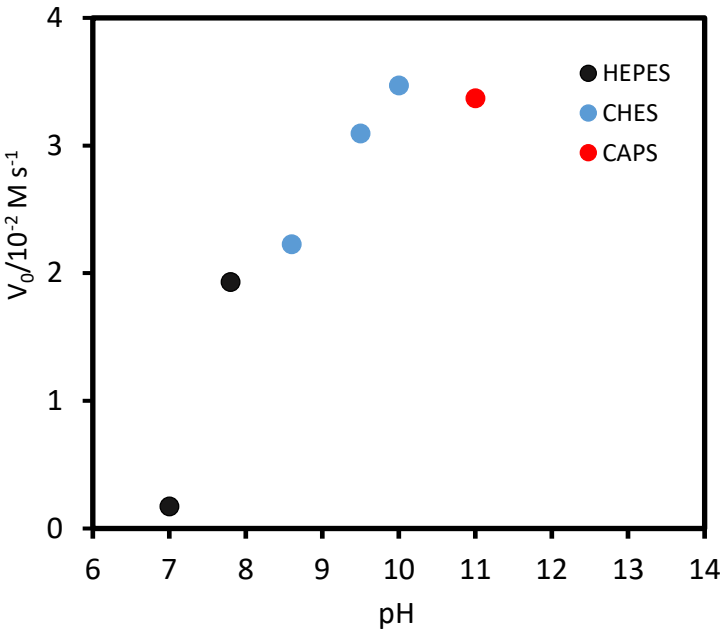

Figure 75. Initial rate of BPNPP hydrolysis with the background reaction subtracted, [**2.21**·Zn^{2+}] = 50 µM, [BPNPP] = 500 µM, [Buffer] = 10 mM, variable pH.

2.4.3. Determination of CAC and structural data

Next, we proceeded to study the aggregation properties of the system (**Figure 76**). Nile red was used again as a fluorescent probe to determine the critical aggregation concentration, but this time, a slightly different method was used. Instead of plotting the fluorescence emission intensity versus increasing concentration of amphiphile, the maximum wavelength for the fluorescence spectra was plotted against increasing concentrations of the amphiphile. This method measures the shift in the fluorescence emission maximum, which is highly dependent on the polarity of the environment around the fluorescent probe.[98] As Nile red is highly non-polar, once aggregates

are formed, it is solubilised in the hydrophobic compartments of the assemblies, resulting in a shift in the maximum fluorescence emission. The reason this method was chosen for determining the CAC of the system in the presence of BPNPP instead of using the method used previously was the observation of a wavelength shift for Nile red during the titration of the amphiphiles. This shift was more significant than the change in fluorescent emission intensity, and so using this method, the CAC could be determined with higher precision.

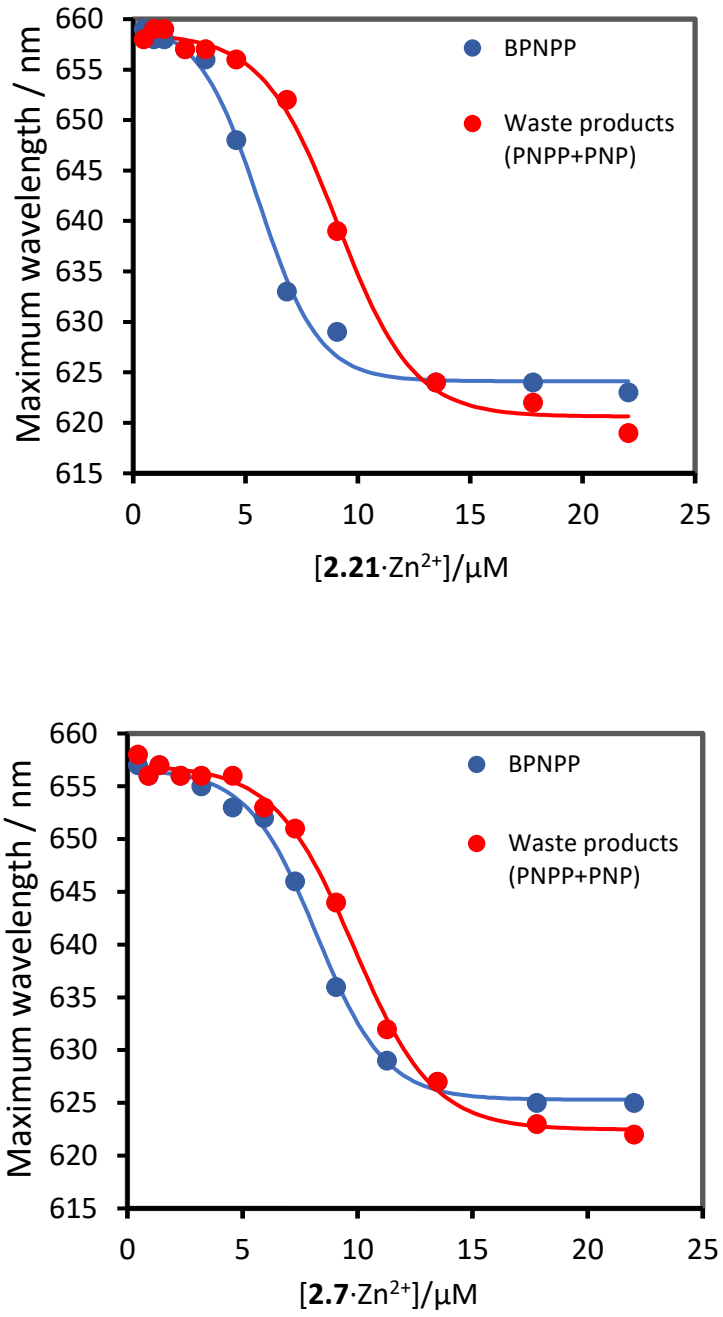

Figure 76. Fluorescence emission maximum vs [C_nTACN·Zn^{2+}], λ_{ex} = 570 nm, [CHES] = 10 mM, pH 10, blue: [BPNPP] = 500 µM; red: [PNPP] = [PNP] = 500 µM, [Nile Red] = 2 µM.

By fitting the points into the Boltzmann sigmoidal equation, the CAC can be determined from the inflection point of the plot. The CAC was determined to be 5.6 μM of **2.21**·Zn^{2+} in the presence of 500 μM of BPNPP. On the other hand, in the presence of the products of the reaction (500 μM of PNPP and 500 μM of PNP), the CAC was determined to be 9.1 μM for **2.21**·Zn^{2+}. For **2.7**·Zn^{2+}, the CAC was determined to be 8.2 μM of **2.7**·Zn^{2+} in the presence of 500 μM of BPNPP and 9.8 μM of **2.7**·Zn^{2+} in the presence of 500 μM of PNPP and 500 μM of PNP. Theoretically, if the system relies on cooperative catalysis between catalytic units and the self-assembly for reactive catalytic pairs to perform the reaction, these results suggest that at concentrations above the CAC of **2.21**·Zn^{2+} in the presence of BPNPP, but below the CAC of **2.21**·Zn^{2+} in the presence of the hydrolysis products, a chemically fuelled dissipative system would be possible, (see chapter 1, section 1.4.1) . An example of a dissipative cooperative system where the catalyst is assembled only in the presence of the substrate was recently published by Das' research group in 2019.[111]

The size of the assemblies formed in the presence and absence of substrate and waste was determined using dynamic light scattering (DLS) measurements (**Figure 77**). It was decided to utilise **2.21**·Zn^{2+} as the main catalyst because the difference in CAC values in the presence of the substrate and the waste products was more significant than the difference obtained for **2.7**·Zn^{2+}. The assemblies were measured at a catalyst (**2.21**·Zn^{2+}) concentration of 7 μM, as this was between the CAC values obtained for BPNPP and the waste products. In the absence of substrate, a size of 22 ± 4 nm was obtained. Following the addition of BPNPP, the measured structures increased in size to 187 ± 75 nm. In the presence of the waste products, the size of the structures was measured to be 58 ± 24 nm.

The results indicate that at these conditions, the substrate induces the formation of larger aggregates from much smaller assemblies. Furthermore, when the reaction is completed, structures are still formed, but they are much smaller in size than the structures in the presence of BPNPP but much larger than the aggregates observed with only the catalyst present. To represent a complete reaction cycle and a refuelling after the substrate would be completely cleaved, BPNPP was added to the waste product experiment, and the size was measured again and a size of 171.40 ± 52.70 nm was obtained. A new experiment containing double the amount of waste was performed to represent the cleavage of the extra BPNPP added and the size of the assemblied obtained became 121.70 ± 40.82 nm. These results indicate that after performing various cycles, the differences in the effects induced by the substrate and the effects induced by the waste is diminished. This, unfortunately, means that it would be difficult to follow this reaction by DLS after the first cycle.

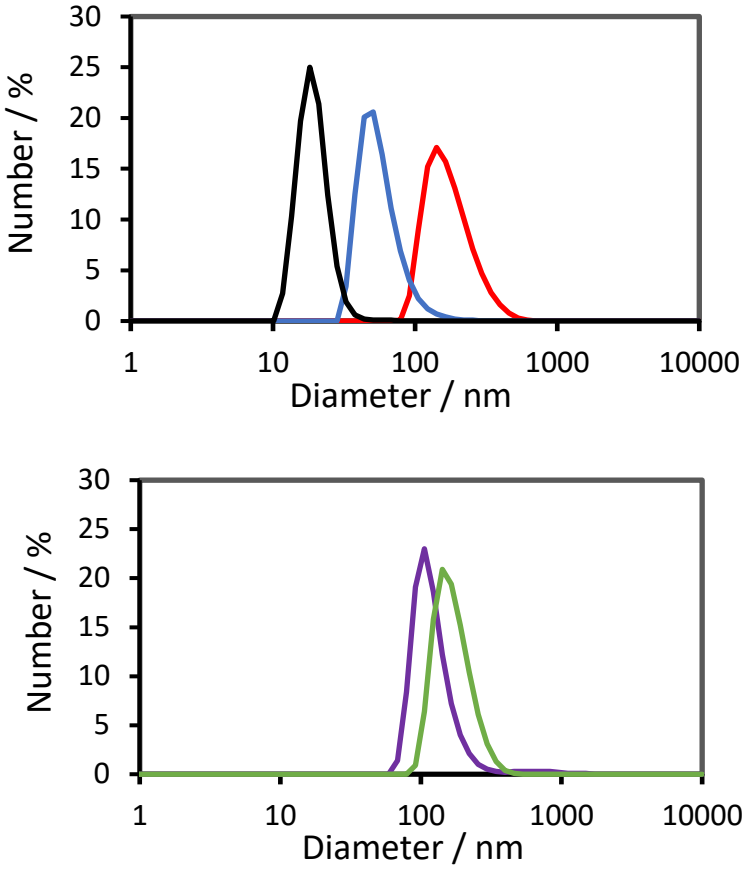

Figure 77. Hydrodynamic diameter of assemblies measured with dynamic light scattering. a) Black line: [**2.21**·Zn^{2+}] = 7 μM, [BPNPP] = 0 μM. Red line: [**2.21**·Zn^{2+}] = 7 μM, [BPNPP] = 500 μM , measurement performed just after addition of BPNPP, Blue line: [**2.21**·Zn^{2+}] = 7 μM, [PNPP] = 500 μM, [PNP] = 500 μM. b) Green line: [**2.21**·Zn^{2+}] = 7 μM, [PNPP] = 500 μM, [PNP] = 500 μM, [BPNPP] = 500 μM, Purple line: [**2.21**·Zn^{2+}] = 7 μM, [PNPP] = 1000 μM, [PNP] = 1000 μM. All measurements were performed in aqueous buffer solution (CHES, 10 mM, pH 10) at 25 ℃.

2.4.4. Catalytic activity of the system

Next, we measured the rate of BPNPP hydrolysis at different concentrations of **2.21**·Zn^{2+} (**Figure 78**, a) and **2.7**·Zn^{2+} (**Figure 78**, b). The concentration of **2.21**·Zn^{2+} at which the reaction rate increases dramatically (6.0 μM) matches closely with the CAC of the system determined under the same conditions (5.6 μM) using fluorescence. For **2.7**·Zn^{2+}, the concentration at which the rate increases (8.1 μM) also match closely with the CAC determined under the same conditions (8.2 μM). These studies support the hypothesis that the assembly of the catalytic units to form active species is essential to achieve cooperativity and effective catalysis.

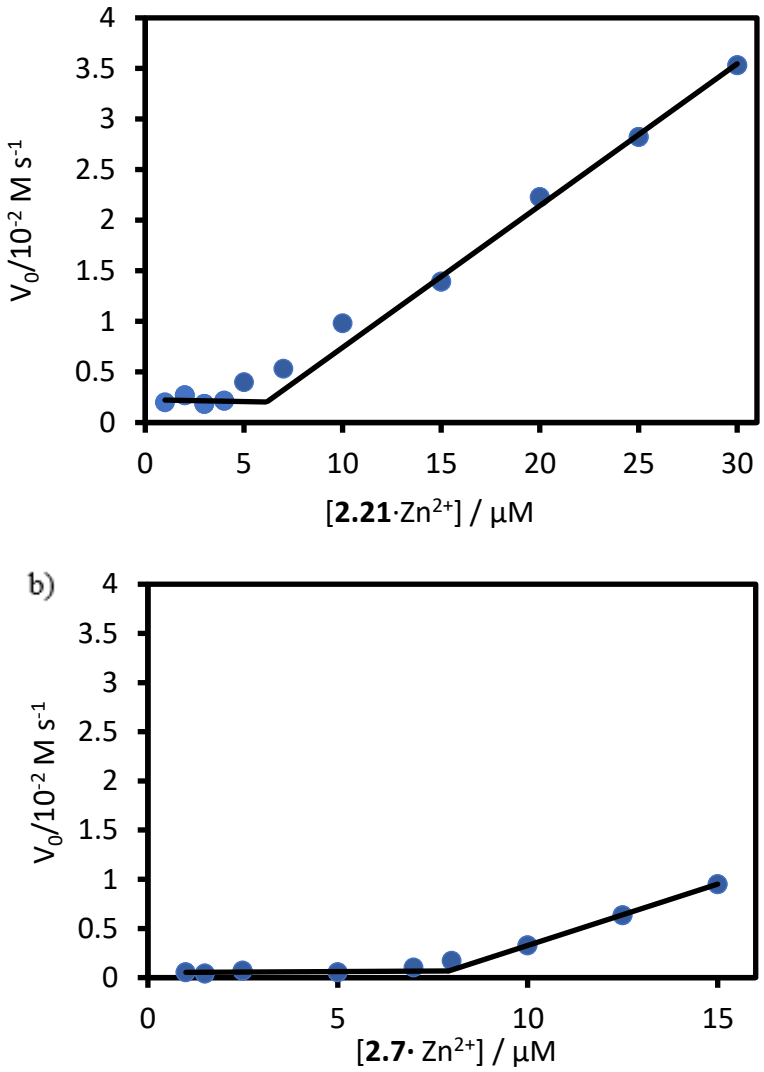

Figure 78. a) Initial rate of BPNPP hydrolysis, [**2.21**·Zn^{2+}] = Variable, [BPNPP] = 500 µM, [CHES] = 10 mM, pH 10. The trend lines are the linear fits to the first four and last four data points. b) Initial rate of BPNPP hydrolysis, [**2.21**·Zn^{2+}] = Variable, [BPNPP] = 500 µM, [CHES] = 10 mM, pH 10, 40 ºC. The trend lines are the linear fits to the first four and last three data points.

The catalytic activity of the different analogous catalysts containing different chain lengths was also investigated (**Table 1**). At a concentration of 50 µM, it can be seen that an increase in the catalytic rate is seen with analogues containing longer hydrocarbon chains. In parallel with what was observed with the HPNPP studies, observing different catalytic rates at concentrations above the CAC can seem counterintuitive since it might be expected that the catalyst is fully formed above the CAC so that the apparent concentration of catalyst should be the same. However, in this example, the CAC has been calculated only for **2.7**·Zn^{2+} and **2.21**·Zn^{2+}. In both cases, these studies have been performed the studies above the CAC.

Entry	Catalyst employed	Initial rate ± standard deviation ($\times 10^{-2}$ M s^{-1})
a	Zn^{2+}	0.47 ± 0.04
b	**2.18**·Zn^{2+}	0.73 ± 0.19
c	**2.19**·Zn^{2+}	1.75 ± 0.05
d	**2.7**·Zn^{2+}	3.70 ± 0.24
e	**2.21**·Zn^{2+}	4.14 ± 0.35

Table 1. Initial rate of BPNPP hydrolysis, entry **a** [Zn^{2+}] = 50 μM, entries **b c d e** [C_nTACN·Zn^{2+}] = 50 μM, all entries [BPNPP] = 500 μM, all entries [CHES] = 10 mM, all entries pH 10, 40 °C, three repetitions performed per entry to obtain the average rate and the standard deviation.

To study the origin of the rate difference observed with **2.7**·Zn^{2+} and **2.21**·Zn^{2+}, we measured the rate of BPNPP hydrolysis at a range of different substrate concentrations. By fitting the resulting curve to Michaelis-Menten kinetics, we were able to obtain the V_{max} and K_M values. **Figure 79** shows a plot of the hydrolysis rate at a constant concentration of C_nTACN·Zn^{2+} plotted against increasing concentrations of the BPNPP substrate. Fitting of the saturation profiles to the Michaelis-Menten equation yielded similar V_{max} values for **2.21**·Zn^{2+} (4.5 ± 0.1× 10^{-2} mol s^{-1}) and **2.7**·Zn^{2+} (4.1 ± 0.1× 10^{-2} mol s^{-1}). The K_M value for **2.21**·Zn^{2+} was 30.7 ± 4.4 μM and was similar to the K_M value for **2.7**·Zn^{2+} (26.9 ± 3.7 μM).

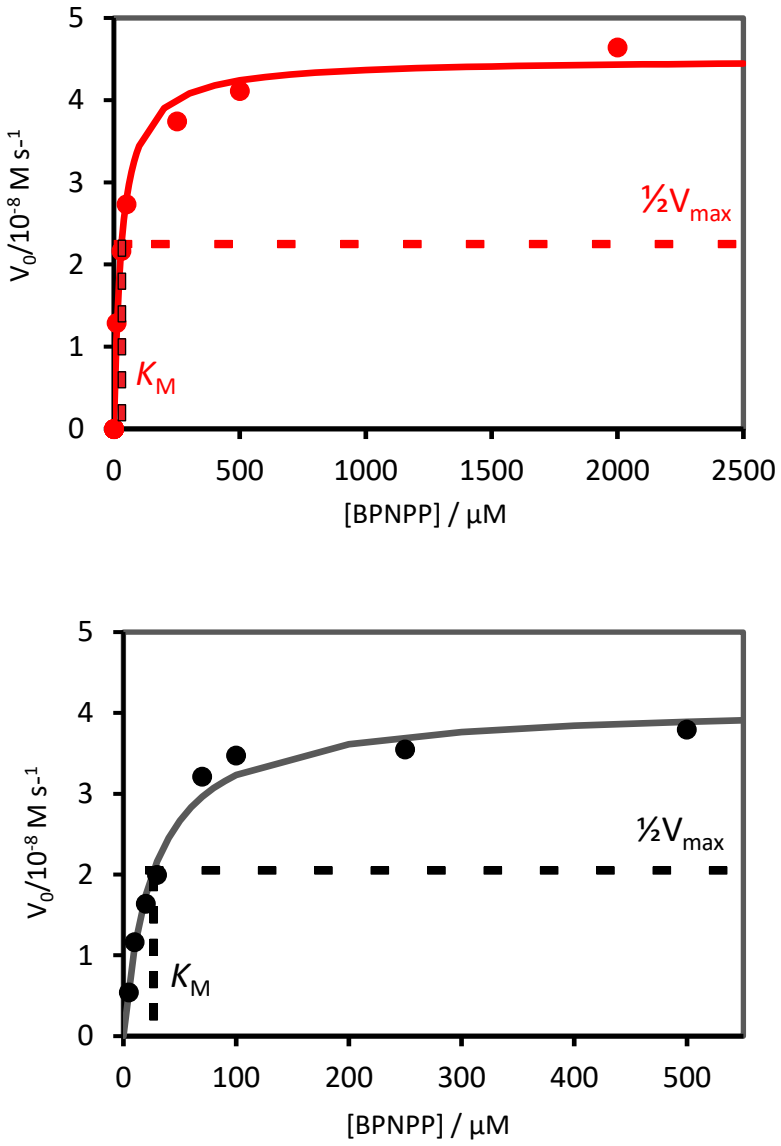

Figure 79. Initial rate of BPNPP hydrolysis at increasing BPNPP concentration, fixed C_nTACN·Zn^{2+} concentration – [C_nTACN·Zn^{2+}] = 50 µM , a) **2.21**·Zn^{2+}, b): **2.7**·Zn^{2+}, [CHES buffer] = 10 mM), the solid lines are the data fit according to a Michaelis-Menten mechanism. Experiments were performed in aqueous buffer at pH 10, at 40 °C.

To provide further proof that the reaction needed two Zn^{2+} ions in close proximity to accelerate the catalysis, the reaction rate was plotted at different Zn^{2+} concentrations, keeping the rest of the components in the reaction the same: [CHES buffer] = 10 mM, pH 10, [C_nTACN] = 50 µM, [BPNPP] = 500 µM, 40 °C (**Figure 80**). As observed with the HPNPP system, when the reaction contained a low concentration of Zn^{2+}, there is a low probability for the Zn^{2+} to find neighbouring cations. This results in a lack of cooperativity, and the catalytic rate of the reaction is slow. There is a point where the concentration of Zn^{2+} is high enough so the probability increases, strong

cooperativity emerges, and the rate of the reaction increases dramatically with increasing concentrations of Zn^{2+}. At even higher concentrations of Zn^{2+} the system reaches saturation. It can be observed that increasing the concentration of Zn^{2+} further above this point does not increase the reaction rate. The sigmoidal profile from these experiments strongly supports that the system relies on cooperativity between two Zn^{2+} cations to perform the reaction effectively.

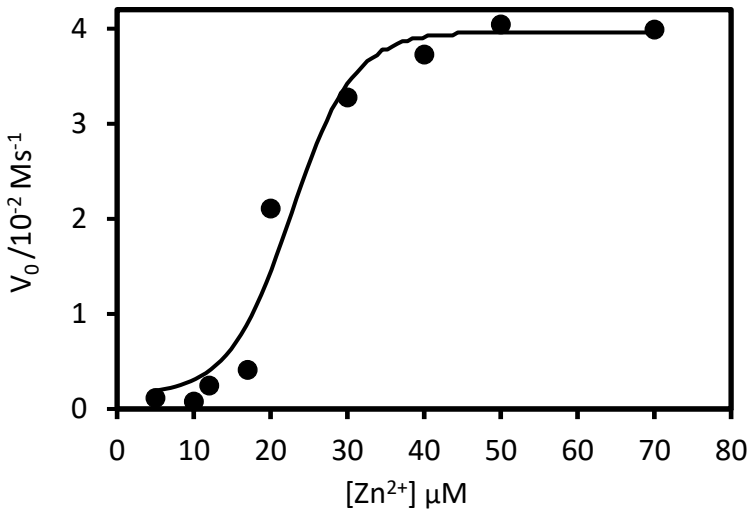

Figure 80. Initial rate of BPNPP hydrolysis at a fixed concentration of **2.21** and varying Zn^{2+} concentrations ([CHES buffer] = 10 mM, [**2.21**] = 50 µM, [BPNPP] = 500 µM, 40 °C).

2.4.5. Study of the dissipative properties

Satisfied with the cooperative nature of the BPNPP hydrolysis with our self-assembled system, we proceeded to study the dissipative properties for the system with catalyst **2.21**·Zn^{2+}. As reported in **Figure 76**, the CAC of the system in the presence of BPNPP was 5.6 µM, and the CAC of the system in the presence of the waste products of the reaction was 9.1 µM. In theory, this could mean that at a concentration of **2.21**·Zn^{2+} between 5.6 µM and 9.1 µM, the system would form large assemblies in the presence of BPNPP and disassemble (or form alternative structures) when all or some of the substrate is consumed.

Working at 7 µM of **2.21**·Zn^{2+}, 500 µM of BPNPP, 10 mM CHES (pH 10) and in aqueous solution, the maximum wavelength of fluorescence emission spectra was measured over time, utilising Nile red as a fluorescence probe. We expected to observe a change in the structures formed in solution over time, also resulting in a shift of the maximum wavelength of the emission spectra from ≈ 650 nm to ≈ 630 nm. Unfortunately, after 24 hours, the emission peak of Nile red became undetectable by the fluorimeter, and a pale pink precipitate could be observed at the bottom of the fluorescence cuvette by the naked eye. We hypothesise that, over time and in the

presence of Nile red, a new larger aggregate is formed by the system that is able to trap and precipitate the Nile red in solution. This precipitate did not disappear over time, and unfortunately, the dissipative properties could not be confirmed for this system using this fluorescence method. Even though the results obtained from DLS were promising and indicated a dissipative system, further studies need to be carried to provide further evidence of a substrate fuelled out-of-equilibrium supramolecular system that exploits cooperative catalysis to consume the chemical fuel.

2.5. Conclusion of the chapter

To summarise, in this chapter, two cooperative catalytic systems have been presented, both utilising hydrophobic forces to induce the formation of assemblies that possess catalytic activity. The first example introduces a novel, substrate-induced cooperative catalytic system involving the RNA model substrate HPNPP. The catalytic units are amphiphiles that form vesicular assemblies above a specific critical aggregation concentration. Once these assemblies are formed, the Zn^{2+}-containing polar heads of the assemblies are brought into close proximity by hydrophobic forces, allowing the cooperative cleavage of HPNPP accelerated by two metallic centres. The system exhibits turnover and saturation kinetics which can be described by Michaelis-Menten kinetics. Furthermore, it has been shown that the substrate (HPNPP) decreases the critical aggregation concentration of the system, meaning that it is able to template the formation of the assemblies, that once formed, are able to cleave that same substrate. The products of HPNPP **2.1** cleavage (PNP **2.2** and cP **2.3**) have also been shown to decrease the critical aggregation concentration of the system. For this reason, disassembly of the vesicles could not be observed once the fuel of the reaction is consumed.[107]

The second example consists of a similar system that utilises cooperative catalysis to cleave a different phosphate ester, the DNA model substrate BPNPP. This substrate is much more stable than HPNPP and requires longer reaction times at a higher pH. We have shown that BPNPP can also be cleaved by catalysts formed by a dynamic supramolecular assembly. Intending to create a truly dissipative catalyst system, we were able to demonstrate that the critical aggregation concentration of the catalyst is different in the presence of the BPNPP substrate and the waste products in the reaction. This is a crucial step in demonstrating that chemical fuel-driven, dissipative, out-of-equilibrium systems can be created from these simple components – however, further work still needs to be done to demonstrate dissipation and reformation of the cooperative catalyst.

To the best of our knowledge, prior to the studies presented in this thesis, the only other examples of self-assembled catalytic systems where cooperativity between the units was clearly demonstrated, involved hydrogen bonding,[50,51,53,54,112–115], or electrostatic interactions[55] to bring

the required catalytic units into proximity to achieve cooperativity. These examples were able to show improved efficiency relative to the monomeric non-assembled analogues.

A few early examples of metallomicelles confirmed an increase in the reaction rate involving aggregated catalytic units.[116–118] However, even though in some cases the increase in rate was probably achieved in part due to cooperative effects, this was not clearly demonstrated or even hypothesized, and classic micellar concentration effects, solvation effects and local concentration effects were used to rationalise the improved rates/efficiencies. For instance, Menger *et al.* presented a study in 1987 showing how an amphiphile containing Cu^{2+} **2.32** effectively cleaved a phosphate ester **2.31** under mild conditions (**Figure 81**).[116] In the article, it was claimed that *"possible reasons for the huge rate accelerations include enhanced electrophilicity of the micellized metal (…) and acidity of copper-bound water (…)."* Nowadays, we know that this kind of phosphate esters are likely to be cleaved by the cooperation of two metal centres cooperating close in space,[28,86,88,89,119] and the cooperativity of various Cu^{2+} centres induced by self-assembly of the catalytic units makes a plausible explanation for the enhanced rates in this example.

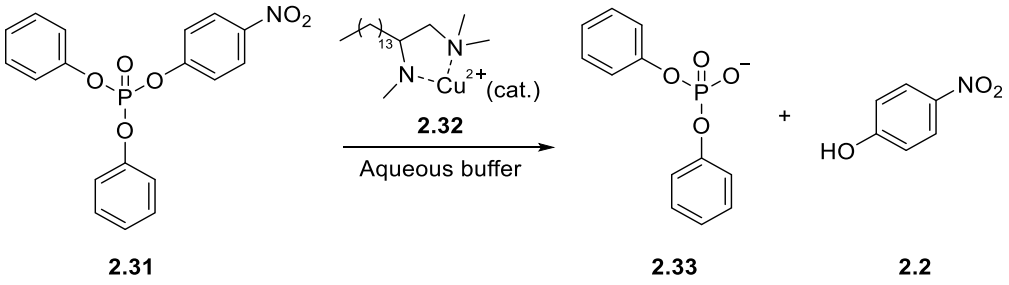

Figure 81. Phosphate ester cleavage by an amphiphilic catalyst containing Cu^{2+}.[116]

To the best of our knowledge, this chapter presents the first catalytic systems that evidently demonstrate the use of hydrophobic interactions to enhance the reactivity of a self-assembled cooperative catalyst. Furthermore, the HPNPP system presents exciting properties due to its dynamism, where presence of the substrate induces formation of the active catalyst that then cleaves the substrate. This is in analogy with the formation and degradation of microtubules in nature, which is seen as a classic example of a chemically-fuelled dissipative system. Other substrate-induced systems include the dimerisation of the key protease in SARS-coronavirus-1.[120]

The described cooperative mechanism is crucial for the future development of dissipative self-assembled systems. It provides an example for the preparation of high-energy assemblies and eliminates the necessity for external elements to dissipate the energy of the activated state. Dissipation, once the substrate is completely consumed, has not been observed in this study.

Continued efforts are aimed at developing alternative and viable systems that present a higher affinity for the catalyst compared to the waste, which theoretically would allow spontaneous dissipation of the catalyst system after the substrate is converted to waste.

Chapter Three

Utilising hydrophobic interactions to develop more efficient catalysts for the hydrolytic kinetic resolution of terminal epoxides

3.1. The importance of epoxides

Epoxides are common functional groups present in numerous bioactive natural products. It can be found, for example, in the antileukemic diterpenoid triptolide (**3.1**)[121] and to the antitumor and antibiotic azinomycin B (**3.2**)[122] (**Figure 82**). However, the importance of epoxides (and especially chiral epoxides) lies in the ability to perform ring-opening reactions in a regioselective and stereospecific way, which allows the creation of complex functionality and appealing building blocks for synthetic chemistry (**Figure 83**).[123]

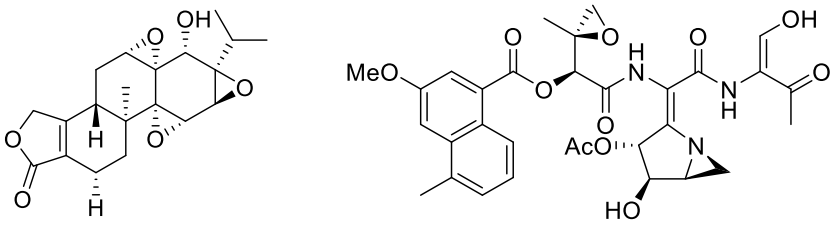

3.1 **3.2**

Figure 82. Molecular structure of triptolide (left) and azinomycin B (right).[121,122]

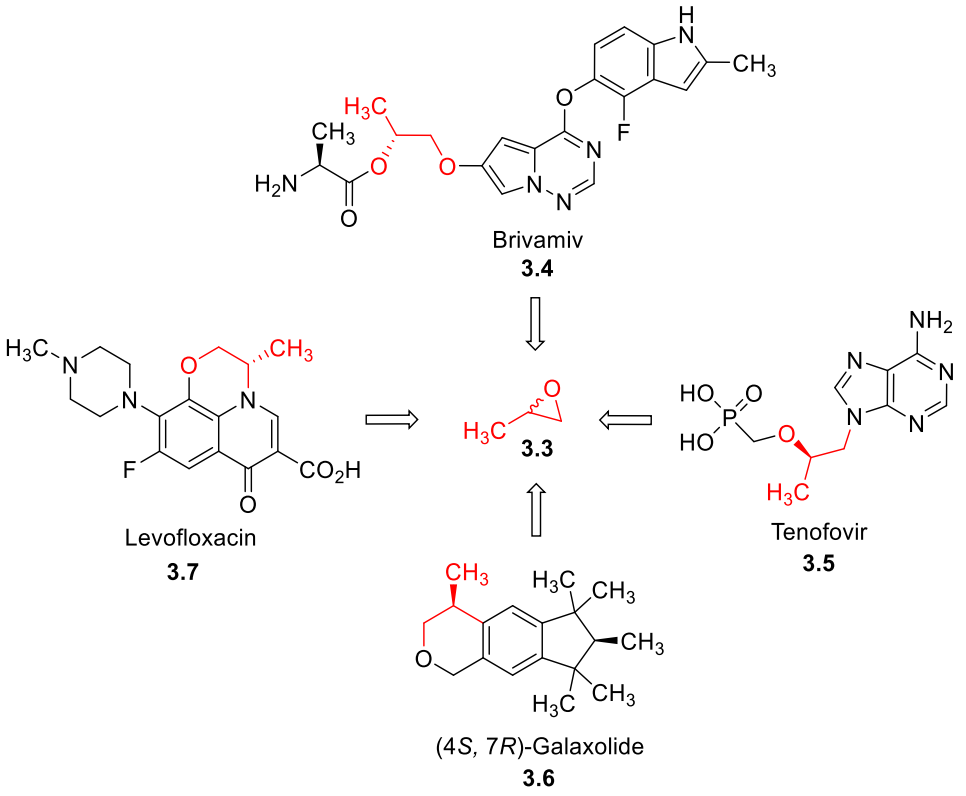

Figure 83. Potential applications of resolved propylene oxide (**3.3**).[123]

3.2. Hydrolytic kinetic resolution of epoxides

In 1997, Eric N. Jacobsen reported the hydrolytic kinetic resolution (HKR) of epoxides utilizing chiral (salen)Cobalt catalysts (**3.8**, **3.9**, **3.10**, **3.11**).[124] This reaction has since been established as an efficient method to obtain enantiopure terminal epoxides and 1,2-diols from racemic mixtures of terminal epoxides (**Figure 84**). Its importance relies on its broad substrate scope, high selectivity[125], and practical applications in both academic and industrial contexts.[123,126] The fact that the reaction utilises water as a reagent, that the catalysts can often be recovered and recycled, and that the reaction can be performed in mild, neat conditions, makes it also interesting from a green chemistry point of view.[19] The active catalyst is a (salen)Co(III)complex, generated from an inactive (salen)Co(II) complex by its oxidation in the presence of air. The first generation of catalysts are the two enantiomeric complexes shown in **Figure 84**.

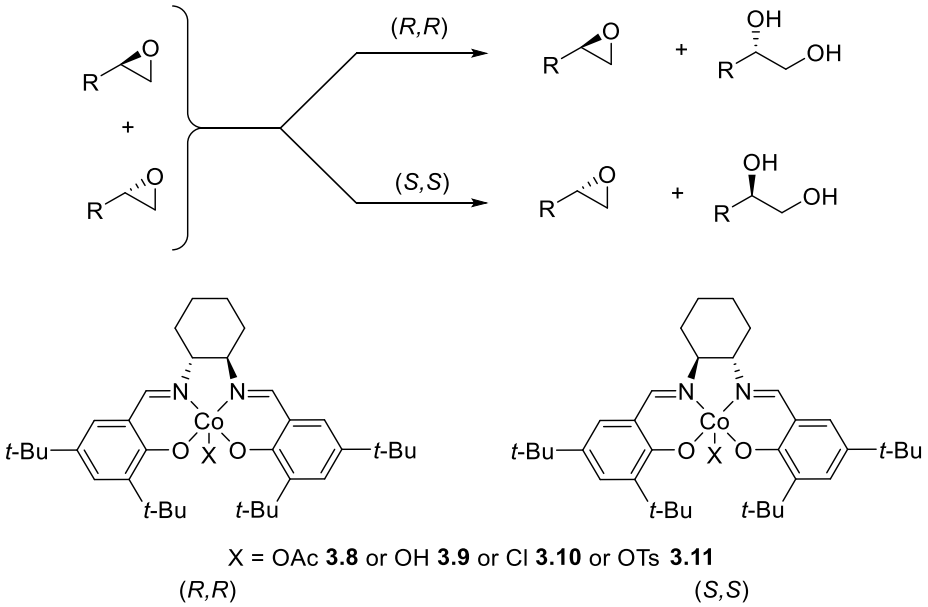

Figure 84. General representation of the hydrolytic kinetic resolution of epoxides and the first generation of catalysts.

3.3. Theoretical aspects of kinetic resolution

A kinetic resolution is a method of separating two enantiomers by exploiting a chemical reaction where two enantiomers of a racemic mixture react at different velocities to form a product mixture that is enriched in the slower reacting enantiomer. The relative reaction rates of the two enantiomers can be expressed as $k_{rel} = k_{fast}/k_{slow}$, and the value of k_{rel} is dictated by the term $\Delta\Delta G^{\ddagger}$ as shown in **Equation 8.** The difference in rates between enantiomers come from achieving

different transition state energies for the chemical transformation by the use of chiral reagents or catalysts (**Figure 85**).[126]

$$k_{rel} = \frac{k_{fast}}{k_{slow}} = e^{\Delta\Delta G‡/RT} \qquad \textbf{Equation 8}$$

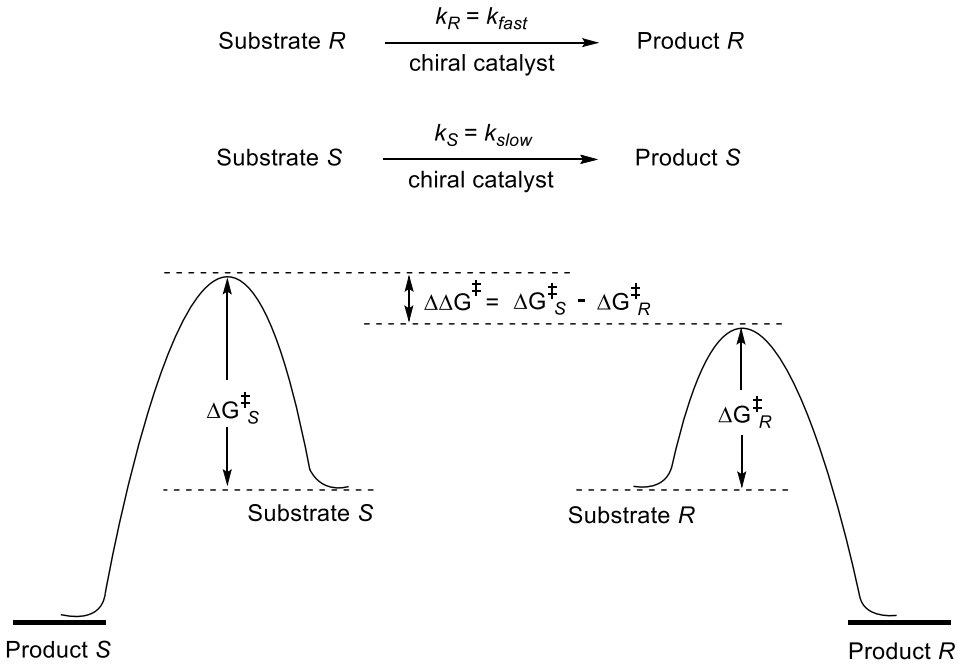

Figure 85. Exemplar energy diagrams showing the relative rates in kinetic resolutions.[126]

The *e.e.* observed in a kinetic resolution grows as the conversion of the reaction increases before the conversion of the faster enantiomer reaches 100%. From a synthetic point of view, an advantage of a kinetic resolution is that the unreacted substrate can be recovered in high *e.e.* without the need of an especially high k_{rel}. By simply letting the reaction progress to higher conversion, the enantiomerically pure compound can typically be obtained.

3.4. Mechanistic aspects of the HKR of epoxides

Kinetic data from the original 1997 paper suggested that the hydrolytic kinetic resolution of epoxides had a second-order rate dependency with respect to catalyst concentration.[124] Later on, this was explained mechanistically by Jacobsen's research group in two different articles,[127,128] demonstrating the need for two catalytic units in the transition state of the rate-determining step (**Figure 86**).

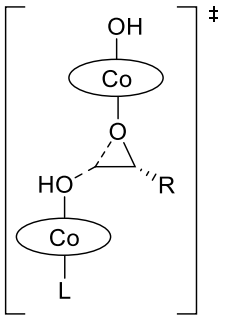

Figure 86. Suggested general TS of the rate-determining step of the HKR of epoxides by (salen)Co catalysts.[124]

While one catalytic unit increases the electrophilicity of the epoxide, the other one stabilises the hydroxide anion that opens up the epoxide. In the mechanistic study,[128] it was experimentally demonstrated that the reaction works most efficiently when 50% of the catalytic units were available to act as a Lewis acid, and 50% of the catalyst acted to stabilise the nucleophile (**Figure 87**). Also, it was found that when the counterion used was tosyl, the catalyst equilibrates over time, leading to a close to 50% mixture of Lewis acid and nucleophile in reaction conditions, which makes it the fastest counterion to use. When utilising other counterions like acetate, chlorine, triflate or hydroxyl, the mixture does not lead to a 50% mixture of Lewis acid and nucleophile, and the rate of the HKR is slower than when utilising tosyl.

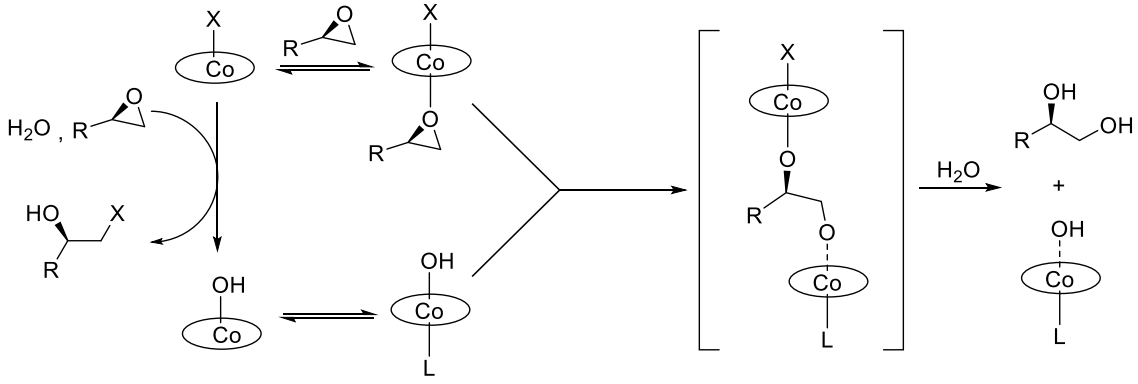

Figure 87. Proposed mechanism of catalysis for HKR reactions catalysed by mixtures of (salen)Co−X and (salen)Co−OH.

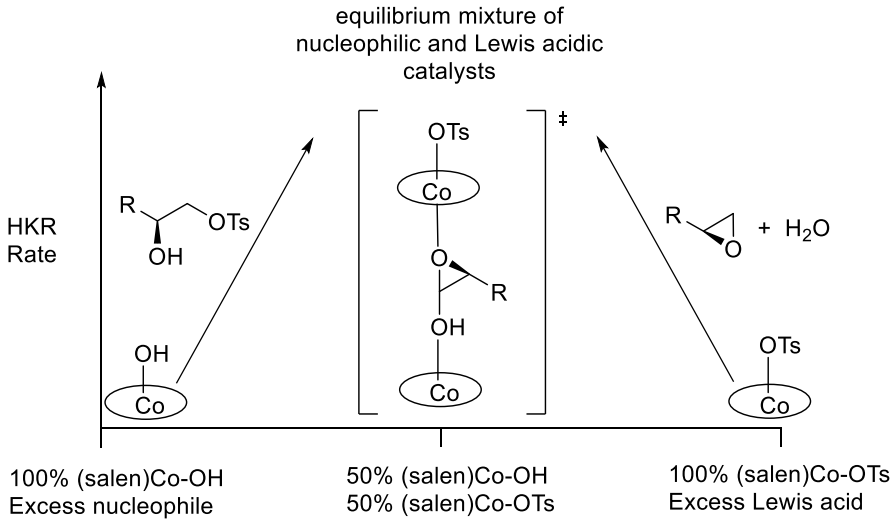

Figure 88. Catalyst partitioning in the (salen)Co−OTs-catalysed HKR.[127]

From this study, it was observed that the deactivation of the catalyst results from the addition of the counterion of the complex (salen)Co(III)-X to the epoxide and the corresponding formation of a substituted alcohol and a (salen)Co(III)-OH species. As illustrated in **Figure 88**, the reaction rate achieves its maximum when 50% of the catalytic units acts as Lewis acid, and 50% acts as a nucleophile. If there is extra formation of (salen)Co(III)-OH, this causes a change in the catalytic unit ratio, which causes a decrease in the rate. This fact makes tosyl an excellent counterion for the HKR.

3.5. Strategies for accelerating the HKR of epoxides

As seen in previous chapters, reactions that are second-order with respect to the catalyst can be improved by bringing the required catalytic units close together in space. A detailed study by Konsler, Jacobsen, *et. al.* of a closely related asymmetric ring opening of epoxides by hydrazoic acid (HN_3), utilises a similar (salen)Cr catalyst to perform the reaction. The kinetics of the transformation were studied for the monomeric and dimeric versions of the catalyst, with the rate expressed as a two-term rate equation that involves both intramolecular and intermolecular components (**Equation 9**).[129]

$$\text{Rate} = k_{intra}[\text{catalyst}] + k_{inter}[\text{catalyst}]^2 \qquad \textbf{Equation 9}$$

Later, Wezenberg and Kleij used the same equation to explain the increase in rate in the hydrolytic kinetic resolution (HKR) of epoxides in a system where the catalytic units were attached covalently in a calix[4]arene scaffold **3.12** (**Figure 89**). Interestingly, while there is a k_{intra} component for this dimeric catalyst that is not present in the monomeric version of the catalyst,

they also observe a decrease in the k_{inter} term, expected due to a decrease in the randomization of the Co sites, meaning a halving the total amount of dimeric catalysts. This makes the approach more efficient at low concentration of catalyst, however, at higher concentrations of catalyst the k_{intra} term cannot compensate the loss of randomization, making the monomeric catalyst more efficient than the dimeric one at high concentration conditions.[30]

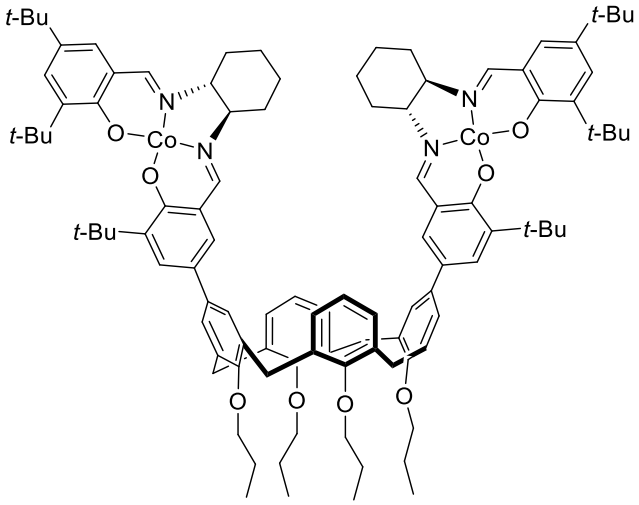

3.12

Figure 89. A Calix[4]arene supported dimeric (salen)Co(III) catalyst.[30]

Several other studies have been performed to improve the HKR of terminal epoxides. Examples include linking the catalytic units covalently into dendritic systems, anchoring the catalytic units onto surfaces, and the use of hydrogen bonding between catalytic units.

3.5.1. (salen)Cobalt catalysts linked covalently

The work by Breinbauer and Jacobsen.[34] describes how a dendrimeric system was used to achieve cooperativity between catalytic units, reporting a relative rate per [(salen)Co] site up to 24 times faster than the monomeric catalyst (**Figure 90**). Interestingly, the dendrimer containing four [(salen)Co] sites (shown below) was observed to be more reactive than the dendrimer containing eight or 16 [(salen)Co] sites when the rate per [(salen)Co] site was calculated. This work represented the first time an increased rate due to enhanced cooperativity between neighbouring catalytic groups had been observed in a dendrimer.

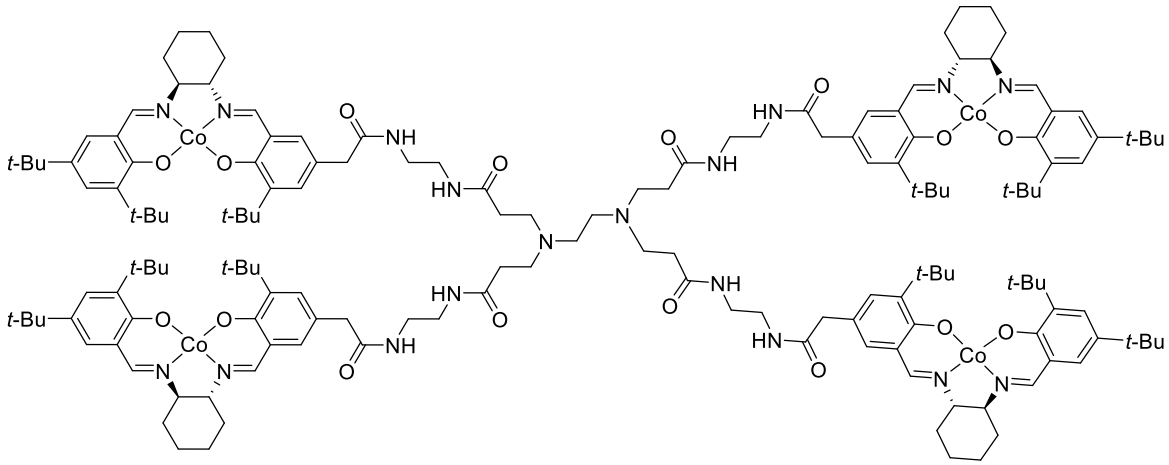

3.13

Figure 90. A dendrimeric [(salen)Co] catalyst.[34]

Further work by the same research group focused on oligomeric versions of the catalyst **3.14** demonstrating an enhancement in reaction rates with this kind of system.[31,130] In those examples, the catalyst loading was reduced with respect to the control catalyst when using terminal epoxides for the same reaction conditions (**Figure 91**).

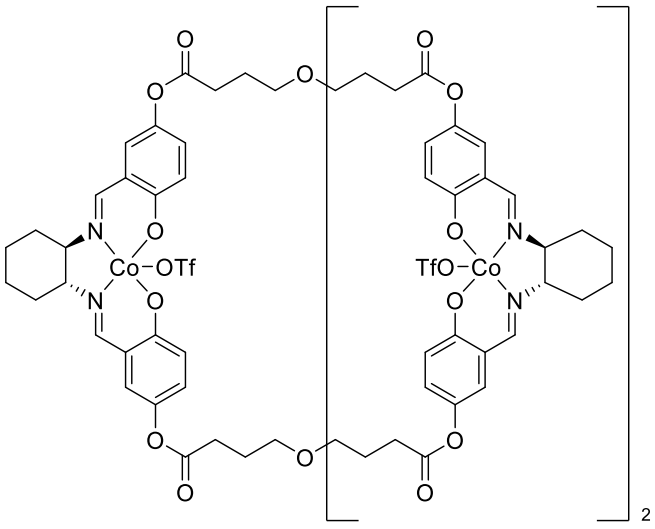

3.14

Figure 91. Oligomeric [(salen)Co] catalyst.[130]

Weck and co-workers presented another methodology utilising oligomeric versions of the catalyst.[131] The oligomeric compound **3.15** is achieved by ring-expanding olefin metathesis. Their catalyst was proven to be highly efficient at low concentrations of catalysts, routinely utilising 0.01% loading (**Figure 92**).

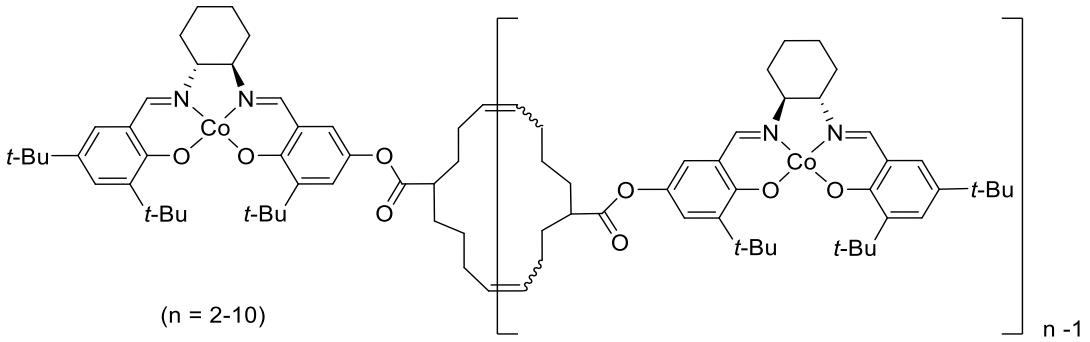

3.15

Figure 92. Macrocyclic oligomeric (salen)Co catalysts forming by ring-expanding metathesis.[131]

An interesting example by Rossbach *et al.* presents a polymeric, water soluble catalyst that combines the enhancement in cooperativity by reducing distances between catalytic units, with the homogenising capability of the catalyst. Excellent results are achieved with a range of substrates including with the challenging aromatic epoxides. The polymeric catalyst forms micelles in the reaction mixture, which locally concentrates the catalyst and creates a hydrophobic core that limits any extra water reacting with the epoxide. This means that the reaction can be performed in aqueous solution, where there is excess water (note that usually the HKR of epoxides is performed with 0.55-0.60 equivalents of water to prevent over-reaction). After treatment the catalyst could be reused up to four times (**Figure 93**).[132]

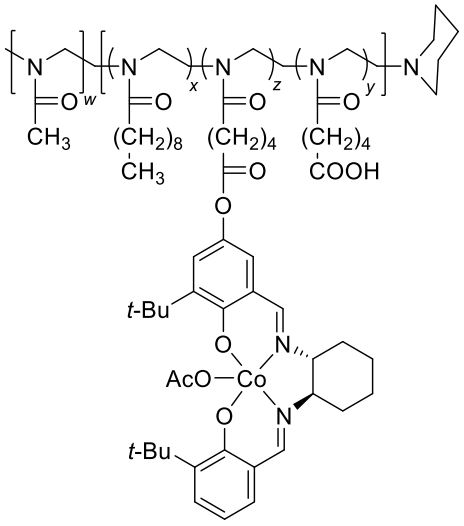

w=41, x=4.5, y=2.8, z=2.3

3.16

Figure 93. A polymeric, water-soluble (salen)Co(III) catalyst.[132]

3.5.2. (salen)Cobalt catalysts anchored onto surfaces

A report by Belser and Jacobsen demonstrates how the incorporation of (salen)Co catalysts onto gold nanoparticles can also significantly increase the reaction rate relative to the monomeric catalysts.[41] This was achieved by attaching the (salen)Co complexes onto gold nanoparticles using long-chain thiols, which accelerates the reaction by bringing the catalytic units together to enhance cooperativity. Immobilising the catalyst onto a nanoparticle also allows the catalyst to be recovered by filtration. After a re-oxidisation step, the catalyst **3.17** could be reused up to seven times, showing the enormous potential of functionalised nanoparticles as cooperative catalysts (**Figure 94**).

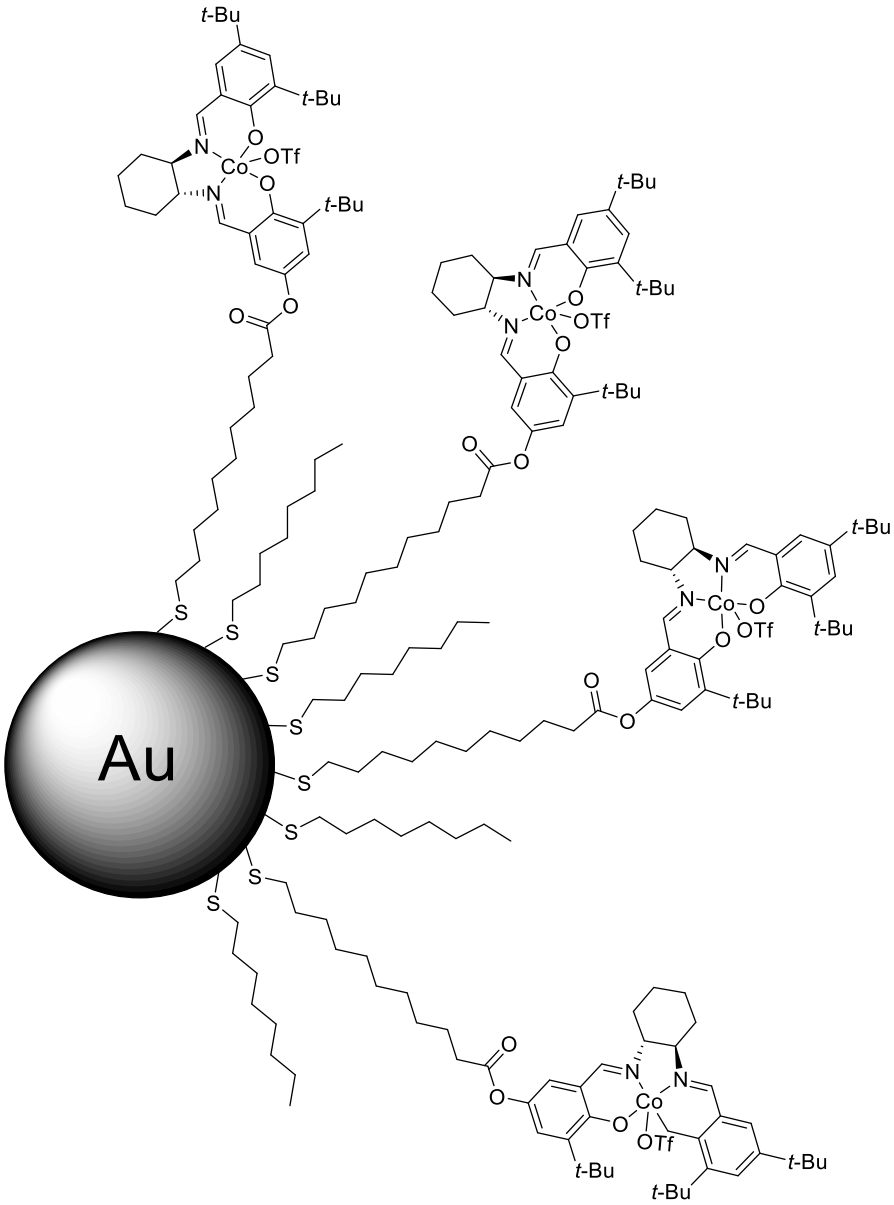

3.17

Figure 94. (salen)Co catalysts immobilised onto gold nanoparticles.[41]

Another immobilised catalytic system was presented by Zhu *et al*., who immobilised catalytic units SiO_2 particles. By using these supported, insoluble catalysts, the catalyst loading was able to be reduced up to 5 times relative to the monomeric one (**Figure 95**).[45]

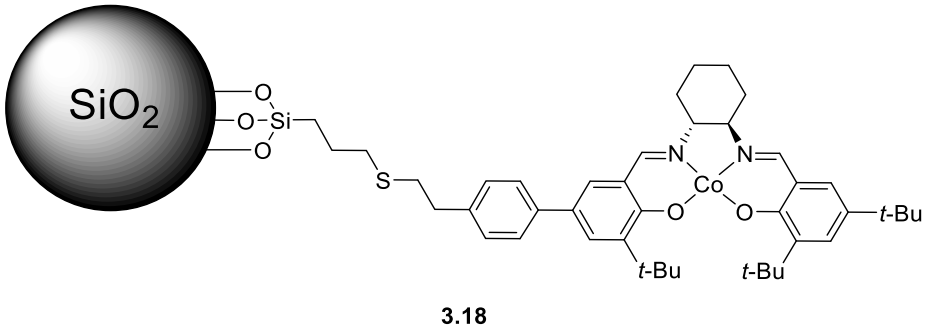

Figure 95. Silica supported (salen)Co catalyst.[45]

3.5.3. (salen)Cobalt catalysts brought together by hydrogen bonding

Hong and co-workers reported a conceptually different way of enhancing cooperativity.[54] This example holds great importance to this thesis as the enhancement in cooperativity is achieved by bringing the catalyst units close together by self-assembly – by utilising hydrogen bonding. In this study, catalyst **3.19** is functionalised with urea functional groups, enabling hydrogen bonding between these functional groups on separate catalyst units. This system showed an increase in the rate of up to 13 times relative to the monomeric catalyst, demonstrating that hydrogen-bonded self-assembly can be used to enhance cooperativity between catalytic units (**Figure 96**).

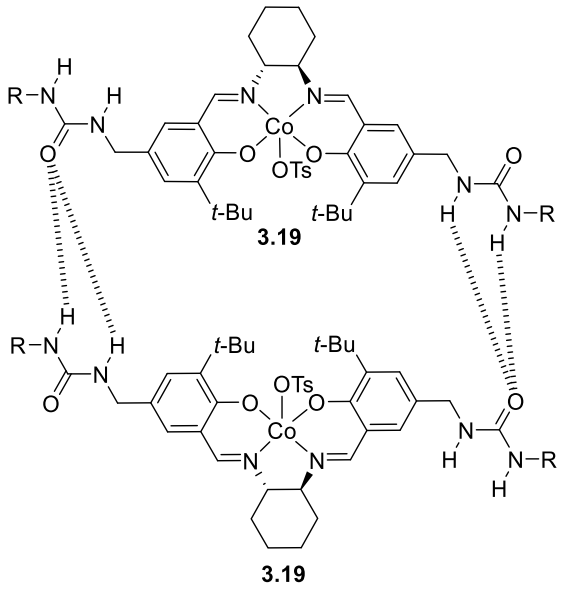

Figure 96. Self-assembly of (salen)Co catalysts by hydrogen bonding.[54]

3.6. Aims of the chapter

This chapter aims to demonstrate that the concepts explored in the previous chapter — the self-assembly of catalytic units to enhance cooperative catalysis — can be applied to a synthetically useful system. As seen in the introduction to this chapter, we have chosen to apply these concepts to the hydrolytic kinetic resolution of epoxides. The reasons for this choice are: 1. the reaction requires two catalytic units to stabilise the transition state of the rate-determining step; 2. the reaction is practically useful, with applications in both industrial and academic contexts; and 3. the reaction has been studied using a large number of systems exploring the cooperative properties of the catalyst used. Our objective was to design a (salen)Co catalyst with enhanced intramolecular interactions by introducing hydrophobic chains to make an amphiphilic molecule that would self-assemble (**Figure 97**).

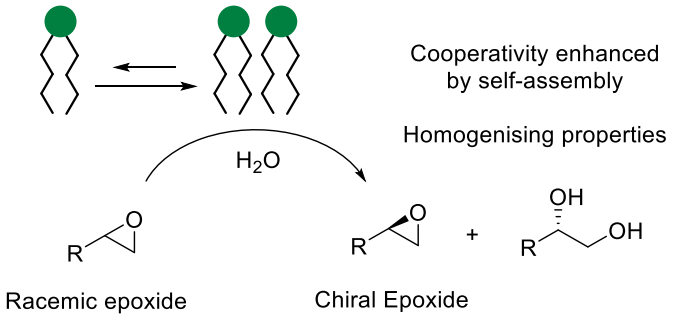

Figure 97. Desired properties of the system.

The HKR of epoxides is often performed in neat conditions, forming two phases in the majority of the cases from the hydrophobic epoxide and water that acts as a reagent. The system differs considerably from the systems studied in the previous chapter, which were homogenous aqueous systems known to be well suitable for the formation of aggregates (micelles, vesicles). Amphiphiles are also well known for homogenising water-in-oil[133] and oil-in-water mixtures[134] to form emulsions. One of our aims was to therefore study this effect on the rate of reaction to see if our proposed catalysts can enhance the homogenisation of the reaction mixture in neat conditions. This would presumably increase the surface area of the reaction mixture and accelerating the reaction.

Interestingly, an article from Jacobs *et al*. reported no significant benefits of adding external surfactants to increase the miscibility of water and the epoxides.[135] We had, however, reasons to expect different results since our designed system would contain both the catalyst and the

amphiphile in the same molecule. This would prevent an external surfactant from interfering with the ability for two to be situated next to each other to act cooperatively (further discussion below).

3.7. Results and Discussion

3.7.1. Catalyst design

The design of amphiphilic catalysts needed to consider the inclusion of long hydrocarbon chains to enhance the hydrophobicity without resulting in a loss of enantioselectivity. Since the classic Jacobsen's catalyst (**Figure 98**, left) already exhibited excellent enantioselectivity for a large number of epoxides, we decided to change as little of the structure as possible in order to not lose any chiral control. We rationalised that the best positions to make synthetic changes were at the sites circled in **Figure 98**, as they are relatively easy to functionalise and far away from the chiral centres.

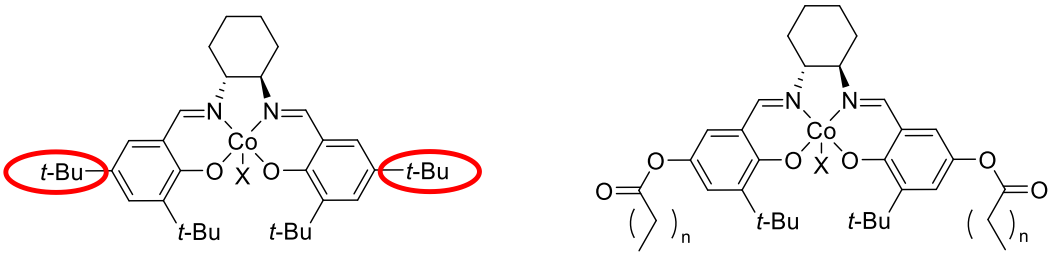

Figure 98. Positions where the chemical changes were planned to be made (left) and design of the amphiphilic catalyst (right).

It was decided to replace the two outward-pointing *tert*-butyl groups on the aromatic ring with long-chain esters, preferably at both positions simultaneously instead of just one. This would simplify the synthesis due to the preservation of a degree of symmetry. The proposed structure of the amphiphilic catalyst is shown in **Figure 98**.

Retrosynthetic analysis for the proposed catalyst is shown in **Figure 99**. After removing the cobalt ion from the complex, a disconnection is made at the two imine functional groups to give commercially available diamine **3.29** and an aromatic aldehyde. In the forward direction, this is formed by a straightforward condensation between amines and aldehydes to form imines. Next, an ester disconnection is made to give a phenol (**3.30**) and a long-chain fatty acid. There are two hydroxyl groups present in the molecule where the reaction could occur. However, it was thought that the proximity of the *tert*-butyl group to one of the hydroxyls could make the reaction selective enough to occur only at the less hindered hydroxyl group. Finally, aldehyde **3.30** can be synthesised from commercially available 2-*tert*-butylhydroquinone (**3.31**) and formaldehyde.

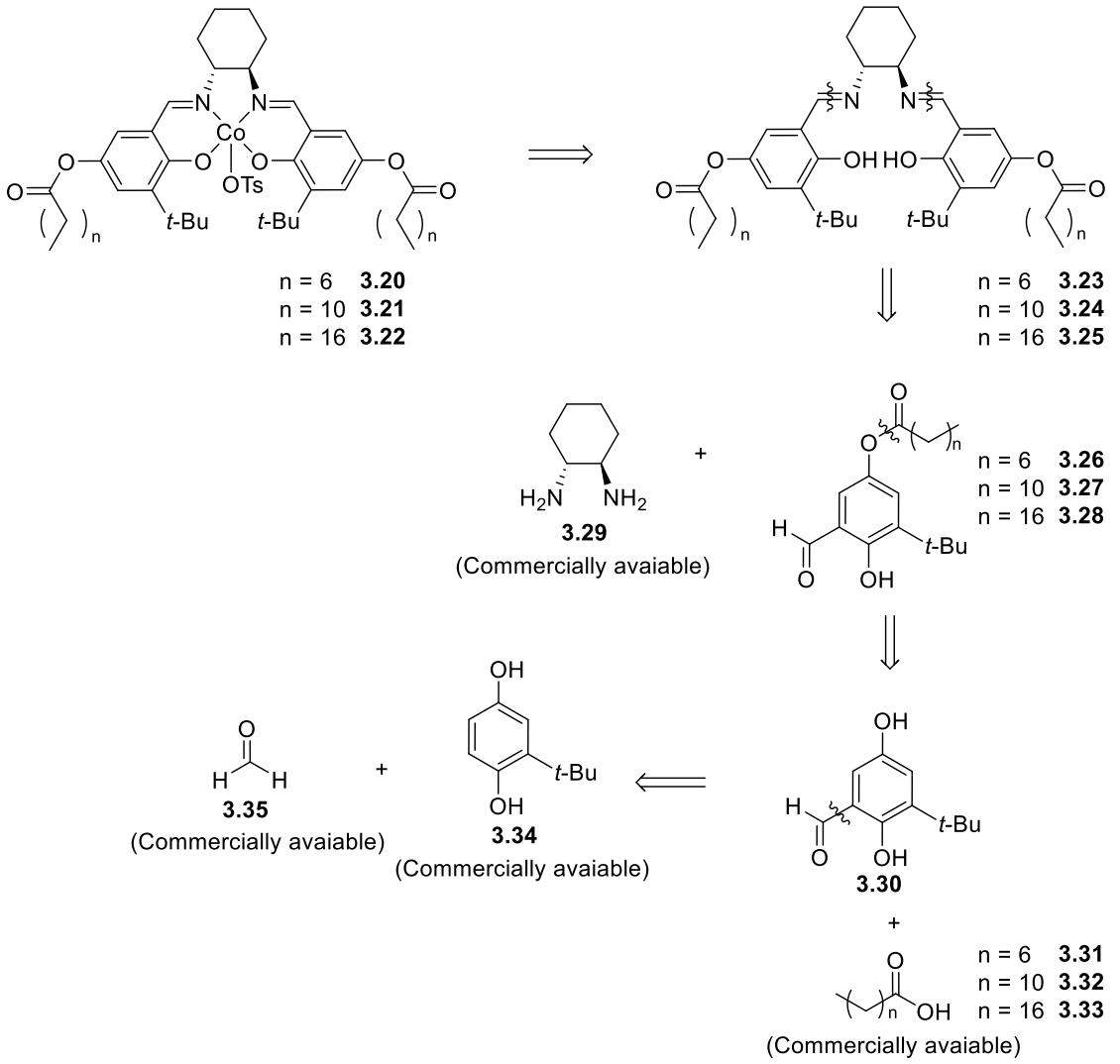

Figure 99. Retrosynthetic analysis of the amphiphilic (salen)Co catalyst.

3.7.2. Synthesis of the amphiphilic (salen)Co complex

The synthetic route for the amphiphilic catalyst can be seen in **Figure 100**. The first step is the addition of a protecting group selectively to the less hindered alcohol of 2-*tert*-butylhydroquinone (**3.34**). This step is essential to avoid polyacylation in the following synthetic step. A pivaloyl group was introduced onto the phenol by using pivaloyl chloride in the presence of the nucleophilic catalyst *N*,*N*-dimethylpyridin-4-amine (DMAP, **3.39**).

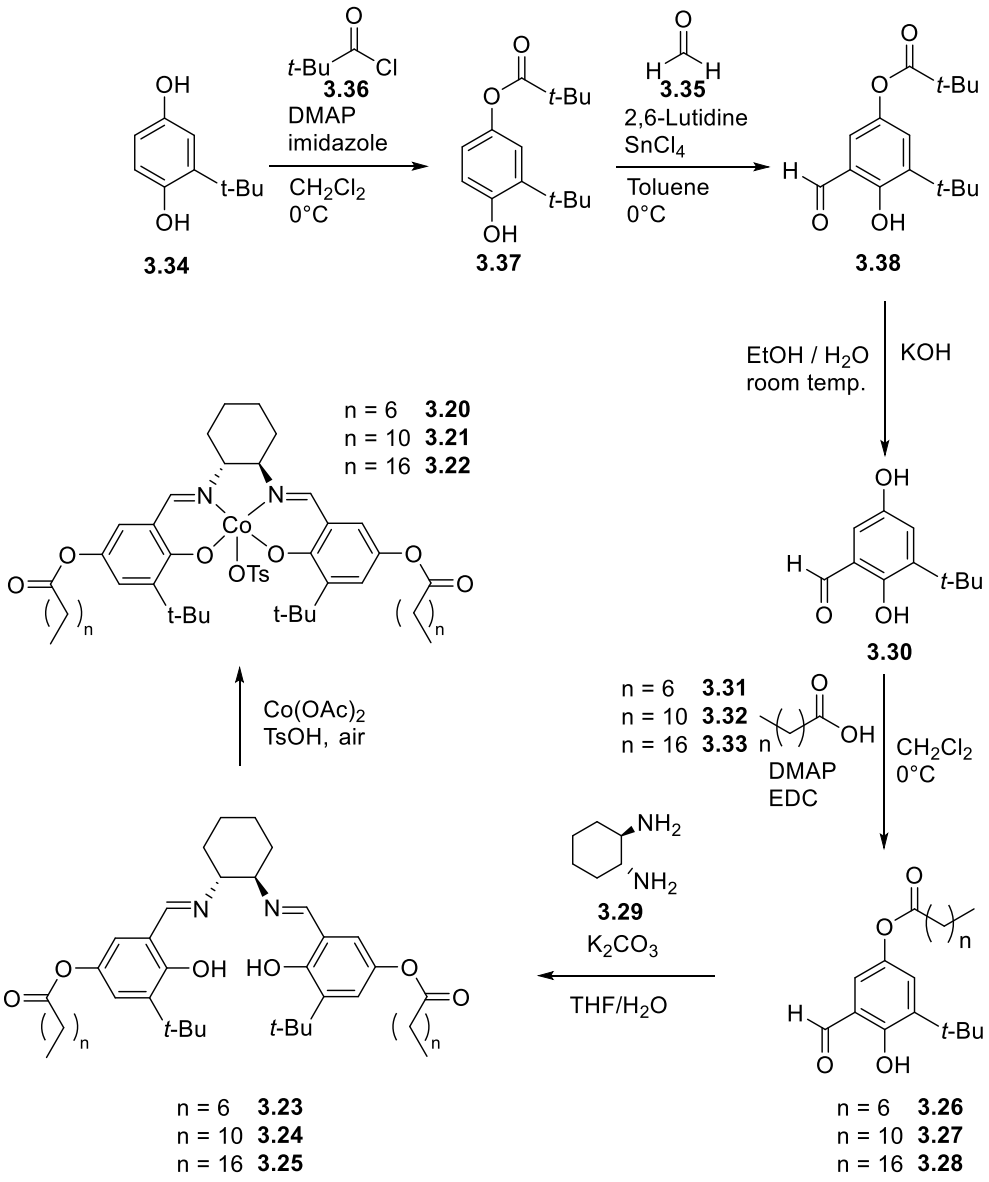

Figure 100. The synthetic route to amphiphilic (salen)Co(III) catalysts.

The mechanism of the ester formation begins with the pyridine nitrogen of DMAP **3.39** attacking the carbonyl of pivaloyl chloride **3.36**, releasing chloride, and forming an intermediate with a better leaving group and a more reactive carbonyl group (**Figure 101**). The less hindered hydroxyl group of 2-*tert*-butylhydroquinone **3.20** is deprotonated by imidazole **3.40**, and the nucleophilic phenoxide attacks the reactive intermediate, releasing DMAP and the desired ester **3.38**. The reaction was conducted in dichloromethane at 0 °C and under a N_2 atmosphere. The product was obtained in a quantitative yield and was pure enough to be used directly in the following step without further purification.

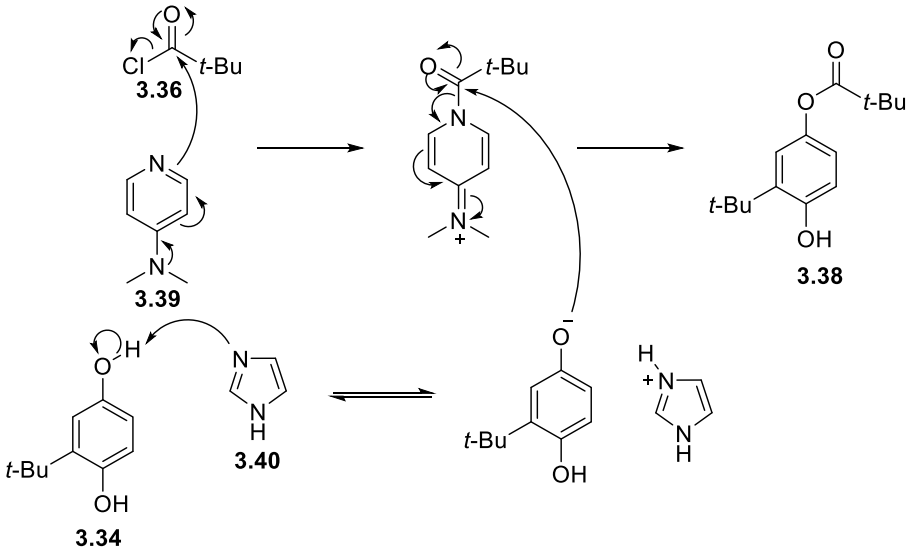

Figure 101. Esterification mechanism of 2-*tert*-butylhydroquinone.

The second synthetic step was the Friedel-Crafts acylation of 3-(*tert*-butyl)-4-hydroxyphenyl pivalate (**3.36**). $SnCl_4$ was used as a Lewis acid that helps generate an acylium ion from paraformaldehyde (**Figure 102**). The reaction occurs selectively due to the steric hindrance from the *tert*-butyl groups present in the starting material. In the mechanism, $SnCl_4$ reacts with paraformaldehyde (**3.35**) to form a more electrophilic acylium ion which is attacked by the nucleophilic aromatic ring of 3-(*tert*-butyl)-4-hydroxyphenyl pivalate (**3.36**). A final deprotonating step and a work-up gave the product **3.38** in 57% yield.

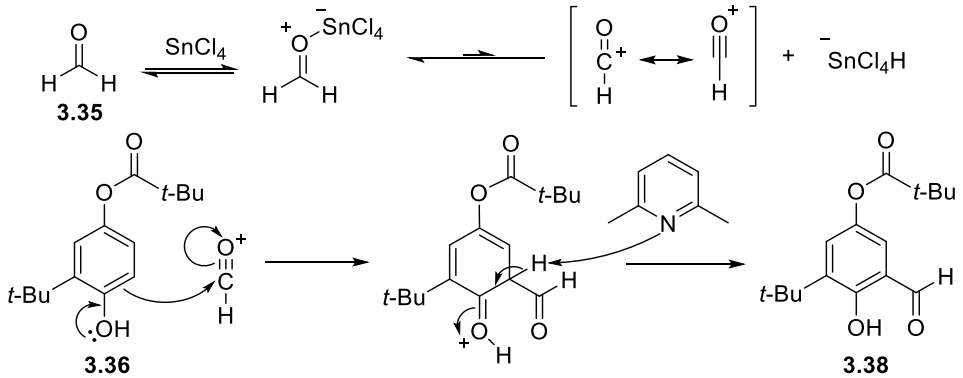

Figure 102. Acylation 3-(*tert*-butyl)-4-hydroxyphenyl pivalate.

A deprotection reaction was required next to reveal the alcohol for the following esterification reaction (**Figure 103**). To achieve this, the starting material was treated with a Brønsted base

(KOH). A hydroxyl attacks the carbonyl of the ester **3.38**, which releases the phenolate of the desired product **3.30** and pivalic acid (**3.41**). Following a work-up with a Brønsted acid, the deprotected product **3.30** is obtained in 49% yield.

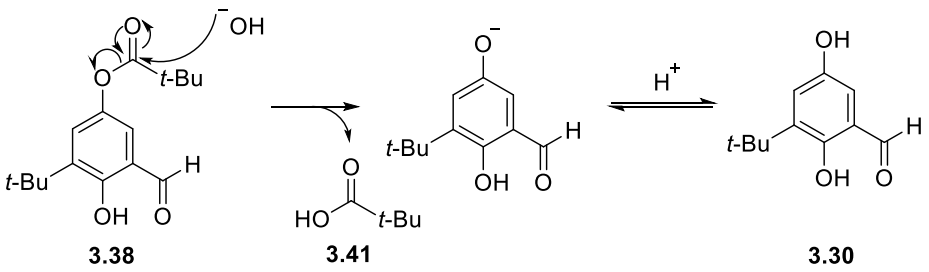

Figure 103. Deprotection of 3-(*tert*-butyl)-5-formyl-4-hydroxyphenyl pivalate.

Next, a Steglich esterification was used to introduce the hydrophobic chains. This reaction occurs selectively at the less hindered alcohol of the starting material **3.30** and DMAP (**3.39**) is used as a catalyst and *N*-(3-dmethylaminopropyl)-*N*′-ethylcarbodiimide (EDC, **3.42**) as a coupling agent (**Figure 104**). In the mechanism, DMAP (**3.39**) first deprotonates the carboxylic acid **3.31**, **3.32**, or **3.33**, and the carboxylate attacks the carbodiimide carbon of EDC (**3.42**). Protonation by the conjugated acid of DMAP followed by a second protonation gives an intermediate, which effectively turns OH group on the carboxylic acid into an excellent leaving group. DMAP now attacks the carbonyl group forming a reactive intermediate, and the phenol reacts with this intermediate to form the desired ester products **3.26**, **3.27**, **3.28**. This reaction forms a urea derivative as a side product. After purification with flash column chromatography, the esterification product was obtained in 82% yield when using octanoic acid, 52% when using dodecanoic acid and 88% when using stearic acid.

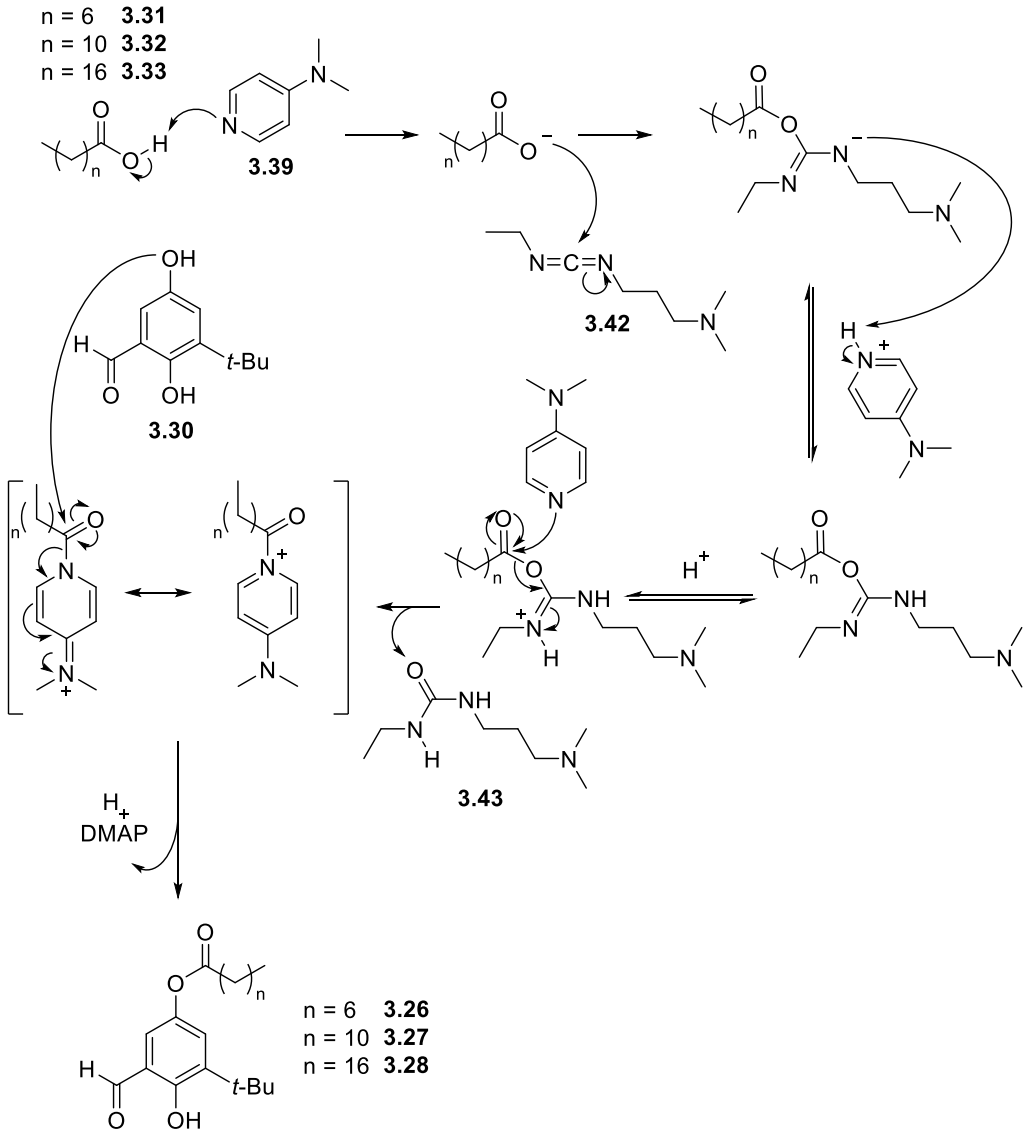

Figure 104. Mechanism of the Steglich esterification.

The following synthetic step consists of two condensation reactions between the optically active diaminocyclohexane (**3.29**) and two aldehydes (**3.26, 3.27** or **3.28**) to give the final ligands **3.23-3.25** (**Figure 105**). The reaction was conducted in a mixture of THF and water in the presence of K_2CO_3. The oily residue from the reaction was purified by flash chromatography on silica gel to obtain the condensation products, in 50% for ligand **3.23**, 36% for ligand **3.24** and 33% for ligand **3.25**.

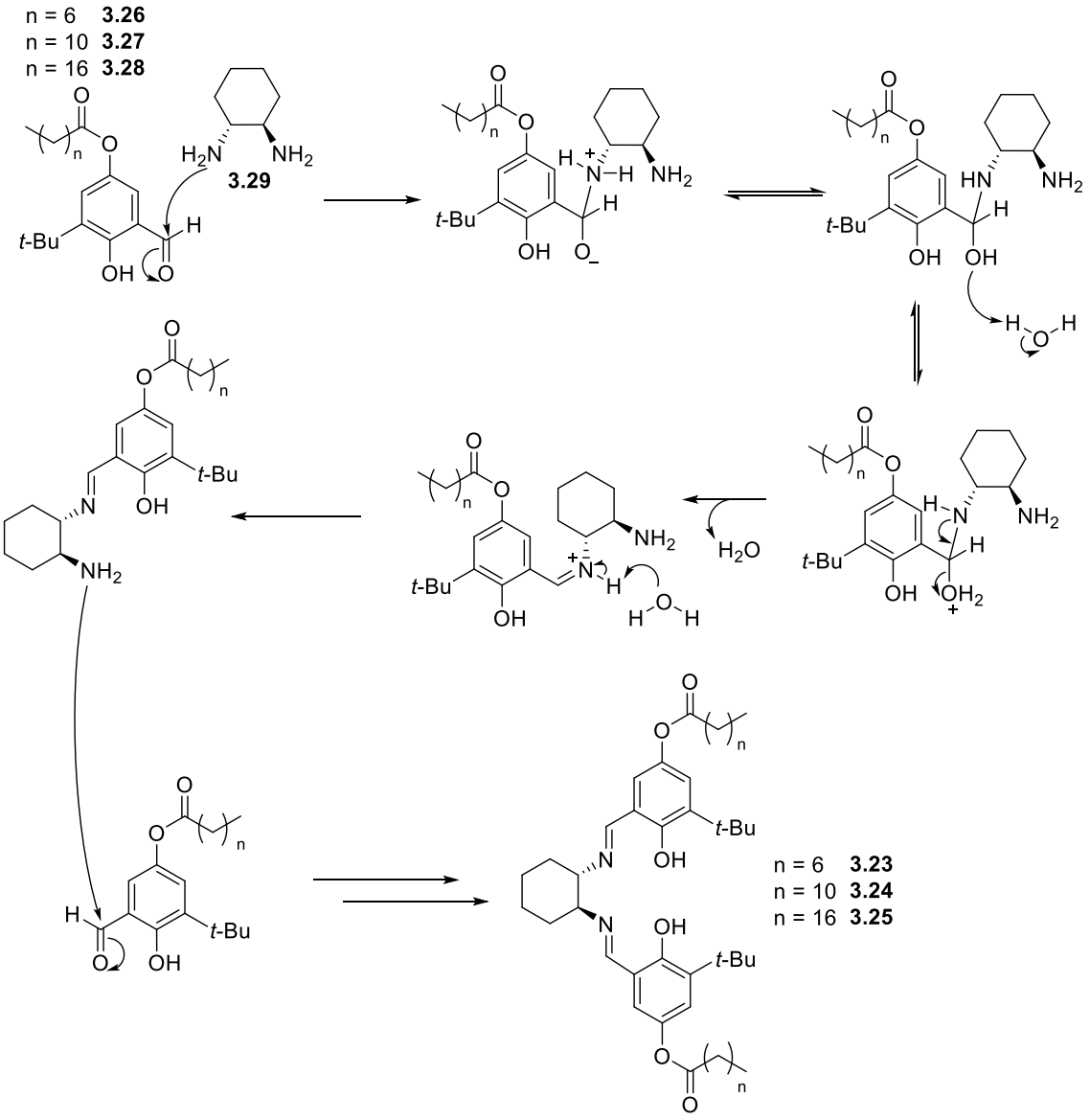

Figure 105. Mechanism of the condensation reaction.

The last two steps are the introduction of the cobalt to the ligand and its oxidation to obtain the (salen)Co(III) species. The introduction of the cobalt(II) was performed by mixing a solution of the ligand with a solution of cobalt(II) acetate in strictly O_2-free conditions. Any oxygen present during the reaction causes it to oxidise rapidly to cobalt(III). Even though the cobalt(III) complex is the eventually desired one, if oxidation occurs at this step, the counterion of the complex is not controlled, and that is of high importance for the reaction rate of the hydrolytic kinetic resolution, as we saw above.

The last step of the synthesis consisted of oxidising the cobalt(II) complex to obtain the catalytically active cobalt(III) complex. To achieve this, the cobalt(II) complex is dissolved in a mixture of methanol, toluene, and dichloromethane, and *para*-toluenesulfonic acid monohydrate

is immediately added, and the reaction is stirred open air for 3 hours. After solvent removal and a work-up, the active versions of the catalysts were obtained in 62% yield for complex **3.20**, 68% yield for complex **3.21**, 64% yield for complex **3.22** and 59% for complex **3.11**. To ensure a reliable comparison between the control Co(III) complex **3.11** and the functionalised, amphiphilic Co(III) complex **3.22**, both compounds were generated in parallel. The reaction scheme for these last steps is shown in **Figure 106**. Remarkably, the entire synthetic route requires just one purification with flash chromatography.

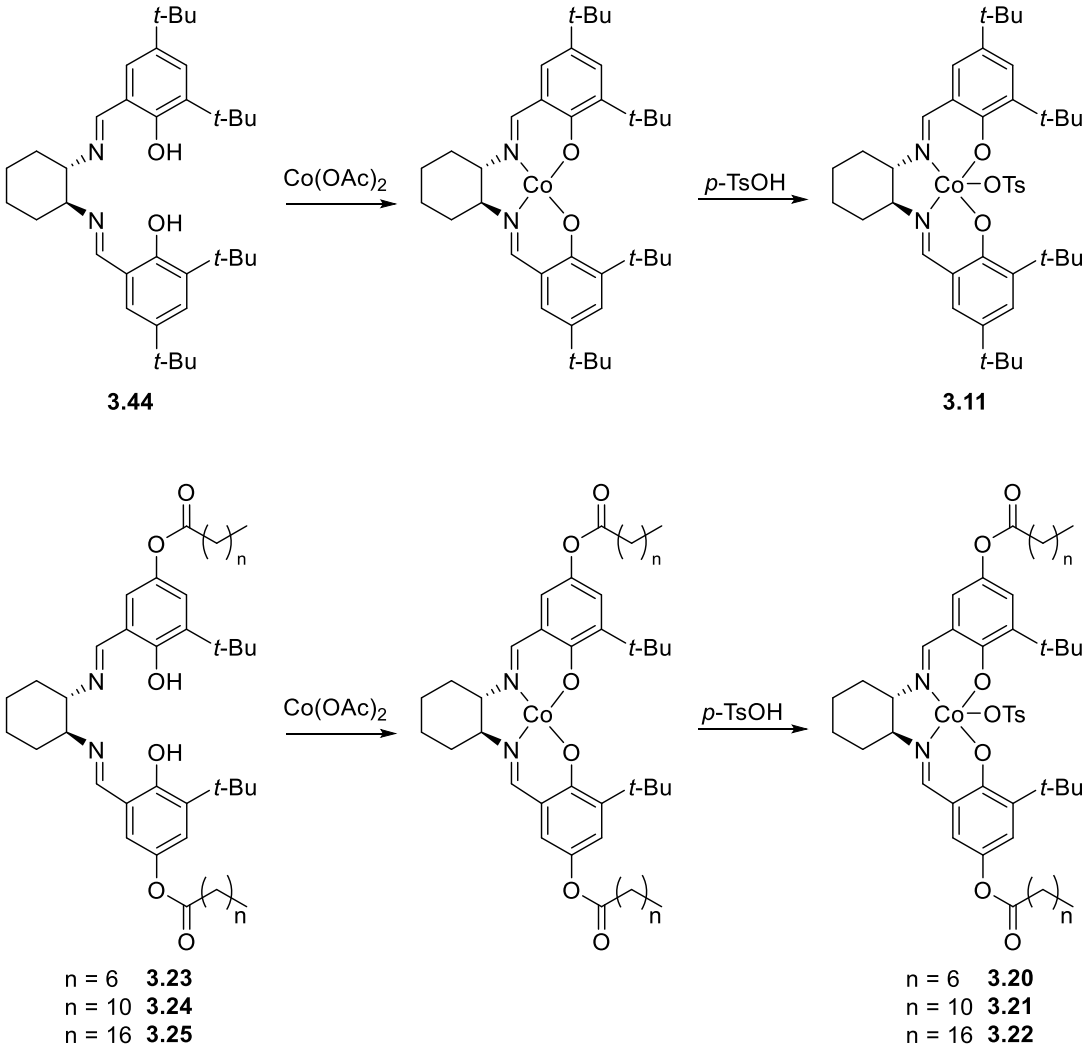

Figure 106. Formation of the final (salen)Co(III) complexes.

3.7.3. Preliminary catalytic experiments

We next examined our synthesised catalysts in the hydrolytic kinetic resolution of terminal epoxides. We chose epichlorohydrin as our test substrate as this had been used in several previous literature studies, including the example by Hong *et al.*, where they compared the effect of

hydrogen bonding-induced self-assembly on catalytic activity.[54] This would allow us to directly compare our results and the effect of the hydrophobic interactions on enhancing cooperativity. Epichlorohydrin (**3.45**) is an attractive building block since it has potential functionalities in all three carbons, with complementary reactivity approachable at any of the three sites with different conditions.[123]

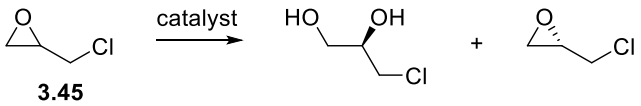

Figure 107. HKR model system with epichlorohydrin.

Since neat conditions are commonly used for the HKR of epoxides, which is considered a green process that does not require the addition of extra solvents, we began by examining the HKR of epichlorohydrin in the absence of solvent (**Figure 107**). To do so, a volume of a solution of the catalyst in chloroform was introduced into a vial and the chloroform was next evaporated to give a specific quantity of catalyst. Next, milli-Q water was added (0.6 eq.), followed by racemic epichlorohydrin (1.0 eq., 1 volume). The reaction mixtures were stirred at 400 rpm, and aliquots of the reaction mixture were taken at specific time intervals to monitor the reaction progress. The aliquots were filtered through a plug of silica and eluted with Et_2O to remove the catalyst and the diol side product, and the filtrate was analysed by chiral gas chromatography. The initial rates of the reaction was determined from plots of -ln([epoxide]/[epoxide]$_0$) versus time, with the conversion estimated from the enantioselectivity. We determined the rate for different analogues of the catalyst: catalyst **3.20** is the functionalised (salen)Co(III) complex with two hydrocarbon chains that contain 8 carbons each, catalyst **3.21** is functionalised with 12 carbons in each chain, catalyst **3.22** with 18 carbons in each chain and finally, catalyst **3.11** is the classic, unfunctionalised version of the catalyst. To determine the rates, we utilised 0.1 moles % of catalyst, 50 µL of epichlorohydrin and 6.9 µL of water (1.2 equivalents). **Figure 108** shows the enantiomeric excess over time at those conditions for the different catalysts utilised. We were pleased to obtain an initial rate more than 10 times faster utilising catalyst **3.22** compared to the control catalyst **3.11**, achieving >99% *e.e.* in 70 minutes with catalyst **3.22**, whereas when utilising the control catalyst **3.11**, the *e.e.* observed at the same time was 37%.

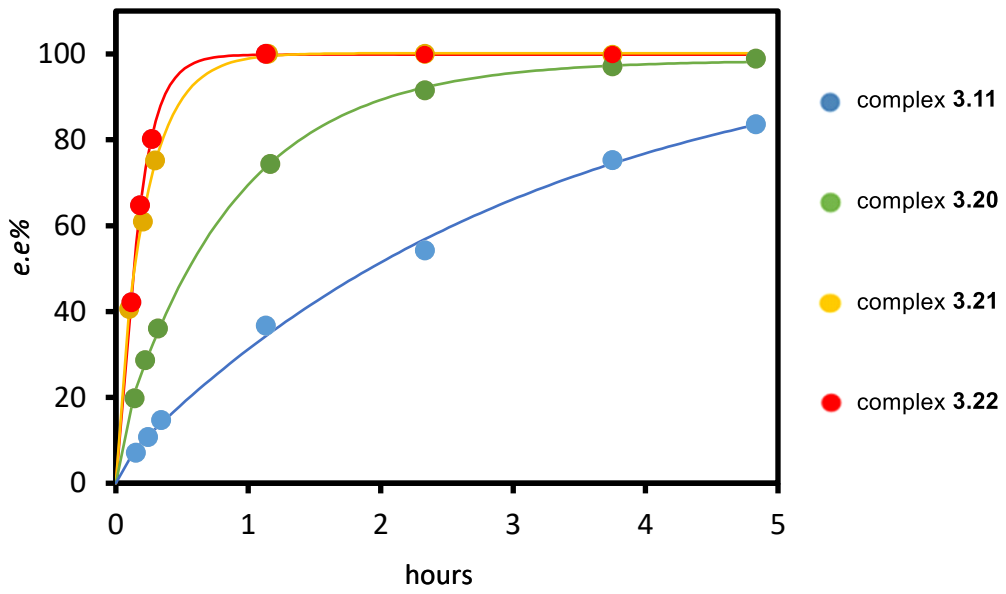

Figure 108. Hydrolytic kinetic resolution of epichlorohydrin utilising complexes **3.11**, **3.20**, **3.21** and **3.22** under solvent free conditions. [Catalyst] = 0.1 mol%, epichlorohydrin 1 equiv., H_2O 0.6 equiv.

Analysis of the initial rates revealed an almost ten-fold increase in rate between complex **3.11** (0.88 h^{-1}) and complex **3.22** (8.18 h^{-1}). The k_{obs} values were determined from plots of -ln([epoxide]/[epoxide]$_0$) (obtained by chiral GC) versus time (see **Appendix**). When plotting the *e.e* of the reaction versus time for catalysts **3.20** and **3.21**, a correlation can be seen between the length of the functionalised catalyst and the rate of the reaction (**Figure 109**), even though the correlation is not linear (2.52 h^{-1} for complex **3.20** and 6.85 h^{-1} for complex **3.21**). The control catalyst **3.11** is considered as having 4 carbon long chains due to its *t*-Bu group.

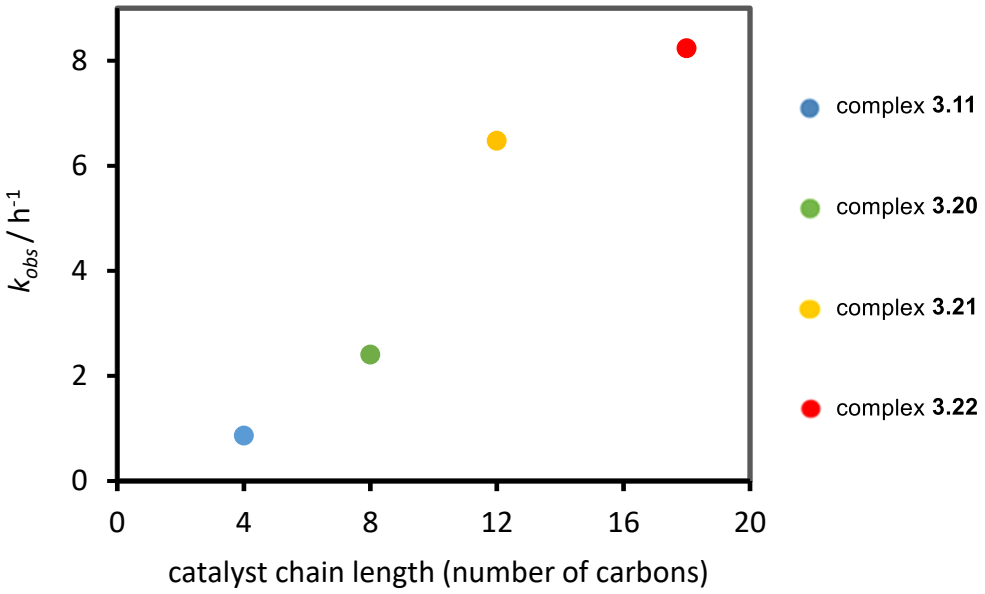

Figure 109. Initial rate of the reaction utilising different analogues of the catalysts, [Catalyst] = 0.1 mol%, epichlorohydrin 1 equiv., H_2O 0.6 equiv., the graph assumes catalyst **3.11** as containing 4 carbon long chains taking in consideration the *tert*-butyl group.

3.7.4. Kinetics of the homogeneous system

Epichlorohydrin and water are non-miscible, making the system heterogeneous and hard to study from a kinetic point of view. We decided to study the kinetics of the system of the equivalent homogeneous system by adding THF to the system. The addition of THF makes the whole system monophasic, and these conditions are commonly used for the HKR of various epoxides.[125] Jacobsen *et al*. commonly added THF and other water-soluble solvents such as CH_3CN, or the diol product, to ensure homogeneous systems when conducting kinetic experiments.[30,54,127,128,136]

Kinetic experiments showed that the rate increase was second-order with respect to the catalyst concentration for both the control catalyst **3.11** and the functionalised catalyst **3.22** (**Figure 110**, **Figure 111**). This can be shown by plotting the k_{obs} of the reaction against the mol % of catalyst, fitting the data into a power equation and checking the exponential that is obtained (**Figure 110**). An exponential close to 2 was obtained for both complexes **3.11** and **3.22**. The same can also be confirmed with the linearity of the data when plotting the initial rate of the reaction vs mol %^{2}, obtaining an R^2 of 0.997 for **3.11** and 0.999 for **3.22**. The slope of the graph obtained for catalyst **3.22** is 265.48 and 51.33 for catalyst **3.11**, indicating that catalyst **3.22** is around 4 times more effective than catalyst **3.11**.

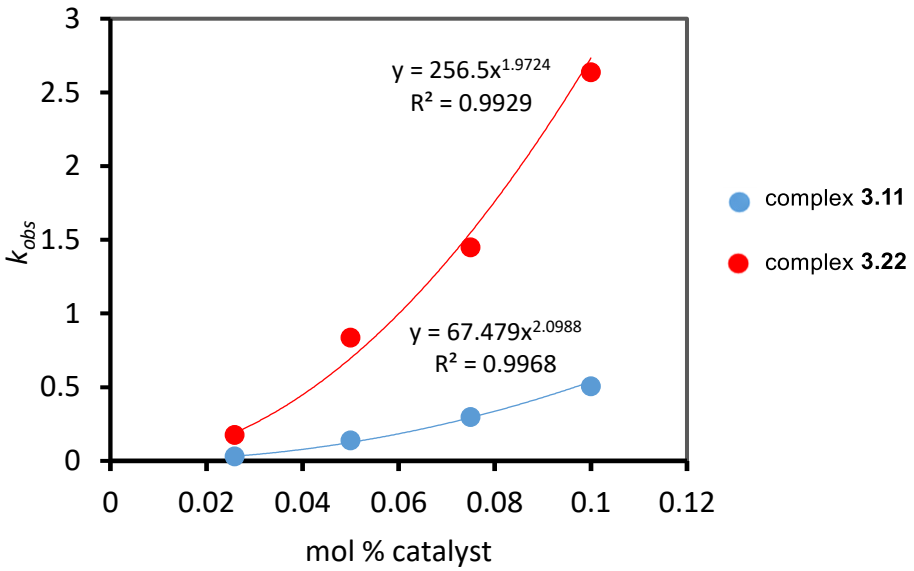

Figure 110. Catalyst concentration (mol %) vs initial rate for HKR of epichlorohydrin, catalyst loading = variable, epichlorohydrin = 1 equiv. 1 volume, THF = 1 volume, H_2O = 0.6 equiv., rt. Blue dots: catalyst **3.11**. Red dots: catalyst **3.22**

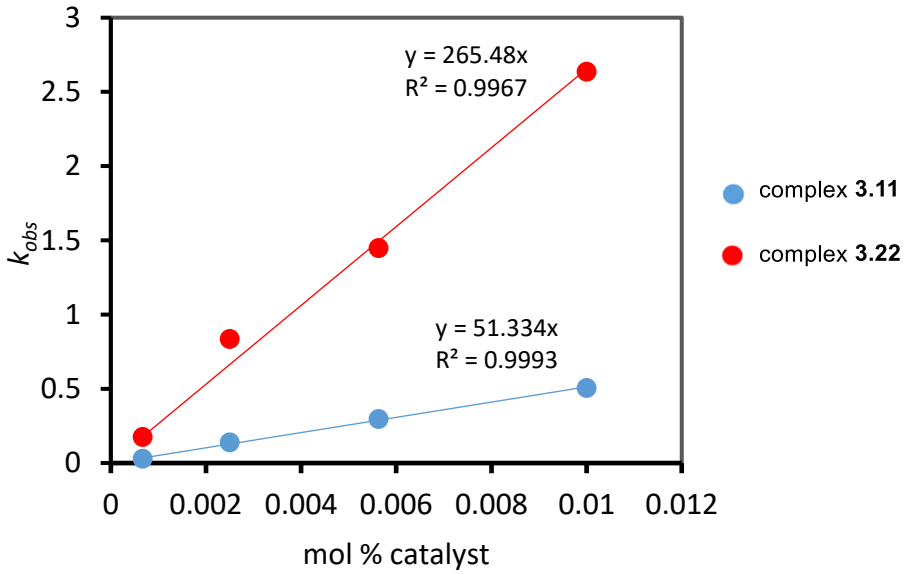

Figure 111. Catalyst concentration squared (mol %^{2}) vs initial rate for HKR of epichlorohydrin, catalyst loading = variable, epichlorohydrin = 1 equiv. 1 volume, THF = 1 volume, H_2O = 0.6 equiv., rt. Blue dots: catalyst **3.11**. Red dots: catalyst **3.22**.

It was hypothesized that the rate increase could originate from a change in the dimerisation constant between two ligands which would promote cooperativity. This would be similar to the example from Hong *et al*. where the assembled state is stabilised by hydrogen bonding

interactions resulting in a shift in the equilibrium between the monomeric forms of the catalyst and the reactive dimers.[54] In such a reaction, the equilibrium between the self-assembled dimer and the catalyst monomers can be represented by **Equation 10**.

The rate of the reaction can be expressed as **Equation 11**, making the assumption that two catalytic units are needed for this reaction. We will consider that the catalytic pairs (or dimers) are the catalytic active species for both the control catalyst and the functionalised ones. Next, we can substitute the [Co(III)dimer] term for K_2[Co(III)monomer]^2 to obtain **Equation 12**. The total amount of catalyst can be expressed as the sum of the dimerised catalyst and the monomeric catalyst as shown in **Equation 13**.

$$K_2 = [\text{Co(III)dimer}]/[\text{Co(III)monomer}]^2 \qquad \textbf{Equation 10}$$

$$\text{rate} = k[\text{Co(III)dimer}] \qquad \textbf{Equation 11}$$

$$\text{rate} = kK_2[\text{Co(III)monomer}]^2 \qquad \textbf{Equation 12}$$

$$[\text{Co(III)total}] = 2[\text{Co(III)dimer}] + [\text{Co(III)monomer}] \qquad \textbf{Equation 13}$$

If [Co(III)dimer] << [Co(III)total]

$$\text{Rate} = kK_2([\text{Co(III)total}]-2[\text{Co(III)dimer}])^2 \approx kK_2[\text{Co(III)total}]^2 \qquad \textbf{Equation 14}$$

If [Co(III)monomer] << [Co(III)dimer], then the rate of the reaction would have first-order dependence on catalyst concentration, as shown in the systems presented in **Chapter 2** of this thesis (see **Equation 7**). We can conclude that this is not the case for the catalyst presented in this chapter since we observe a rate with a second-order dependence with respect to the catalyst. This means that we can assume that [Co(III)monomer] is much larger than [Co(III)dimer], and so the overall rate can be approximated by the last part of **Equation 14**. According to this equation, the reaction rate can be affected by K_2, which is the equilibrium constant between the dimeric and monomeric forms of the catalyst. With our newly synthesised catalyst, we believed that the increased hydrophobic interactions would present a larger K_2 than the control catalyst, resulting in the higher k_{obs} observed in our system.

To support the hypothesis that the origin of the rate increase was due to stabilisation of an assembled state of the catalysts, and to exclude electronic effects, we determined the k_{obs} also of complexes **3.20** and **3.21**, with each catalyst containing side chains of different lengths (**Figure 112**). We observed a linear correlation between the length of the attached hydrocarbon chains and the k_{obs}, which supported the hypothesis that a greater degree of hydrophobic interactions was giving rise to the larger dimerisation constants and resulting in faster reaction rates.

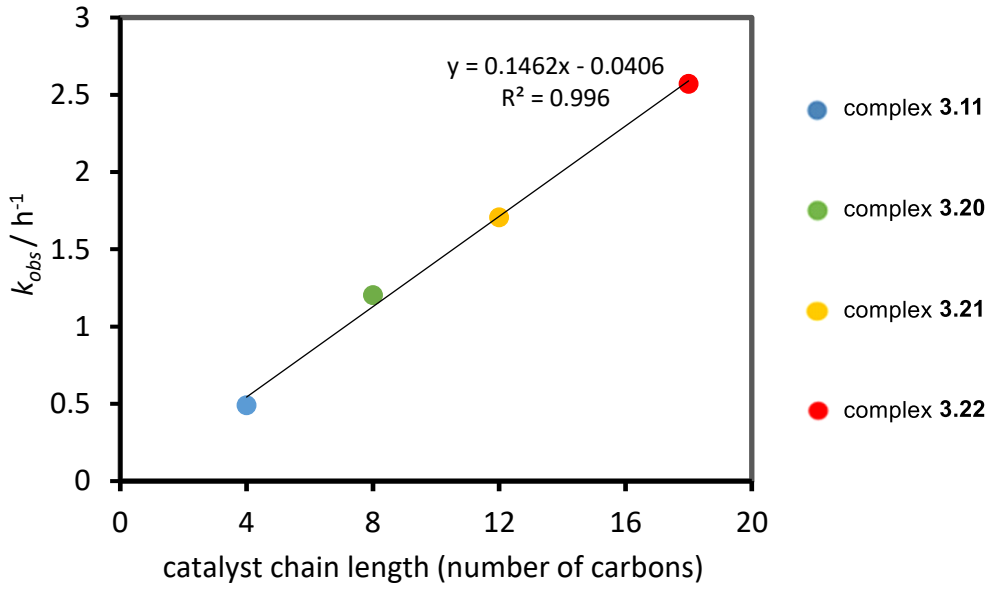

Figure 112. Initial rate of the reaction utilising catalyst analogues **3.11**, **3.20**, **3.21**, and **3.22**. catalyst loading = 0.1 mol %, epichlorohydrin = 1 equiv. 1 volume, THF = 1 volume, H_2O = 0.6 equiv., rt., the graph approximates the *tert*-butyl group of catalyst **3.11** as a 4-carbon chain.

Our self-assembled system has a crucial advantage over systems where the two (salen)Co ligands are linked together to induce cooperativity. Looking back at the calixarene-bound system described by Wezenberg and Kleij, they noted how the rate in covalently tethered systems could be described by the sum of first-order and second-order contributions as expressed in **Equation 15**.[30]

$$\text{rate} = k_{intra}[\text{Co(III)}] + k_{inter}[\text{Co(III)}]^2 \qquad \textbf{Equation 15}$$

The intramolecular component is due to catalysis by (salen)Co sites on the same molecule (bimetallic complexes), whereas the intermolecular component is due to the reaction catalysed the interaction between one bimetallic complex and another. At low concentrations, the k_{intra} term is larger due to preorganisation, which promotes cooperativity, and this term increases linearly at higher concentrations. However, the k_{inter} term increases at higher concentrations at second order. Also note that for these covalently-linked systems, the effective catalyst concentration in the k_{inter} is effectively halved due to their attachment onto the molecular scaffold. Therefore, when comparing this covalently-linked catalyst to Jacobsen's original catalyst, at higher concentrations, the k_{intra} value obtained from linking the catalytic sites is not able to overcome the loss of k_{inter} component. This means that above a certain concentration of catalyst, the benefit of complexing the complex onto a molecular scaffold is no longer seen. Such a problem would not be expected in our dynamic/self-assembled system, as our systems do not involve pre-formed dimers and the

association of monomers to form reactive dimers will only increase at higher concentrations, meaning higher activity.

3.7.5. Estimation of dimerisation constants

It is known that the assembly of specific molecules, such as nucleic bases, results in shifts in the NMR spectra.[137,138] This effect was also observed by Hong and co-workers when they studied the self-assembly of their hydrogen-bonded catalysts with a nickel version of their (salen)Co complexes.[54] In an attempt to estimate the equilibrium constants for dimerisation, we synthesised nickel variants of our functionalised catalyst **3.22** and for Jacobsen's original catalyst **3.11** (**Figure 113**). Cobalt complexes were not used as the cobalt(III) version of the catalysts resulted in broad peaks that were difficult to interpret, and the cobalt(II) compounds are paramagnetic.

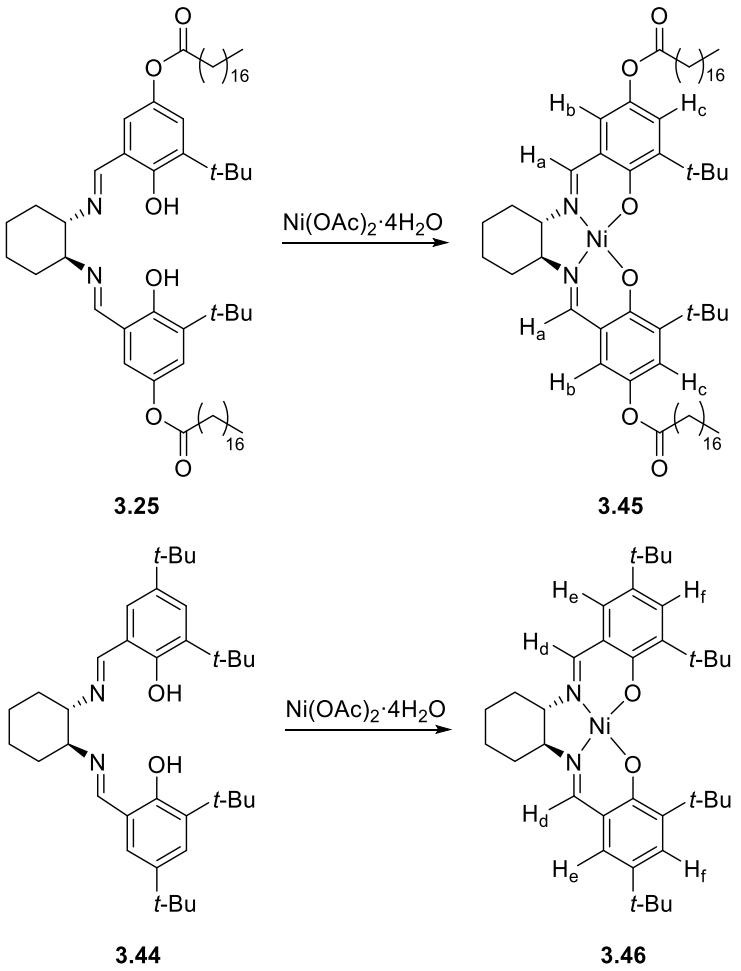

Figure 113. Synthesis of the (salen)Ni complexes **3.45** and **3.46** for NMR spectroscopy.

The ^{1}H NMR chemical shifts for protons H_a, H_b, H_c, of compound **3.45** and H_d, H_e, H_f for compound **3.46** were monitored at a range of concentrations in a mixture of THF-d_8 and D_2O (95.5: 4.5) to simulate reaction conditions. For both complexes **3.45** and **3.46**, the chemicals shifts of these aromatic protons were observed to shift when higher concentrations of the complex were achieved. These shifts were more significant for complex **3.45** than for complex **3.46**. The differences in chemical shifts could be observed when stacking the ^{1}H NMR data for all the concentrations (**Figure 114**).

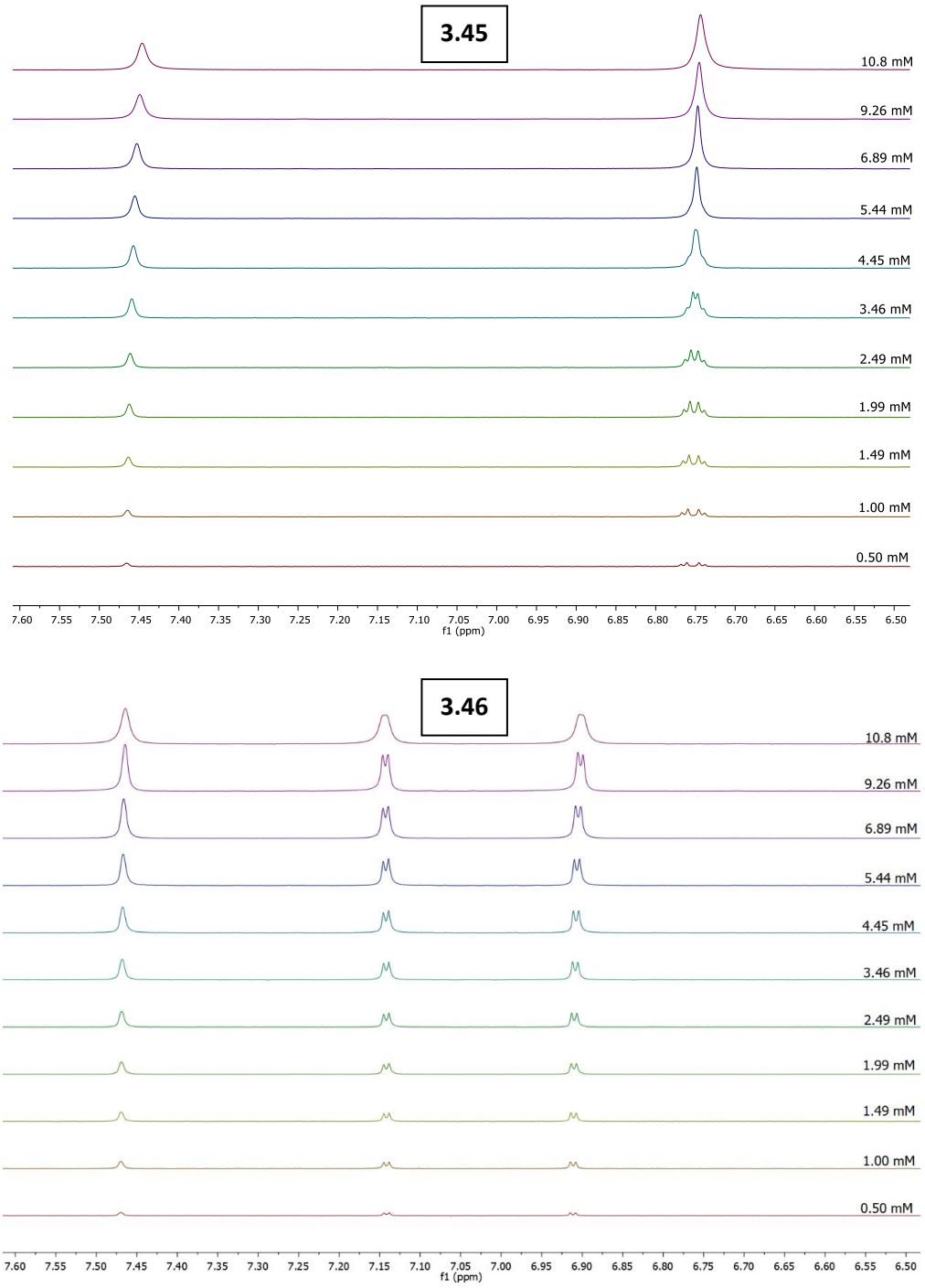

Figure 114. ^{1}H NMR spectra of varying concentrations of compound **3.45** (above) and compound **3.46** (below) in a mixture of THF-d_8 and D_2O (95.5: 4.5).

The ^{1}H NMR chemical shifts of protons H_a, H_b and H_c from complex **3.45**, and for protons H_d, H_e and H_f from complex **3.46** are presented in **Tables 2** and **3.**

[Complex **3.45**] mM	H_a ppm	H_b ppm	H_c ppm
0.50	7.4656	6.7645	6.7418
1.00	7.4646	6.7632	6.7421
1.49	7.4635	6.7618	6.7424
1.99	7.4623	6.7606	6.7426
2.49	7.4612	6.7593	6.7428
3.46	7.4592	6.7531	6.7459
4.45	7.4573	6.7510	6.7471
5.44	7.4554	6.7484	6.7484
6.89	7.4529	6.7471	6.7471
9.26	7.4492	6.7454	6.7454
10.8	7.4460	6.7434	6.7434

Table 2. Chemical shifts of protons H_a, H_b and H_c of complex **3.45** in a mixture of THF-d_8 and D_2O (95.5: 4.5).

[Complex **3.46**] mM	H_d ppm	H_e ppm	H_f ppm
0.50	7.4697	7.1415	6.9115
1.00	7.4696	7.1417	6.9111
1.49	7.4692	7.1417	6.9106
1.99	7.4689	7.1419	6.9102
2.49	7.4685	7.1419	6.9098
3.46	7.4679	7.1420	6.9086
4.45	7.4674	7.1422	6.9076
5.44	7.4667	7.1425	6.9065
6.89	7.4665	7.1428	6.9051
9.26	7.4646	7.1430	6.9021
10.8	7.4642	7.1436	6.9007

Table 3. Chemical shifts of protons H_a, H_b and H_c of complex **3.46** in a mixture of THF-d_8 and D_2O (95.5: 4.5).

This data was then fitted into two different models, the monomer-dimer model (MD) (**Equation 16**) and the isodesmic model (EK) (**Equation 17**) using a non-linear least-squares method.[139] The monomer-dimer model assumes that just dimers are formed from the monomers; in other words, it considers that no larger aggregates are formed. The isodesmic model considers all the equilibrium constants for self-association as equal, and it does not assume that only dimers are formed, but also trimers, tetramers, pentamers, etc. Origin Pro was the software used to perform the non-linear fitting.

Monomer-dimer (MD) model:

$$\delta = \delta_2+((1-(8K_2[(salen)Ni]+1)^{1/2})/(4K_2[(salen)Ni]))/(\delta_2- \delta_1) \qquad \textbf{Equation 16}$$

Isodesmic (EK) model:

$$\delta = \delta_{aso}+((1-(4K_{asso}[(salen)Ni]+1)^{1/2})/(2K_{asso}[(salen)Ni]))/(\delta_{asso}-\delta_{mono}) \quad \textbf{Equation 17}$$

For protons H_b and H_c of compound **3.45,** the 3 more concentrated points were ignored for fitting into the models as the chemical shifts merge into one, and they become indiscernible (see **Figure 114,** 6.89 mM, 9.26 mM, 10.8 mM). The equilibrium constants estimated from the fitting into the two models are shown in **Table 4** and **Table 5** for compounds **3.45** and **3.46**, respectively. The fitting plots can be found in the **Appendix** section of this thesis.

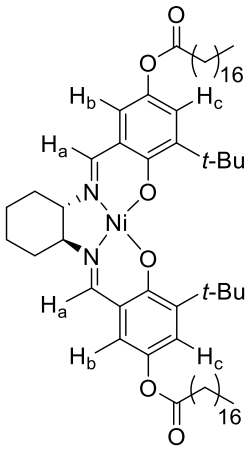

3.45

Proton	MD model	EK model
H_a	K_2 = 0.70 (R^2 = 0.99)	K_{asso} = 1.63 (R^2 = 0.99)
H_b	K_2 = 2.20 (R^2 = 0.97)	K_{asso} = 5.35 (R^2 = 0.97)
H_c	K_2 = 1.40 (R^2 = 0.91)	K_{asso} = 1.49 (R^2 = 0.91)
Avg ± Std dev	K_2 = 1.43 ± 0.75	K_{asso} = 2.82 ± 2.19

Table 4. Calculated dimerisation/association constants for compound **3.45** in a mixture of THF-d_8 and D_2O (95.5: 4.5).

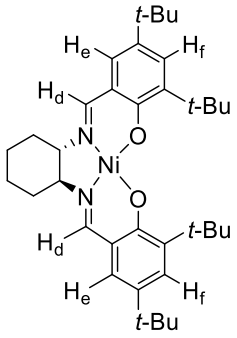

3.46

Proton	MD model	EK model
H_d	K_2 = 0.20 (R^2 = 0.99)	K_{asso} = 0.47 (R^2 = 0.99)
H_e	K_2 = 0.29 (R^2 = 0.98)	K_{asso} = 0.25 (R^2 = 0.98)
H_f	K_2 = 0.59 (R^2 = 0.99)	K_{asso} = 1.33 (R^2 = 0.99)
Avg ± Std dev	K_2 = 0.36 ± 0.20	K_{asso} = 0.68 ± 0.57

Table 5. Calculated dimerisation/association constants for compound **3.46** in a mixture of THF-d_8 and D_2O (95.5: 4.5).

When utilising the MD model, the average dimerisation constant obtained was 1.43 M^{-1} for complex **3.45**, and 0.36 M^{-1} for complex **3.46**, 4 times higher for the functionalised complex. When utilising the EK model, the average association constant was 2.82 M^{-1} for complex **3.45** and 0.68 M^{-1} for complex **3.46**. The difference in the calculated association constants was again slightly above 4 times higher for complex **3.45** than for complex **3.46**. These differences in the equilibrium constant match well with the rate difference observed for catalyst **3.22**, which was 5 times faster than catalyst **3.11** for the HKR of epichlorohydrin (**Figure 111**, **Figure 112**).

K_2 and K_{asso} were also calculated for complex **3.45** in THF-d_8 in the absence of D_2O. Under these conditions, the average values of K_2 and K_{asso} were 0.55 M^{-1} and 1.16 M^{-1} for the MD model and the EK model, respectively. Interestingly, these lower equilibrium constants indicate that the presence of water has an important role in the association of the monomers in solution, likely due to an increase in solvent polarity, which would reinforce hydrophobic interactions. In the case of the HKR, as water is a reagent that is consumed during the reaction, it is likely that the dimerisation constant will become lower as the reaction progresses.

3.7.6. Kinetic observations in the heterogeneous system

The rate differences observed with catalyst **3.22** and catalyst **3.11** in the homogeneous system were around 5 times and were not as large as the initial rates differences obtained in the preliminary experiments using epichlorohydrin in neat conditions. We hypothesized that additional effects could be present under heterogeneous conditions that result in further enhancements in reactivity. We proceeded to compare the initial rate for the HKR of epichlorohydrin at different concentrations of **3.22** and **3.11** in the absence of solvent. **Figure 115** shows a plot of the k_{obs} observed at different catalyst concentrations for both complex **3.22** and complex **3.11**.

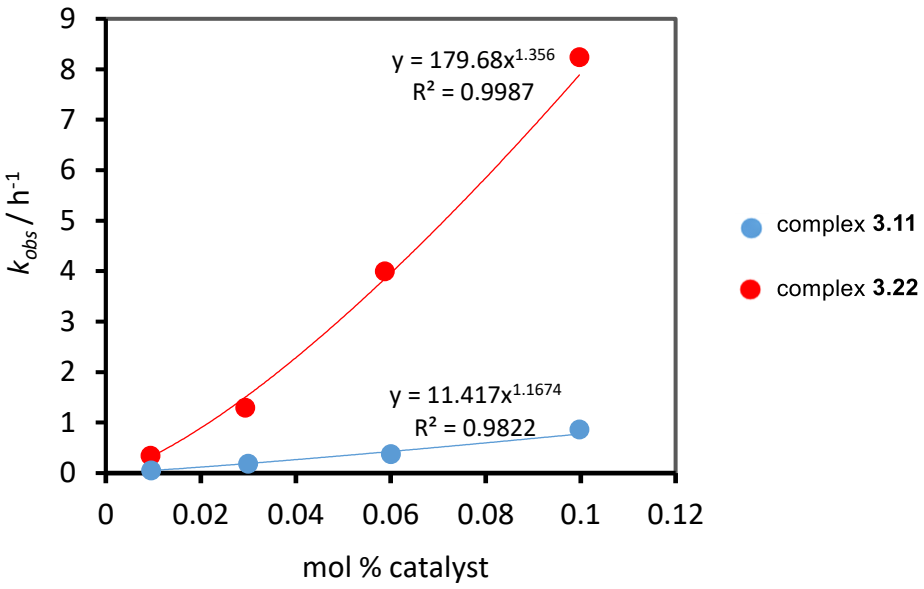

Figure 115. k_{obs} vs concentration of catalyst (mol %) for the HKR of epichlorohydrin under neat conditions, catalyst loading variable, epichlorohydrin 50 µL, H_2O 6.9 µL. Blue dots: catalyst **3.11**.Red dots: catalyst **3.22**.

From **Figure 15**, it can be observed that the difference in rate observed between complexes **3.22** and **3.11** increases at higher concentrations of catalyst. We hypothesised that this further increase in the rate difference could be originating from better homogenisation of the non-miscible mixture of the water and epoxide phases due to the greater amphiphilicity of our functionalised catalyst. This would result in a greater surface area for the reaction to occur at the interface between the two phases. To investigate this hypothesis, we proceeded to analyse the ability of the different catalysts in stabilising emulsions in a biphasic mixture. Since plenty of terminal epoxides used in the HKR reaction are immiscible with water, these functionalised catalysts could be of great utility, especially with less reactive epoxides.

3.7.7. Origin of rate acceleration in the heterogeneous system

To better understand the mixing occurring between the two phases in the heterogeneous system, we investigated the size of the emulsions formed. Structural data were obtained using dynamic light scattering (DLS) of a mixture of styrene oxide as the substrate and water as the reagent. Styrene oxide was chosen for the HKR as this substrate reacted much slower. With epichlorohydrin, the reaction progressed too quickly, leading to diol formation, which changes the miscibility of the system. The heterogeneous samples were stirred vigorously for 2 minutes in the absence of catalyst and in the presence of either complex **3.22** or complex **3.11**. The mixtures were then left to rest for 10 minutes before being examined by dynamic light scattering. The size of the water in oil (styrene oxide) emulsions in the absence of catalyst were 2-3 µm, suggesting the formation of microemulsions under these conditions. The same mixture with 0.1 mol% of catalyst **3.11** gave objects ~1 µm in size, suggesting that catalyst **3.11** has some effect in increasing the homogeneity of the reaction mixture. The application of catalyst **3.22** has a more significant effect, decreasing the size of the emulsions to the range of 400-600 nm in size. These results suggest that catalyst **3.22** increases the rate of the HKR reaction not only by increasing the equilibrium constant for dimerisation in homogeneous systems, but also, in heterogeneous systems by enhanced emulsification and increasing the surface area between water and the substrate (**Figure 116**).

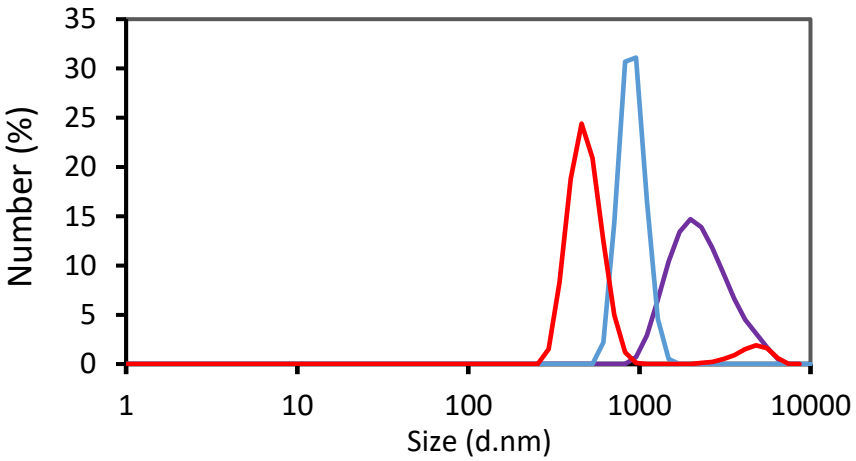

Figure 116. Diameter of water droplets measured with dynamic light scattering. Purple: styrene oxide = 375 µL, milli-Q water = 36 µL, no catalyst. Blue: styrene oxide = 375 µL, milli-Q water = 36 µL, **3.11** = 0.1 mol %. Red: styrene oxide = 375 µL, milli-Q water = 36 µL, **3.22** = 0.1 mol %. The samples were stirred for 2 minutes and left to rest for 10 minutes.

3.7.8. Substrate scope

To demonstrate that our modified catalyst is practically useful, the reactivity of (salen)Co(III) complex **3.22** was examined with several different substrates under neat conditions (**Table 6**). The reaction of terminal epoxides with an aliphatic chain proceeded quickly with 0.1 mol% catalyst loading; for example, the HKR of 1,2-epoxyhexane was complete within 1 hour while in 1 hour, 66% *e.e*. was achieved utilising the control catalyst. Complete chiral resolution (>99% *e.e*.) of 2-vinyloxirane was achieved in 5 hours, while in the same time period, 40.5% *e.e*. was achieved with catalyst **3.11**. Epoxides containing ether side chains were also good substrates, with the HKR of butyl glycidyl ether complete within 25 min and the HKR of benzyl glycidyl ether complete within 80 min using 0.1 mol% of complex **3.22**. Within the same time period, catalysis with complex **3.11** arrived at 67% and 78% *e.e*., respectively. HKR of styrene oxide, known to be a slow-reacting substrate in the HKR reaction, commonly requiring long reaction times, was conducted using 0.5 mol% of catalyst **3.22**. Under neat conditions, we reached 99% *e.e*. within three hours, while with catalyst **3.11**, 73% *e.e*. was achieved under the same conditions. Note that these reactions were conducted without the addition of additional organic solvent, as opposed to some previous catalysts, which required the addition of solvents such as THF for homogenisation.[30,54,125,127,128,136]

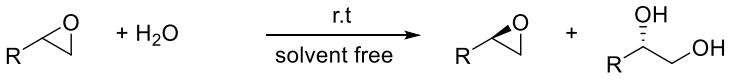

Entry	R	Co loading [mol %]	Catalyst	Water loading (equiv.)	Time	*e.e.* epoxide
1	$(CH_2)_3CH_3$	0.1	**3.11**	0.6	60 min	66%
2	$(CH_2)_3CH_3$	0.1	**3.22**	0.6	60 min	>99%
3	CH_2Cl	0.1	**3.11**	0.6	70 min	37%
4	CH_2Cl	0.1	**3.22**	0.6	70 min	>99%
5	Ph	0.5	**3.11**	0.6	3h	73%
6	Ph	0.5	**3.22**	0.6	3h	>99%
7	$CH_2O(CH_2)_3CH_3$	0.1	**3.11**	0.6	25 min	67%
8	$CH_2O(CH_2)_3CH_3$	0.1	**3.22**	0.6	25 min	>99%
9	$CHCH_2$	0.1	**3.11**	1.2	5 h	40.5%
10	$CHCH_2$	0.1	**3.22**	1.2	5 h	>99%
11	CH_2OPh	0.1	**3.11**	0.6	80 min	78%
12	CH_2OPh	0.1	**3.22**	0.6	80 min	98.5%
13	*t*-Bu	0.1	**3.11**	0.6	4 days	49%
14	*t*-Bu	0.1	**3.22**	0.6	4 days	>99%

Table 6. Substrate scope HKR of terminal epoxides using complexes **3.11** and **3.22**.

3.8. Conclusions

In this chapter, we demonstrated that the introduction of hydrophobic interactions can be used to enhance cooperative catalysis and applied this successfully to the hydrolytic kinetic resolution of terminal epoxides. This reaction is synthetically useful and has received much attention in both academic and industrial contexts. The catalysts prepared are (salen)Co(III) complexes that are functionalised with alkyl chains to increase their hydrophobic properties. The functionalisation resulted in higher rates compared to Jacobsen's original catalyst when performing the reaction in homogeneous conditions (by adding THF) and even faster rates when working in heterogeneous conditions (neat conditions).

In homogeneous conditions, the initial reaction rates were found to be directly proportional to the length of the chains added to the salen ligand. Their dimerisation constants were estimated by modelling the ^{1}H NMR chemical shift changes of two Ni model compounds. We obtained equilibrium constants 4 times greater when utilising the functionalised complex with C_{16} chains compared to the control complex. This value matched closely with the rate acceleration observed under homogeneous conditions, supporting the hypothesis that this rate enhancement originates

from a more effective assembly of the functionalised catalyst due to the attachment of hydrophobic chains.

For the heterogeneous system, the reaction rate was also observed to increase with the attachment of long alkyl chains, but this increase was not directly proportional to the length of the chains attached. It was hypothesised that this accelerated rate origin may be due to other effects not yet examined. DLS experiments showed that smaller water droplets below 1 micrometre were present when utilising the functionalised catalyst, which were much smaller than the droplets formed in the presence of the unmodified catalyst. These results suggested that a better homogenisation of the phases due to the amphiphilic nature of the functionalised catalysts is the reason behind the rate acceleration. That rate acceleration turned to be up to 10 times faster than the unmodified catalyst.

The modified cobalt complex presented in this chapter shows several advantages over other published catalysts for the HKR of epoxides. Firstly, in homogeneous conditions, as the reaction rate is enhanced by increasing the dimerisation constant between catalytic units due to functionalising the catalysts with hydrocarbon chains, the reaction rate is enhanced without introducing the rigidity that a covalently linked catalyst would exhibit. This non-rigidity is preferable when working with high catalyst concentrations. This is due to the non-randomization of the Co sites exhibited by covalently linked systems, as explained above with **Equation 15**. The utilisation of hydrocarbon chains to increase the dimerisation constant can also be a better choice than utilising hydrogen bonding, due to the higher reactivity of the functional groups needed for hydrogen bonding. Fewer side reactions could be expected by the use of inert hydrocarbon chains. Secondly, in neat, heterogeneous conditions, the catalyst becomes even more effective. The capacity to work in neat conditions avoids using additional organic solvents and is beneficial from a green chemistry point of view. Even higher catalytic rates are observed under these conditions, with the catalyst acting as an efficient homogenising agent. It is worth noting that Jacobs has previously shown that the addition of external surfactants does not result in rate enhancement in the HKR reaction.[135] This is likely because any added surfactants will dilute the concentration of Co complexes at the interface, preventing the required cooperativity for effective catalysis. With our catalysts, this is not a problem as the amphiphilic properties are introduced directly to the catalyst itself.

Our modified catalyst was found to be effective with a wide range of terminal epoxide substrates, consistently achieving higher rates than the unmodified catalyst. Unreactive epoxides such as styrene oxide, 2-vinyloxirane or 3,3-dimethyl-1,2-epoxybutane were resolved efficiently, and excellent enantioselectivities were achieved (>99% *e.e.* in almost all of the cases). This catalyst becomes especially useful with less reactive epoxides, allowing lower catalyst loadings and shorter reactions times.

Future Work

A self-assembled catalytic triad

Catalytic triads are found at the heart of many biological catalysts. They have three amino acids in the active site that act cooperatively to facilitate the chemical transformation, one acting as an acid, one as a base and one acting as a nucleophile.[140] The serine-histidine-aspartate (Ser-His-Asp) combination is a classic example of a catalytic triad, where the aspartate residue acts as an acid that increases the basicity of histidine, which is then able to deprotonate the serine residue, making it a better nucleophile for various reactions (**Figure 117**).[141] Since catalytic triads involve individual catalytic units acting cooperatively, they could also benefit from self-assembly, forcing them into close proximity.

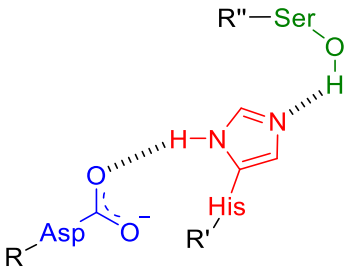

Figure 117. The serine-histidine-aspartate catalytic triad.

An interesting example by Nothling *et al.* shows a covalently linked catalytic triad supported on a resin. Aside from the strategic placement of the catalytic units in space, the system benefits from the local hydrophobic environment of the resin to enhance the cleavage of nitrophenyl butyrate (**Figure 118**).[37]

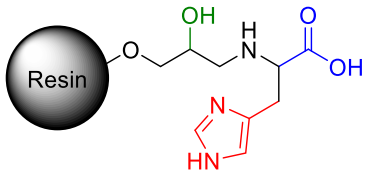

Figure 118. Artificial catalytic triad supported onto a hydrophobic resin.[37]

After seeing the results obtained from this thesis, the design of a catalytic triad made from three amphiphilic amino acids could be plausible for the same reaction. To attempt the idea,

amphiphilic versions of the catalytic units would need to be synthesised or acquired; for example, histidine functionalised with a hydrophobic chain could be used as the base of the triad, a fatty acid as stearic acid as the acid, and a long-chain functionalised alcohol such as some of Brij surfactants as the nucleophile. For the catalyst to have a high catalytic activity, the catalytic units would need to not self-sort separately, but to self-assemble in a homogeneous manner, creating aggregates that contain all the three catalytic units (**Figure 119**).

Our research group has recently proved that a system including two different kinds of amphiphilic catalytic units acting cooperatively to perform catalysis is possible.[142] This demonstrated that the self-assemblies are formed by the homogeneous mixing of two different catalytic units. The proportion of each catalyst in the assemblies can be changed *in situ* by changing the relative proportion of catalytic units in the solution.

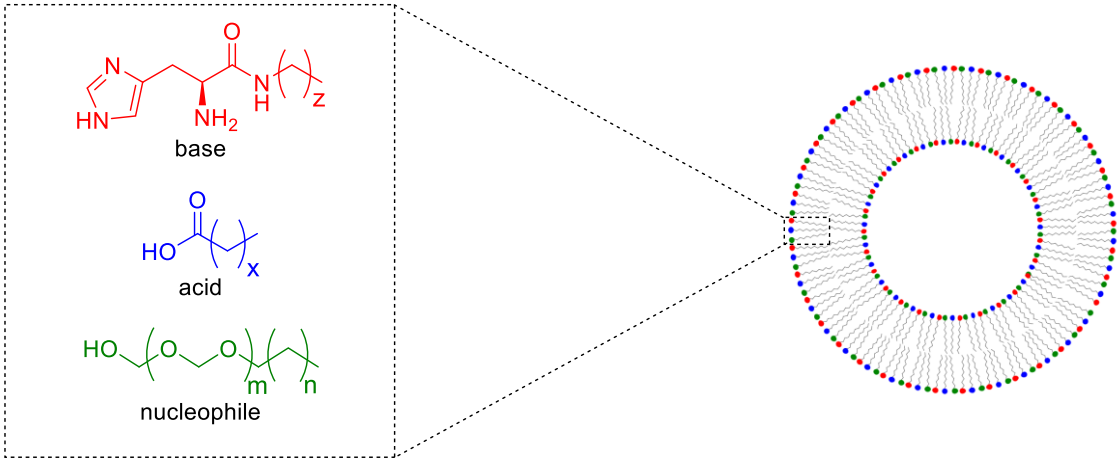

Figure 119. A catalytic triad formed from the self-assembly of amphiphilic ligands.

The catalytic triad could, in theory, be used to cleave phosphoesters and esters. Nitrophenyl butyrate would be an interesting substrate to start testing this idea, as it has been used in the resin-supported example mentioned above, and because its cleavage releases *para*-nitrophenolate, allowing the reaction to be monitored easily by a UV spectrophotometer.

Amphiphilic (salen)Co(II) catalysts for nitro-aldol reactions

Nitroaldol reactions are a straightforward way to create carbon-carbon bonds, and (salen)metal complexes have been effectively used to perform these reactions in an asymmetric way.[143,144] The examples by Hong's research group are of high importance for this thesis, since they use hydrogen bonding self-assembled catalysts to perform the reaction cooperatively involving two catalytic units.[53,113]

In the third chapter of this thesis, we successfully developed (salen)Co(III)catalysts for the HKR of terminal epoxides, enhancing cooperativity by modifying their hydrophobic interactions. Utilising these same, non-oxidised (salen)Co(II) catalysts could potentially be effective as more efficient catalysts for nitro-aldol reactions (**Figure 120**).

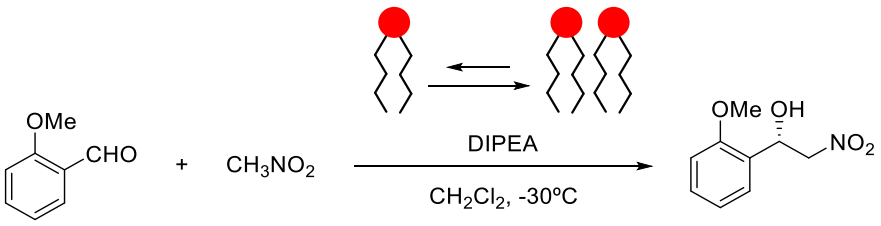

Figure 120. Modification of hydrophobic interactions of (salen)Co(II) catalysts for nitro-aldol reactions.

The reaction conditions for the hydrogen bonding example utilise DCM as the solvent. Potentially for our idea to work, we would need to change the solvent or add additional solvents to reinforce the hydrophobic effect. To determine the success of this idea, we would have to determine both the rate and the enantioselectivity of the reaction and make sure that enantioselectivity is not diminished by utilising a self-assembled system.

Divergent regioselectivity using self-assembled cooperative catalysts

In this thesis, numerous examples where cooperative catalyst are brought into close proximity to achieve enhanced reaction rates have been described. In 1999, Jacobsen's research group showed that it was also possible to change the regioselectivity of an intramolecular nucleophilic attack by switching from utilising a monomeric catalyst to a covalently linked, dimeric version of the catalyst. The catalysts utilised for this reaction were (salen)Co(III)catalysts (**Figure 121**).[145] In this example, they showed that monomeric catalyst **A** preferably catalyses the pathway that forms the exo product, while the dimeric catalyst **B** preferably catalyses the pathway that forms the endo product.

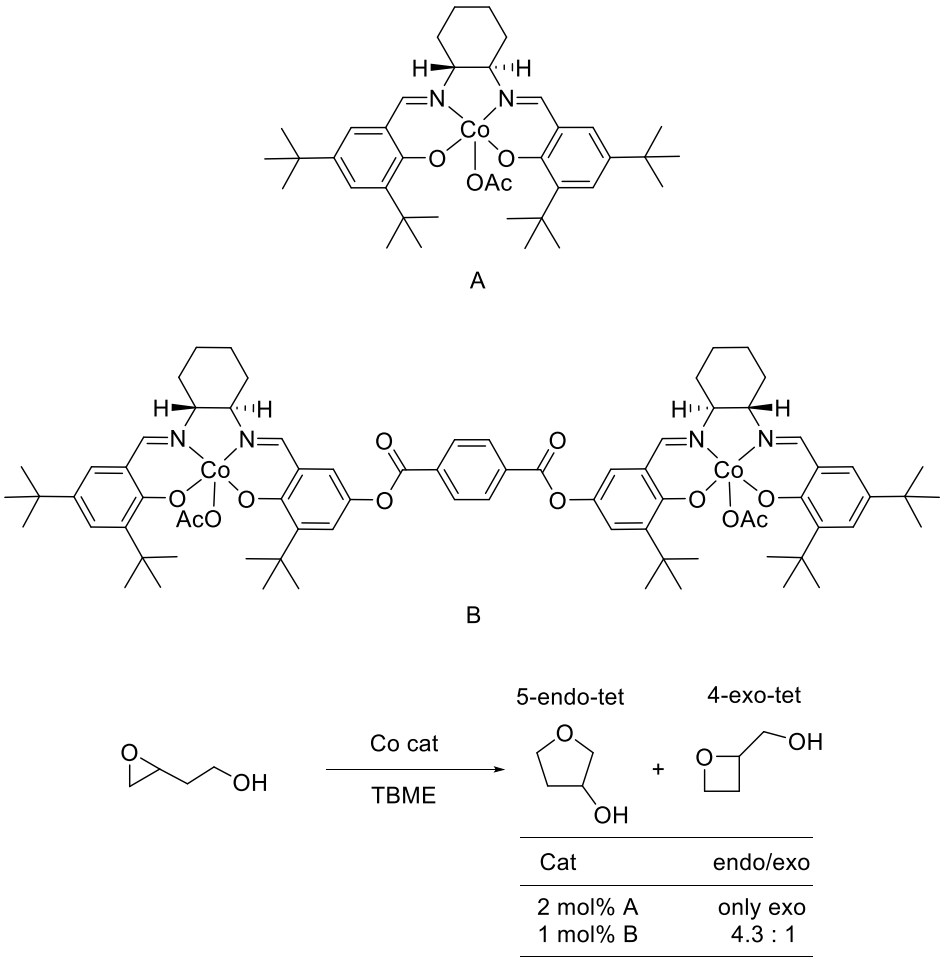

Figure 121. Regioselectivity control by the usage of monomeric/dimeric (salen)Co(III)catalysts.[145]

An interesting future study related to this concept would be to investigate if this effect could also be observed using our amphiphilic (salen)Co catalysts. If this were the case, one could also imagine a dynamic system where control of the self-assembly process could be used to control the regioselectivity of the reaction. For example, our research group recently demonstrated that the self-assembly (and therefore activity) of a cooperative catalyst could be switched on and off by irradiation with different wavelengths of light.[146] These concepts could be used to control the regioselectivity of a reaction on demand. Such ideas are interesting as novel concepts in organic chemistry and have potential applications in nanotechnology and systems chemistry.

Experimental

General details

All fine chemicals were sourced from Sigma-Aldrich and AK Scientific and were used directly without purification unless mentioned. Compounds lacking experimental details were prepared according to the literature as cited and are in agreement with published spectra. All air- and water-sensitive reactions were carried out in flame-dried glassware under argon atmosphere using standard Schlenk manifold technique. NMR solvents including deuterated tetrahydrofuran-d^8 and deuterated chloroform were purchased from EURISO-TOP. Acetone and hexanes (analytical grade) were purchased from ECP chemicals along with dichloromethane and ethyl acetate of laboratory quality. Hydrochloric acid 37% and methanol were purchased from Thermo Fisher Scientific. Celite® 545 was purchased from VELP Scientifica.

Organic compounds were synthesized and characterized by ^{1}H, ^{13}C NMR, IR and HRMS and the data compared to literature values where available. Flash column chromatography was performed using silica gel 60 (Aldrich) and a suitable eluent. Analytical TLC was performed on aluminium backed plates pre-coated (0.25 mm) with Merck Silica Gel 60 F254 with a suitable solvent system and was visualized using UV fluorescence (254 nm) and/or developed with phosphomolybdic acid (PMA) or potassium permanganate.

^{1}H and ^{13}C NMR spectra were recorded using a Bruker Ascend 400 NMR spectrometer operating at 400 MHz for ^{1}H nuclei and 101 MHz for ^{13}C nuclei. ^{31}P NMR spectra were recorded using a Bruker AV300 spectrometer operating at 300 MHz. Chemical shifts (δ) are quoted in parts per million (ppm) and coupling constants (*J*) are in Hertz (Hz). Residual solvent peaks were used as the internal reference for ^{1}H and ^{13}C NMR. A solution of K_2HPO_4 at pH 7 (HEPES buffer 10 mM) was used as a coaxial reference (δ = 0 ppm) for ^{31}P-NMR spectra. Abbreviations for multiplicity are as follows: s = singlet, br s = broad singlet, d = doublet, t = triplet, q = quartet, pent = pentet, m = multiplet, dd = doublet of doublet, etc.).

Infrared (IR) spectra were recorded using a Nicolet iS10 spectrometer (Thermo Fisher Scientific Inc.) with the absorption peaks expressed in wavenumbers (cm^{-1}) and recorded using a range of 450 to 4000 cm^{-1}. IR spectra were analysed using OMNIC 9.2.86. High resolution mass spectrometry (HRMS) measurements were obtained using a VG-70SE spectrometer at a nominal resolution of 5000 to 10000 as appropriate.

Dynamic light scattering (DLS) analysis were performed on a Malvern Zetasizer Nano-S instrument.

Curve fitting was performed using Origin fitting tools.

General Procedures

General procedure 1 (GP1): N-Alkylation of di-tert-butyl 1,4,7-triazonane-1,4-dicarboxylate

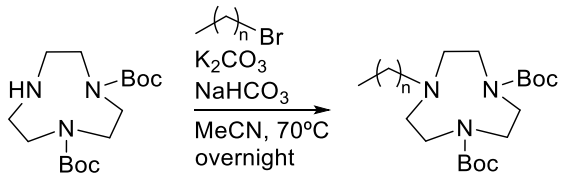

2.12

To a solution of di-*tert*-butyl 1,4,7-triazonane-1,4-dicarboxylate (1 equiv.) in MeCN (0.1 M) were added K_2CO_3 (3 equiv.), $NaHCO_3$ (3 equiv.) and the corresponding 1-bromoalkane (2.5 equiv.). The reaction mixture was further stirred overnight at 70 ºC. The next day, after evaporation under reduced pressure, the crude product was purified by flash chromatography to obtain the alkylation product.

General procedure 2 (GP2): Boc deprotection of di-tert-butyl 7-alkyl-1,4,7-triazonane-1,4-dicarboxylate

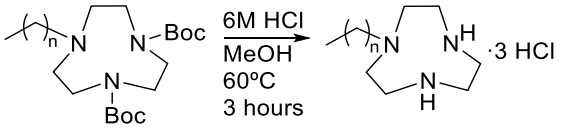

To a solution of the corresponding di-*tert*-butyl 7-alkyl-1,4,7-triazonane-1,4-dicarboxylate in MeOH (0.5 M) was added 6M HCl (45 mL / mmol). The reaction mixture was further stirred for 3 hours at 60 ºC. The crude was evaporated under reduced pressure and the deprotected product was obtained without further purification.

Procedures

di-*tert*-Butyl 7-ethyl-1,4,7-triazonane-1,4-dicarboxylate (2.13)

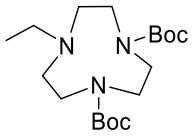

2.13

According to **GP1**, to a solution of di-*tert*-butyl 1,4,7-triazonane-1,4-dicarboxylate **2.12** (76 mg, 0.23 mmol) in MeCN (5 mL) were added K_2CO_3 (99 mg, 0.69 mmol), $NaHCO_3$ (63 mg, 0.69 mmol) and 1-bromoethane (62 mg, 0.55 mmol). The crude product was purified by flash chromatography (50% EtOAc/hexanes) to obtain the title compound as a yellow oil (54 mg, 0.15 mmol, 66%). **^{1}H NMR** (400 MHz, $CDCl_3$) δ 3.55–3.41 (m, 4H, NC*H*$_2$C*H*$_2$N), 3.33–3.18 (m, 4H, NCH$_2$C*H*$_2$N), 2.67–2.51 (m, 6H, CH$_3$C*H*$_2$N and NC*H*$_2$CH$_2$N), 1.47 (s, 18H, C(C*H*$_3$)$_3$), 1.00 (t, *J* = 7.3 Hz, 3H, C*H*$_3$CH$_2$N). **^{13}C NMR** (101 MHz, $CDCl_3$) δ 155.9 (CO), 79.5 (*C*(CH$_3$)$_3$), 79.4*, 79.4*, 53.6 (NCH$_2$*C*H$_2$N), 53.5*, 53.4 (N*C*H$_2$CH$_2$N), 53.1*, 51.0 (CH$_3$*C*H$_2$N), 50.9*, 50.8 (NCH$_2$*C*H$_2$N), 50.6*, 50.5*, 50.3*, 50.2 (NCH$_2$*C*H$_2$N), 50.1*, 50.0*, 49.9*, 28.7 (C(*C*H$_3$)$_3$), 28.7*, 12.9 (*C*H$_3$CH$_2$N). Spectral data is concordant with the literature.[147]

*Extra signals due to the presence of rotamers.

1-Ethyl-1,4,7-triazonane (2.18·3HCl)

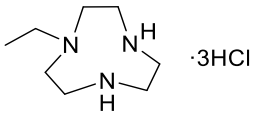

2.18·3HCl

According to **GP2,** to a solution of **2.13** (30 mg, 0.08 mmol) in MeOH (1 mL) was added 6M HCl (3 mL). The crude was evaporated under reduced pressure and *the title compound* was obtained without further purification as a white solid (22 mg, 0.08 mmol, 97%). **^{1}H NMR** (400 MHz, D_2O) δ 3.43 (s, 4H, NC*H*$_2$C*H*$_2$N), 3.36 (dd, *J* = 6.9, 4.5 Hz, 4H, NCH$_2$C*H*$_2$N), 3.26 (dd, *J* = 6.7, 4.7 Hz, 4H, NC*H*$_2$CH$_2$N), 3.06 (q, *J* = 7.2 Hz, 2H, NC*H*$_2$CH$_3$), 1.19 (t, *J* = 7.2 Hz, 3H, NCH$_2$C*H*$_3$).**^{13}C NMR** (101 MHz, D_2O) δ 50.7 (NCH$_2$*C*H$_2$N), 47.8 (N*C*H$_2$CH$_2$N), 42.0 (N*C*H$_2$*C*H$_2$N), 41.8 (N*C*H$_2$CH$_3$), 9.0 (N*C*H$_2$CH$_3$). **IR** ν_{max}(film)/cm^{-1} 3351, 1646, 1457, 1319, 1156, 1043, 877, 669. **HRMS** Found (ESI): MH$^+$, 158.1651; $C_8H_{20}N_3$ requires 158.1652.

di-*tert*-Butyl 7-dodecyl-1,4,7-triazonane-1,4-dicarboxylate (2.14)

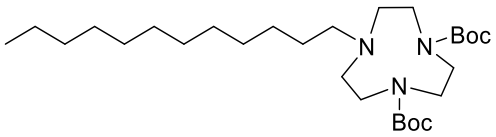

2.14

According to **GP1**, to a solution of di-*tert*-butyl 1,4,7-triazonane-1,4-dicarboxylate **2.12** (75 mg, 0.23 mmol) in MeCN (5 mL) were added K_2CO_3 (94 mg, 0.68 mmol), $NaHCO_3$ (57 mg, 0.68 mmol) and 1-bromododecane (142 mg, 0.57 mmol). The crude product was purified by flash chromatography (20% EtOAc/hexanes) to obtain *the title compound* as a yellow oil (72 mg, 1.6 mmol, 71%). **^{1}H NMR** (400 MHz, $CDCl_3$) δ 3.53–3.40 (m, 4H, NC*H*$_2$C*H*$_2$N), 3.32–3.16 (m, 4H, NC*H*$_2$CH$_2$N), 2.66–2.57 (m, 4H, NCH$_2$C*H*$_2$N), 2.51–2.41 (m, 2H, CH$_3$(CH$_2$)$_{10}$C*H*$_2$N), 1.47 (s, 18H, C(C*H*$_3$)$_3$), 1.26 (s, 20H, CH$_3$(C*H*$_2$)$_{10}$CH$_2$N), 0.87 (t, *J* = 7.0 Hz, 3H, C*H*$_3$(CH$_2$)$_{10}$CH$_2$N). **^{13}C NMR** (101 MHz, $CDCl_3$) δ 155.7(CO), 79.3 (*C*(CH$_3$)$_3$), 79.3*, 79.3*, 79.2*, 57.0 (NCH$_2$*C*H$_2$N), 54.1(NCH$_2$CH$_2$N), 54.1*, 54.0*, 50.7 (CH$_3$(CH$_2$)$_{10}$*C*H$_2$N), 50.6*, 50.4*, 49.8 (NCH$_2$*C*H$_2$N), 31.9, 29.7, 29.7, 29.6, 29.3, 28.6, 28.6*, 27.9, 27.5, 22.7 (CH$_3$(*C*H$_2$)$_{10}$CH$_2$N), 14.1(*C*H$_3$(CH$_2$)$_{10}$CH$_2$N). **IR** ν_{max}(film)/cm^{-1} 2922, 2846, 1696, 1458, 1411, 1365, 1260, 1152, 1094, 1027, 801. **HRMS** Found (ESI): MH$^+$, 498.4251; $C_{28}H_{56}N_3O_4$ requires 498.4265.

*Extra peaks due to the presence of rotamers.

1-Dodecyl-1,4,7-triazonane (2.19·3HCl)

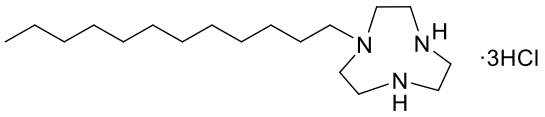

2.19·3HCl

According to **GP2,** to a solution of **2.14** (34 mg, 0.07 mmol) in MeOH (1 mL) was added 6M HCl (3 mL). The crude was evaporated under reduced pressure and *the title compound* was obtained without further purification as a white solid (26 mg, 0.07, 96%).**^{1}H NMR** (400 MHz, D_2O) δ 3.51 (s, 4H, NC*H*$_2$C*H*$_2$N), 3.28 (t, *J* = 5.7 Hz, 4H, NCH$_2$C*H*$_2$N), 3.02 (d, *J* = 6.2 Hz, 4H, NC*H*$_2$CH$_2$N), 2.84-2.70 (m, 2H, NC*H*$_2$CH$_2$(CH$_2$)$_9$CH$_3$), 1.52–1.45 (m, 2H, NCH$_2$C*H*$_2$(CH$_2$)$_9$CH$_3$), 1.18 (s, 18H, NCH$_2$CH$_2$(C*H*$_2$)$_9$CH$_3$), 0.82–0.73 (m, 3H, NCH$_2$CH$_2$(CH$_2$)$_9$C*H*$_3$). **^{13}C NMR** (101 MHz, D_2O) δ 55.3 (N*C*H$_2$(CH$_2$)$_{10}$CH$_3$), 47.6 (N*C*H$_2$CH$_2$N), 43.0 (NCH$_2$*C*H$_2$N), 41.8 (N*C*H$_2$*C*H$_2$N), 31.9, 29.8, 29.8, 29.7, 29.6, 29.4, 27.3, 24.1, 22.6 (NCH$_2$(*C*H$_2$)$_{10}$CH$_3$, 13.9 (NCH$_2$(CH$_2$)$_{10}$*C*H$_3$). **IR** ν_{max}(film)/cm^{-1} 3379, 2922, 2852, 1456, 689. **HRMS** Found (ESI): MH$^+$ 298.3206; $C_{18}H_{40}N_3$ requires 298.3217.

di-*tert*-Butyl 7-tetradecyl-1,4,7-triazonane-1,4-dicarboxylate (2.15)

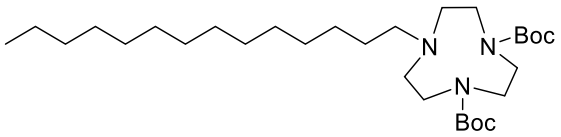

2.15

According to **GP1**, to a solution of di-*tert*-butyl 1,4,7-triazonane-1,4-dicarboxylate **2.12** (76 mg, 0.23 mmol) in MeCN (5 mL) were added K_2CO_3 (96 mg, 0.69 mmol), $NaHCO_3$ (58 mg, 0.69 mmol) and 1-bromotetradecane (160 mg, 0.58 mmol). The crude product was purified by flash chromatography (20% EtOAc/hexanes) to obtain *the title compound* as a yellow oil (68 mg, 0.19 mmol, 82%). **^{1}H NMR** (400 MHz, $CDCl_3$) δ 3.55–3.38 (m, 4H, NC*H*$_2$C*H*$_2$N), 3.32–3.17 (m, 4H, NC*H*$_2$CH$_2$N), 2.67–2.56 (m, 4H, NCH$_2$C*H*$_2$N), 2.51–2.43 (m, 2H, CH$_3$(CH$_2$)$_{12}$C*H*$_2$N), 1.47 (s, 18H, C(C*H*$_3$)$_3$), 1.26 (s, 24H, CH$_3$(C*H*$_2$)$_{12}$CH$_2$N), 0.9–0.86 (m, 3H, C*H*$_3$(CH$_2$)$_{12}$CH$_2$N).^{13}C NMR (101 MHz, $CDCl_3$) δ 155.7 (CO), 155.6*, 155.4*, 79.4 (*C*(CH$_3$)$_3$), 56.9 (N*C*H$_2$*C*H$_2$N), 54.0 (N*C*H$_2$CH$_2$N), 53.6*, 50.8 (CH$_3$(*C*H$_2$)$_{13}$N), 49.7 (N*C*H$_2$*C*H$_2$N), 31.9, 29.7, 29.7, 29.7, 29.4 (CH$_3$(*C*H$_2$)$_{13}$N), 28.6 (C(*C*H$_3$)$_3$), 28.6*, 27.6, 27.5, 22.7 (CH$_3$(*C*H$_2$)$_{13}$N), 14.1(*C*H$_3$(CH$_2$)$_{13}$N). **IR** ν_{max}(film)/cm^{-1} 2923, 2853, 1687, 1460, 1412, 1365, 1247, 1153, 731. **HRMS** Found (ESI): MH$^+$ 526.4565 $C_{30}H_{60}N_3O_4$ requires 526.4578.

*Extra peaks due to the presence of rotamers.

1-Tetradecyl-1,4,7-triazonane (2.20·3HCl)

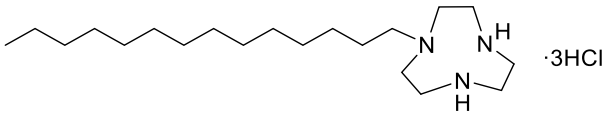

2.20·3HCl

According to **GP2,** to a solution of **2.15** (41 mg, 0.08 mmol) in MeOH (1 mL) was added 6M HCl (3 mL). The crude was evaporated under reduced pressure and *the title compound* was obtained without further purification as a white solid (12 mg, 0.03 mmol, 40%). **^{1}H NMR** (400 MHz, D_2O) δ 3.49 (s, 4H, NC*H*$_2$C*H*$_2$N), 3.24 (t, *J* = 5.7 Hz, 4H, NCH$_2$C*H*$_2$N), 2.95 (d, *J* = 5.7 Hz, 4H, NC*H*$_2$CH$_2$N), 2.69 (m, 2H, NC*H*$_2$CH$_2$(CH$_2$)$_{11}$CH$_3$), 1.44 (s, 2H, NCH$_2$C*H*$_2$(CH$_2$)$_{11}$CH$_3$), 1.14 (d, *J* = 10.3 Hz, 22H, NCH$_2$CH$_2$(C*H*$_2$)$_{11}$CH$_3$), 0.82–0.66 (m, 3H, NCH$_2$CH$_2$(CH$_2$)$_{11}$C*H*$_3$). **^{13}C NMR** (101 MHz, D_2O) δ 55.2 (N*C*H$_2$(CH$_2$)$_{12}$CH$_3$), 47.6 (N*C*H$_2$CH$_2$N), 46.7 (NCH$_2$*C*H$_2$N), 43.1 (N*C*H$_2$*C*H$_2$N), 41.9, 32.0, 30.0, 30.0, 29.9, 29.8, 29.5, 27.5 (NCH$_2$(*C*H$_2$)$_{12}$CH$_3$), 24.2, 22.7 (NCH$_2$(CH$_2$)$_{12}$*C*H$_3$, 13.9 (NCH$_2$(CH$_2$)$_{12}$*C*H$_3$), 8.2 (NCH$_2$(*C*H$_2$)$_{12}$CH$_3$). **IR** ν_{max}(film)/cm^{-1} 3360, 2923, 2853, 1635, 1457, 669. **HRMS** Found (ESI): MH$^+$ 326.3525; $C_{20}H_{44}N_3$ requires 326.3530.

di-*tert*-Butyl 7-hexadecyl-1,4,7-triazonane-1,4-dicarboxylate (2.16)

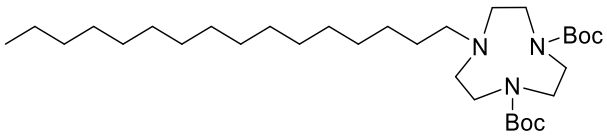

2.16

According to **GP1**, to a solution of di-*tert*-butyl 1,4,7-triazonane-1,4-dicarboxylate **2.12** (10 mg, 0.03 mmol) in MeCN (0.6 mL) were added K_2CO_3 (27 mg, 0.09 mmol), $NaHCO_3$ (7.6 mg, 0.09 mmol) and 1-bromohexadecane (24.4 mg, 0.08 mmol). The crude product was purified by flash chromatography (20% EtOAc/hexanes) to obtain *the title compound* as a yellow oil (8.8 mg, 0.16 mmol, 52%).**^{1}H NMR** (400 MHz, $CDCl_3$) δ 3.53–3.42 (m, 4H, NC*H*$_2$C*H*$_2$N), 3.29–3.20 (m, 4H, NC*H*$_2$CH$_2$N), 2.62 (dt, *J*=10.9, 4.8 Hz, 4H, NCH$_2$C*H*$_2$N), 2.47 (t, *J*=7.6 Hz, 2H, $CH_3(CH_2)_{14}CH_2$N), 1.47 (s, 18H, C(C*H*$_3$)$_3$), 1.25 (s, 28H, $CH_3(CH_2)_{14}CH_2$N), 0.9 –0.85 (m, 3H, $CH_3(CH_2)_{14}CH_2$N).^{13}C NMR (101 MHz, $CDCl_3$) δ 155.7 (CO), 155.6*, 79.3 (*C*(CH$_3$)$_3$), 57.0 (NCH$_2$*C*H$_2$N) , 54.0 (NCH$_2$*C*H$_2$N), 50.6 (CH_3(*C*H$_2$)$_{15}$N), 49.7 (NCH$_2$*C*H$_2$N), 31.9, 31.6, 29.7, 29.7, 29.4 (CH_3(*C*H$_2$)$_{15}$N),, 28.6 (C(*C*H$_3$)$_3$), 28.6*, 27.5, 22.7 (CH_3(*C*H$_2$)$_{15}$N), 14.1(*C*H$_3$(CH$_2$)$_{15}$N). **IR** ν_{max}(film)/cm^{-1} 2922, 2853, 1694, 1411, 1364, 1247, 1151, 1096, 989, 772. **HRMS** Found (ESI): MH$^+$ 554.4878; $C_{32}H_{64}N_3O_4$ requires 554.4891.

*Extra peaks due to the presence of rotamers.

1-Hexadecyl-1,4,7-triazonane (2.7·3HCl)

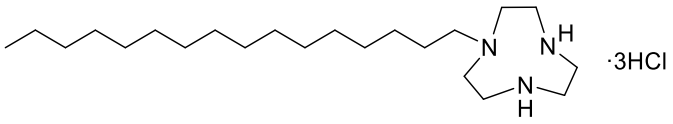

2.7

According to **GP2,** to a solution of **2.16** (36 mg, 0.06 mmol) in MeOH (1 mL) was added 6M HCl (3 mL). The crude was evaporated under reduced pressure and the title compound was obtained without further purification as a white solid (19 mg, 0.05 mmol, 84%).**^{1}H NMR** (400 MHz, MeOD) δ 3.50 (s, 4H, NC*H*$_2$C*H*$_2$N), 3.29 (s, 4H, NCH$_2$C*H*$_2$N), 3.09 (s, 4H, NC*H*$_2$CH$_2$N), 2.81 (m, 2H, NC*H*$_2$CH$_2$(CH$_2$)$_{13}$CH$_3$), 1.57 (s, 2H, NC*H*$_2$CH$_2$(CH$_2$)$_{13}$CH$_3$), 1.30 – 1.11 (m, 26H, NC*H*$_2$CH$_2$(CH$_2$)$_{13}$CH$_3$), 0.81 (t, *J* = 6.4 Hz 3H, NC*H*$_2$CH$_2$(CH$_2$)$_{13}$CH$_3$). **^{13}C NMR** (101 MHz, MeOD) δ 56.0 (N*C*H$_2$(CH$_2$)$_{16}$CH$_3$), 48.2 (N*C*H$_2$CH$_2$N), 43.2 (NCH$_2$*C*H$_2$N), 42.23 (N*C*H$_2$*C*H$_2$N), 32.7, 29.4, 29.4, 29.3, 29.3, 29.2, 29.1, 27.0, 24.2, 22.3, (NCH$_2$(*C*H$_2$)$_{13}$CH$_3$), 13.0 (NCH$_2$(CH$_2$)$_{16}$*C*H$_3$). Spectral data is concordant with the literature.[82]

di-*tert*-Butyl 7-octadecyl-1,4,7-triazonane-1,4-dicarboxylate (2.17)

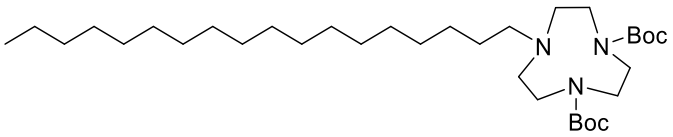

2.17

According to **GP1**, to a solution of di-*tert*-butyl 1,4,7-triazonane-1,4-dicarboxylate **2.12** (76 mg, 0.23 mmol) in MeCN (xx mL) were added K_2CO_3 (96 mg, 0.69 mmol), $NaHCO_3$ (58 mg, 0.69 mmol) and 1-bromooctadecane (192 mg, 0.58 mmol). The crude product was purified by flash chromatography (20% EtOAc/hexanes) to obtain *the title compound* as a yellow oil (43 mg, 0.07 mmol, 32%).**^{1}H NMR** (400 MHz, $CDCl_3$) δ 3.55–3.43 (m, 4H, NC*H*$_2$C*H*$_2$N), 3.30–3.19 (m, 4H, NC*H*$_2$CH$_2$N), 2.67–2.57 (m, 4H, NCH$_2$C*H*$_2$N), 2.52–2.42 (m, 2H, CH$_3$(CH$_2$)$_{16}$C*H*$_2$N), 1.47 (s, 18H, C(C*H*$_3$)$_3$), 1.26 (s, 24H, CH$_3$(C*H*$_2$)$_{16}$CH$_2$N), 0.92–0.84 (m, 3H, C*H*$_3$(CH$_2$)$_{16}$CH$_2$N). **^{13}C NMR** (101 MHz, $CDCl_3$) δ 155.7 (CO), 79.3 (*C*(CH$_3$)$_3$), 57.0 (N*C*H$_2$*C*H$_2$N), 54.1 (N*C*H$_2$*C*H$_2$N), 53.7 (N*C*H$_2$CH$_2$N), 50.7(CH$_3$(*C*H$_2$)$_{17}$N), 50.4* 50.1(NCH$_2$*C*H$_2$N), 49.8*, 31.9, 29.7, 29.7, 29.7, 29.4 (CH$_3$(*C*H$_2$)$_{17}$N), 28.6 (C(*C*H$_3$)$_3$), 28.6*, 28.0, 27.6, 27.5, 22.7 (CH$_3$(*C*H$_2$)$_{17}$N), 14.1(*C*H$_3$(CH$_2$)$_{13}$N). **IR** ν_{max}(film)/cm^{-1} 2922, 2852, 1693, 1459, 1364, 1247, 1150, 1094, 989, 860, 732. **HRMS** Found (ESI): MH$^+$ 582.5184; $C_{34}H_{68}N_3O_4$ requires 582.5204.

*Extra peaks due to the presence of rotamers.

1-Octadecyl-1,4,7-triazonane (2.21·3HCl)

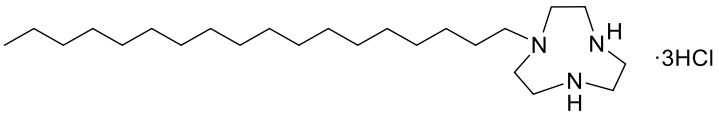

2.21·3HCl

According to **GP2,** to a solution of **2.17** (22 mg, 0.04 mmol) in MeOH (1 mL) was added 6M HCl (3 mL). The crude was evaporated under reduced pressure and the *title compound* was obtained without further purification as a white solid (17 mg, 0.04 mmol, 89%).**^{1}H NMR** (400 MHz, D_2O) δ 3.60 (s, 4H, NC*H*$_2$C*H*$_2$N), 3.34 (d, *J* = 5.9 Hz, 4H, NCH$_2$C*H*$_2$N), 3.04 (d, *J* = 5.9 Hz, 4H, NC*H*$_2$CH$_2$N), 2.77 (dd, *J* = 10.5, 2H, NC*H*$_2$CH$_2$(CH$_2$)$_{15}$CH$_3$), 1.53 (s, 2H, NCH$_2$C*H*$_2$(CH$_2$)$_{15}$CH$_3$), 1.14 (s, 30H, NCH$_2$CH$_2$(C*H*$_2$)$_{15}$CH$_3$), 0.83 (t, *J* = 6.4 Hz 3H, NCH$_2$CH$_2$(CH$_2$)$_{15}$C*H*$_3$). **^{13}C NMR** (101 MHz, D_2O) δ 55.2 (N*C*H$_2$(CH$_2$)$_{16}$CH$_3$), 47.5 (N*C*H$_2$CH$_2$N), 43.2 (NCH$_2$*C*H$_2$N), 41.9 (N*C*H$_2$*C*H$_2$N), 32.1, 30.3, 30.0, 29.6, 27.6, 24.2, 22.7 (NCH$_2$(*C*H$_2$)$_{16}$CH$_3$), 13.9 (NCH$_2$(CH$_2$)$_{16}$*C*H$_3$). **IR** ν_{max}(film)/cm^{-1} 3413, 2917, 2850, 1635, 1468, 669. **HRMS** Found (ESI): MH$^+$ 382.4141; $C_{24}H_{52}N_3$ requires 382.4156.

Hydroxypropyl *para*-nitrophenyl phosphate barium

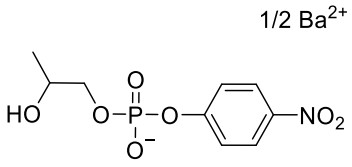

HPNPP (2.1)

Disodium *p*-nitrophenyl phosphate **2.22** (500 mg, 1.35 mmol) was dissolved in water (2.5 mL), the solution was passed through a column of IR-120 (H^+) resin, the pH was raised to 8.0 with aqueous ammonia, then 1,2-epoxypropane (5 mL, 74 mmol) was added, and the mixture stirred for 40 h at 35°C. The remaining epoxide was removed by rotatory evaporation, and the solution was passed through a column of IR-120 (H^+) resin. The solution was brought to pH no higher than 7 with a barium hydroxide aqueous solution and concentrated. Ethanol (15 mL) was added, and unreacted phosphate was filtered off. The filtrate was reduced to a small volume, then a mixture of 10% ethanol in acetone (100 mL) was added. HPNPP precipitate was collected by filtration as a white solid (95 mg, 0.27 mmol, 20%). **^{1}H NMR** (400 MHz, D_2O) δ 8.29 (d, *J* = 9.2 Hz, 2H), 7.38 (d, *J* = 9.2 Hz, 2H), 4.11 – 3.93 (m, 2H), 3.93 – 3.77 (m, 1H), 1.17 (d, *J* = 6.5 Hz, 3H). **^{13}C NMR** (101 MHz, D_2O) δ 157.4, 125.8, 120.5, 120.4, 71.0, 66.5, 17.7.

3-(*tert*-Butyl)-4-hydroxyphenyl pivalate (3.37)

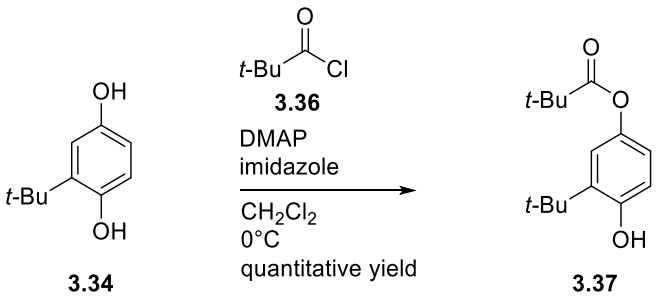

A dried round-bottomed flask was charged with 2-*tert*-butylhydroquinone **3.34** (5.03 g, 30.3 mmol), DMAP (0.51 g, 4.17 mmol), and imidazole (4.10 g, 60.2 mmol). The flask was flushed with N_2 and the positive N_2 line was replaced with a N_2 balloon. Anhydrous CH_2Cl_2 (30 mL) was added. The solution was cooled to 0 ºC in an ice bath, and pivaloyl chloride (4.4 mL, 36 mmol) was added through a syringe. The reaction was stirred at 0 ºC for 18 h; then the reaction mixture was warmed to room temperature and diluted with CH_2Cl_2 (100 mL). The solution was washed with 1 M HCl (2 × 75 mL), saturated $NaHCO_3$ (1 × 100 mL) and brine (100 mL), respectively. The mixture was dried over $MgSO_4$; the solvent was removed under reduced pressure to obtain the title compound as a white solid (7.56 g, 30.2 mmol, quantitative yield). The material was pure by ^{1}H NMR and was used in the next step without further purification. **^{1}H NMR** (400 MHz $CDCl_3$) δ 6.89 (d, *J* = 2.8 Hz, 1H), 6.74 (dd, *J* = 8.5, 2.7 Hz, 1H), 6.61 (d, *J* = 8.5 Hz, 1H), 4.97 (s, 1H), 1.39 (s, 9H), 1.35 (s, 9H). **^{13}C NMR** (101 MHz, $CDCl_3$) δ 177.7, 151.7, 144.4, 137.3, 120.0, 119.4, 116.78, 39.0, 34.6, 29.4, 27.2. Spectral data is concordant with the literature.[130]

3-(*tert*-Butyl)-5-formyl-4-hydroxyphenyl pivalate (3.38)

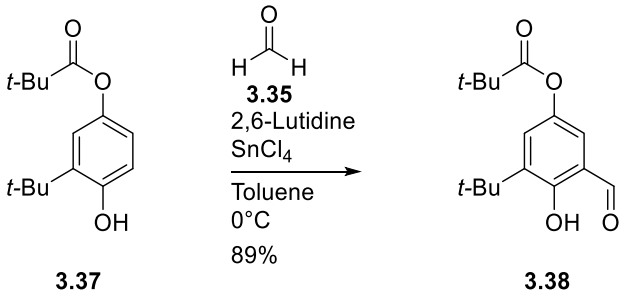

A dried round-bottomed flask under N_2 atmosphere was charged with dry toluene (235 mL) and cooled to 0 ºC in an ice bath. Hydroquinone **3.37** (7.0 g, 28 mmol) was added under N_2 positive pressure. The mixture was stirred for 10 min at 0 ºC. 2-6 Lutidine (6.5 mL, 56 mmol) and $SnCl_4$ (1.6 mL, 14 mmol) were added via syringe, respectively. The reaction mixture was stirred at 0 ºC for 1 h; then, paraformaldehyde was added (7.60 g, 252 mmol) under positive N_2 pressure. The N_2 line was then replaced for a N_2 balloon, and the reaction was stirred at 90 ºC for 18 h. The reaction was cooled to room temperature and filtered through a pad of Celite®, eluting with EtOAc (200 mL). The solvent was removed under reduced pressure and the residue was dissolved in EtOAc (100 mL). The solution was washed with H_2O (100 mL) and the organic layer was separated and washed with 0.1 M HCl (150 mL). The solution was dried over $MgSO_4$ and the solvent was removed under reduced pressure. The product obtained was then purified by recrystallization from 15% (v/v) H_2O/MeOH (8.3 mL/g); to obtain the title compound as a white powder (6.88 g, 24.7 mmol, 89%). **^{1}H NMR** (400 MHz $CDCl_3$) δ 11.69 (s, 1H), 9.82 (d, *J* = 1.1 Hz, 1H), 7.17 (d, *J* = 2.9 Hz, 1H), 7.15 (d, *J* = 2.8 Hz, 1H), 1.41 (s, 9H), 1.37 (s, 8H). **^{13}C NMR** (101 MHz, $CDCl_3$) δ 196.4, 177.4, 158.8, 142.8, 140.1, 127.9, 123.1, 120.0, 39.1, 35.0, 29.0, 27.2. Spectral data is concordant with the literature.[130]

3-(*tert*-Butyl)-2,5-dihydroxybenzaldehyde (3.30)

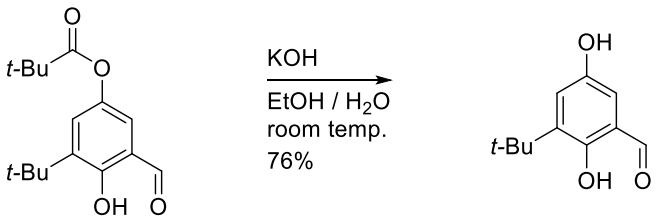

3.38 **3.30**

A round-bottomed flask was charged with KOH (12.2 g, 217 mmol) and a 50% (v/v) EtOH/H_2O mixture (50 mL). This solution was deoxygenated by bubbling N_2 for 1.5 h at room temperature. A second round-bottomed flask was charged with aldehyde **3.38** (6.0 g, 22 mmol). The KOH solution was added to the flask containing **3.38** via cannula under positive N_2 pressure, and then stirred for 5 h at room temperature under constant N_2 flow. After 5 h, the reaction mixture was added to a 1 M HCl (aq.) solution (200 mL) via cannula under positive N_2 flow. The mixture was stirred and a yellow solid precipitated. This solid was collected by vacuum filtration through a Büchner funnel, rinsing the product remaining with 10% (v/v) EtOH/H_2O solution (2 × 50 mL). The cake was then washed with 2% $NaHCO_3$ (2 × 50 mL) and 10% (v/v) EtOH/H_2O (2 × mL) respectively. The solid was dissolved in 100 mL Et_2O, and the residual water was separated. The organic layer was washed with brine (125 mL) and dried over $MgSO_4$. The solvent was removed under reduced pressure to obtain the title compound as a yellow solid (3.19 g, 16.4 mmol, 76%). The material was used in the next step without further purification. **^{1}H NMR** (400 MHz $CDCl_3$) δ 11.38 (s, 1H), 9.79 (s, 1H), 7.10 (dd, *J* = 3.1, 0.6 Hz, 1H), 6.83 (d, *J* = 3.1 Hz, 1H), 1.41 (s, 9H). **^{13}C NMR** (101 MHz, $CDCl_3$) δ 196.5, 155.7, 147.7, 140.1, 123.4, 120.1, 115.4, 35.0, 29.1.

Spectral data is concordant with the literature.[130]

3-(*tert*-Butyl)-5-formyl-4-hydroxyphenyl octanoate (3.26)

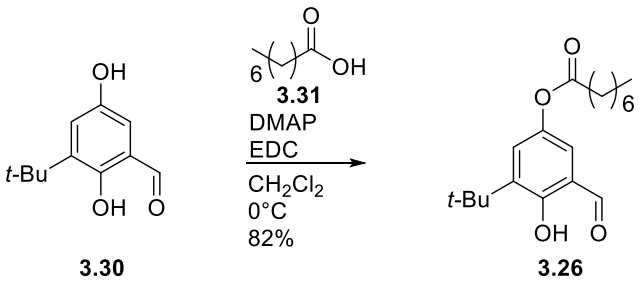

A round-bottomed flask was charged with octanoic acid **3.31** (740 mg, 5.15 mmol), **3.30** (1.0 g, 5.1 mmol), DMAP (130 mg, 1.03 mmol) and EDC (1.18 g, 6.18 mmol). The flask was flushed with N_2 for 1 h, then the positive N_2 line was replaced with a N_2 balloon and cooled to 0 ºC utilizing an ice bath. DMF (0.5 mL) and CH_2Cl_2 (5 mL) were added, and the reaction mixture was stirred at 0 ºC for 5 min. After that time, the reaction was allowed to warm up to room temperature and was stirred for 3 hours. The reaction was then diluted with Et_2O (100 mL) and 0.1 M HCl (50 mL), and the organic layer was separated. The organic layer was washed with 2% K_2CO_3 (2 × 25 mL) and brine (50 mL), respectively. The solution was dried over $MgSO_4$, and the solvent was reduced to 2 – 3 mL. MeOH (25 mL) was added to this solution and the solvent was removed completely under reduced pressure to obtain a yellow solid. MeOH (50 mL) was then added to the solution and stirred vigorously. H_2O (75 mL) was added dropwise via addition funnel while stirring. Once all the H_2O was added, the flask was placed in an ice bath and stirred at 0 ºC for 30 min. The suspension was vacuum filtered through a medium porosity fritted funnel, rinsing the flask with 40% (v/v) H_2O/EtOH (25 mL). The product was transferred to a separatory funnel and dissolved with Et_2O (100 mL). After separating the aqueous layer, the organic layer was washed with brine (100 mL) and then dried over $MgSO_4$. The solvent was removed under reduced pressure to obtain the *title compound* (1.29 g, 4.20 mmol, 82%) as a yellow solid with minimum baseline impurities by ^{1}H NMR. **^{1}H NMR** (400 MHz $CDCl_3$) δ 11.69 (d, *J* = 0.6 Hz, 1H), 9.82 (s, 1H), 7.20 (dd, *J* = 2.8, 0.6 Hz, 1H), 7.17 (d, *J* = 2.9 Hz, 1H), 2.56 (t, *J* = 7.5 Hz, 2H), 1.81 – 1.71 (m, 2H), 1.41 (d, *J* = 2.4 Hz, 9H), 1.35 – 1.28 (m, 8H), 0.94 – 0.85 (m, 3H). **^{13}C NMR** (101 MHz, $CDCl_3$) δ196.4, 172.6, 158.9, 142.5, 140.1, 128.1, 123.2, 120.0, 35.0, 34.3, 31.7, 29.1, 29.0, 28.9, 24.9, 22.6, 14.1. **IR** ν_{max}(film)/cm^{-1} 2956, 2925, 2856, 1758, 1653, 1432, 1314, 1220, 1202, 1144, 1101. **HRMS** Found (ESI): MNa^+ 343.1860, $C_{19}H_{28}NaO_4$ requires 343.1885.

3-(*tert*-Butyl)-5-formyl-4-hydroxyphenyl dodecanoate (3.27)

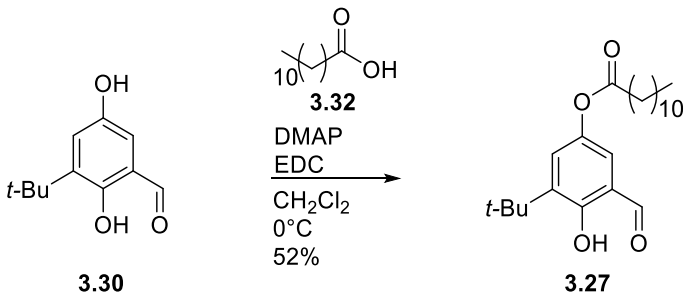

A round-bottomed flask was charged with dodecanoic acid **3.32** (757 mg, 3.80 mmol), **3.30** (734 mg, 3.80 mmol), DMAP (93 mg, 0.76 mmol) and EDC (646 mg, 4.16 mmol). The flask was flushed with N_2 for 1 h, then the positive N_2 line was replaced with a N_2 balloon and cooled to 0 ºC utilizing an ice bath. DMF (0.8 mL) and CH_2Cl_2 (4 mL) were added, and the reaction mixture was stirred at 0 ºC for 5 min. After that time, the reaction was allowed to warm up to room temperature and was stirred for 3 hours. The reaction was then diluted with Et_2O (100 mL) and 0.1 M HCl (50 mL), and the organic layer was separated. The organic layer was washed with 2% K_2CO_3 (2 × 25 mL) and brine (50 mL), respectively. The solution was dried over $MgSO_4$, and the solvent was reduced to 2 – 3 mL. MeOH (25 mL) was added to this solution and the solvent was removed completely under reduced pressure to obtain a yellow solid. MeOH (50 mL) was then added to the solution and stirred vigorously. H_2O (75 mL) was added dropwise via addition funnel while stirring. Once all the H_2O was added, the flask was placed in an ice bath and stirred at 0 ºC for 30 min. The suspension was vacuum filtered through a medium porosity fritted funnel, rinsing the flask with 40% (v/v) H_2O/EtOH (25 mL). The product was transferred to a separatory funnel and dissolved with Et_2O (100 mL). After separating the aqueous layer, the organic layer was washed with brine (100 mL) and then dried over $MgSO_4$. The solvent was removed under reduced pressure to obtain the *title compound* (737 mg, 1.96 mmol, 52%) as a yellow solid with minimum baseline impurities by ^{1}H NMR. **^{1}H NMR** (400 MHz $CDCl_3$) δ 11.69 (s, 1H), 9.82 (s, 1H), 7.20 (d, *J* = 2.8 Hz, 1H), 7.17 (d, *J* = 2.8 Hz, 1H), 2.56 (t, *J* = 7.5 Hz, 2H), 1.76 (pent., *J* = 7.4 Hz, 2H), 1.41 (s, 9H), 1.29 (d, *J* = 14.1 Hz, 16H), 0.88 (t, *J* = 6.7 Hz, 3H). **^{13}C NMR** (101 MHz, $CDCl_3$) δ 196.4, 172.6, 158.9, 142.5, 140.1, 128.1, 123.2, 120.0, 35.0, 34.3, 31.9, 29.6, 29.5, 29.3, 29.3, 29.1, 29.1, 29.0, 24.9, 22.7, 14.1. **IR** ν_{max}(film)/cm^{-1} 2923, 2853, 1758, 1654, 1433, 1314, 1220, 1144, 1106. **HRMS** Found (ESI): MNa^+ 399.2504, $C_{23}H_{36}NaO_4$ requires 399.5268.

3-(*tert*-Butyl)-5-formyl-4-hydroxyphenyl stearate (3.28)

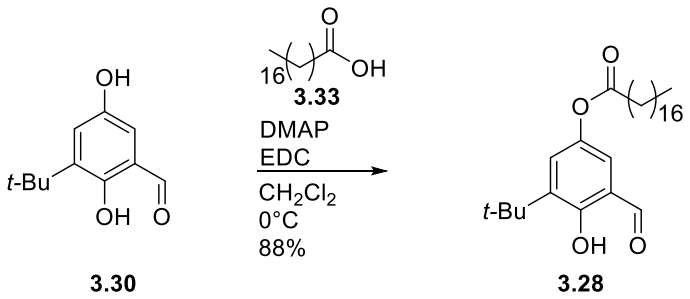

A round-bottomed flask was charged with stearic acid **3.33** (1.5 g, 5.1 mmol), **3.30** (1.0 g, 5.1 mmol), DMAP (0.13 g, 1.03 mmol) and EDC (1.18 g, 7.60 mmol). The flask was flushed with N_2 for 1 h, then the positive N_2 line was replaced with a N_2 balloon and cooled to 0 ºC utilizing an ice bath. DMF (0.5 mL) and CH_2Cl_2 (5 mL) were added, and the reaction mixture was stirred at 0 ºC for 5 min. After that time, the reaction was allowed to warm up to room temperature and was stirred for 3 hours. The reaction was then diluted with Et_2O (150 mL) and 0.1 M HCl (75 mL), and the organic layer was separated. The organic layer was washed with 2% K_2CO_3 (2 x 50 mL) and brine (100 mL), respectively. The solution was dried over $MgSO_4$, and the solvent was reduced to 2–3 mL. MeOH (50 mL) was added to this solution and the solvent was removed completely under reduced pressure to obtain a yellow solid. MeOH (100 mL) was then added to the solution and stirred vigorously. H_2O (150 mL) was added dropwise via addition funnel while stirring. Once all the H_2O was added, the flask was placed in an ice bath and stirred at 0 ºC for 30 min. The suspension was vacuum filtered through a medium porosity fritted funnel, rinsing the flask with 40% (v/v) H_2O/EtOH (50 mL). The product was transferred to a separatory funnel and dissolved with Et_2O (150 mL). After separating the aqueous layer, the organic layer was washed with brine (100 mL) and then dried over $MgSO_4$. The solvent was removed under reduced pressure to obtain the *title compound* (2.12 g, 4.60 mmol, 88%) as a yellow solid with minimum baseline impurities by ^{1}H NMR. **^{1}H NMR** (400 MHz $CDCl_3$) δ 11.70 (s, 1H), 9.82 (s, 1H), 7.20 (d, *J* = 2.8 Hz, 1H), 7.17 (d, *J* = 2.8 Hz, 1H), 2.56 (t, *J* = 7.5 Hz, 2H), 1.76 (pent, *J* = 7.5 Hz, 2H), 1.41 (s, 12H), 1.26 (s, 18H), 0.88 (t, *J* = 6.7 Hz, 3H). **^{13}C NMR** (101 MHz, $CDCl_3$) δ 196.4, 172.6, 158.9, 142.5, 140.1, 128.0, 123.2, 120.0, 35.0, 34.3, 31.9, 29.7, 29.7, 29.7, 29.6, 29.5, 29.4, 29.3, 29.1, 29.0, 24.9, 22.7, 14.1. **IR** ν_{max}(film)/cm^{-1} 2921, 2852, 2360, 2340, 1759, 1655, 1433, 1315, 1221, 1145, 1106. **HRMS** Found (ESI): MNa^+ 483.3429, $C_{29}H_{48}NaO_4$ requires 483.3445.

((1*E*,1'*E*)-(((1*R*,2*R*)-cyclohexane-1,2-diyl)bis(azaneylylidene))bis(methaneylylidene))bis(5-(*tert*-butyl)-4-hydroxy-3,1-phenylene) octanoate (3.23)

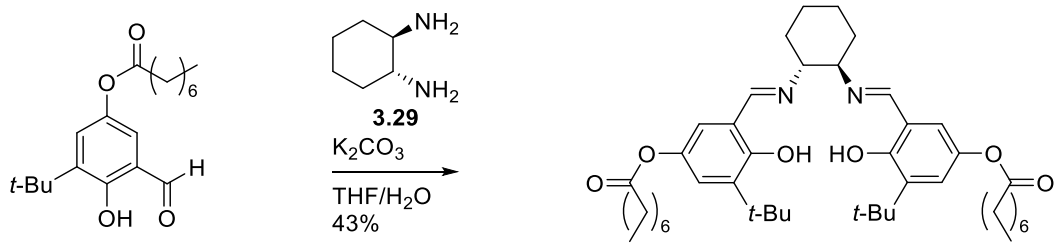

3.26 **3.23**

A round-bottomed flask was charged with (1*R*,2*R*)-(–)-1,2-diaminocyclohexane **3.29** (53 mg, 0.46 mmol) and K_2CO_3 (260 mg, 1.88 mmol). Water was added (2 mL) and the mixture was stirred. Distilled THF (8 mL) was added, and the mixture was heated to reflux. A second round-bottomed flask was charged with **3.26** (300 mg, 0.93 mmol) and dissolved in distilled THF (8 mL). This solution was added to the refluxing mixture via syringe, rinsing the solution with distilled THF. The refluxing mixture was stirred for 3 h, then allowed to cool to room temperature. The mixture was diluted with EtOAc (50 mL), the aqueous layer was separated, and the organic layer was washed with brine (50 mL). The organic layer was dried over a minimal amount of $MgSO_4$, and the solvent was removed under reduced pressure. The residue was dissolved in CH_2Cl_2 (50 mL), and the solvent was removed under reduced pressure to yield a dark, crude oil. This oil was purified by flash chromatography on silica gel (5% EtOAc/hexanes) to obtain the *title compound* as a yellow oil with minor baseline impurities (143 mg, 0.200 mmol, 43%). **^{1}H NMR** (400 MHz $CDCl_3$) δ 13.78 (s, 2H), 8.26 (s, 2H), 6.95 (d, *J* = 2.8 Hz, 2H), 6.79 (d, *J* = 2.8 Hz, 2H), 3.41 – 3.32 (m, 2H), 2.52 (t, *J* = 7.5 Hz, 4H), 2.03 – 1.86 (m, 4H), 1.82 – 1.69 (m, 6H), 1.54 – 1.46 (m, 2H), 1.41 (s, 18H), 1.36 – 1.29 (m, 10H), 0.99 – 0.85 (m, 6H). **^{13}C NMR** (101 MHz, $CDCl_3$) δ 172.7, 164.8, 158.0, 141.7, 138.6, 122.9, 121.4, 118.1, 72.3, 34.9, 34.3, 33.0, 31.7, 29.1, 29.1, 29.0, 28.9, 25.0, 24.2, 22.6, 14.1. **IR** ν_{max}(film)/cm^{-1} 2931, 2859, 2360, 2340, 1758, 1632, 1592, 1436, 1314, 1205, 1149, 1101, 668. **HRMS** Found (ESI): MH^+ 719.4994; $C_{44}H_{67}N_2O_6$ requires 719.4990.

((1*E*,1'*E*)-(((1*R*,2*R*)-cyclohexane-1,2-diyl)bis(azaneylylidene))bis(methaneylylidene))bis(5-(*tert*-butyl)-4-hydroxy-3,1-phenylene) dodecanoate (3.24)

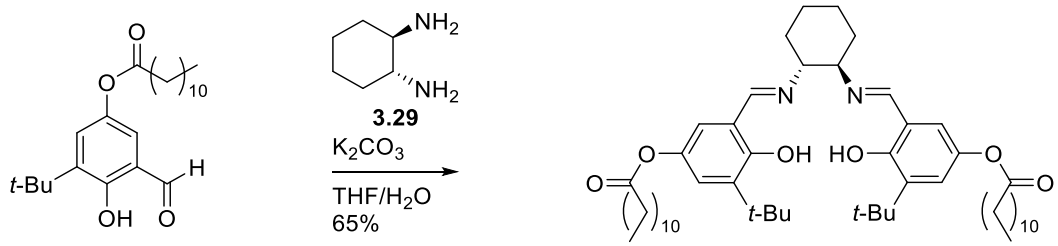

3.27 **3.24**

A round-bottomed flask was charged with (1*R*,2*R*)-(–)-1,2-diaminocyclohexane **3.29** (55 mg, 0.48 mmol) and K_2CO_3 (260 mg, 1.87 mmol). H_2O was added (2mL) and the mixture was stirred. Distilled THF (8 mL) was added, and the mixture was heated to reflux. A second round-bottomed flask was charged with **3.27** (354 mg, 1.00 mmol) and dissolved in distilled THF (8 mL). This solution was added to the refluxing mixture via syringe, rinsing the solution with distilled THF. The refluxing mixture was stirred for 3 h, then allowed to cool to room temperature. The mixture was diluted with EtOAc (50 mL), the aqueous layer was separated, and the organic layer was washed with brine (50 mL). The organic layer was dried over a minimal amount of $MgSO_4$, and the solvent was removed under reduced pressure. The residue was dissolved in CH_2Cl_2 (50 mL), and the solvent was removed under reduced pressure to yield a dark, crude oil. This oil was purified by flash chromatography on silica gel (5% EtOAc/hexanes) to obtain the *title compound* as a yellow oil with minor baseline impurities (263 mg, 0.316 mmol, 65%). **^{1}H NMR** (400 MHz $CDCl_3$) δ 13.77 (s, 2H), 8.26 (s, 2H), 6.95 (d, *J* = 2.8 Hz, 2H), 6.79 (d, *J* = 2.8 Hz, 2H), 3.42 – 3.32 (m, 2H), 2.52 (t, *J* = 7.5 Hz, 4H), 2.06 – 1.86 (m, 4H), 1.74 (pent, *J* = 7.4 Hz, 6H), 1.53 – 1.46 (m, 2H), 1.41 (s, 18H), 1.30 (d, *J* = 6.8 Hz, 30H), 0.91 (t, *J* = 6.7 Hz, 6H).**^{13}C NMR** (101 MHz, $CDCl_3$) δ 172.7, 164.8, 158.0, 141.7, 138.6, 122.9, 121.34, 118.1, 72.3, 34.9, 34.4, 33.1, 31.9, 29.6, 29.5, 29.3, 29.3, 29.1, 25.0, 24.2, 22.7, 14.1. **IR** ν_{max}(film)/cm^{-1} 2922, 2853, 2360, 2341, 1757, 1632, 1435, 1313, 1202, 1181, 1143, 1106. **HRMS** Found (ESI): MH^+ 831.6246, $C_{52}H_{83}N_2O_6$ requires 831.6224.

((1*E*,1'*E*)-(((1*R*,2*R*)-cyclohexane-1,2-diyl)bis(azaneylylidene))bis(methaneylylidene))bis(5-(*tert*-butyl)-4-hydroxy-3,1-phenylene) distearate (3.25)

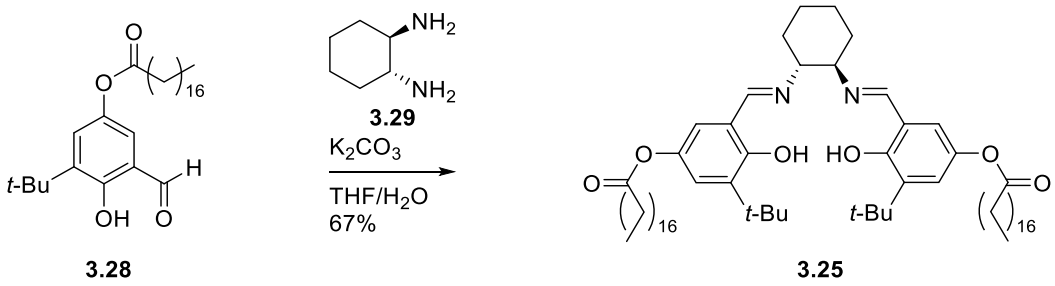

A round-bottomed flask was charged with (1*R*,2*R*)-(–)-1,2-diaminocyclohexane **3.29** (70.1 mg, 0.51 mmol) and K_2CO_3 (260 mg, 1.88 mmol). H_2O was added (2 mL) and the mixture was stirred. Distilled THF (8 mL) was added, and the mixture was heated to reflux. A second round-bottomed flask was charged with aldehyde **3.28** (467 g, 1.01 mmol) and dissolved in distilled THF (8 mL). This solution was added to the refluxing mixture via syringe, rinsing the solution with distilled THF. The refluxing mixture was stirred for 3 h, then allowed to cool to room temperature. The mixture was diluted with EtOAc (100 mL), the aqueous layer was separated, and the organic layer was washed with brine (100 mL). The organic layer was dried over a minimal amount of $MgSO_4$, and the solvent was removed under reduced pressure. The residue was dissolved in CH_2Cl_2 (100 mL), and the solvent was removed under reduced pressure to yield a dark, crude oil. This oil was purified by flash chromatography on silica gel (5% EtOAc/hexanes) to obtain the *title compound* as a yellow oil with minor baseline impurities (680 mg, 0.68 mmol, 67%). **^{1}H NMR** (400 MHz $CDCl_3$) δ 13.73 (s, 2H), 8.24 (s, 2H), 6.92 (d, *J* = 2.8 Hz, 2H), 6.76 (d, *J* = 2.8 Hz, 2H), 3.39 – 3.28 (m, 2H), 2.49 (t, *J* = 7.6 Hz, 4H), 1.92 (dd, *J* = 27.2, 11.4 Hz, 4H), 1.71 (pent, *J* = 7.5 Hz, 4H), 1.56 – 1.44 (m, 4H), 1.38 (s, 18H), 1.26 (s, 38H), 0.87 (t, *J* = 6.7 Hz, 6H). **^{13}C NMR** (101 MHz, $CDCl_3$) δ 172.7, 164.8, 158.0, 141.7, 138.6, 122.9, 121.4, 118.1, 72.3, 34.9, 34.4, 33.1, 31.9, 29.7, 29.7, 29.6, 29.5, 29.4, 29.3, 29.1, 25.0, 24.2, 22.7, 14.1. **IR** ν_{max}(film)/cm^{-1} 2121, 2852, 2360, 2341, 1757, 1632, 1594, 1435, 1360, 1314, 1263, 1202, 1144, 1110, 907, 864, 797, 733. **HRMS** Found (ESI): MH^+ 999.8106, $C_{64}H_{107}N_2O_6$ requires 999.8124.

Bis(caprylate)-(salen)cobalt(II) (A1)

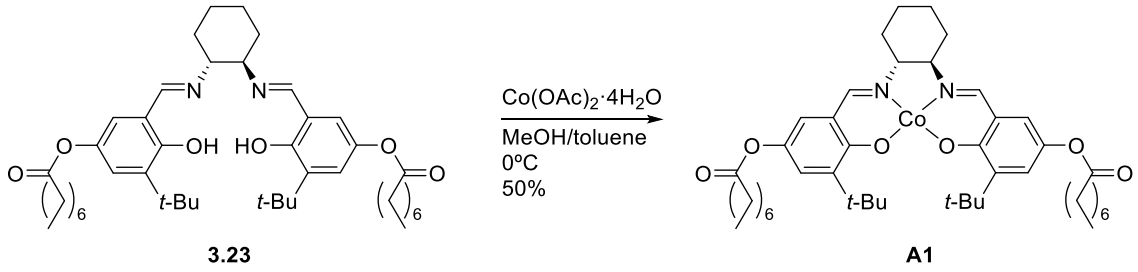

3.23 **A1**

Two round bottom flasks were charged with an excess of dry MeOH and dry toluene separately. The flasks were sealed, and the solvents deoxygenated by bubbling N_2 through them for 2 h. A round-bottomed flask was charged with salen ligand **3.23** (200 mg, 0.290 mmol) and sealed. Another round-bottomed flask was charged with $Co(OAc)_2{\cdot}4H_2O$ (75 mg, 0.30 mmol) and sealed. Each flask was flushed with N_2. To the flask containing **3.23**, deoxygenated dry toluene was added (3.5 mL) via syringe. To the flask containing $Co(OAc)_2{\cdot}4H_2O$ was added deoxygenated MeOH (3.5 mL) via syringe. N_2 was then bubbled through each solution for 1 h. The solution of $Co(OAc)_2{\cdot}4H_2O$ was added to the solution of **3.23** via cannula under positive N_2 pressure. The solution was stirred for 1 h under a constant flow of N_2. The mixture was transferred to a round-bottomed flask containing 10 mL of deoxygenated MeOH via a cannula under positive N_2 pressure. The N_2 line was replaced with a N_2 balloon, and the mixture stirred at 0 ºC for 1 h. The red precipitate was collected via vacuum filtration, washing the cake on the Büchner funnel with room temperature MeOH (15 mL). The solid was transferred to a flask and the remaining solvent was removed under reduced pressure to obtain *the title compound* as a red solid (112 mg, 0.14 mmol, 50%). **IR** ν_{max}(film)/cm^{-1} 2917, 2849, 1752, 1599, 1537, 1354, 1199, 1180, 1156, 1132, 1104. **HRMS** Found (ESI): M^+ 775.4091, requires $C_{44}H_{64}CoN_2O_6$ 775.4091.

Bis(laurate)-(salen)cobalt(II) (A2)

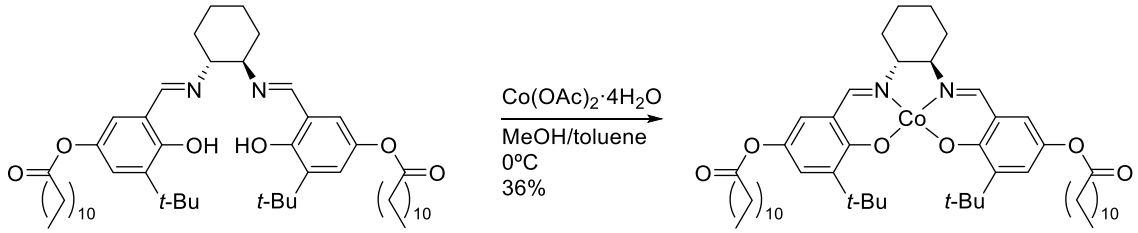

3.24 **A2**

Two round bottom flasks were charged with an excess of dry MeOH and dry toluene separately. The flasks were sealed, and the solvents deoxygenated by bubbling N_2 through them for 2 h. A round-bottomed flask was charged with salen ligand **3.24** (264 mg, 0.320 mmol) and sealed. Another round-bottomed flask was charged with $Co(OAc)_2 \bullet 4H_2O$ (80 mg, 0.42 mmol) and sealed. Each flask was flushed with N_2. To the flask containing **3.24**, deoxygenated dry toluene was added (2.4 mL) via syringe. To the flask containing $Co(OAc)_2 \cdot 4H_2O$ was added deoxygenated MeOH (2.4 mL) via syringe. N_2 was then bubbled through each solution for 1 h. The solution of $Co(OAc)_2 \bullet 4H_2O$ was added to the solution of **3.24** via cannula under positive N_2 pressure. The solution was stirred for 1 h under a constant flow of N_2. The mixture was transferred to a round-bottomed flask containing 10 mL of deoxygenated MeOH via a cannula under positive N_2 pressure. The N_2 line was replaced with a N_2 balloon, and the mixture stirred at 0 ºC for 1 h. The red precipitate was collected via vacuum filtration, washing the cake on the Büchner funnel with room temperature MeOH (15 mL). The solid was transferred to a flask and the remaining solvent was removed under reduced pressure to obtain the *title compound* as a red solid (121 mg, 0.114 mmol, 36%). **IR** ν_{max}(film)/cm^{-1} 2919, 2850, 1755, 1601, 1536, 1353, 1199, 1180, 1149. **HRMS** Found (ESI): M^+ 887.5343, $C_{52}H_{80}CoN_2O_6$ requires 887.5355.

Bis(stearate)-(salen)cobalt(II) (A3)

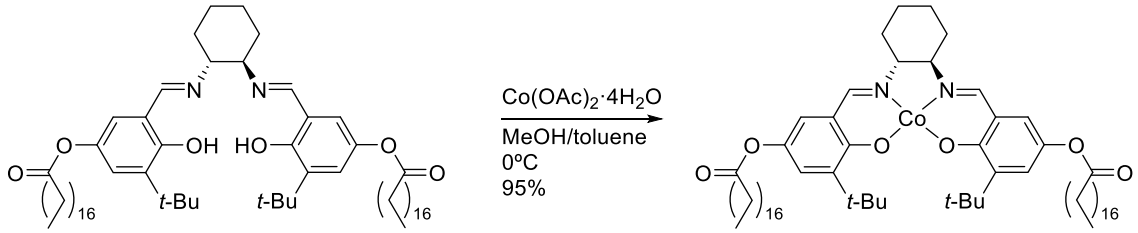

3.25 **A3**

Two round bottom flasks were charged with an excess of dry MeOH and dry toluene separately. The flasks were sealed, and the solvents deoxygenated by bubbling N_2 through them for 2 h. A round-bottomed flask was charged with salen ligand **3.25** (264 mg, 0.264 mmol) and sealed. Another round-bottomed flask was charged with $Co(OAc)_2 \cdot 4H_2O$ (132 mg, 0.53 mmol) and sealed. Each flask was flushed with N_2. To the flask containing **3.25**, deoxygenated dry toluene was added (1.6 mL) via syringe. To the flask containing $Co(OAc)_2 \cdot 4H_2O$ was added deoxygenated MeOH (3.2 mL) via syringe. N_2 was then bubbled through each solution for 1 h. The solution of $Co(OAc)_2 \bullet 4H_2O$ was added to the solution of **3.25** via cannula under positive N_2 pressure. The solution was stirred for 1 h under a constant flow of N_2. The mixture was transferred to a round-bottomed flask containing 5 mL of deoxygenated MeOH via a cannula under positive N_2 pressure. The N_2 line was replaced with a N_2 balloon, and the mixture stirred at 0 ºC for 1 h. The red precipitate was collected via vacuum filtration, washing the cake on the Büchner funnel with room temperature MeOH (10 mL). The solid was transferred to a flask and the remaining solvent was removed under reduced pressure to obtain the *title compound* as a red solid (266 mg, 0.251 mmol, 95%). **IR** ν_{max}(film)/cm^{-1} 2920, 2851, 1601, 1539, 1407, 1345, 1219, 1180, 1028, 672. **HRMS** Found (ESI): M^+ 1055.7218, $C_{64}H_{104}CoN_2O_6$ requires 1055.7221.

Bis(caprylate)-(salen)cobalt(III)OTs (3.20)

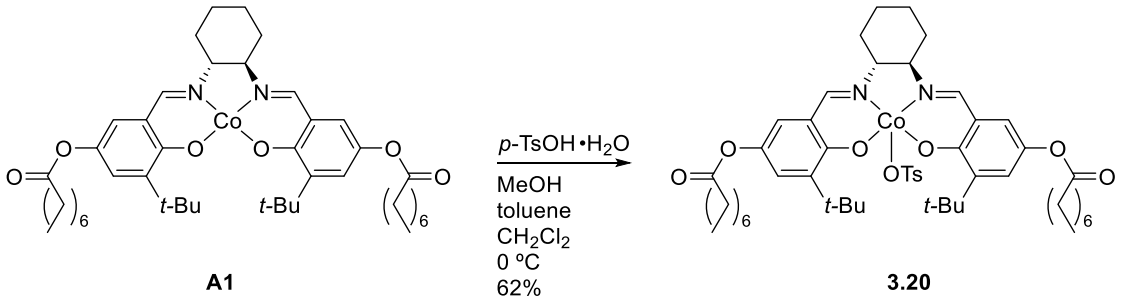

A1 **3.20**

A vial was charged with (salen)cobalt(II) **A1** (10 mg, 13 µmol), *para*-toluenesulfonic acid hydrate (2.2 mg, 13 µmol), and a stirrer bar. Toluene (100 µL), MeOH (30 µL), and CH_2Cl_2 were added to the vial. The reaction was stirred open air for 3 hours. The solvent was removed under reduced pressure; the residue was dissolved in CH_2Cl_2 and filtered through a pad of Celite® eluting with an excess of CH_2Cl_2. The solvent was removed under reduced pressure to obtain the *title compound* as a black oily solid (8 mg, 8 µmol, 62%). **IR** ν_{max}(film)/cm^{-1} 3726, 3709, 3649, 3597, 2925, 2856, 2360, 2341, 1749, 1647, 1541, 1417, 1152, 669. **MS** Found (ESI): $[M - OTs]^+$ 775.3, $C_{44}H_{64}CoN_2O_6$ requires 775.4.

Bis(laurate)-(salen)cobalt(III)OTs (3.21)

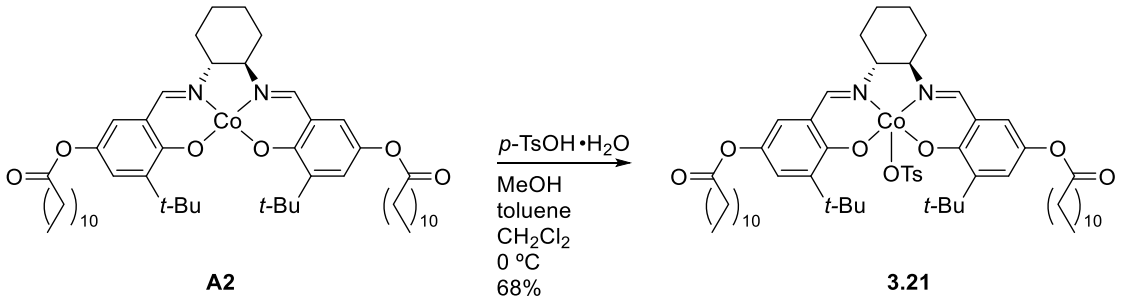

A2 **3.21**

A vial was charged with (salen)cobalt(II) **A2** (10 mg, 11 µmol), *para*-toluenesulfonic acid hydrate (2.1 mg, 11 µmol), and a stirrer bar. Toluene (100 µL), MeOH (30 µL), and CH_2Cl_2 were added to the vial. The reaction was stirred open air for 3 hours. The solvent was removed under reduced pressure; the residue was dissolved in CH_2Cl_2 and filtered through a pad of Celite® eluting with an excess of CH_2Cl_2. The solvent was removed under reduced pressure to obtain the *title compound* as a black oily solid (8 mg, 8 µmol, 68%). **IR** ν_{max}(film)/cm^{-1} 3726, 3708, 3628, 3599, 2922, 2853, 2360, 2341, 1750, 1644, 1542, 1456, 1438, 1417, 1342, 1181, 1037. **MS** Found (ESI): $[M - OTs]^+$ 887.5, $C_{52}H_{80}CoN_2O_6$ requires 887.5.

Bis(stearate)-(salen)cobalt(III)OTs (3.22)

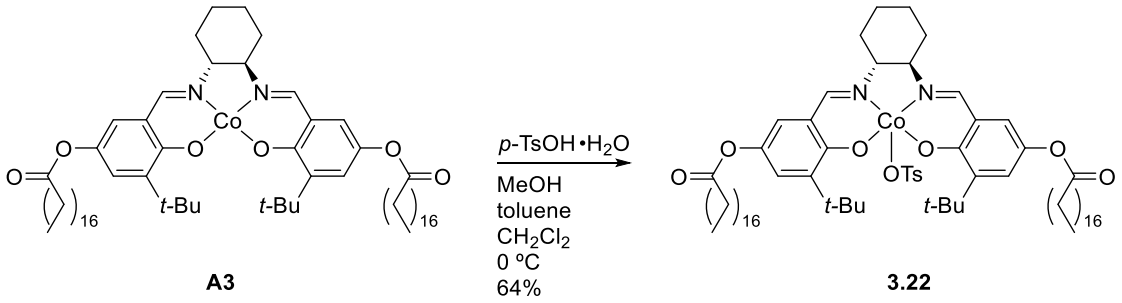

A3 **3.22**

A vial was charged with (salen)cobalt(II) **A3** (10 mg, 9.5 µmol), *para*-toluenesulfonic acid hydrate (1.6 mg, 9.5 µmol), and a stirrer bar. Toluene (100 µL), MeOH (30 µL), and CH_2Cl_2 were added to the vial. The reaction was stirred open air for 3 hours. The solvent was removed under reduced pressure; the residue was dissolved in CH_2Cl_2 and filtered through a pad of Celite® eluting with an excess of CH_2Cl_2. The solvent was removed under reduced pressure to obtain the *title compound* as a black oily solid (7.5 mg, 6.1 µmol, 64%). **IR** ν_{max}(film)/cm^{-1} 3727, 3708, 3627, 3599, 2921, 2852, 2360, 2341, 1748, 1644, 1542, 1456, 1438, 1417, 1384, 1342, 1318, 1227, 1180, 1037, 669. **HRMS** Found (ESI): $[M - OTs]^+$ 1055.7112, $C_{64}H_{104}CoN_2O_6$ requires 1055.7226.

(Salen)cobalt(III)OTs (3.11)

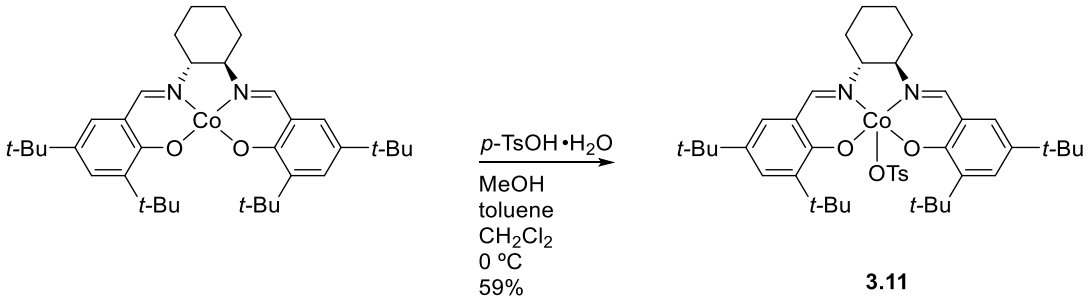

3.11

A vial was charged with commercially available (salen)cobalt(II) (10 mg, 16 µmol), *para*-toluenesulfonic acid hydrate (2.8 mg, 16 µmol) and a stirrer bar. Toluene (100 µL), MeOH (30 µL) and CH_2Cl_2 were added to the vial. The reaction was stirred open air for 3 hours. The solvent was removed under reduced pressure; the residue was dissolved in CH_2Cl_2 and filtered through a pad of Celite® eluting with an excess of CH_2Cl_2. The solvent was removed under reduced pressure to obtain the title compound as a black solid. (7.5 mg, 9.7 mmol, 59%). **IR** ν_{max}(film)/cm^{-1} 3901, 3853, 3838, 3820, 3800, 3726, 3708, 3648, 3628, 3600, 3566, 2952, 2360, 2341, 1647, 1541, 669. **HRMS** Found (ESI): $[M - OTs]^+$ 603.3292, $C_{36}H_{52}CoN_2O_2$ requires 603.3361.

Bis(stearate)-(salen)nickel complex (3.45)

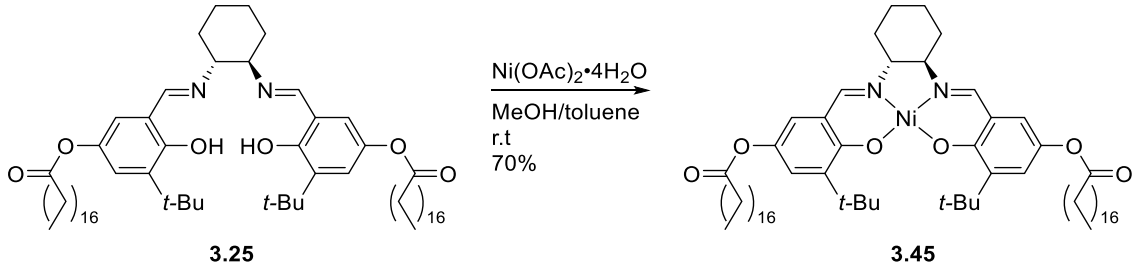

3.25 **3.45**

A round bottom flask with a stirrer bar was charged with **3.25** (100 mg, 0.100 mmol) and dissolved with toluene (300 µL). Another round bottom flask was charged with $Ni(OAc)_2•4H_2O$ (30 mg, 0.12 µmol) and dissolved with MeOH (300 µL). The $Ni(OAc)_2•4H_2O$ solution was added to the **3.25** solution and stirred for 18 hours at room temperature. A dark yellow precipitate could be observed the next day. The solvents were evaporated under reduced pressure and the product was suspended in MeOH, dissolving the remaining $Ni(OAc)_2$. The product was separated by filtration under vacuum and dried under high vacuum to yield *title compound* as a dark yellow solid (74 mg, 0.07 mmol, 70%). **^{1}H NMR** (400 MHz $CDCl_3$) δ 7.33 (s, 2H), 6.90 (d, *J* = 3.0 Hz, 2H), 6.77 (d, *J* = 3.0 Hz, 2H), 3.67 – 3.66 m, 1H), 3.54 – 3.43 (m, 1H), 3.04 – 2.93 (bm, 2H), 2.50 (t, *J* = 7.5 Hz, 4H), 2.43 – 2.35 (bm, 2H), 1.95 – 1.87 (bm, 2H), 1.73 (pent, *J* = 7.5 Hz, 4H), 1.37 (s, 18H), 1.26 (s, 58H), 0.88 (t, *J* = 6.7 Hz, 6H). **^{13}C NMR** (101 MHz, $CDCl_3$) δ 173.0, 162.3, 157.5, 142.1, 138.7, 124.8, 121.4, 119.2, 69.9, 35.7, 34.4, 31.9, 29.7, 29.7, 29.6, 29.5, 29.4, 29.3, 29.12, 28.7, 25.0, 24.4, 22.7, 14.1. **IR** ν_{max}(film)/cm^{-1} 3726, 3628, 2918, 2850, 2360, 2341, 1758, 1624, 1542, 1467, 1437, 1417, 1383, 1343, 1316, 1226, 1199, 1182, 1148, 1134. **HRMS** Found (ESI): MH^+ 1055.7208, $C_{64}H_{105}N_2NiO_6$ requires 1055.7248.

(Salen)nickel complex (3.46)

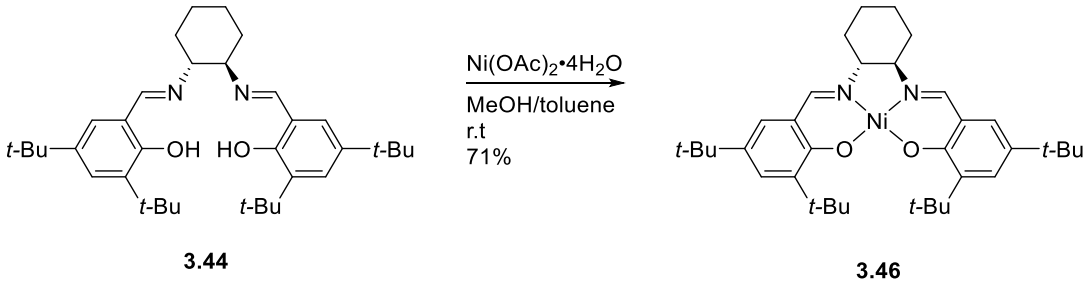

3.44 **3.46**

A round bottom flask with a stirrer bar was charged with commercially available (*R,R*)-(−)-*N,N′*-Bis(3,5-di-*tert*-butylsalicylidene)-1,2-cyclohexanediamine **3.44** (100 mg, 0.182 mmol) and dissolved with toluene (300 µL). Another round bottom flask was charged with $Ni(OAc)_2•4H_2O$ (54.6 mg, 0.22 µmol) and dissolved with MeOH (300 µL). The $Ni(OAc)_2•4H_2O$ solution was added to the (*R,R*)-(−)-*N,N′*-Bis(3,5-di-*tert*-butylsalicylidene)-1,2-cyclohexanediamine solution and stirred for 18 hours at room temperature. A yellow precipitate could be observed the next day. The solvents were evaporated under reduced pressure and the product was suspended in MeOH, dissolving the remaining $Ni(OAc)_2$. The product was separated by filtration under vacuum and dried under high vacuum to yield the title compound as a yellow powder (80 mg, 0.13 mmol, 71%). **^{1}H NMR** (400 MHz $CDCl_3$) δ 7.39 (s, 2H), 7.30 (d, *J* = 2.6 Hz, 2H), 6.88 (d, *J* = 2.6 Hz, 2H), 2.96 (*bm*, 2H), 2.44 (*bm*, 2H), 1.91 (*bm*, 2H), 1.41 (s, 18H), 1.26 (s, 18H). **^{13}C NMR** (101 MHz, $CDCl_3$) δ 162.7, 157.7, 140.2, 135.8, 129.0, 126.2, 119.4, 69.8, 35.8, 33.8, 31.3, 29.6, 28.8, 24.5. **IR** ν_{max}(film)/cm^{-1} 3726, 3704, 3628, 2947, 2360, 2341, 1612, 1530, 1434, 1324. **HRMS** Found (ESI): MH^+ 603.3439, $C_{36}H_{53}N_2NiO_2$ requires 603.3382. Spectral data is concordant with the literature.[148]

Appendix

Spectral data

di-*tert*-Butyl 7-ethyl-1,4,7-triazonane-1,4-dicarboxylate (2.13)

2.13

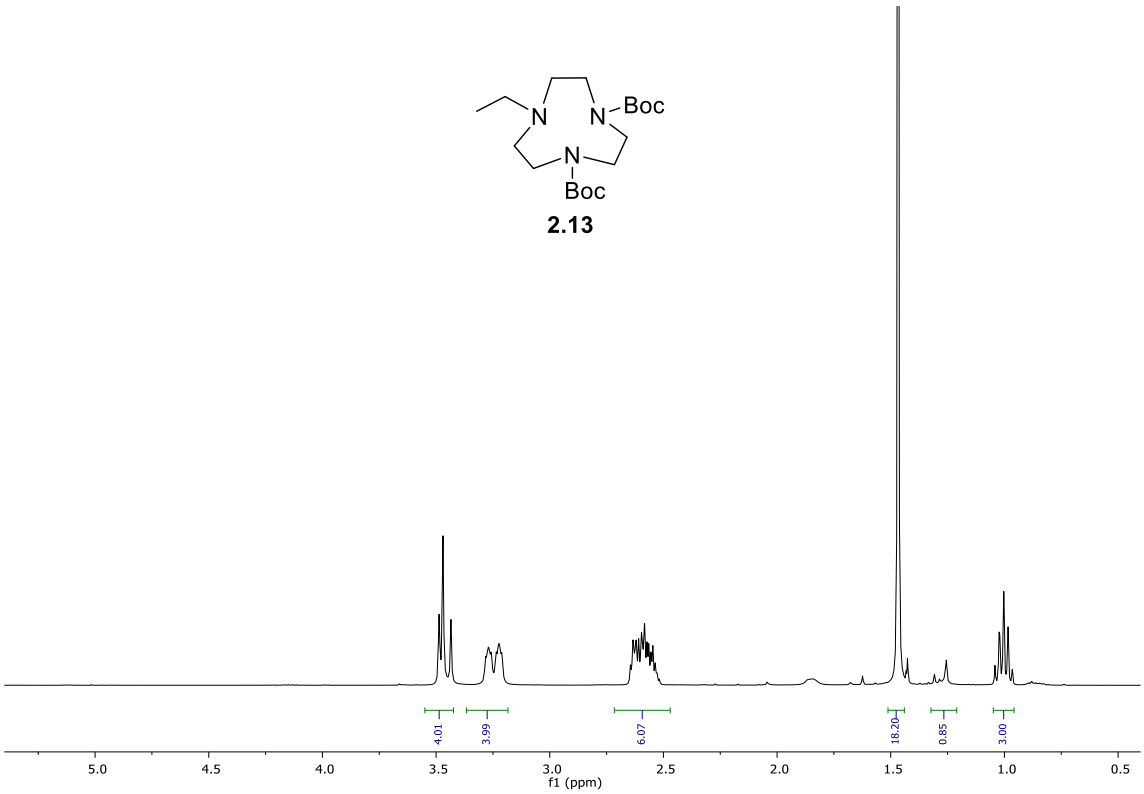

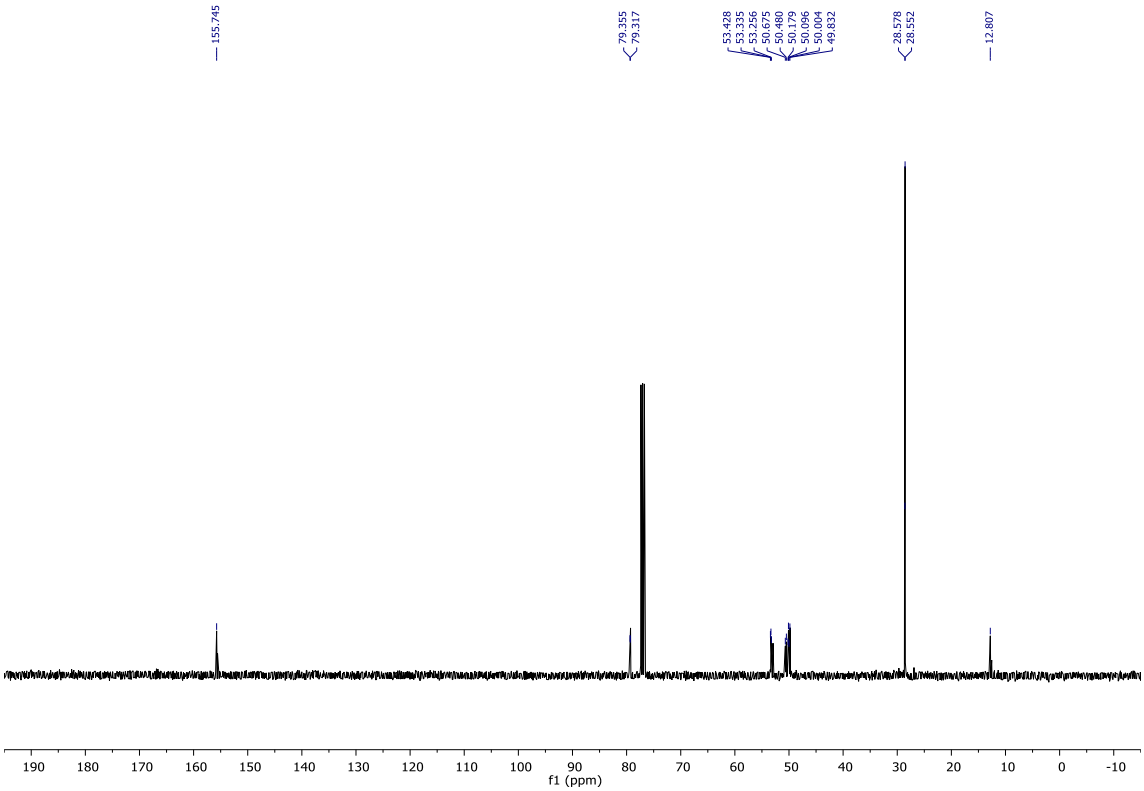

1-Ethyl-1,4,7-triazonane (2.18·3HCl)

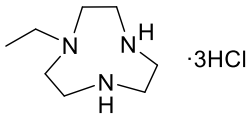

2.18·3HCl

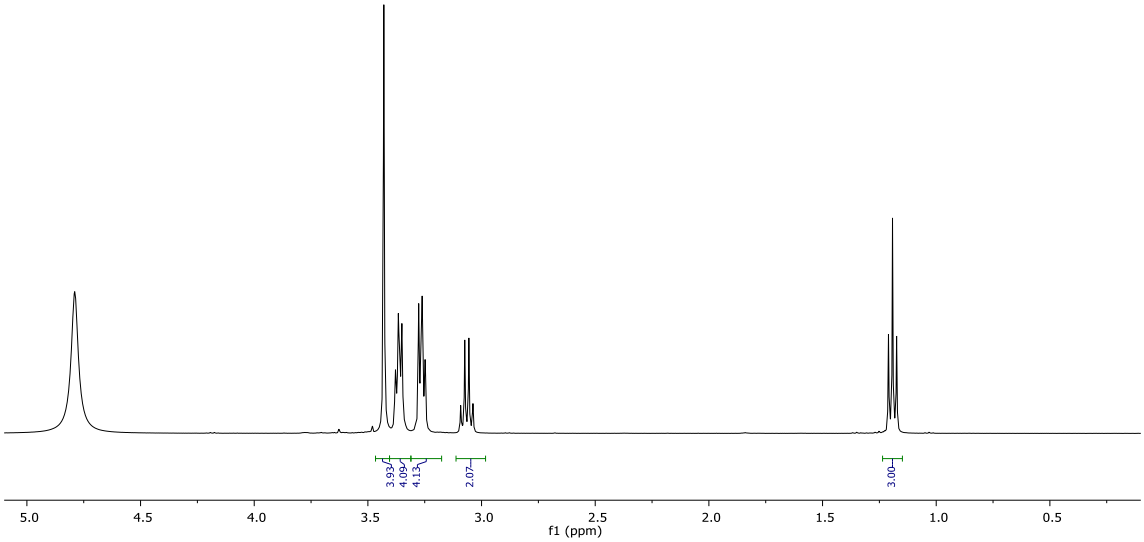

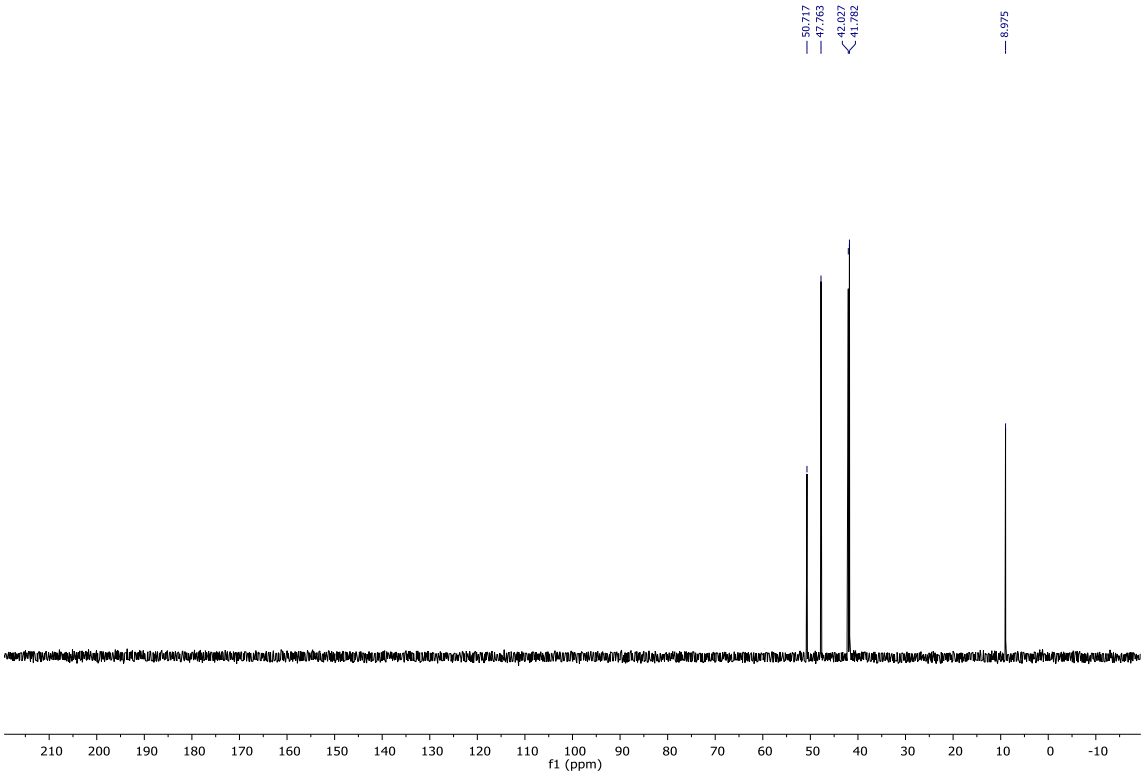

di-*tert*-Butyl 7-dodecyl-1,4,7-triazonane-1,4-dicarboxylate (2.14)

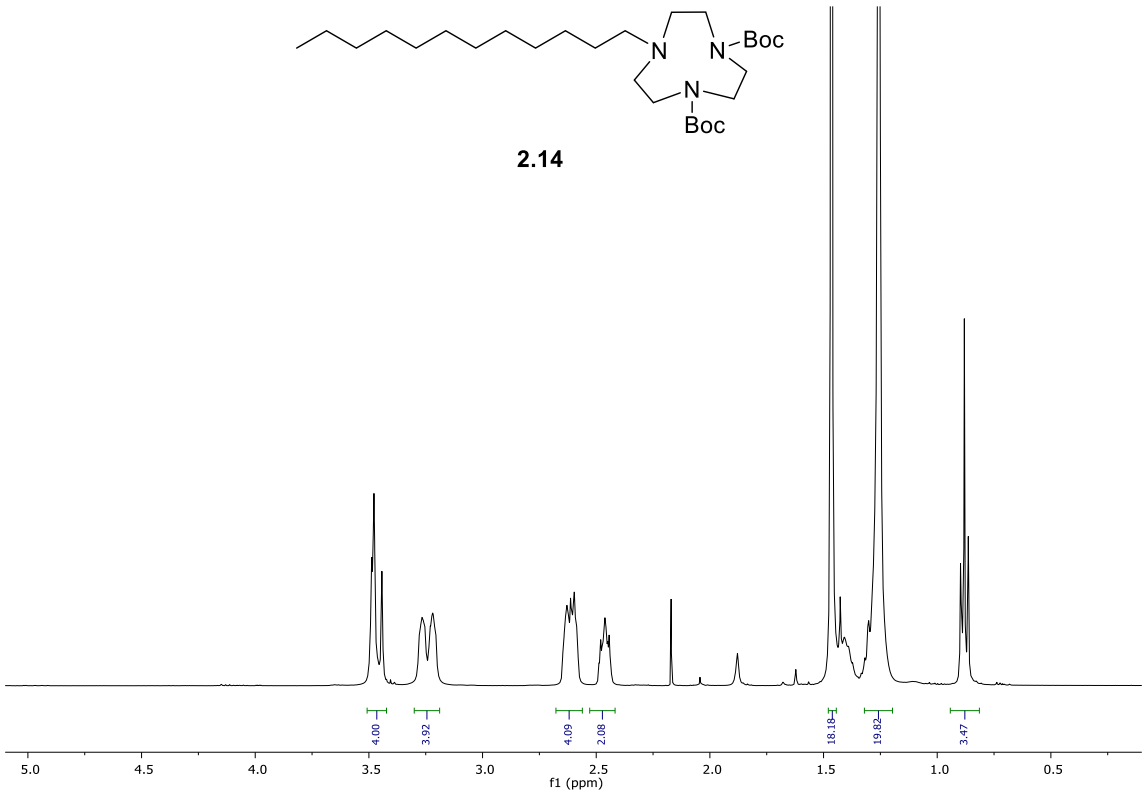

2.14

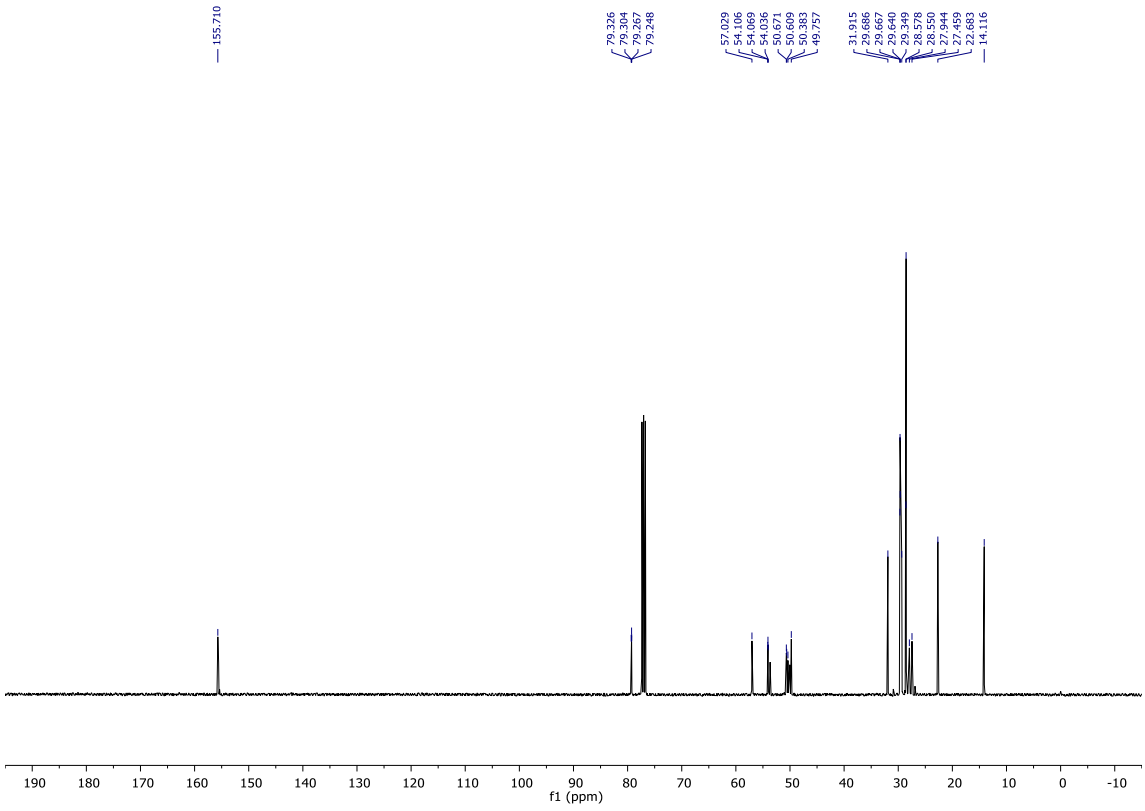

1-Dodecyl-1,4,7-triazonane (2.19·3HCl)

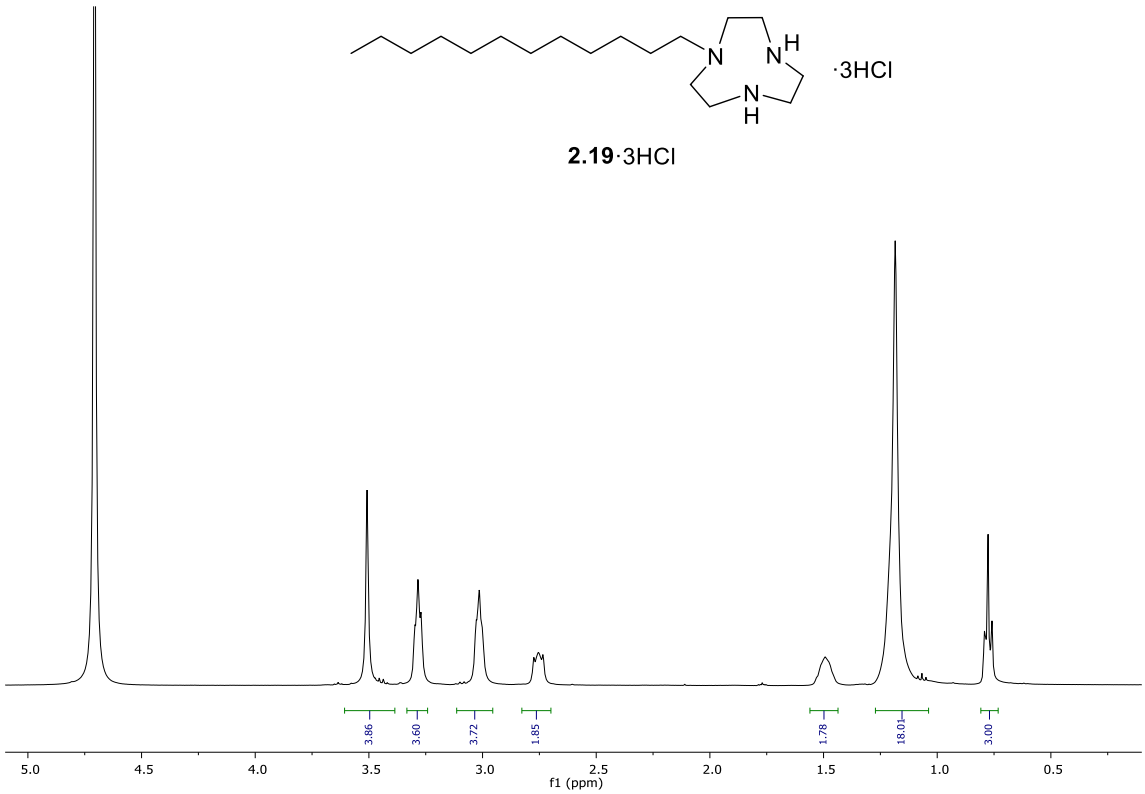

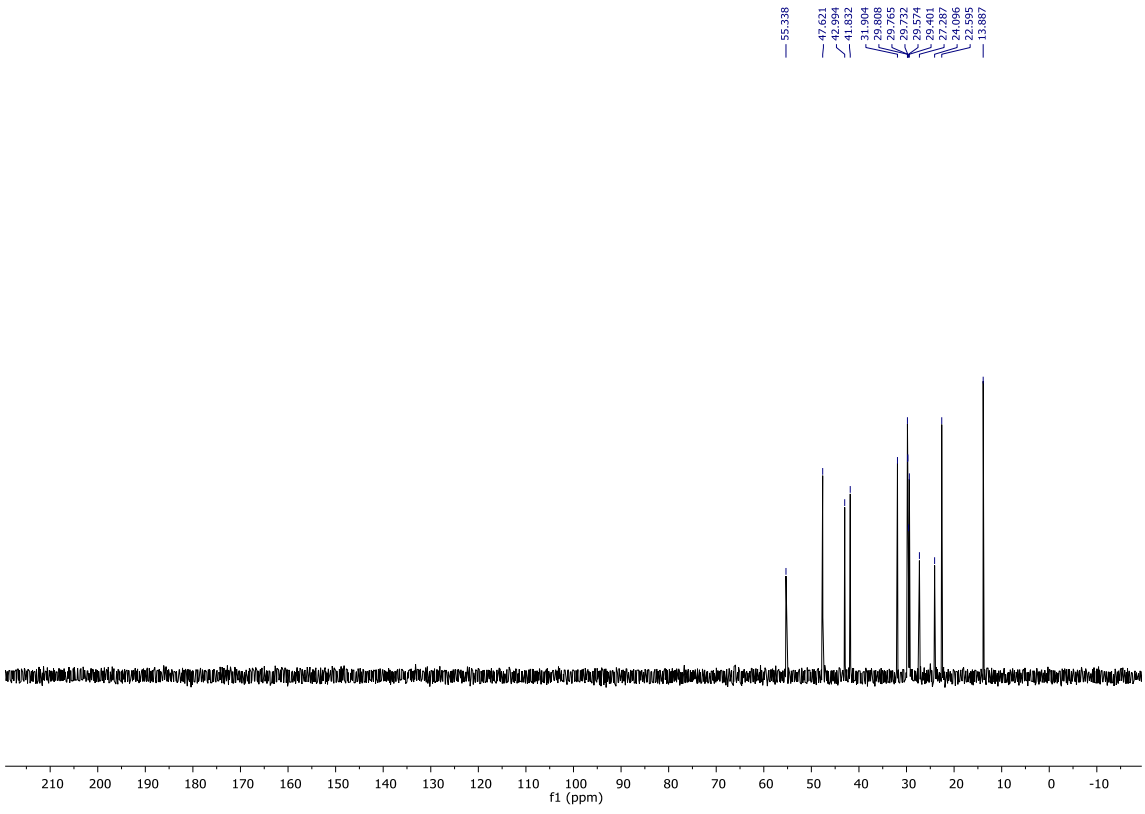

di-*tert*-Butyl 7-tetradecyl-1,4,7-triazonane-1,4-dicarboxylate (2.15)

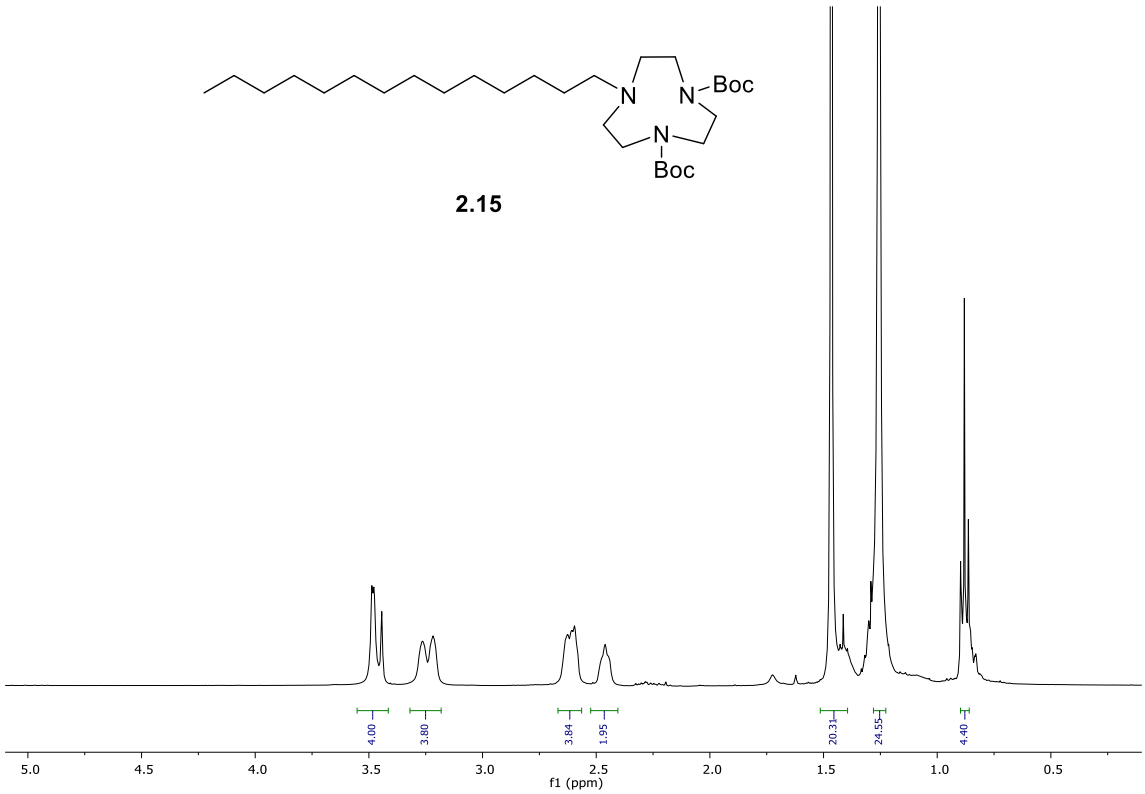

2.15

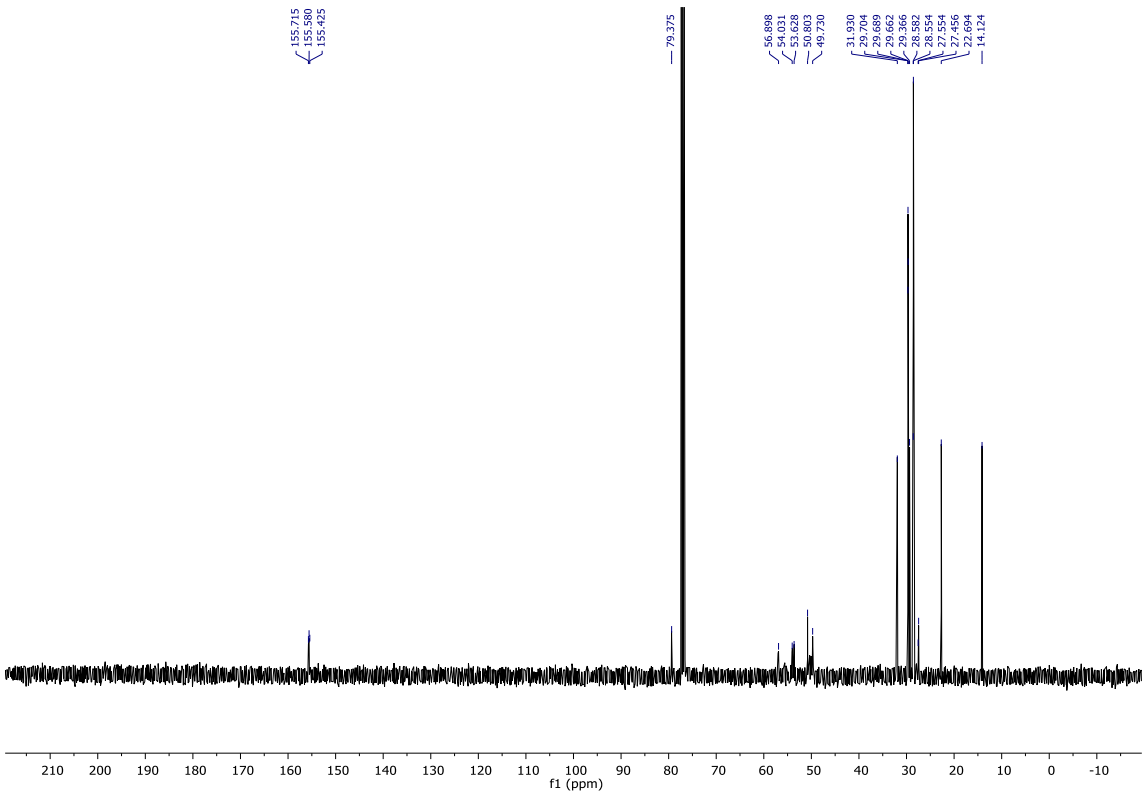

1-Tetradecyl-1,4,7-triazonane (2.20·3HCl)

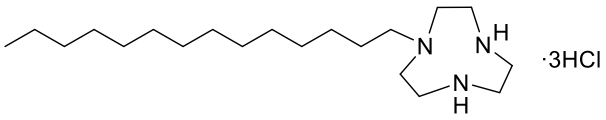

2.20·3HCl

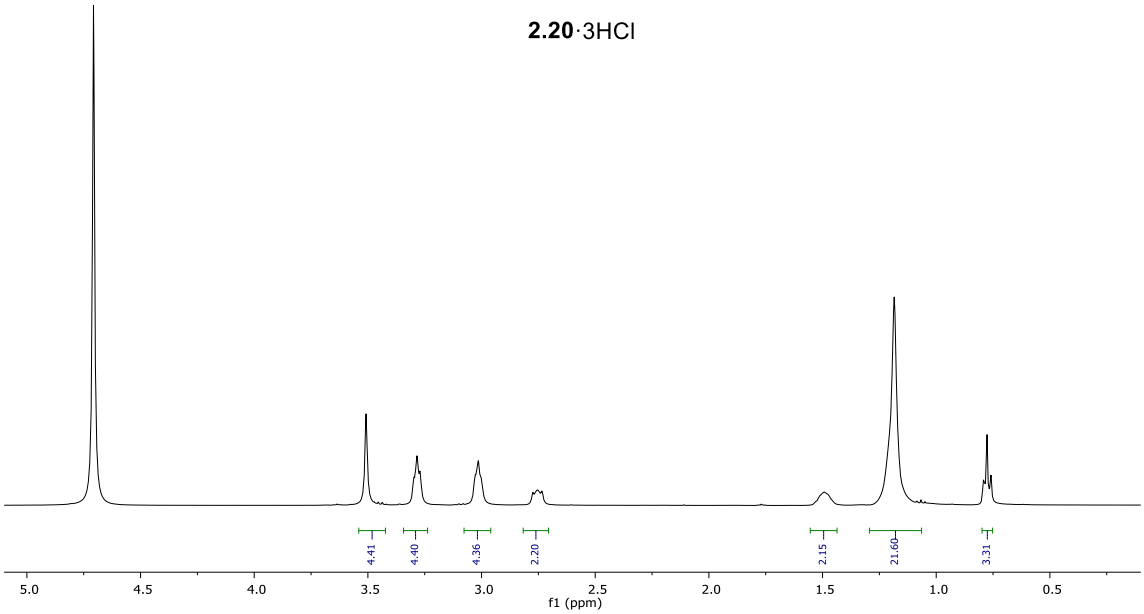

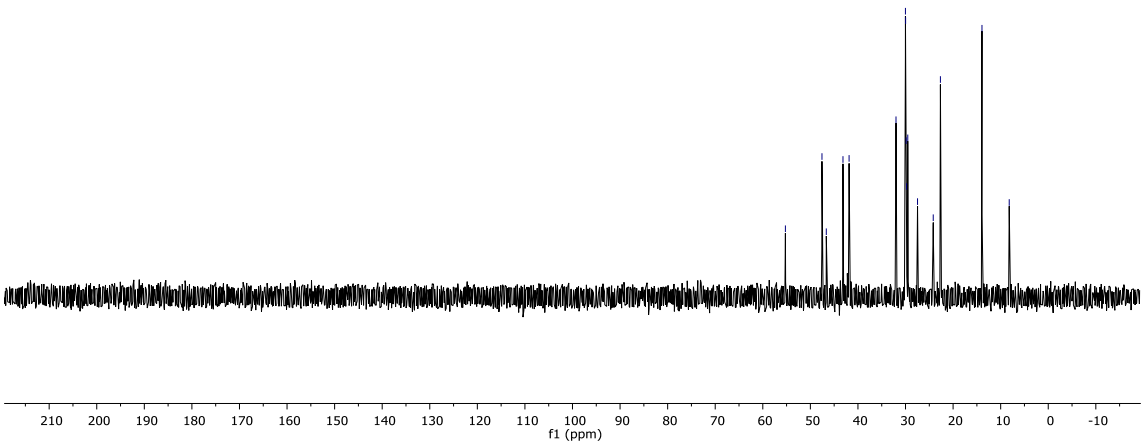

di-*tert*-Butyl 7-hexadecyl-1,4,7-triazonane-1,4-dicarboxylate (2.16)

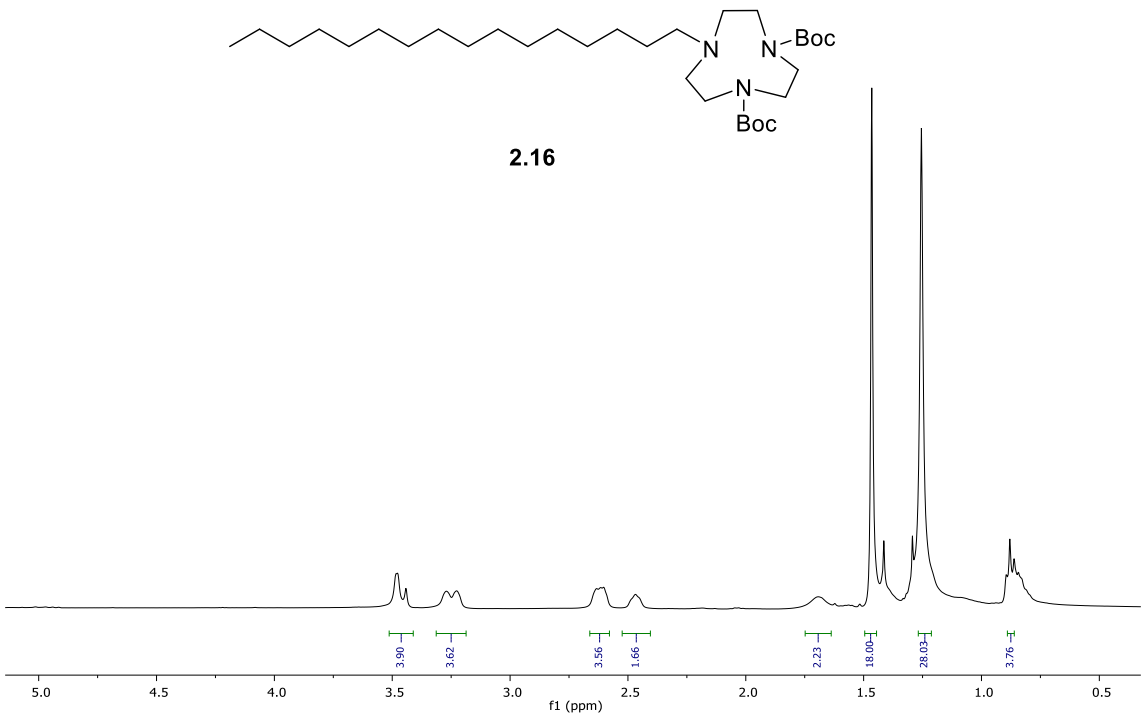

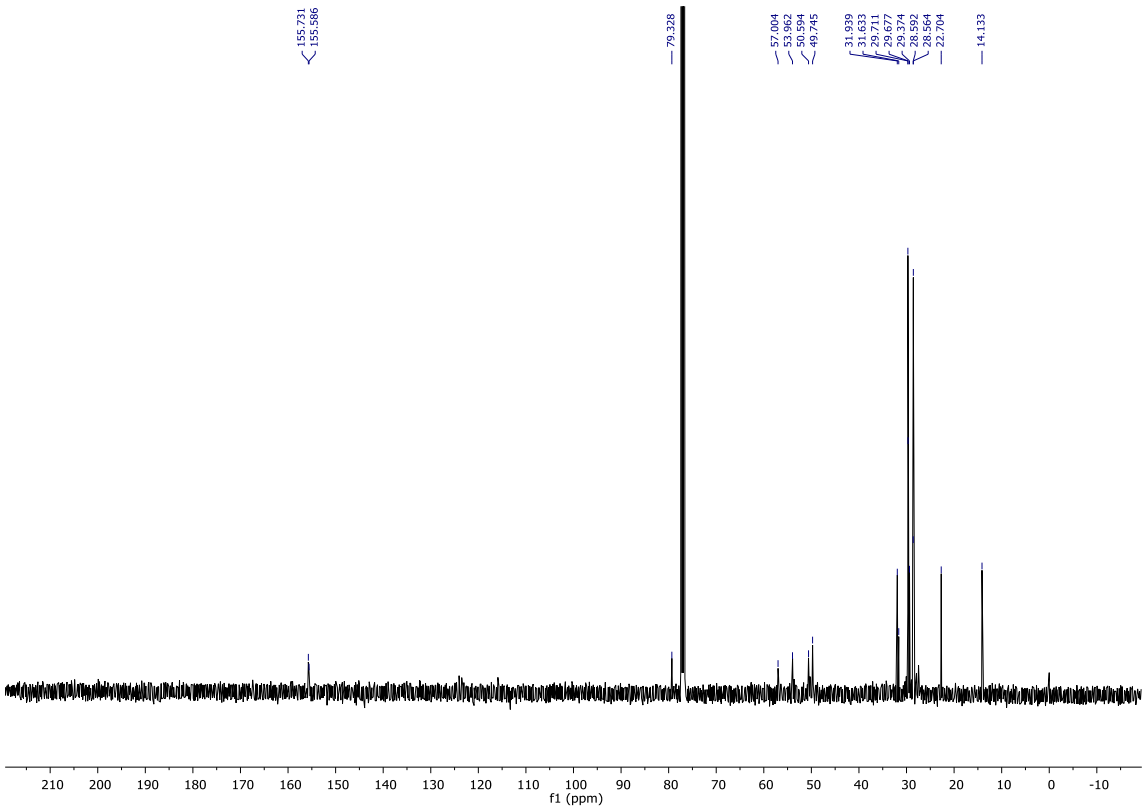

1-Hexadecyl-1,4,7-triazonane (2.7·3HCl)

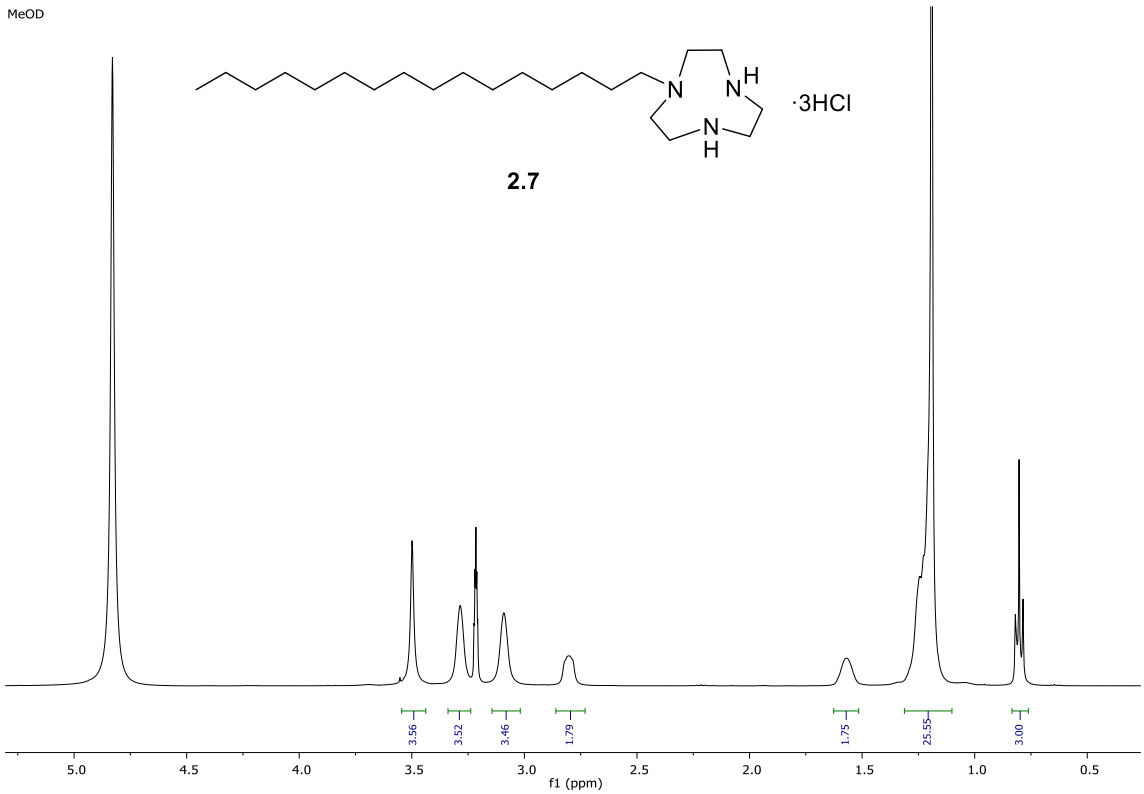

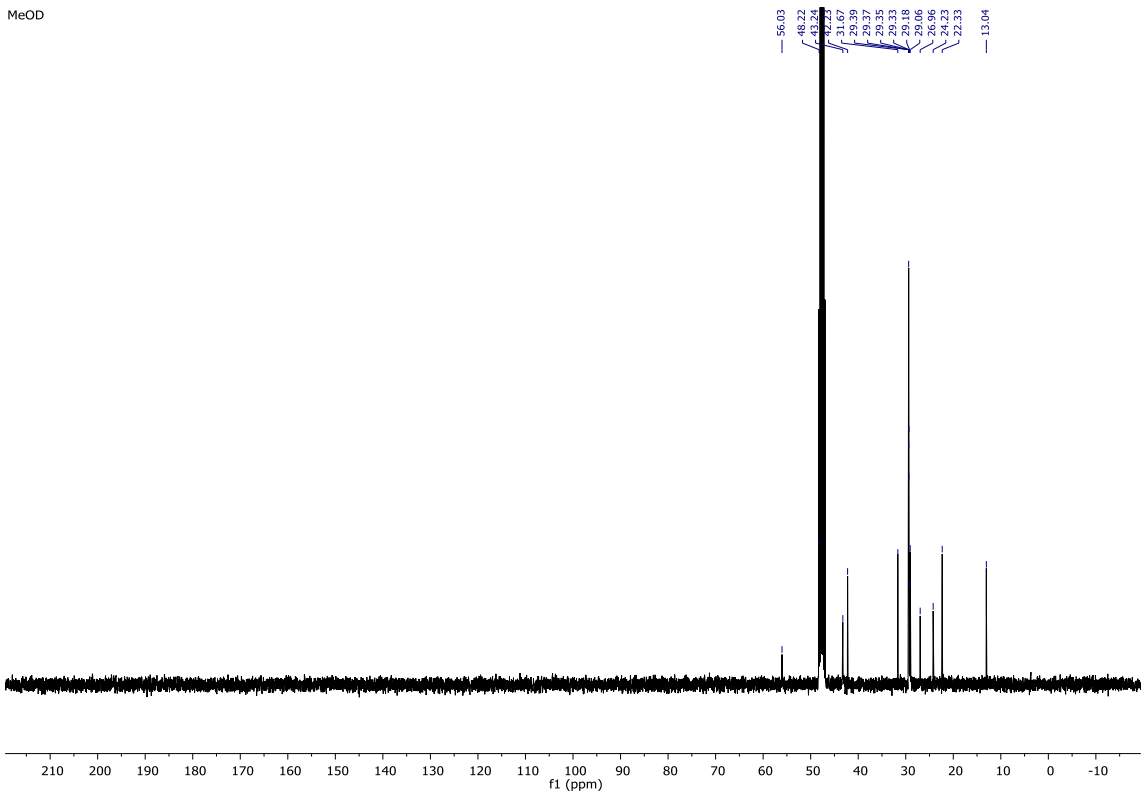

di-*tert*-Butyl 7-octadecyl-1,4,7-triazonane-1,4-dicarboxylate (2.17)

2.17

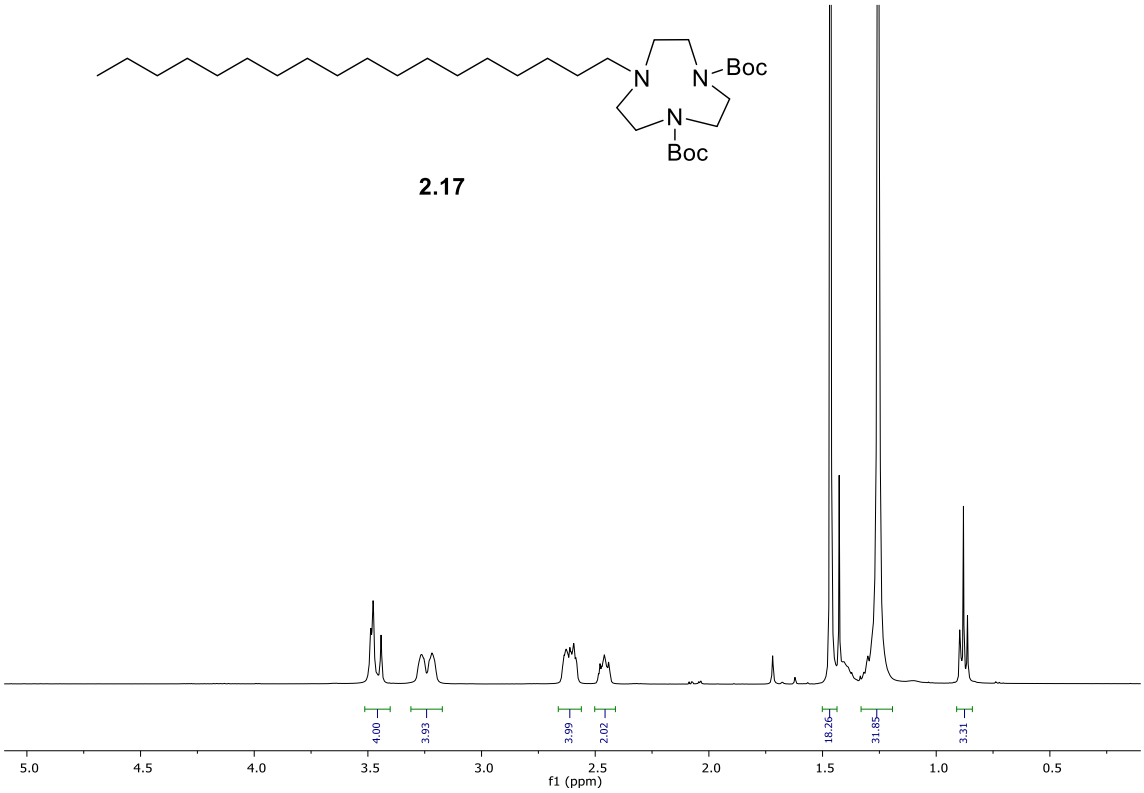

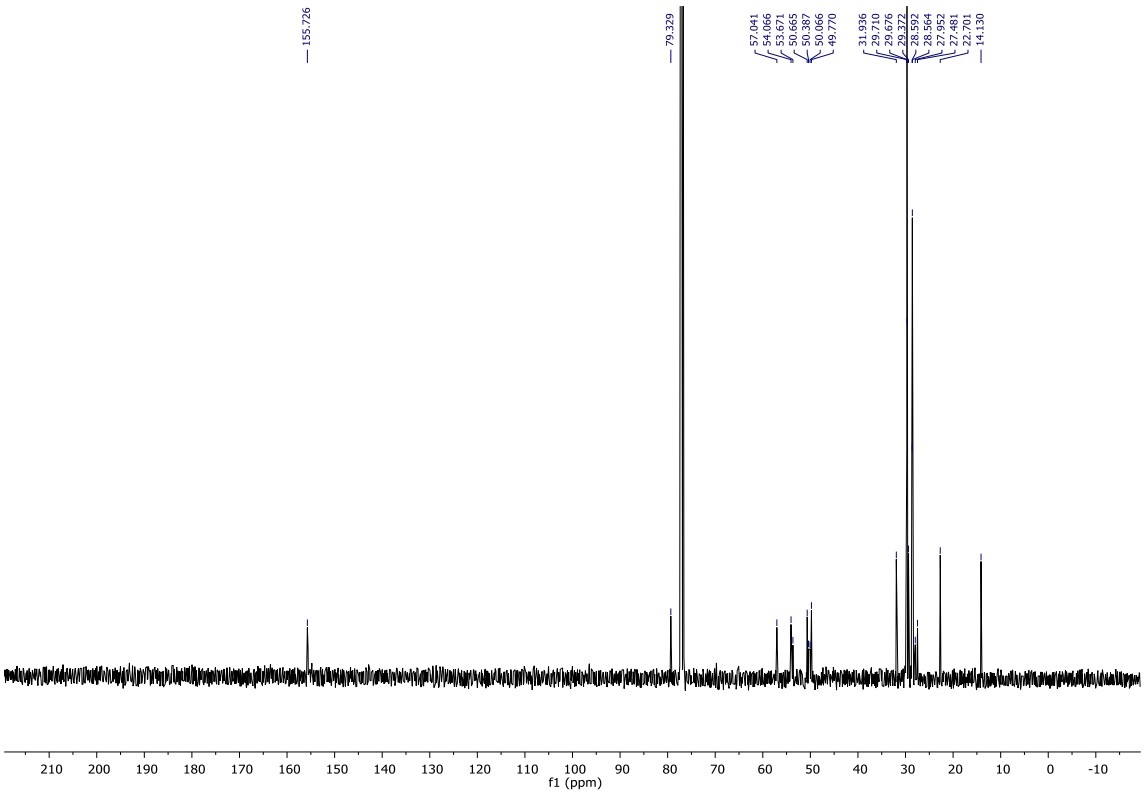

1-Octadecyl-1,4,7-triazonane (2.21·3HCl)

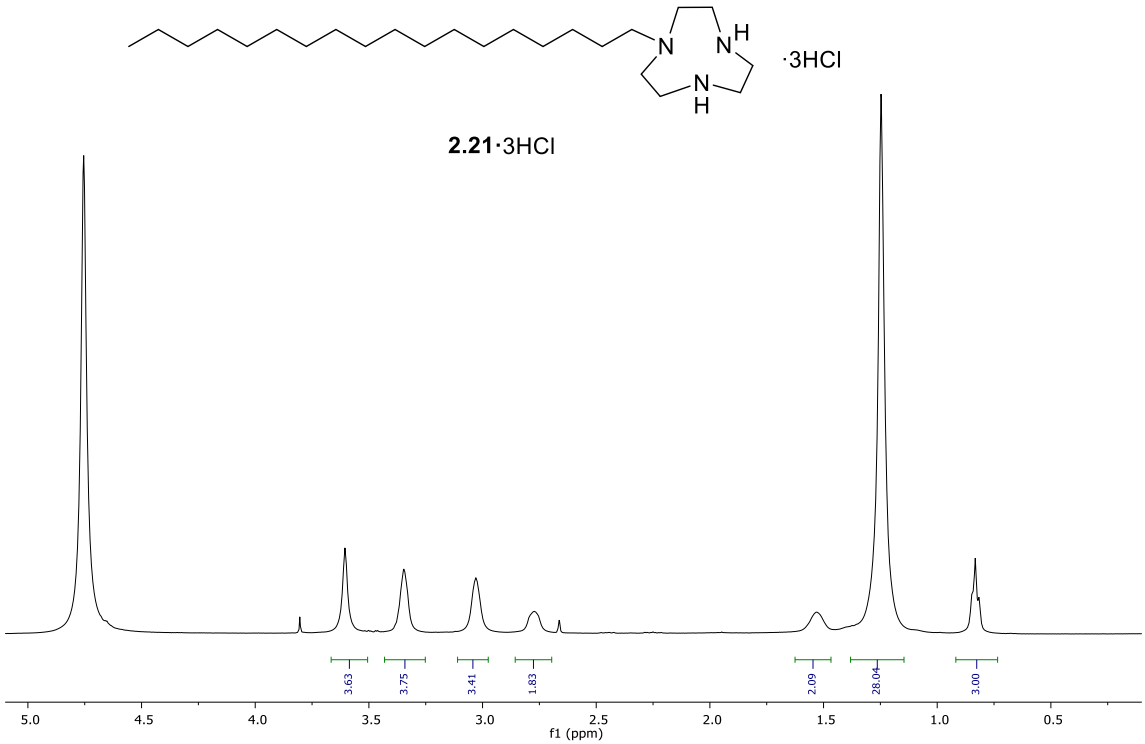

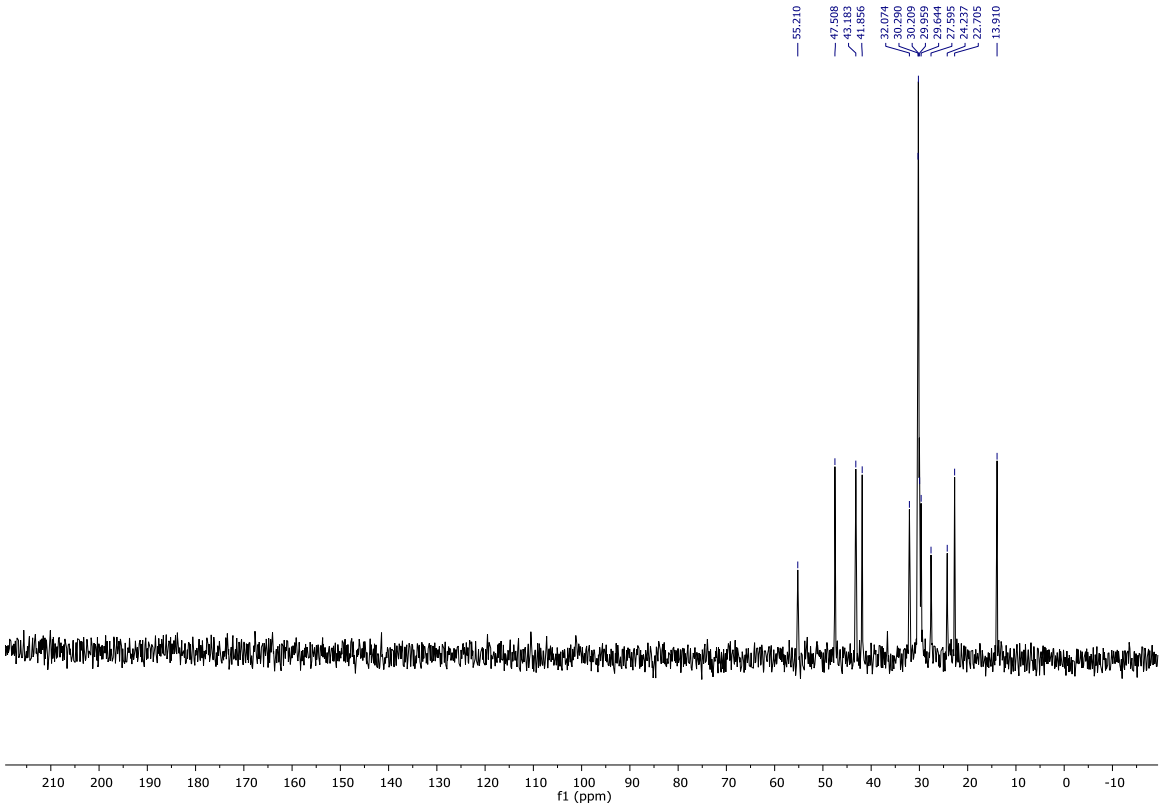

Hydroxypropyl *para*-nitrophenyl phosphate barium (HPNPP 2.1)

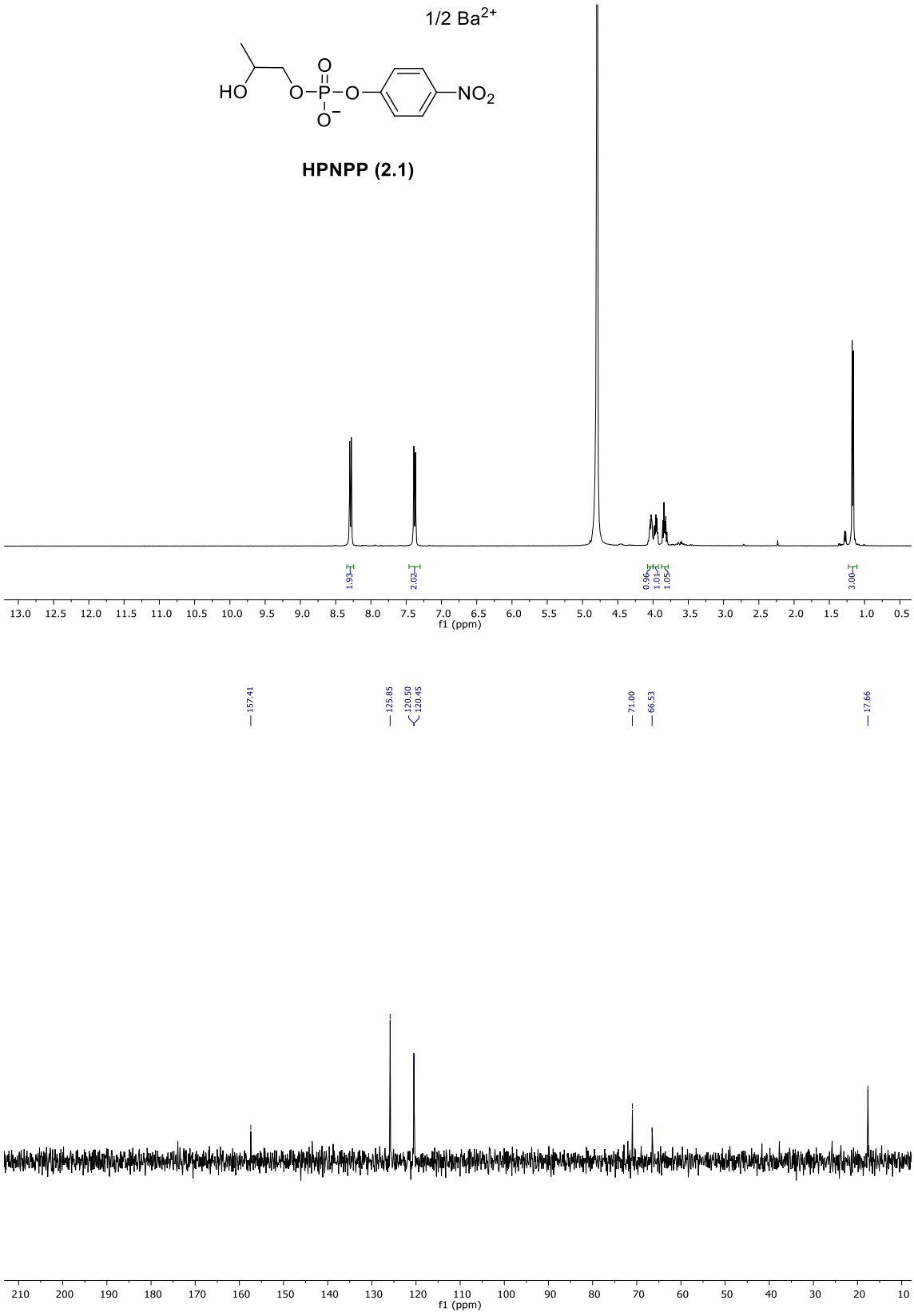

3-(*tert*-Butyl)-4-hydroxyphenyl pivalate (3.37)

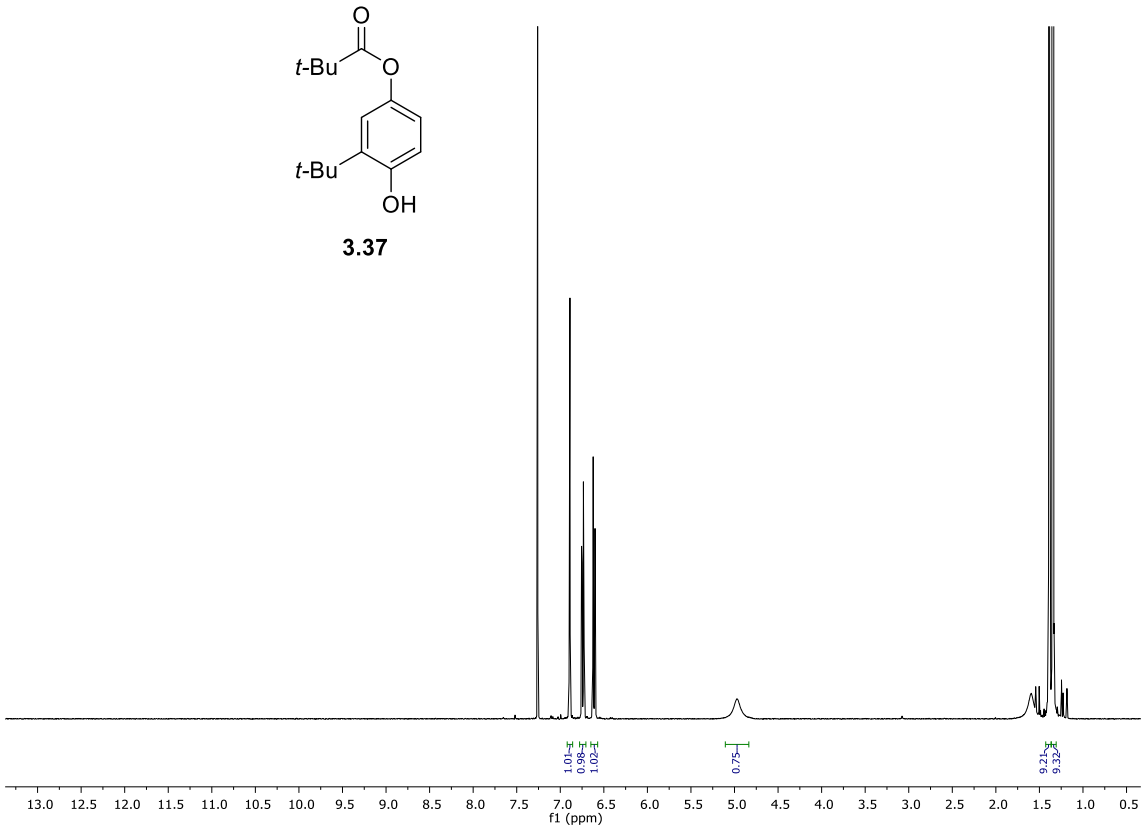

3.37

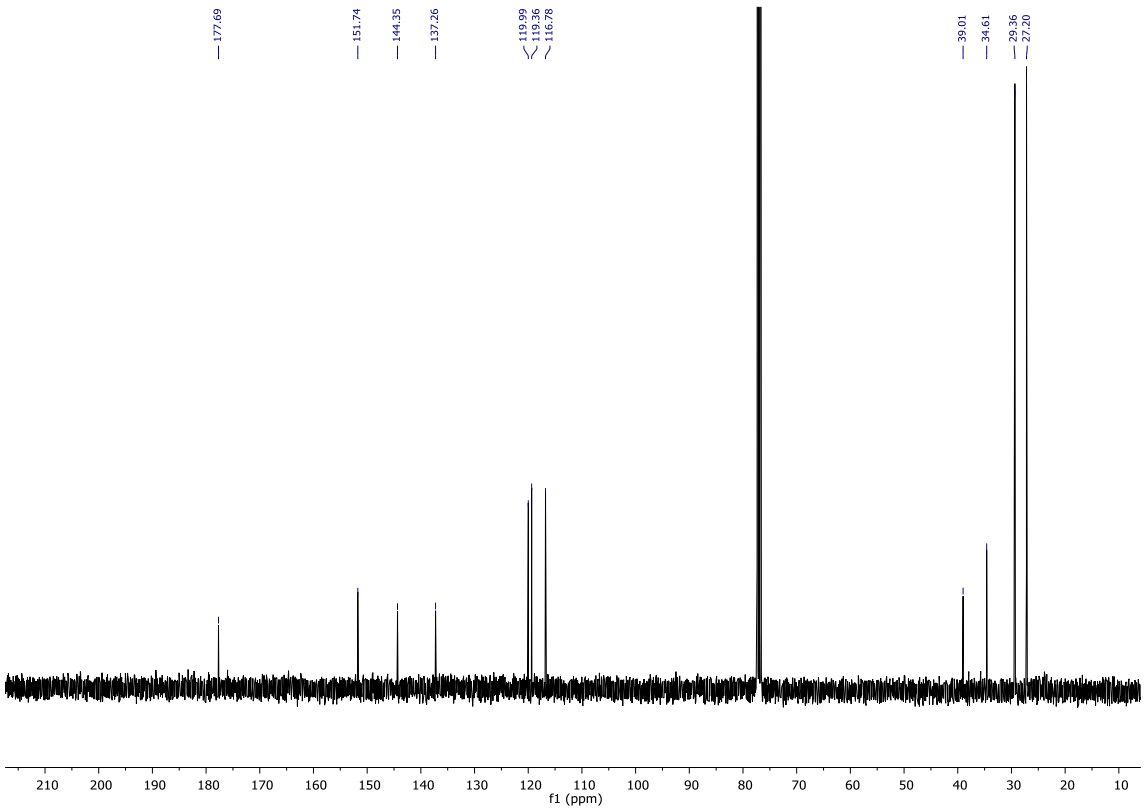

3-(*tert*-Butyl)-5-formyl-4-hydroxyphenyl pivalate (3.38)

3.38

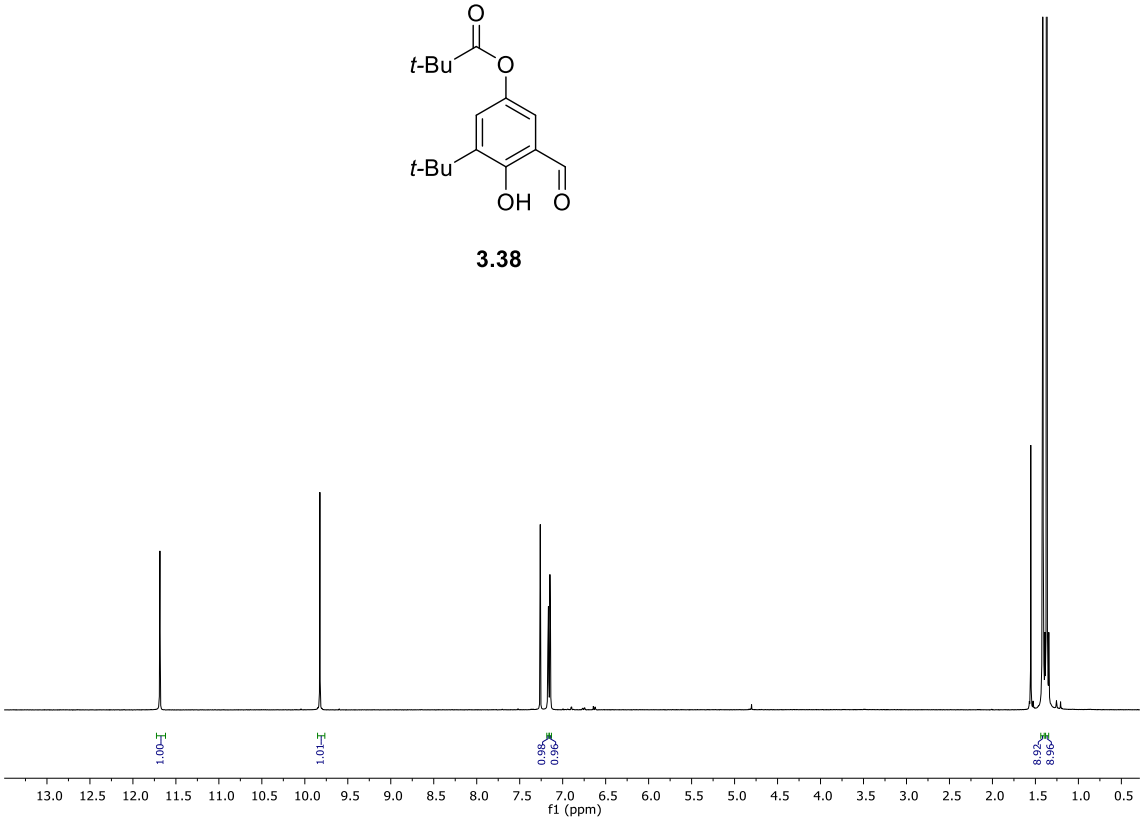

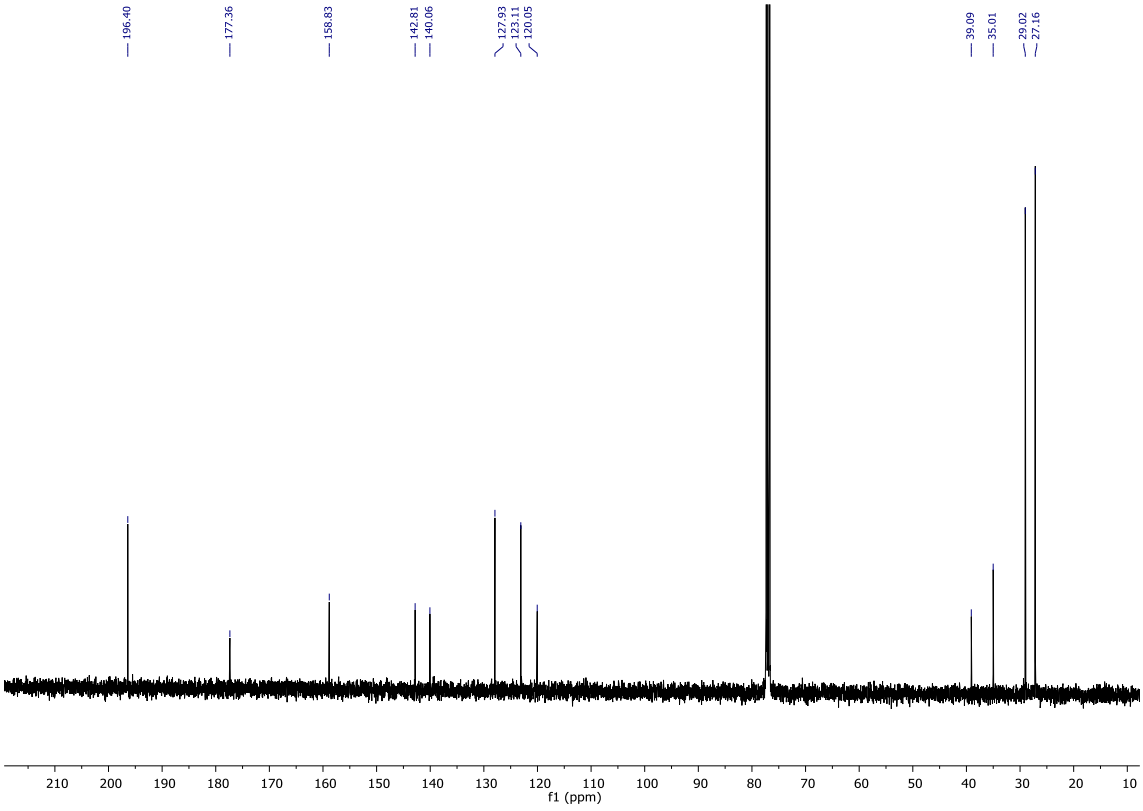

3-(*tert*-Butyl)-2,5-dihydroxybenzaldehyde (3.30)

3.30

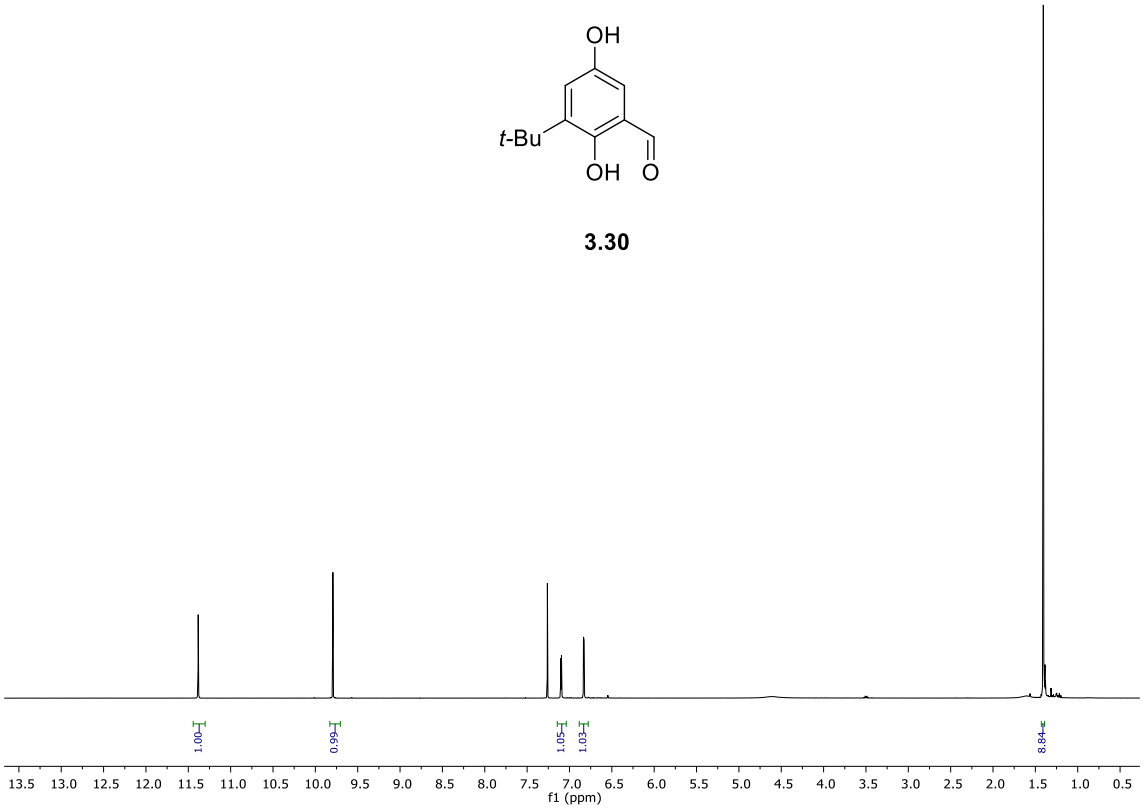

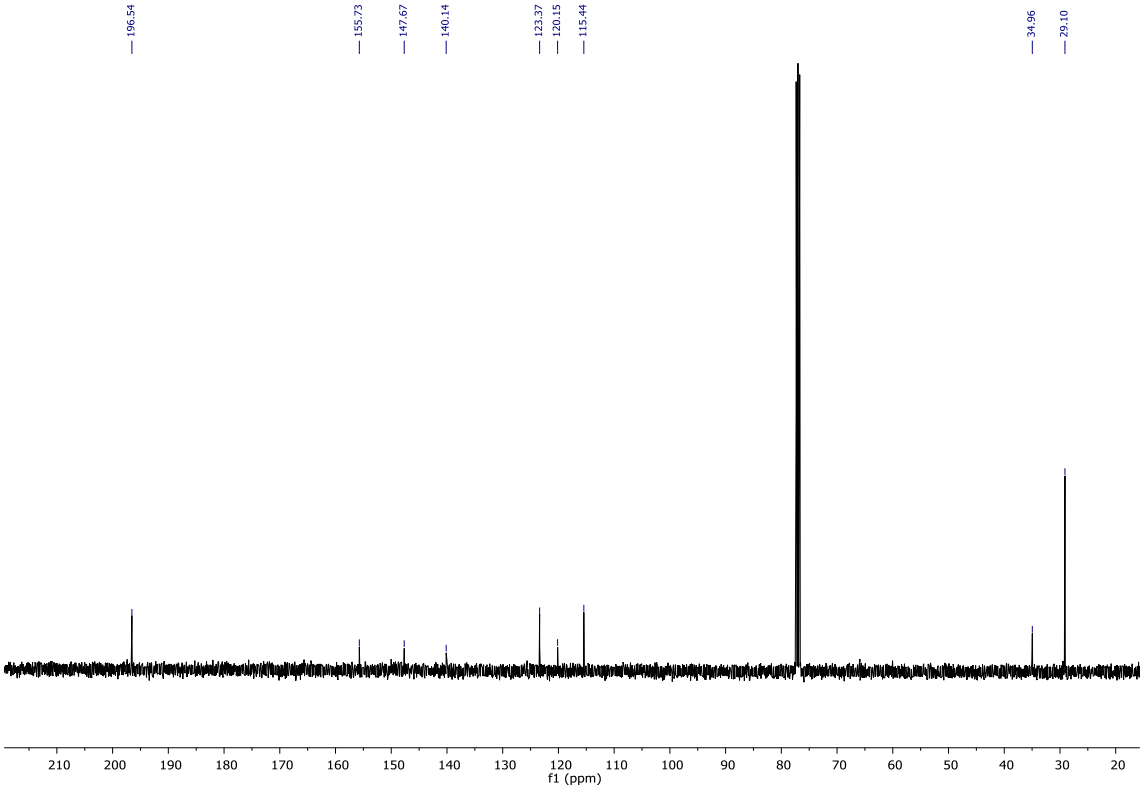

3-(*tert*-Butyl)-5-formyl-4-hydroxyphenyl octanoate (3.26)

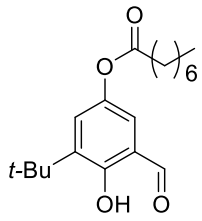

3.26

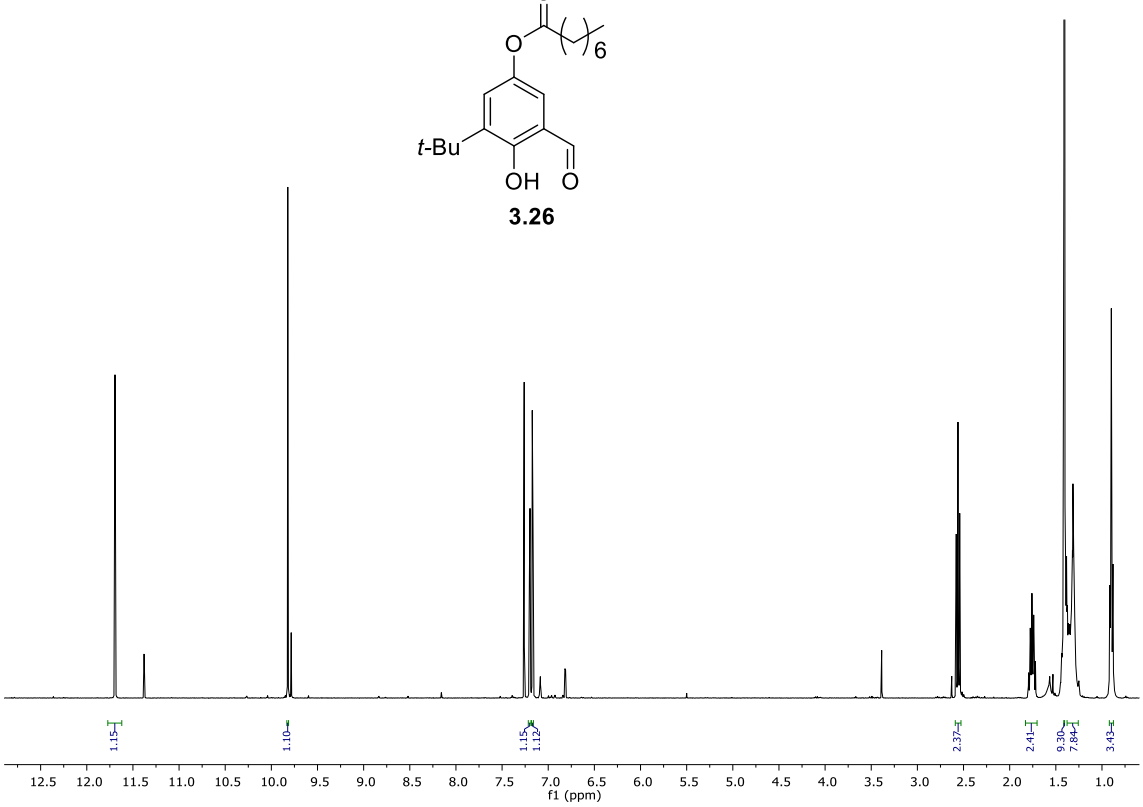

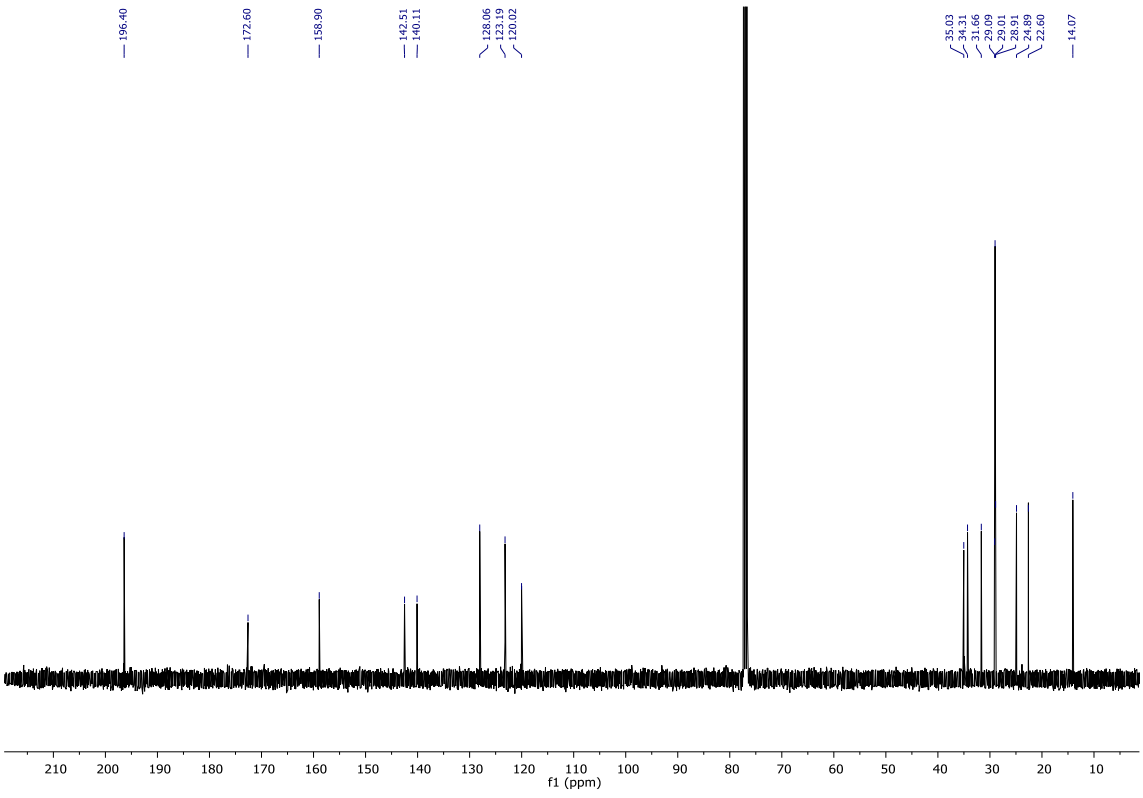

3-(*tert*-Butyl)-5-formyl-4-hydroxyphenyl dodecanoate (3.27)

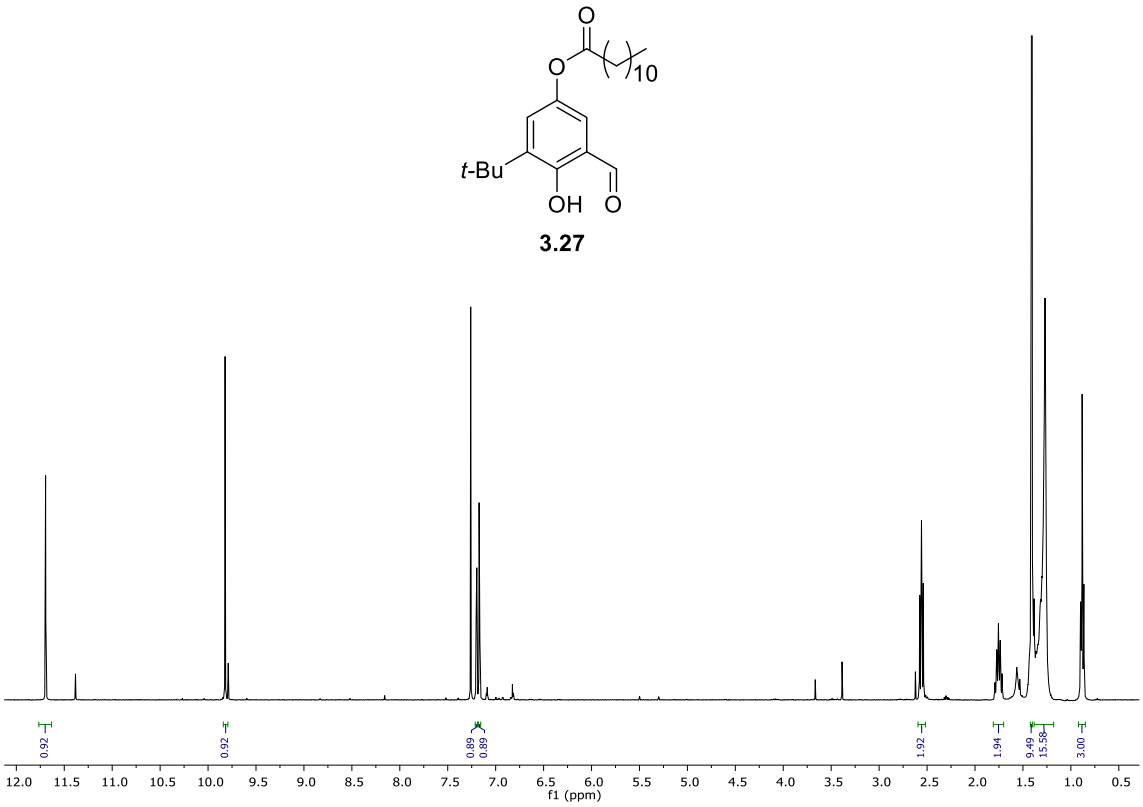

3.27

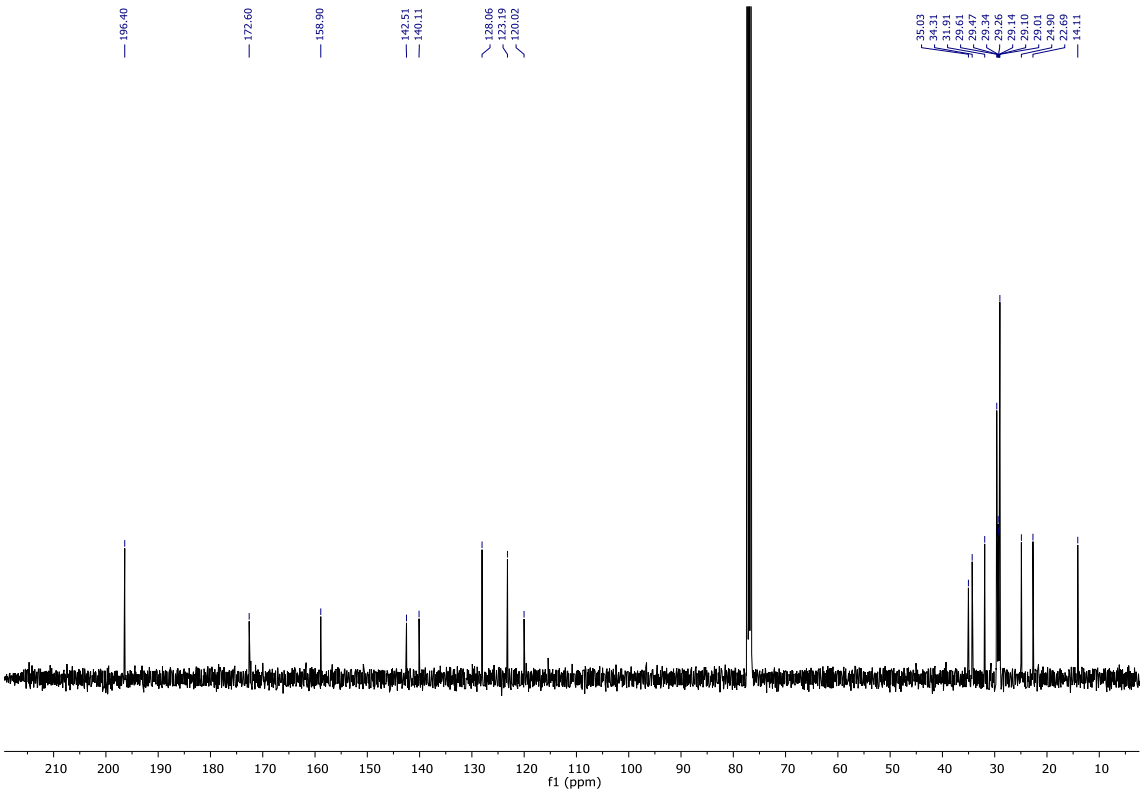

3-(*tert*-Butyl)-5-formyl-4-hydroxyphenyl stearate (3.28)

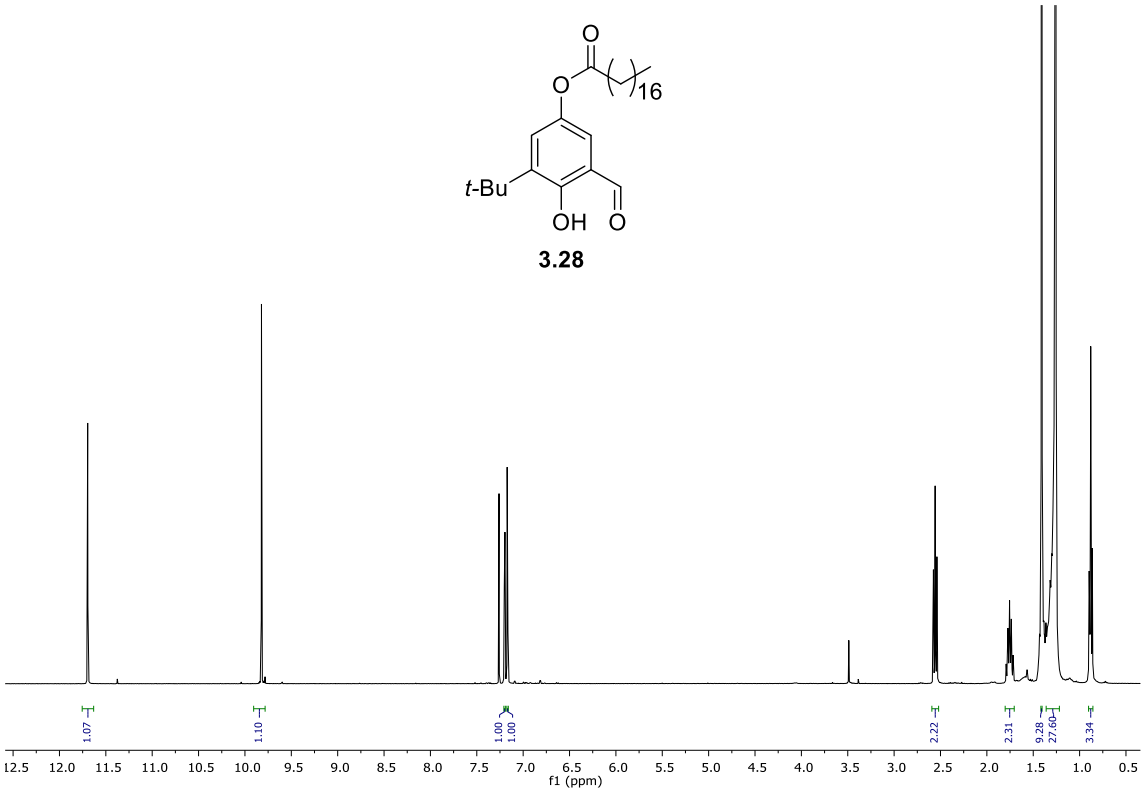

3.28

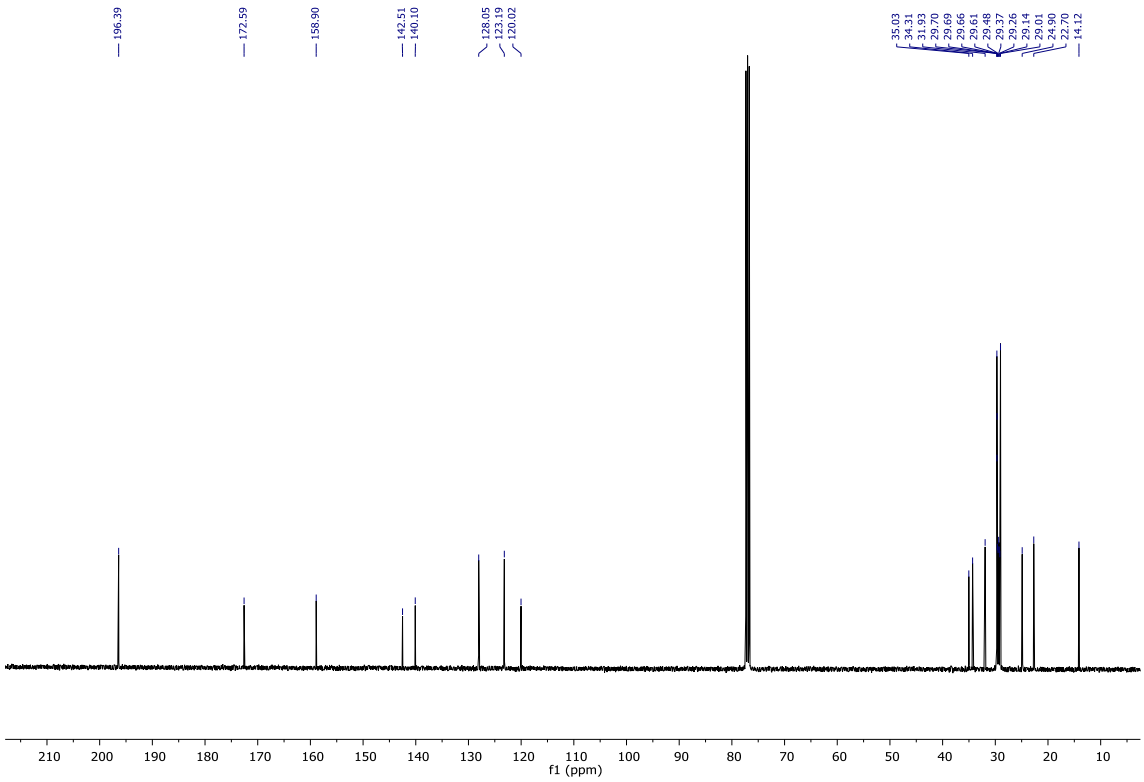

((1*E*,1'*E*)-(((1*R*,2*R*)-cyclohexane-1,2-diyl)bis(azaneylylidene))bis(methaneylylidene))bis(5-(*tert*-butyl)-4-hydroxy-3,1-phenylene) octanoate (3.23)

3.23

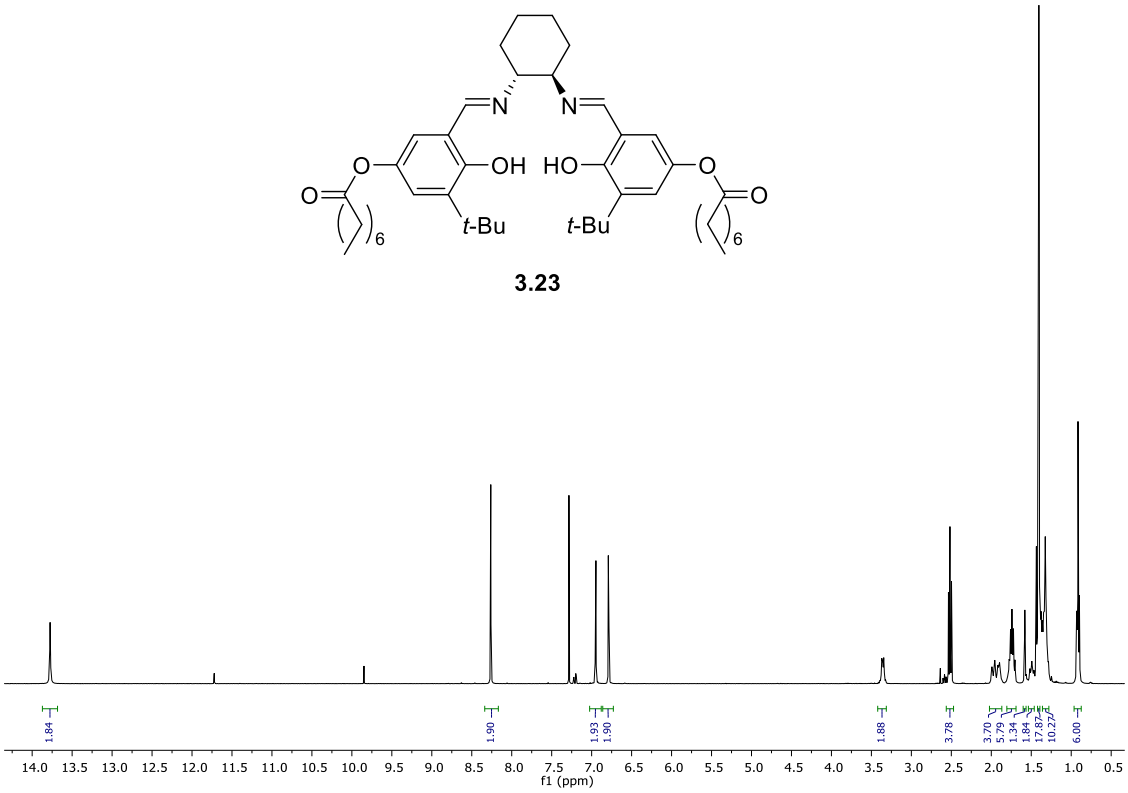

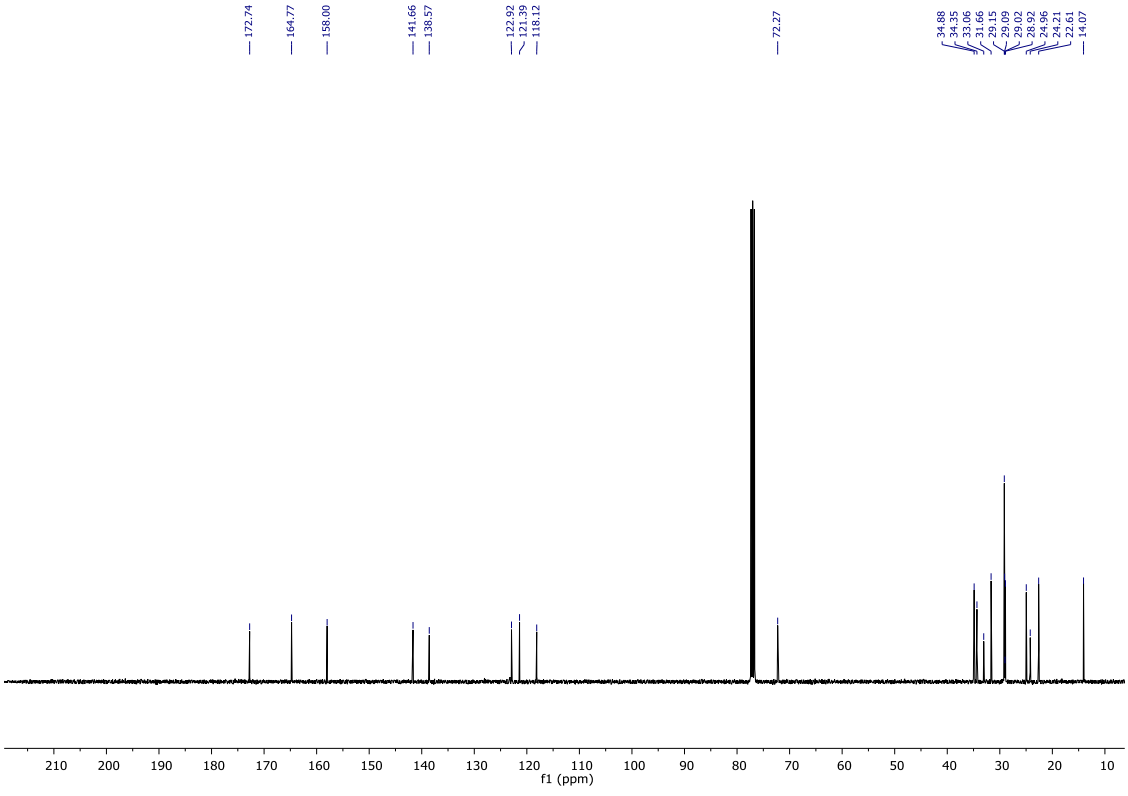

((1*E*,1'*E*)-(((1*R*,2*R*)-cyclohexane-1,2-diyl)bis(azaneylylidene))bis(methaneylylidene))bis(5-(*tert*-butyl)-4-hydroxy-3,1-phenylene) dodecanoate (3.24)

3.24

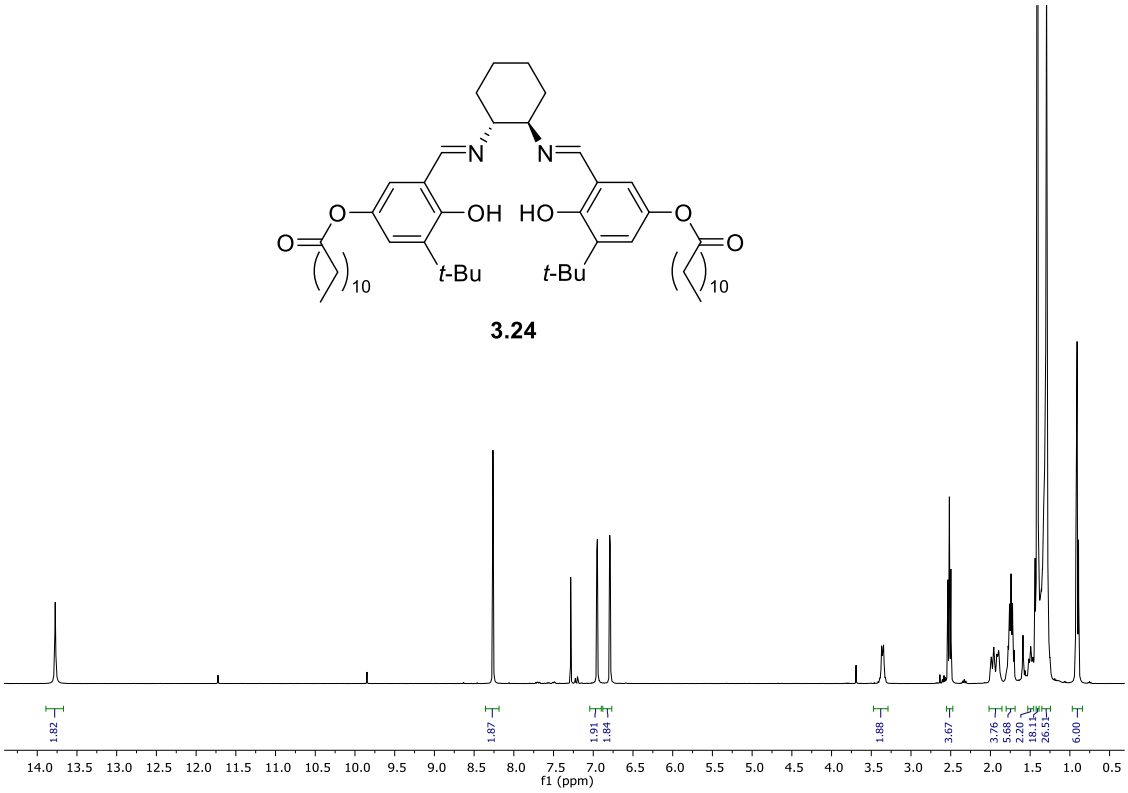

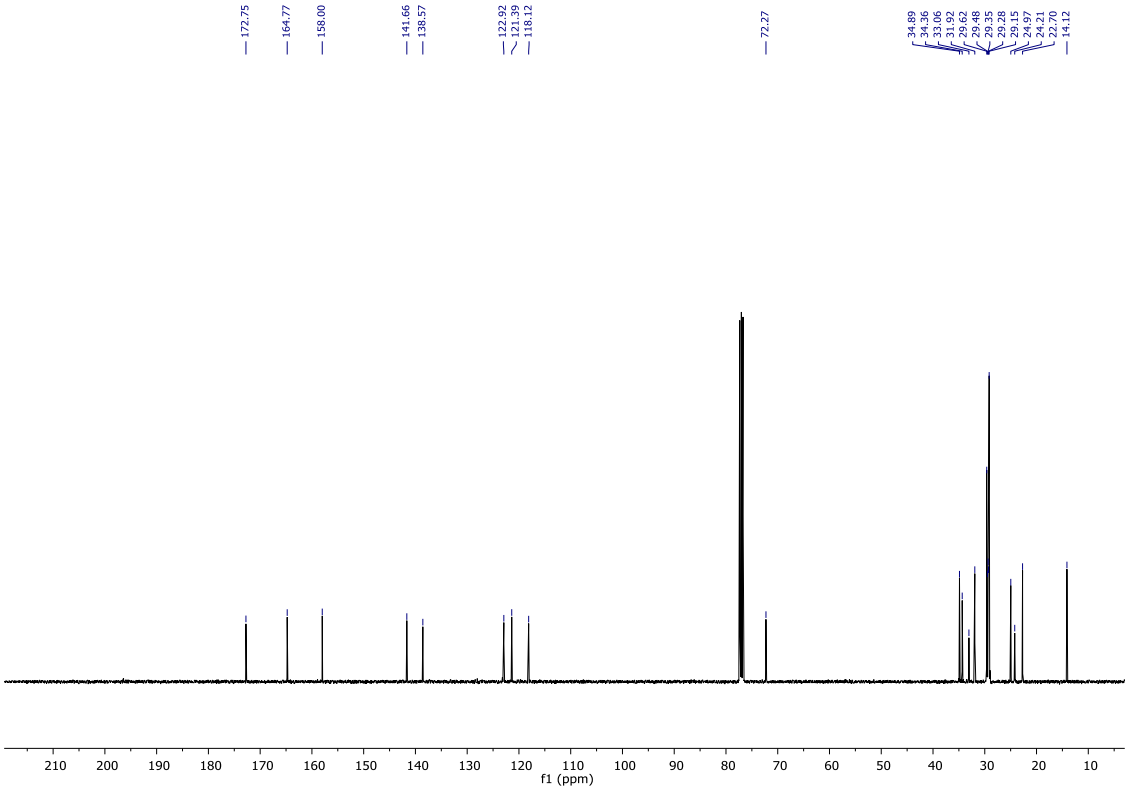

((1*E*,1'*E*)-(((1*R*,2*R*)-cyclohexane-1,2-diyl)bis(azaneylylidene))bis(methaneylylidene))bis(5-(*tert*-butyl)-4-hydroxy-3,1-phenylene) distearate (3.25)

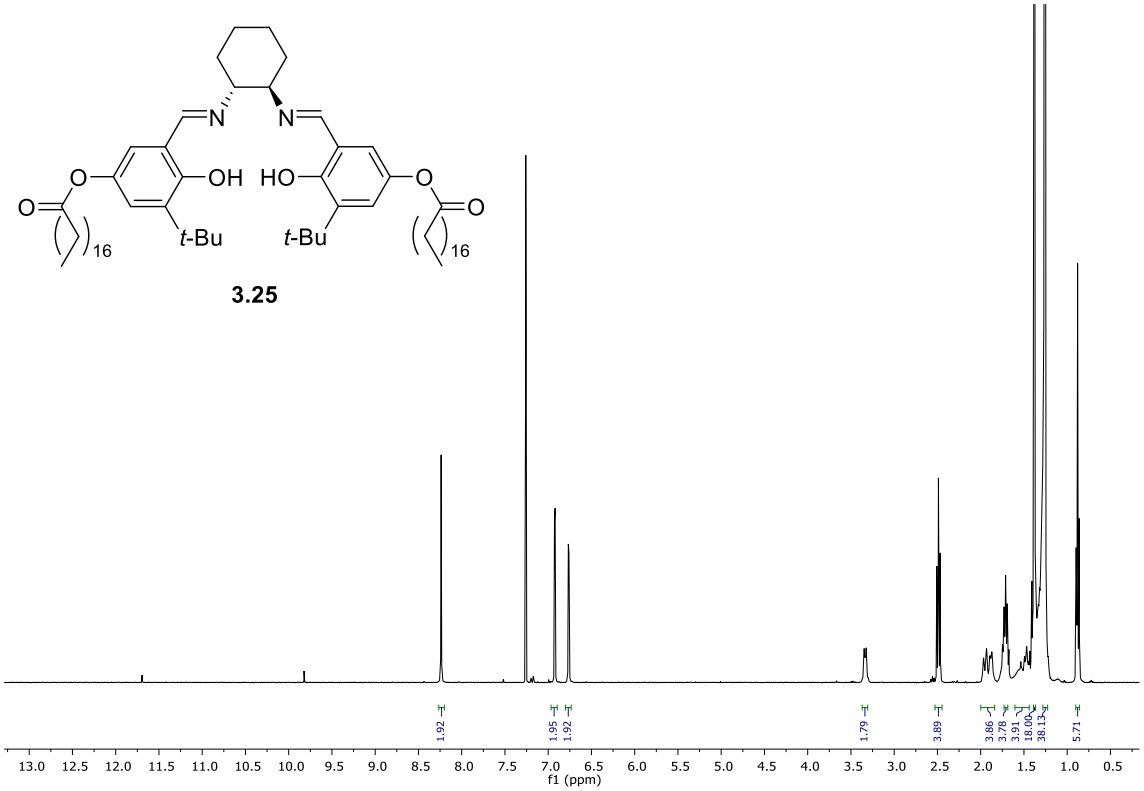

3.25

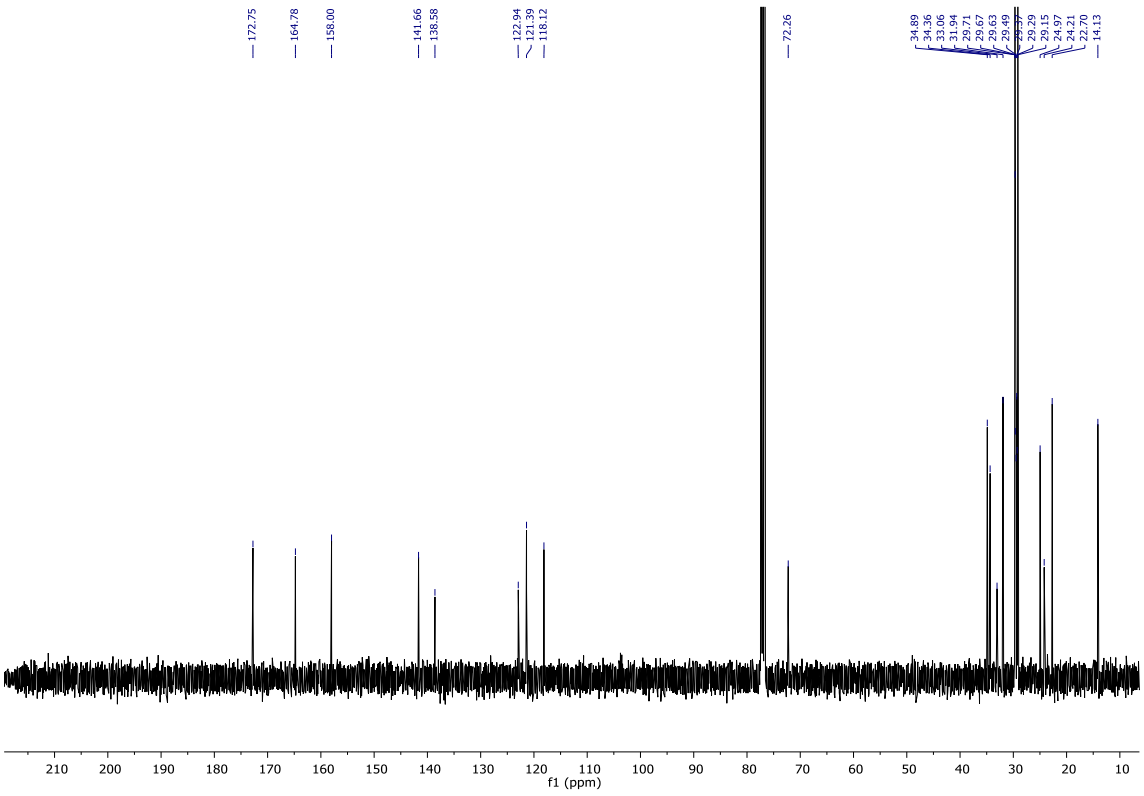

Bis(stearate)-(salen)nickel complex (3.45)

3.45

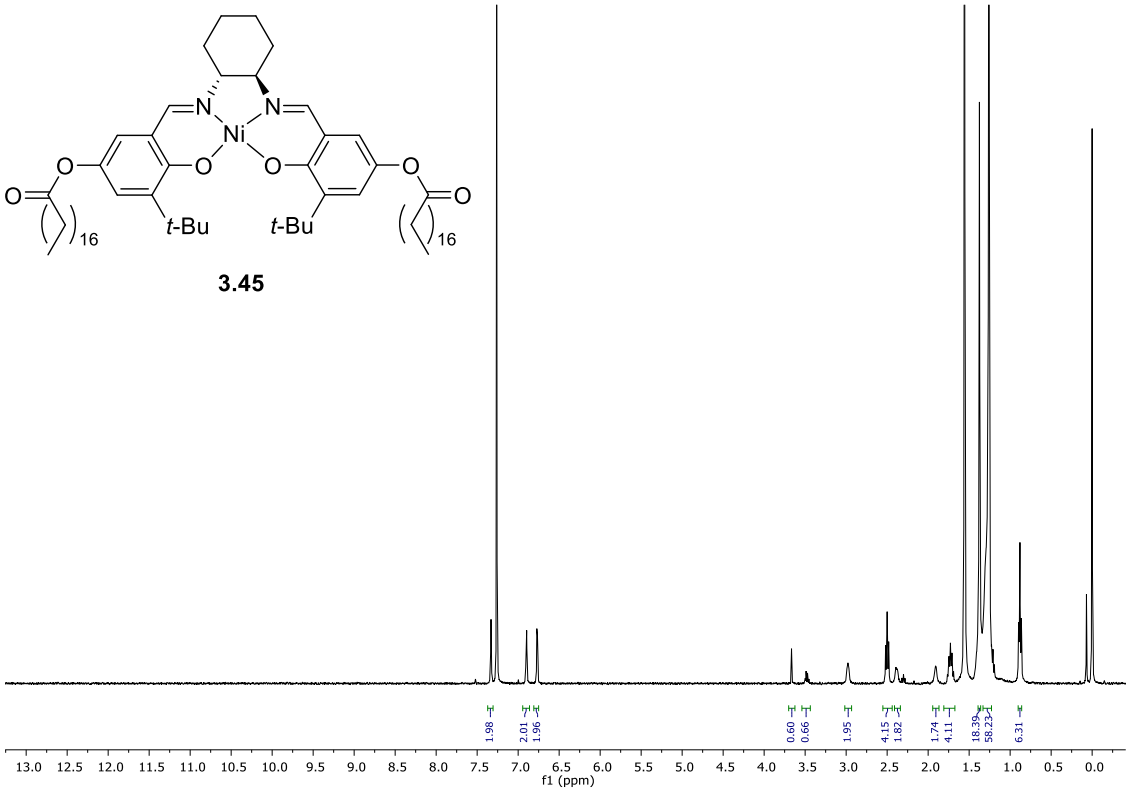

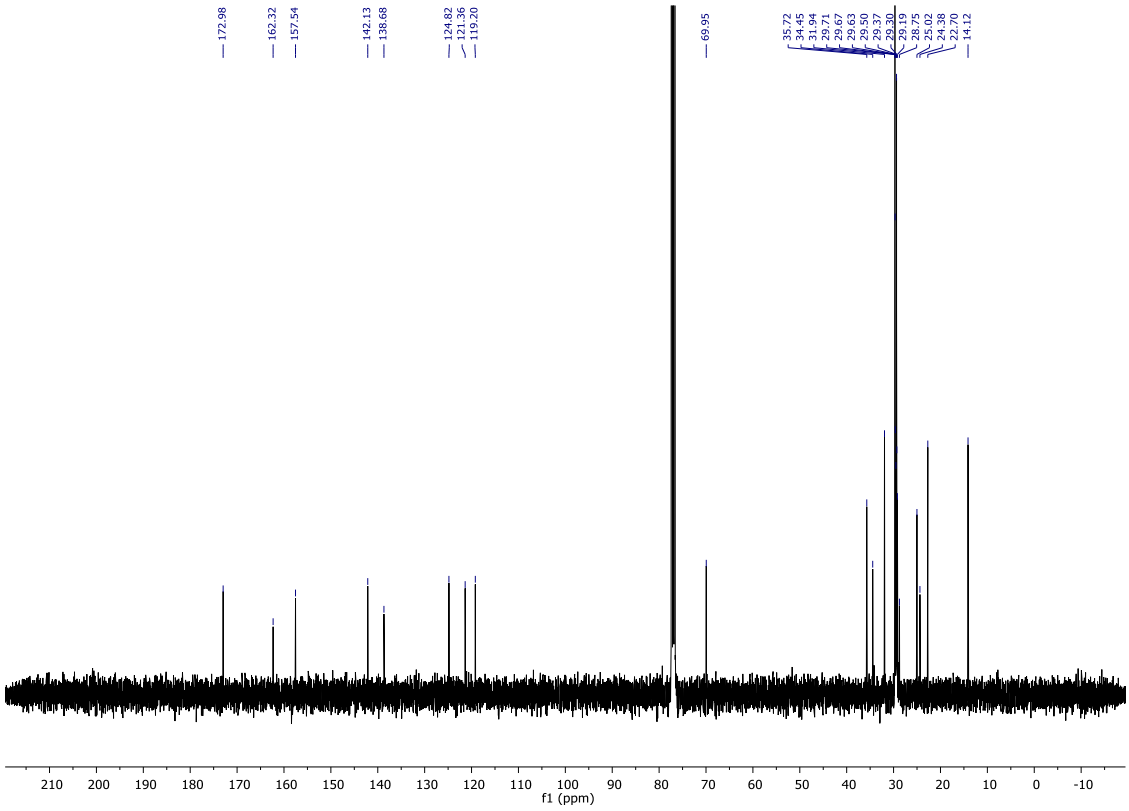

(Salen)nickel complex (3.46)

3.46

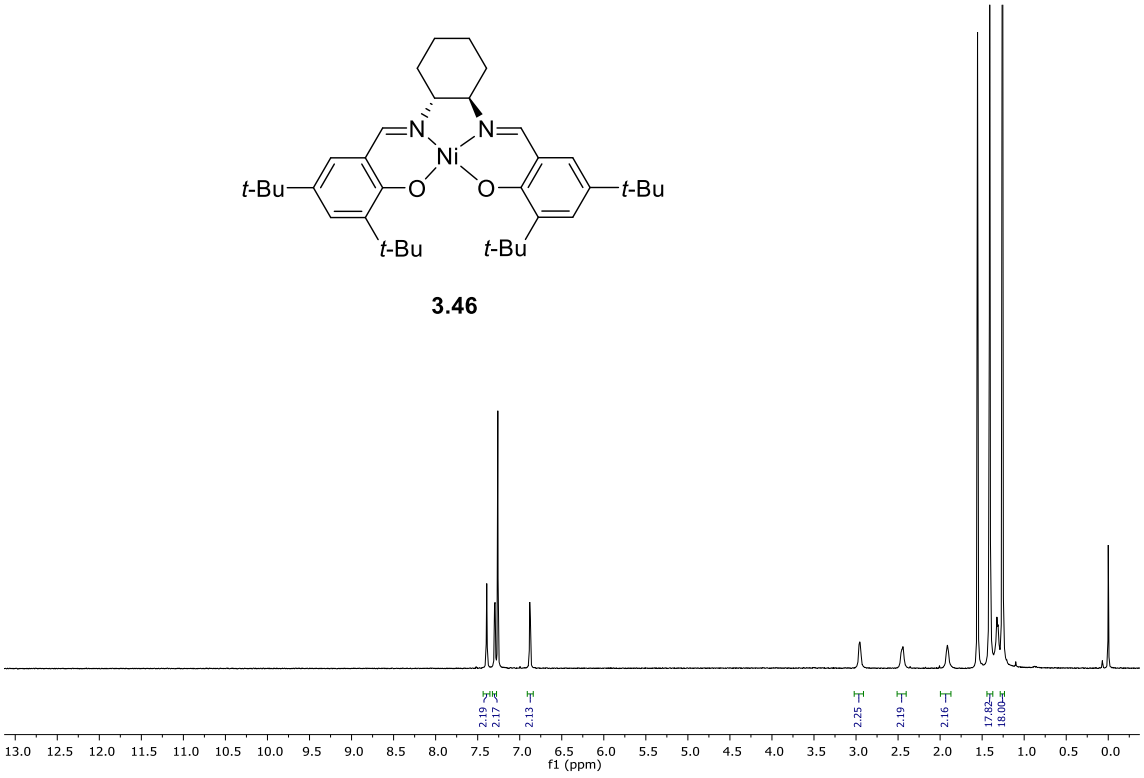

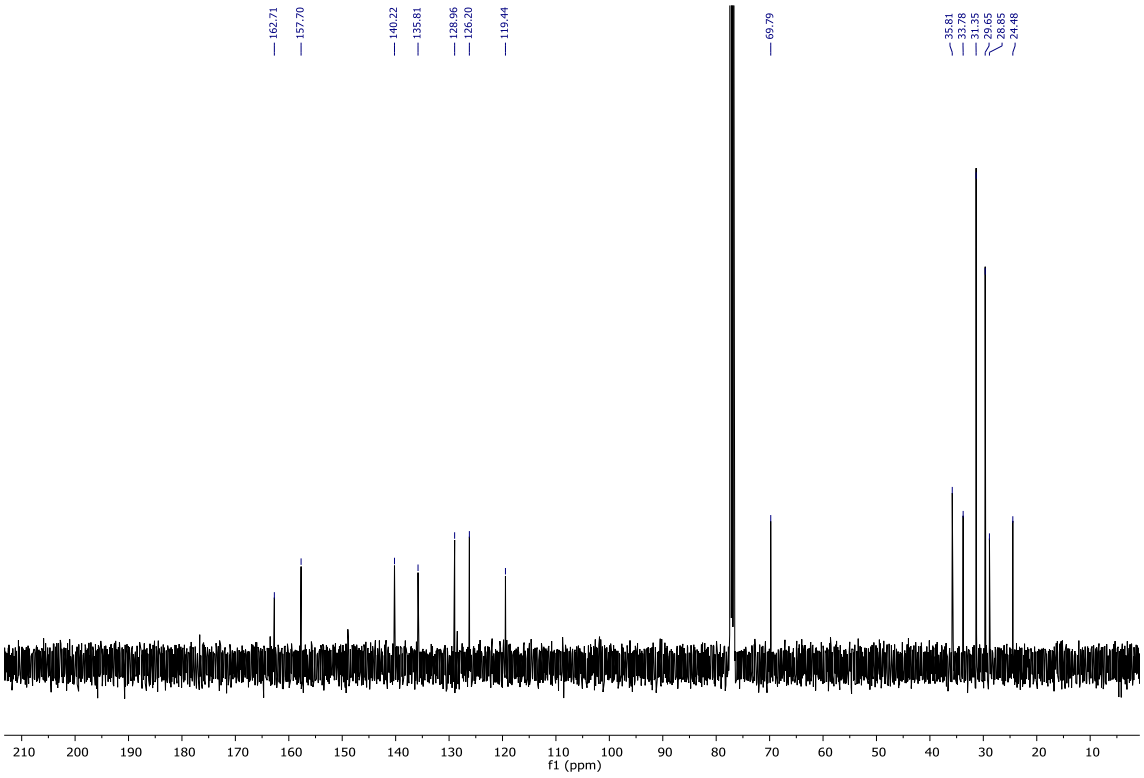

Raw data for refuelling experiments from chapter 2.

Initial rates of HPNPP hydrolysis after successive additions of HPNPP (125 μM each addition) in the presence [HEPES buffer] = 5 mM and [**2.7**·Zn^{2+}] = 50 μM at 40 °C (i) change in absorbance directly after 1st addition of HPNPP; (ii) change in absorbance 48h after 1st addition; (iii) change in absorbance directly after 2nd addition; (iv) change in absorbance 48h after 2nd addition; (v) change in absorbance directly after 3rd addition; (v) change in absorbance 48h after 3nd addition; (v) change in absorbance directly after 4th addition of HPNPP.

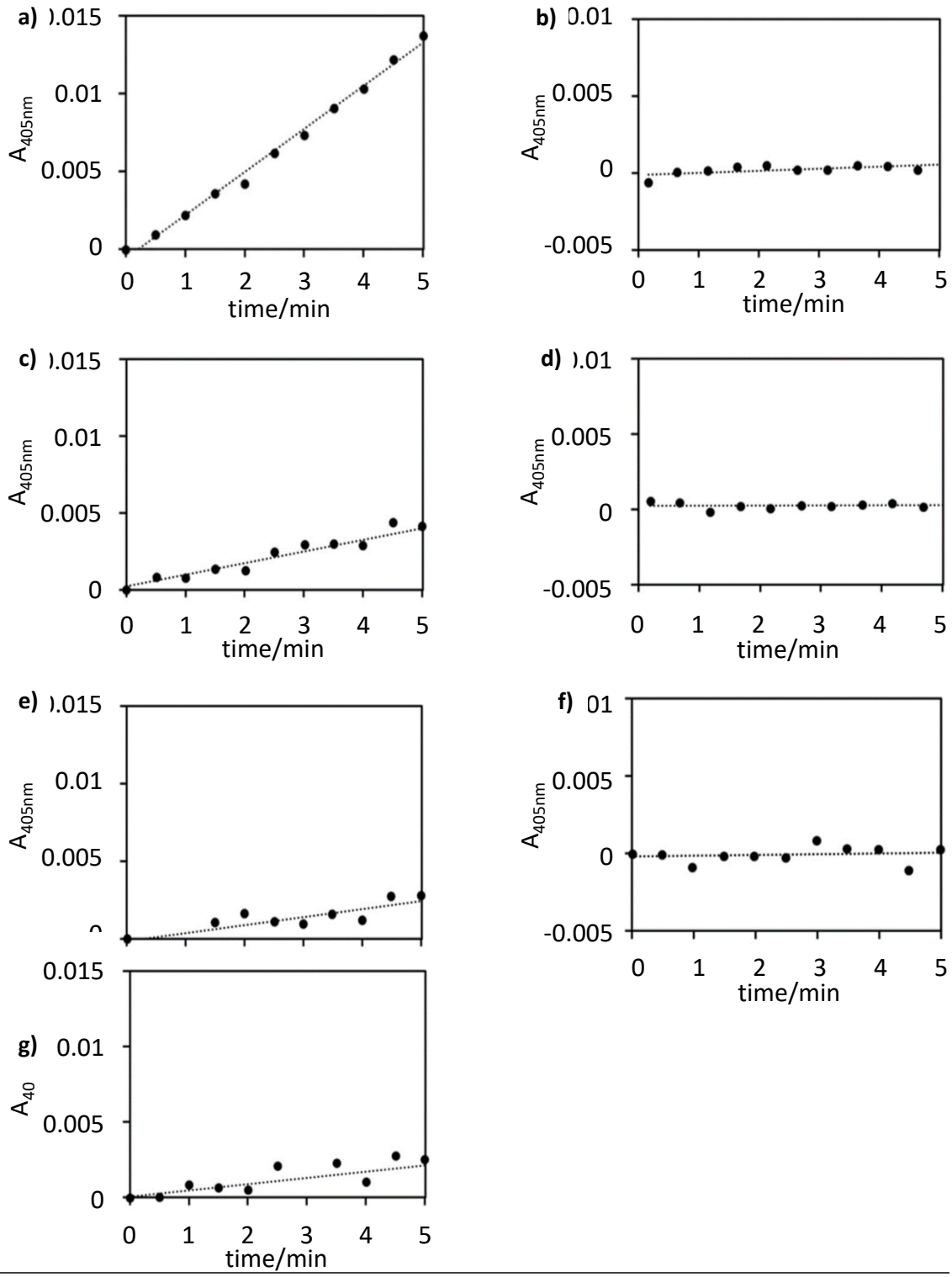

Chiral GC/HPLC analyses.

General procedure for the resolution of epoxides: A specific volume from a solution of the desired catalyst in chloroform was taken via syringe and added to a vial, chloroform was evaporated and a magnetic stirbar was added to the vial. The desired amount of Milli-Q water was added followed by 50 μL of the racemic mixture of the epoxide. The reaction mixtures were magnetically stirred at 400 RPM. The aliquots taken from the reaction mixture were filtered over a silica plug eluting with Et_2O before chiral GC/HPLC analyses. For the experiments at homogeneous conditions the same procedure applies, but 50 μL of THF was added prior the addition of the epoxide.

k_{obs} were determined from plots of ln ([epoxide]/ $[epoxide]_0$) versus time.

Determination of the *e.e.* of 1,2-epoxyhexane was determined by chiral GC analysis [Chiraldex G-TA], 40-100 ºC, 2.5 ºC/minute, t_R(minor) = 16.62 min., t_R(major) = 16.96 min.

Chiral GC data for 1,2-epoxyhexane, racemic mixture and mixture after 60 minutes of conversion with catalyst **3.22**.

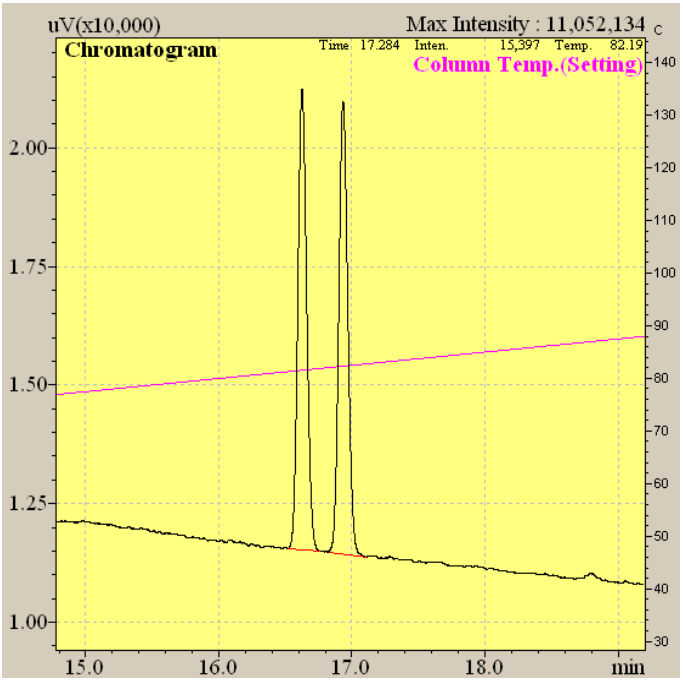

Ret.Time	Area
16.626	44842.9
16.934	44724.9

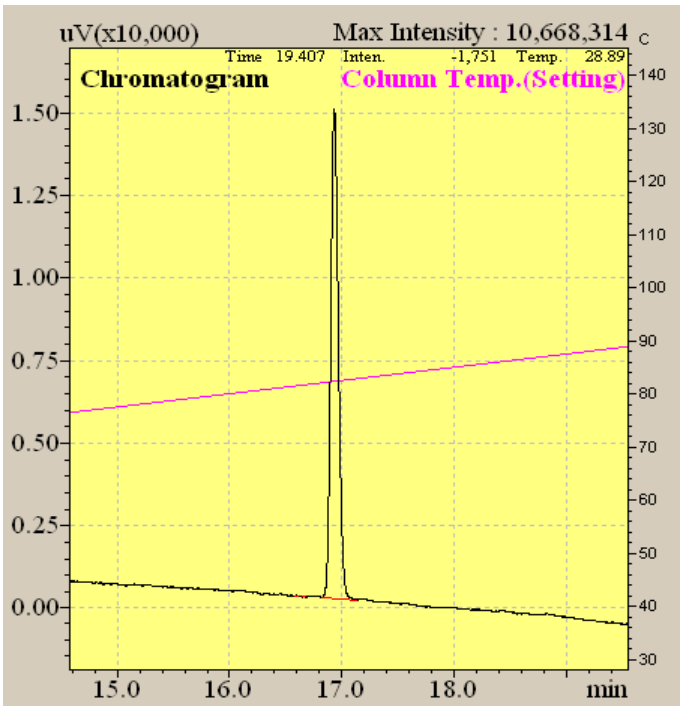

Ret.Time	Area
16.668	13.8
16.932	69488.5

Determination of the *e.e.* of epichlorohydrin was determined by chiral GC analysis [Chiraldex G-TA], 70-130 ºC, 3 ºC/minute, t_R(major) = 9.82 min., t_R(minor) = 10.11 min.

Chiral GC data for epichlorohydrin, racemic mixture and mixture after 70 minutes of conversion with catalyst **3.22**.

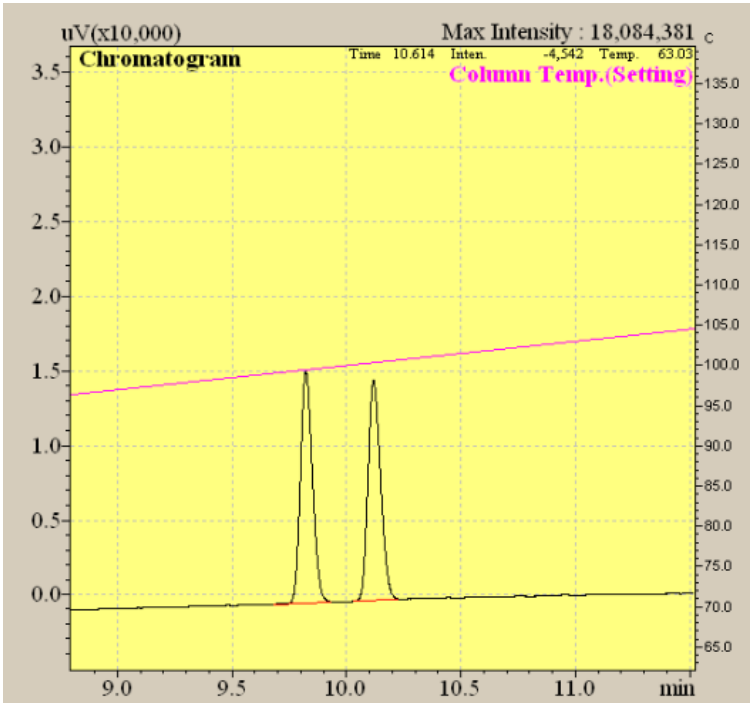

Ret.Time	Area
9.823	57254.3
10.118	57139.8

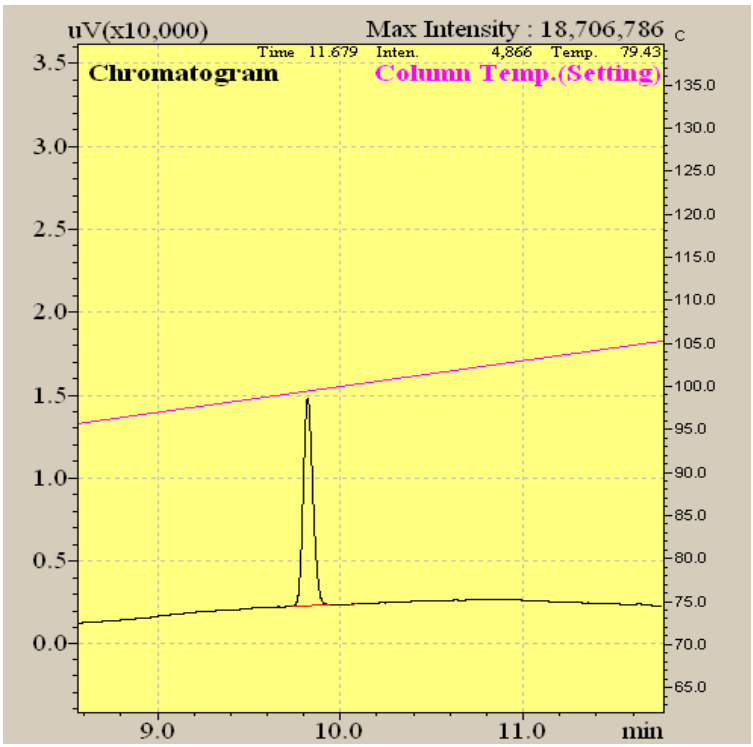

Ret.Time	Area
9.822	45827.7
10.094	39.5

Determination of the *e.e.* of styrene oxide was determined by chiral HPLC analysis [Chiralpak IB], isocratic 99 hexanes: 1 IPA t_R(major) = 6.80 min., t_R(minor) = 7.92 min.

Chiral HPLC data for styrene oxide, racemic mixture and mixture after 80 minutes of conversion with catalyst **3.22**.

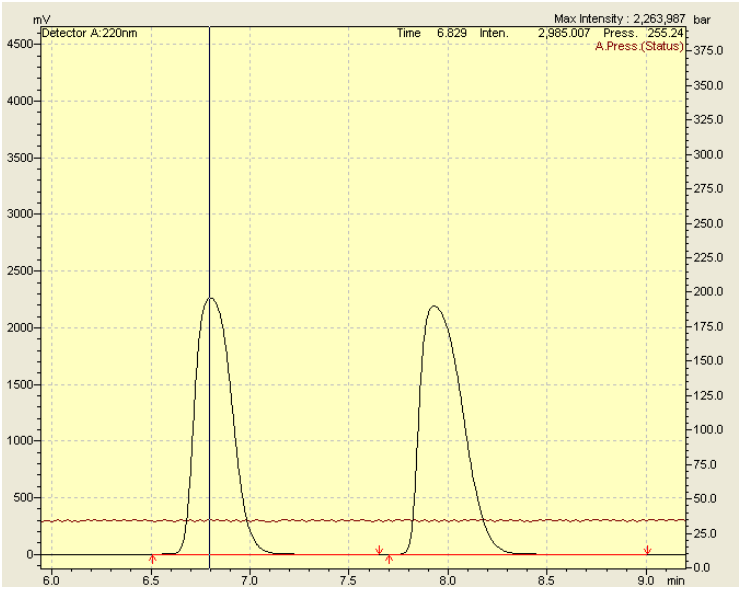

Ret. Time	Area
6.798	28930153.9
7.925	32377674.2

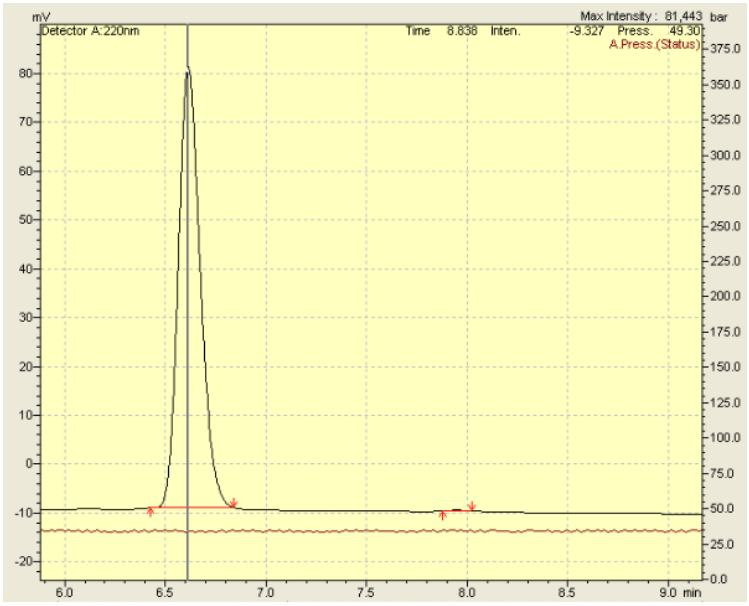

Ret. Time	Area
6.609	685448.1
7.947	771.0

Determination of the *e.e.* of butyl glycidyl ether was determined by chiral GC analysis [Chiraldex G-TA], 85-130 ºC, 0.4 ºC/minute, t_R(minor) = 77.36 min., t_R(major) = 78.18 min.

Chiral GC data for butyl glycidyl ether, racemic mixture and mixture after 25 minutes of conversion with catalyst **3.22**.

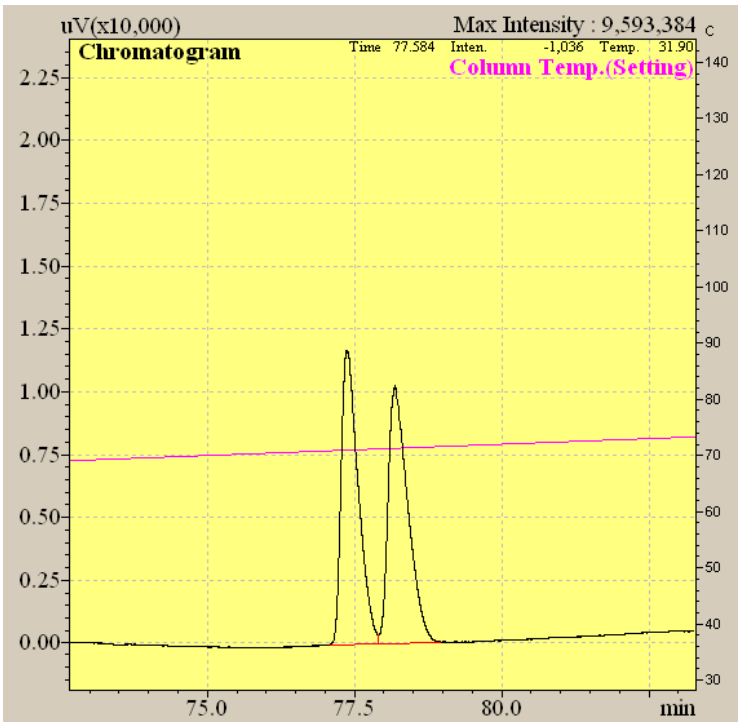

Ret.Time	Area
77.363	237924.1
78.176	238204.9

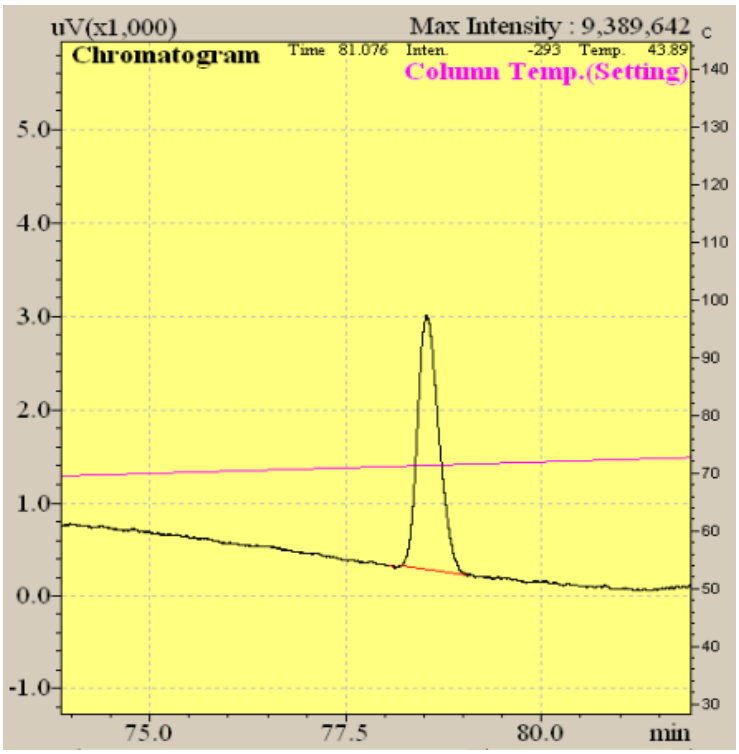

Ret.Time	Area
78.089	24.0
78.526	51541.9

Determination of the *e.e.* of 3,4-epoxy-1-butene was determined by chiral GC analysis [Chiraldex G-TA], 30-70 ºC, 1.5 ºC/minute, t_R(minor) = 12.46 min., t_R(major) = 12.66 min.

Chiral GC data for 3,4-epoxy-1-butene, racemic mixture and mixture after 5 hours of conversion with catalyst **3.22**.

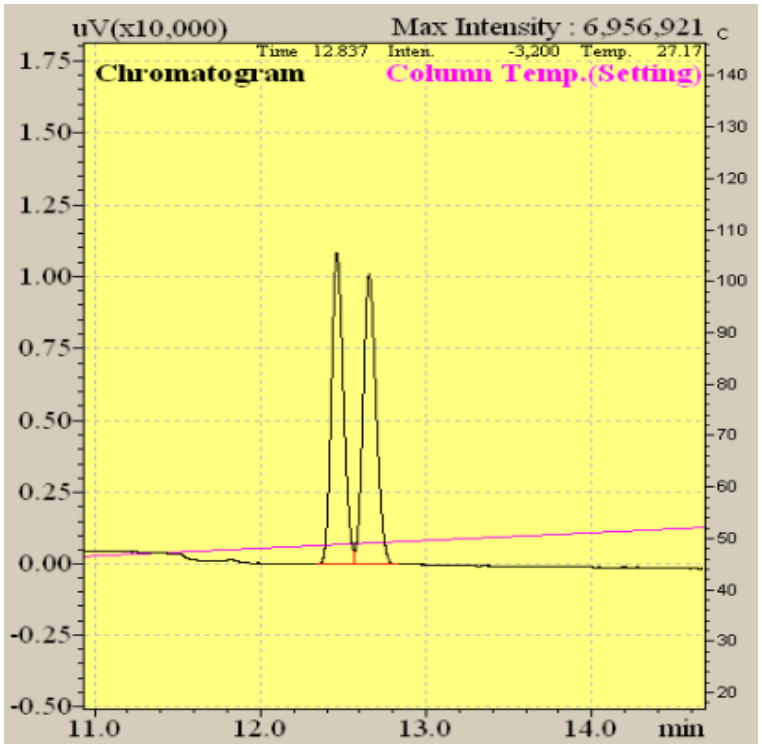

Ret.Time	Area
12.462	55245.5
12.656	55492.6

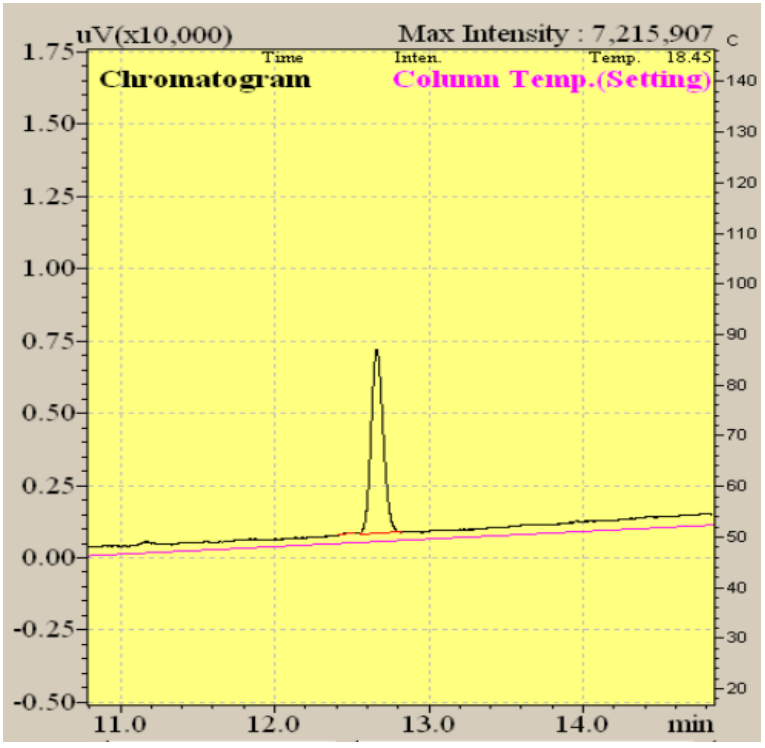

Ret.Time	Area
12.495	162.0
12.662	34370.3

Determination of the *e.e.* of 1,2-epoxy-3-phenoxypropane was determined by chiral HPLC analysis [Chiralpak IC], 99 hexanes: 1 IPA t_R(minor) = 9.66 min., t_R(major) = 15.64 min.

Chiral HPLC data for 1,2-Epoxy-3-phenoxypropane, racemic mixture and mixture after 80 minutes of conversion with catalyst **3.22**.

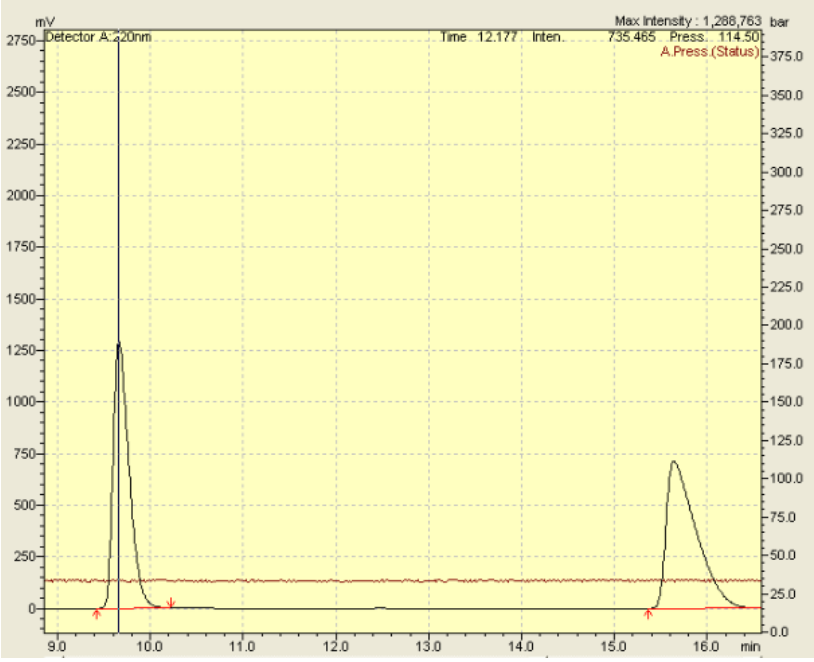

Ret. Time	Area
9.659	15484020.3
15.639	16081594.7

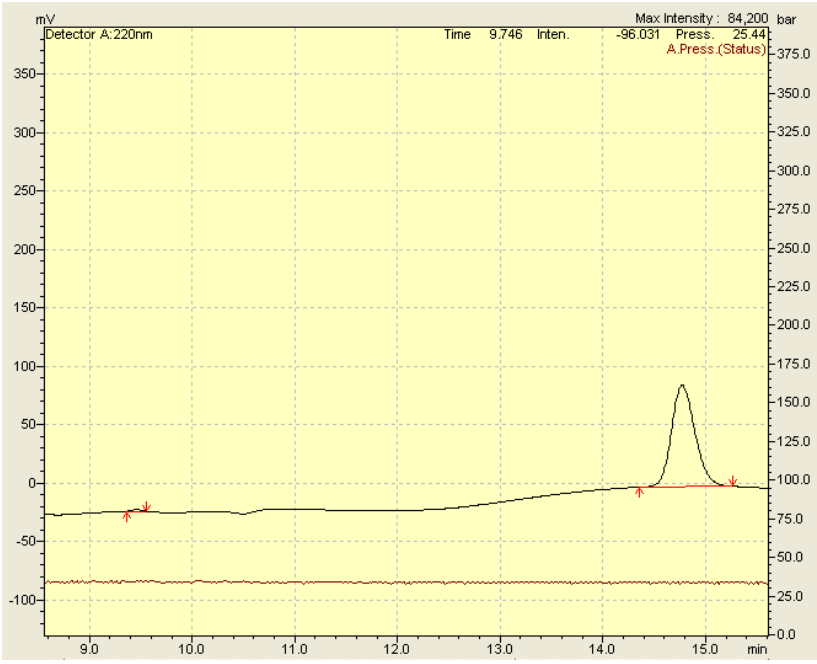

Ret. Time	Area
9.452	10556.8
14.768	1385474.6

Determination of the *e.e.* of 3,3-Dimethyl-1,2-epoxybutane was determined by chiral GC analysis [Chiraldex G-TA], 40-100 ºC, 2.5 ºC/minute, t_R(minor) = 12.76 min., t_R(major) = 13.17 min.

Chiral GC data for 3,3-Dimethyl-1,2-epoxybutane, racemic mixture and mixture after 4 days of conversion with catalyst **3.22**.

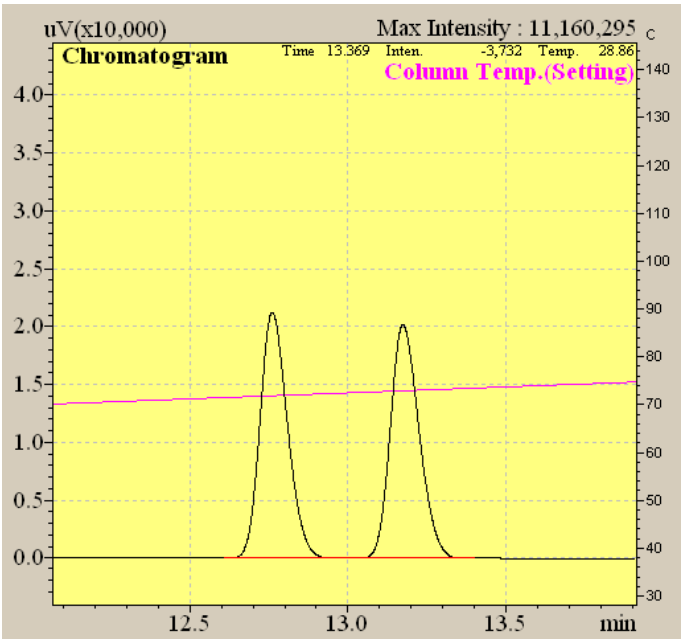

Ret.Time	Area
12.761	129294.1
13.174	128813.8

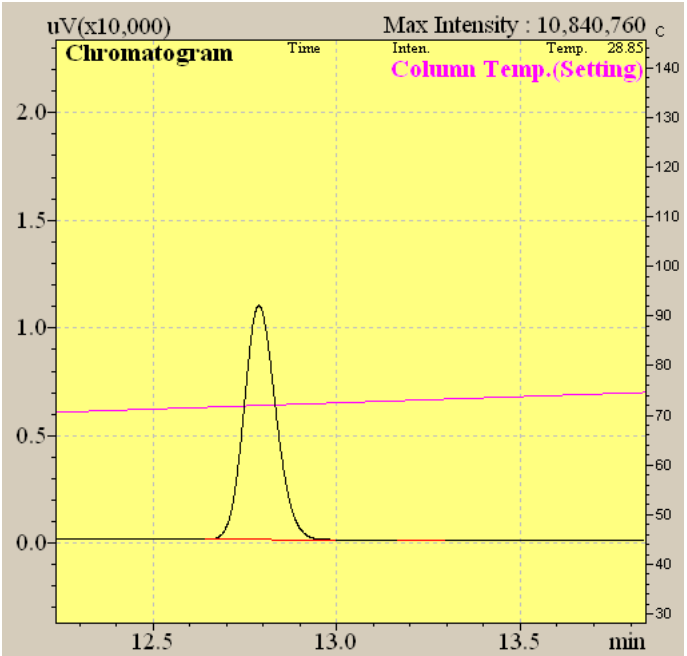

Ret.Time	Area
12.788	65878.0
13.274	72.3

Calculation of k_{obs} from plots of -ln ([epoxide]/ $[epoxide]_0$):

kobs calculated for **Figure 109**. Red dots: Compound **3.22**. Yellow dots: Compound **3.21**. Green dots: Compound **3.20**. Blue dots: Compound **3.4.**:

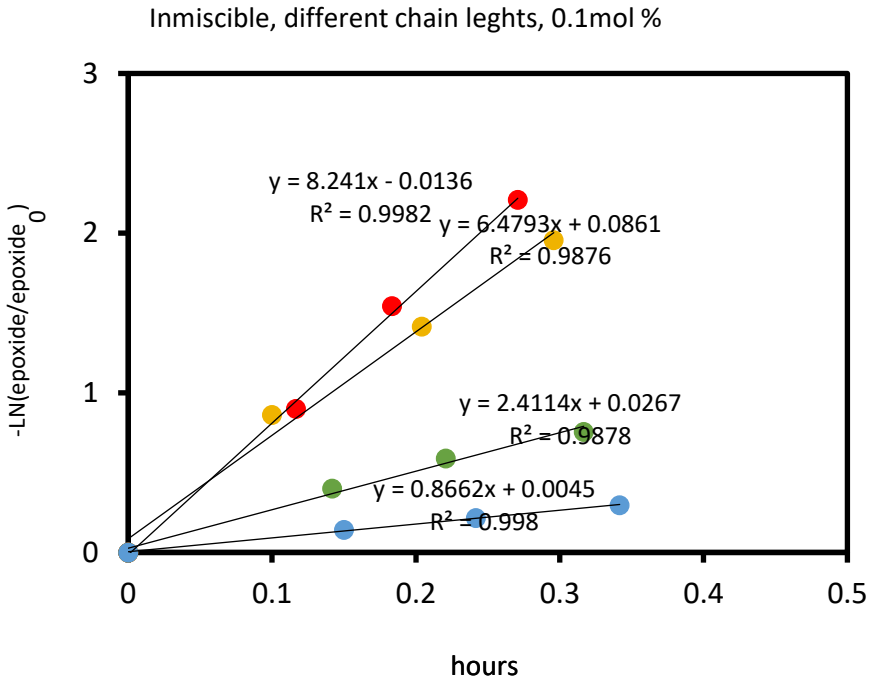

kobs calculated for **Figure 112**. Red dots: Compound **3.22**. Yellow dots: Compound **3.21**. Green dots: Compound **3.20**. Blue dots: Compound **3.4.**:

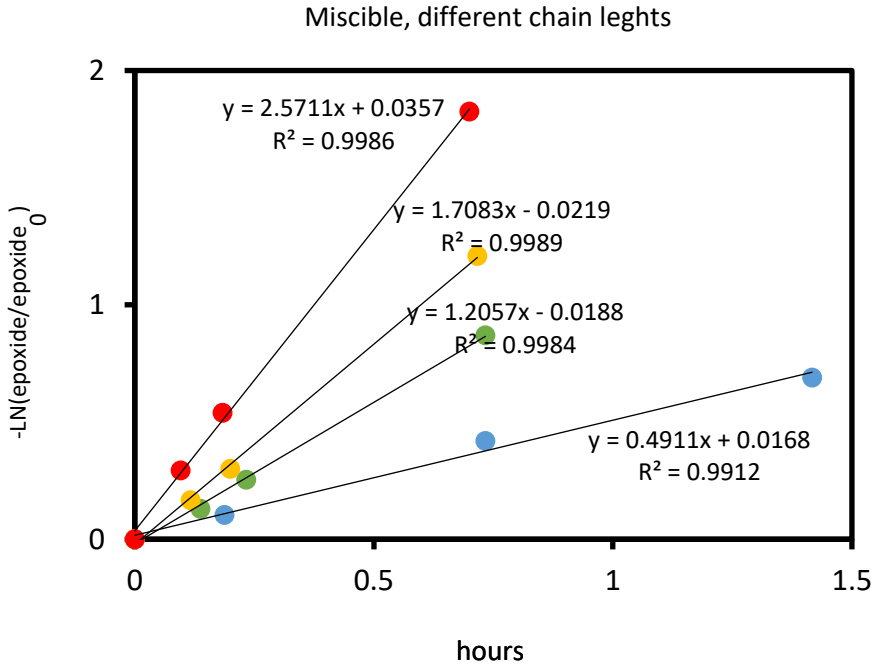

kobs calculated for **Figure 115**. Red dots: Compound **3.22**. Blue dots: compound **3.4**.

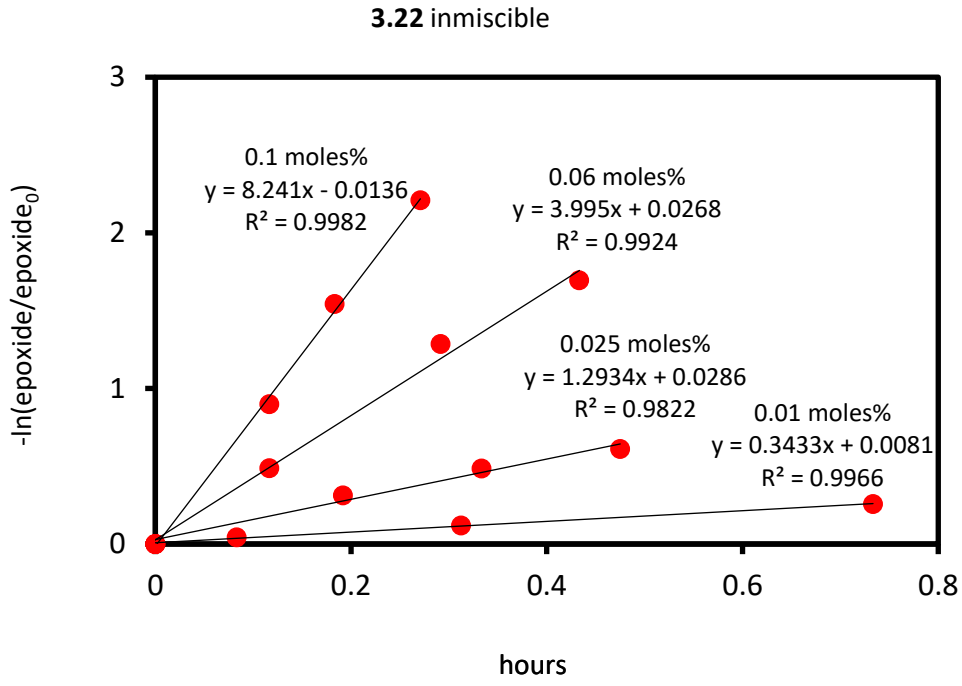

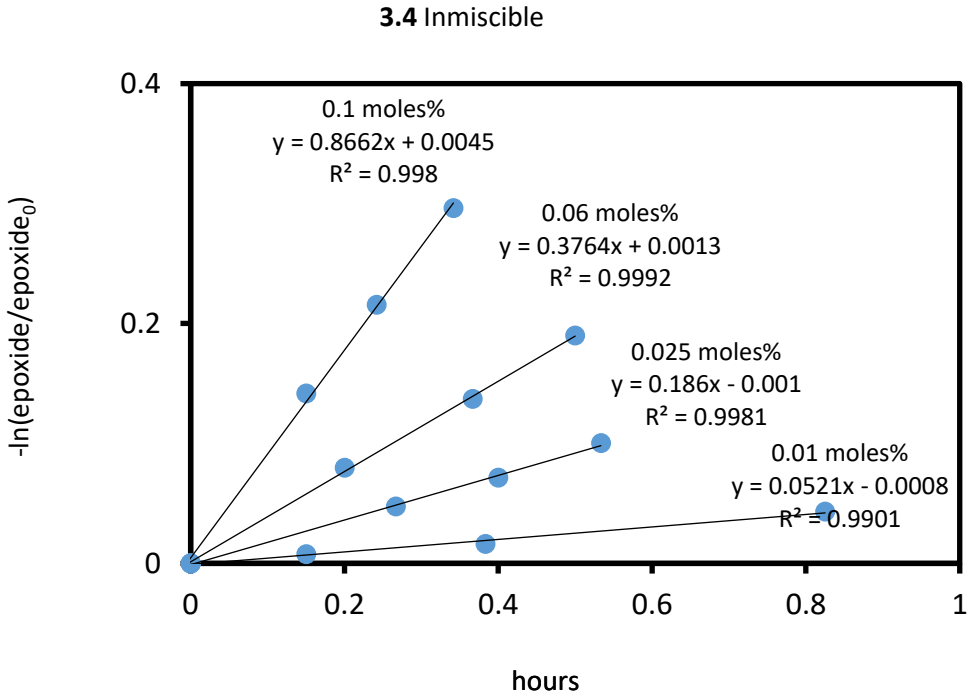

kobs calculated for **Figure 110** and **Figure 111**. Red dots: Compound **3.22**. Blue dots: compound **3.4**.

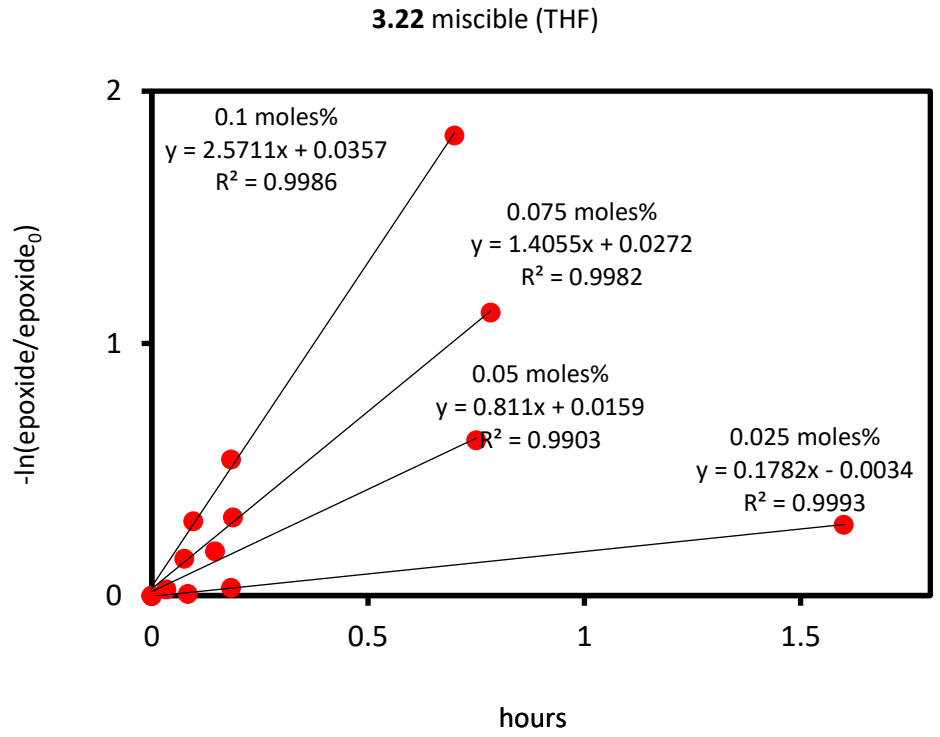

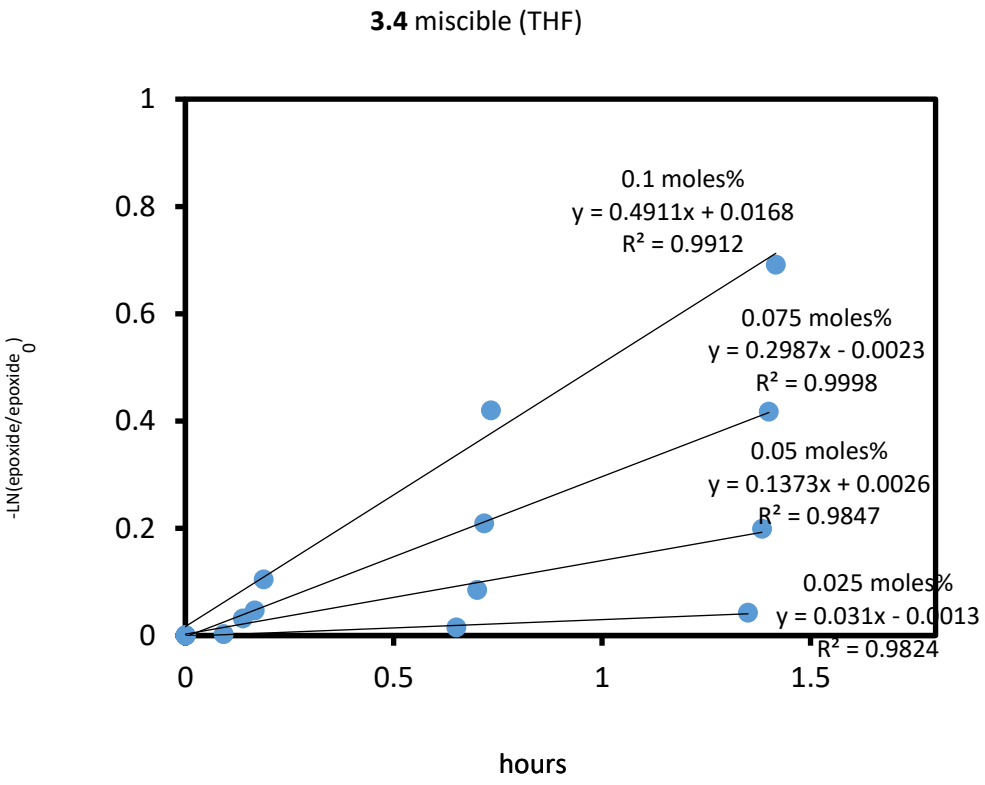

Chemical shifts of protons H_a, H_b, H_c of compound **3.45** and of protons H_d, H_e, H_f of complex **3.46** versus concentration of complex fitted into MD model, experiment done with the presence of D_2O (**Equation 16**).

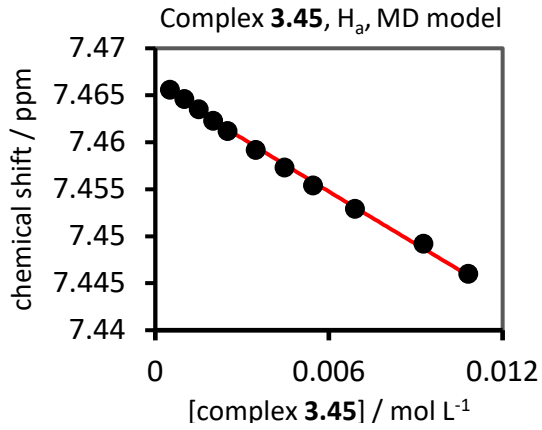

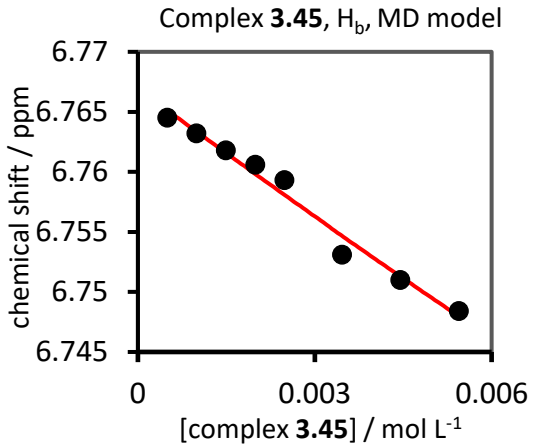

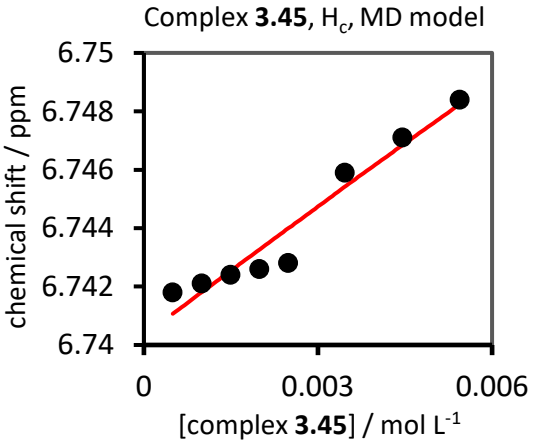

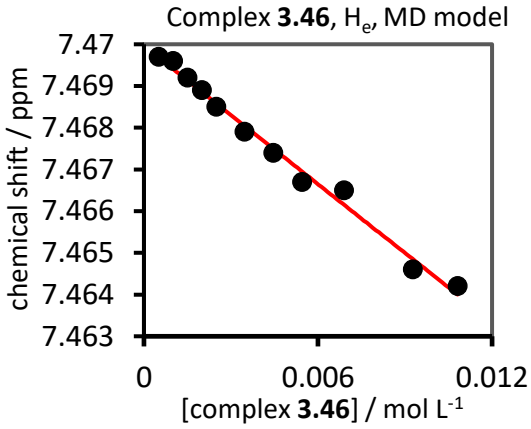

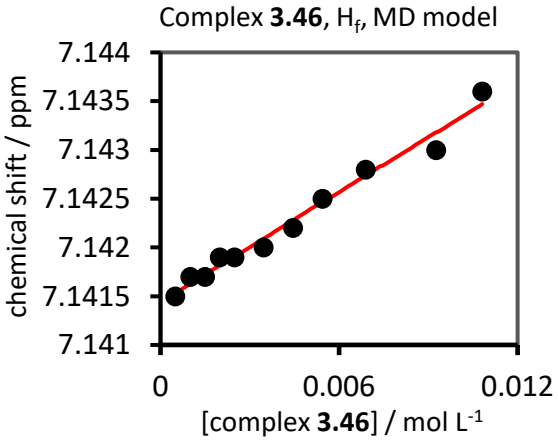

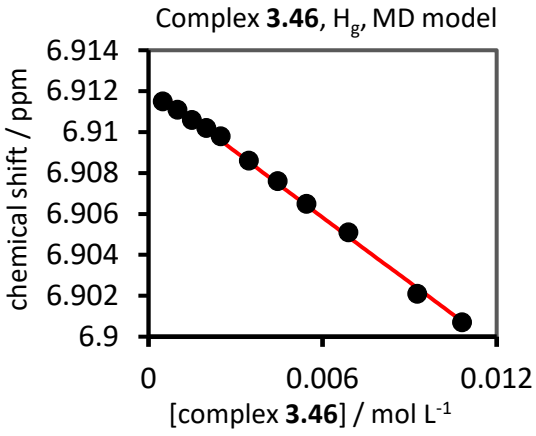

Chemical shifts of protons H_a, H_b, H_c of compound **3.45** and of protons H_d, H_e, H_f of complex **3.46** versus concentration of complex fitted into EK model, experiment done with the presence of D_2O (**Equation 17**).

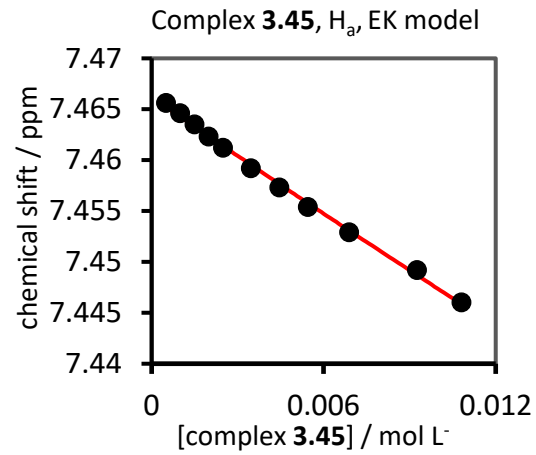

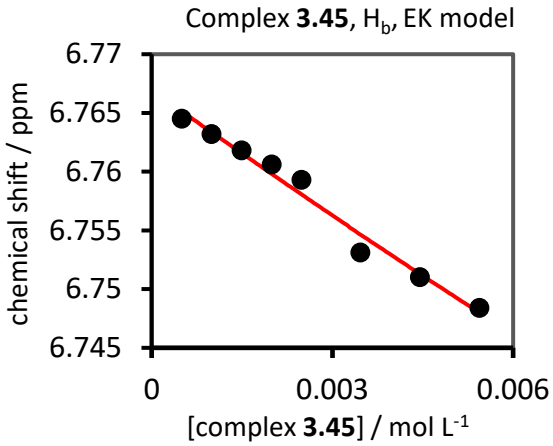

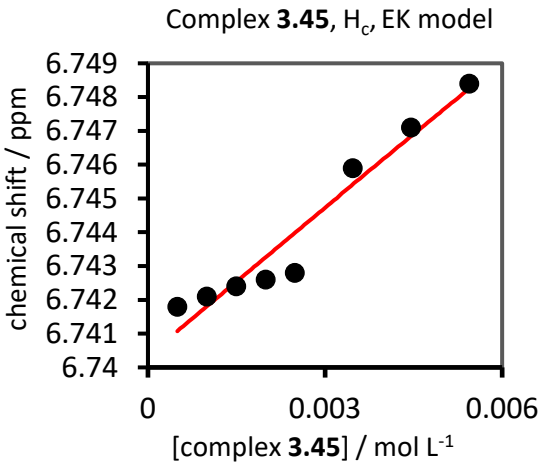

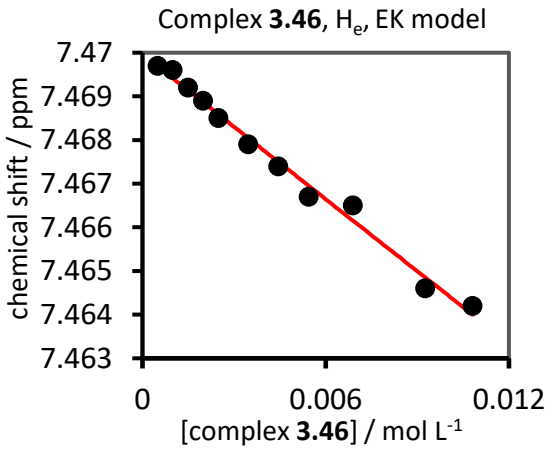

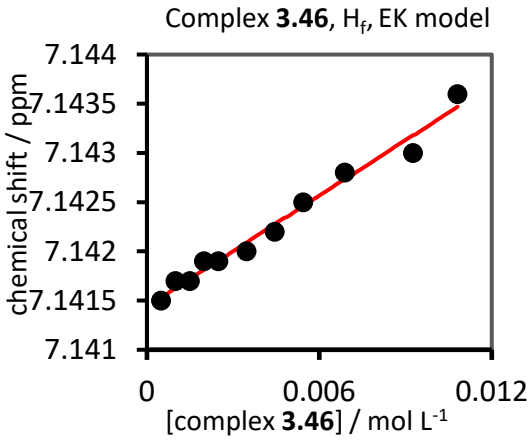

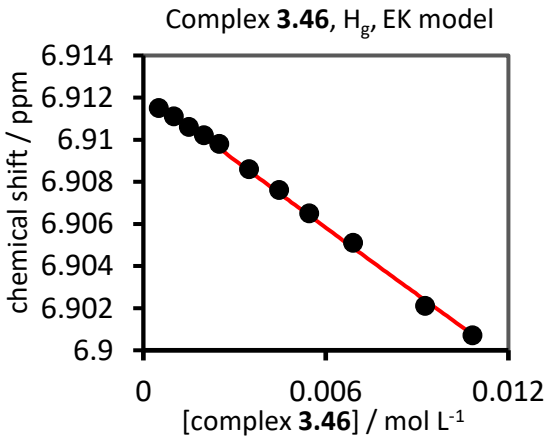

Chemical shifts of protons H_a, H_b, H_c of compound **3.45** and of protons H_d, H_e, H_f of complex **3.46** versus concentration of complex fitted into MD model, experiment done in the absence of D_2O (**Equation 16**).

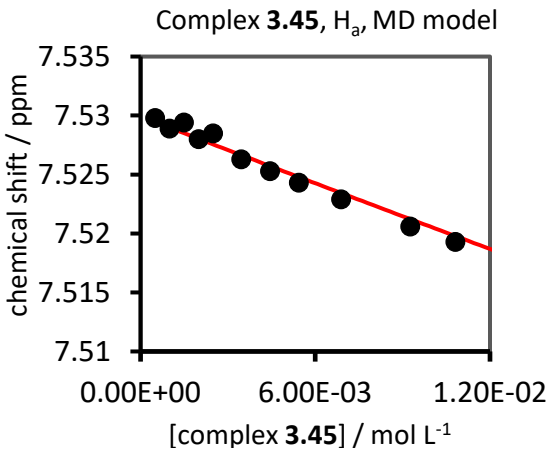

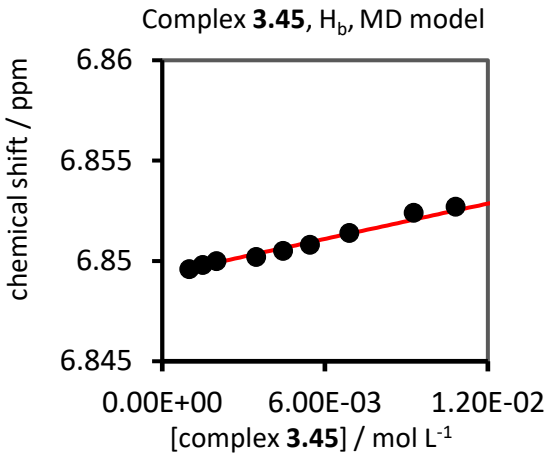

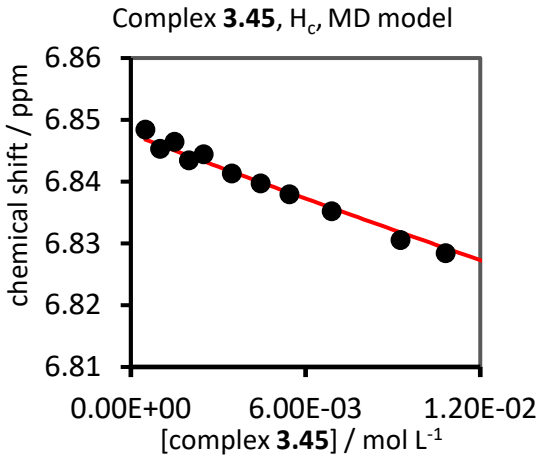

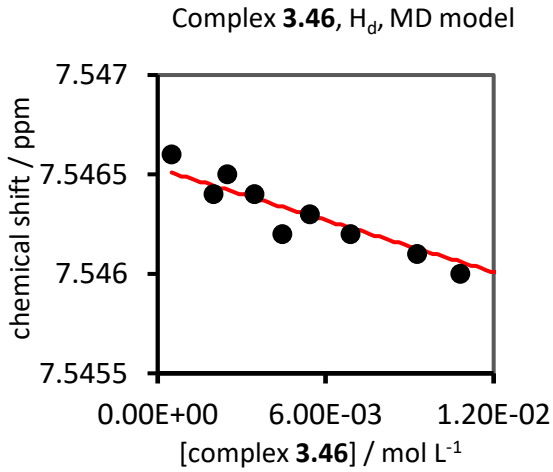

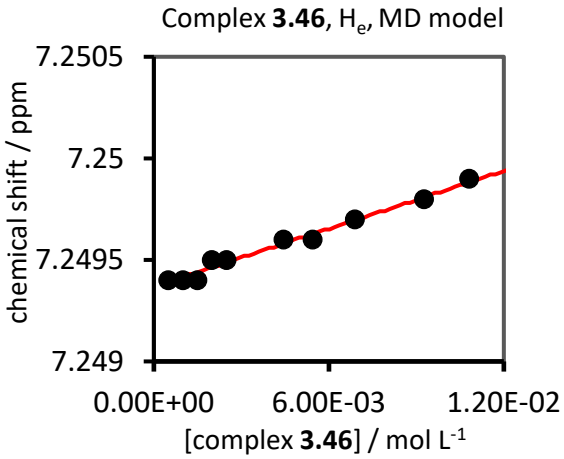

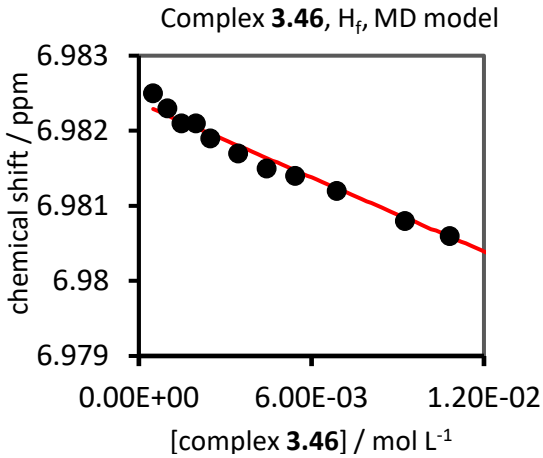

Chemical shifts of protons H_a, H_b, H_c of compound **3.45** and of protons H_d, H_e, H_f of complex **3.46** versus concentration of complex fitted into EK model, experiment done in the absence of D_2O (**Equation 17**).

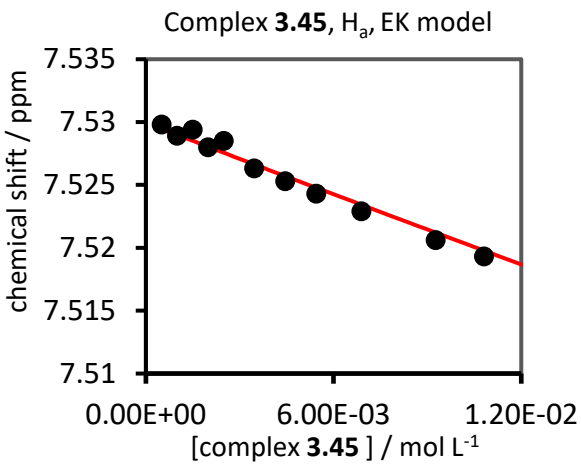

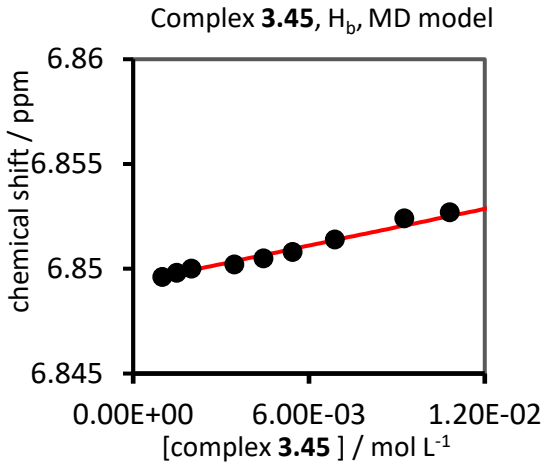

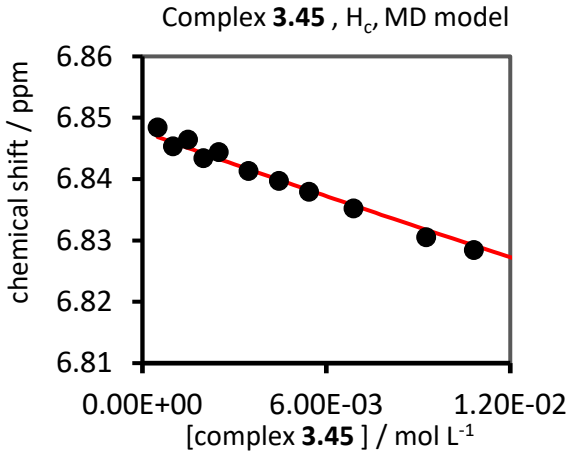

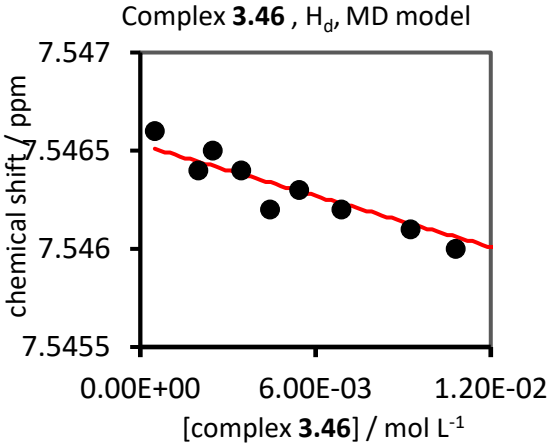

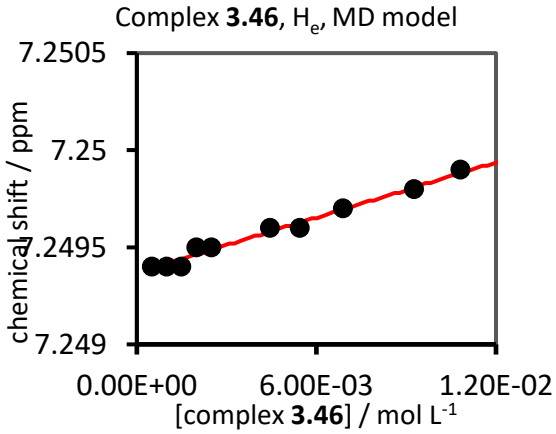

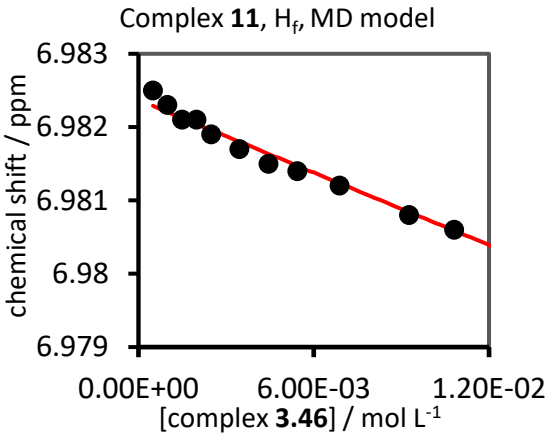

References

[1] J. Hagen, in *Ind. Catal.*, Wiley-VCH, **2015**, pp. 459–462.

[2] I. Chorkendorff, J. W. Niemantsverdriet, in *Concepts Mod. Catal. Kinet.*, Wiley-VCH, **2003**, pp. 2–4.

[3] In *IUPAC Compend. Chem. Terminol. Gold B.*, RSC, **2014**, p. 220.

[4] L. E. Rosebrugh, M. B. Herbert, V. M. Marx, B. K. Keitz, R. H. Grubbs, *J. Am. Chem. Soc.* **2013**, *135*, 1276–1279.

[5] N. Shigeo, T. Hisaaki, *Bull. Chem. Soc. Jpn.* **1963**, *36*, 353–355.

[6] U. Hanefeld, L. Lefferts, in *Catal. An Integr. Textb. Students*, Wiley-VCH, **2018**, pp. 5–10.

[7] R. Callender, R. B. Dyer, *Acc. Chem. Res.* **2015**, *48*, 407–413.

[8] J. Hine, M. S. Cholod, W. K. Chess, *J. Am. Chem. Soc.* **1973**, *95*, 4270–4276.

[9] M. Raynal, P. Ballester, A. Vidal-Ferran, P. W. N. M. Van Leeuwen, *Chem. Soc. Rev.* **2014**, *43*, 1660–1733.

[10] M. Raynal, P. Ballester, A. Vidal-Ferran, P. W. N. M. Van Leeuwen, *Chem. Soc. Rev.* **2014**, *43*, 1734–1787.

[11] A. E. Allen, D. W. C. MacMillan, *Chem. Sci.* **2012**, *3*, 633–658.

[12] M. Jiang, X. Chen, Z. F. Guo, Y. Cao, M. Chen, Z. Guo, *Biochemistry* **2008**, *47*, 3426–3434.

[13] Y. Sun, S. Yin, Y. Feng, J. Li, J. Zhou, C. Liu, G. Zhu, Z. Guo, *J. Biol. Chem.* **2014**, *289*, 15867–15879.

[14] R. Peters, *Cooperative Catalysis: Designing Efficient Catalysts for Synthesis*, Wiley-VHC, **2015**.

[15] M. Shibasaki, M. Kanai, S. Matsunaca, N. Kumagai, *Acc. Chem. Res.* **2009**, *42*, 1117–1127.

[16] A. J. Kirby, *Angew. Chem. Int. Ed.* **1996**, *35*, 706–724.

[17] Y. M. Lin, J. Boucau, Z. Li, V. Casarotto, J. Lin, A. N. Nguyen, J. Ehrmantraut, *Org. Lett.* **2007**, *9*, 567–570.

[18] H. H. Liao, C. C. Hsiao, I. Atodiresei, M. Rueping, *Chem. Eur. J.* **2018**, *24*, 7718–7723.

[19] R. A. Sheldon, I. W. C. E. Arends, U. Hanefeld, *Green Chemistry and Catalysis*, Wiley-VHC, **2007**.

[20] S. Belot, K. A. Vogt, C. Besnard, N. Krause, A. Alexakis, *Angew. Chem. Int. Ed.* **2009**, *48*, 8923–8926.

[21] S. U. Son, K. H. Park, Y. K. Chung, *J. Am. Chem. Soc.* **2002**, *124*, 6838–6839.

[22] H. Xu, S. J. Zuend, M. G. Woll, Y. Tao, E. N. Jacobsen, *Science.* **2010**, *327*, 986–990.

[23] M. Shi, J. K. Jiang, C. Q. Li, *Tetrahedron Lett.* **2002**, *43*, 127–130.

[24] B. M. Trost, X. Luan, *J. Am. Chem. Soc.* **2011**, *133*, 1706–1709.

[25] C. A. Hunter, H. L. Anderson, *Angew. Chem. Int. Ed.* **2009**, *48*, 7488–7499.

[26] A. Whitty, *Nat. Chem. Biol.* **2008**, *4*, 435–439.

[27] I. Ibrahem, A. Córdova, *Angew. Chem. Int. Ed.* **2006**, *45*, 1952–1956.

[28] S. J. Wezenberg, A. W. Kleij, *Adv. Synth. Catal.* **2010**, *352*, 85–91.

[29] W. H. Chapman, R. Breslow, *J. Am. Chem. Soc.* **1995**, *117*, 5462–5469.

[30] P. Molenveld, J. F. J. Engbersen, H. Kooijman, A. L. Spek, D. N. Reinhoudt, *J. Am. Chem. Soc.* **1998**, *120*, 6726–6737.

[31] J. M. Ready, E. N. Jacobsen, *J. Am. Chem. Soc.* **2001**, *123*, 2687–2688.

[32] R. N. Loy, E. N. Jacobsen, *J. Am. Chem. Soc.* **2009**, *131*, 2786–2787.

[33] M. Martin, F. Manea, R. Fiammengo, L. J. Prins, L. Pasquato, P. Scrimin, *J. Am. Chem. Soc.* **2007**, *129*, 6982–6983.

[34] R. Breinbauer, E. N. Jacobsen, *Angew. Chem. Int. Ed.* **2000**, *39*, 3604–3607.

[35] P. Molenveld, J. F. J. Engbersen, D. N. Reinhoudt, *J. Org. Chem.* **1999**, *64*, 6337–6341.

[36] M. D. Nothling, A. Ganesan, K. Condic-Jurkic, E. Pressly, A. Davalos, M. R. Gotrik, Z. Xiao, E. Khoshdel, C. J. Hawker, M. L. O'Mara, M. L. Coote, L. A. Connal, *Chem* **2017**, *2*, 732–745.

[37] G. J. Rowlands, *Tetrahedron* **2001**, *57*, 1865–1882.

[38] S. Matsunaga, J. Das, J. Roels, E. M. Vogl, N. Yamamoto, T. Iida, K. Yamaguchi, M. Shibasaki, *J. Am. Chem. Soc.* **2000**, *122*, 2252–2260.

[39] T. Okino, Y. Hoashi, Y. Takemoto, *J. Am. Chem. Soc.* **2003**, *125*, 12672–12673.

[40] F. Manea, F. B. Houillon, L. Pasquato, P. Scrimin, *Angew. Chem. Int. Ed.* **2004**, *43*, 6165–6169.

[41] T. Belser, E. N. Jacobsen, *Adv. Synth. Catal.* **2008**, *350*, 967–971.

[42] P. Pengo, S. Polizzi, L. Pasquato, P. Scrimin, *J. Am. Chem. Soc.* **2005**, *127*, 1616–1617.

[43] X. Zhu, K. Venkatasubbaiah, M. Weck, C. W. Jones, *ChemCatChem* **2010**, *2*, 1252–1259.

[44] S. Shylesh, W. R. Thiel, *ChemCatChem* **2011**, *3*, 278–287.

[45] A. E. Fernandes, A. M. Jonas, *Catal. Today* **2019**, *334*, 173–186.

[46] N. Kann, *Molecules* **2010**, *15*, 6306–6331.

[47] Y. Zheng, C. Duanmu, Y. Gao, *Org. Lett.* **2006**, *8*, 3215–3217.

[48] R. Bonomi, F. Selvestrel, V. Lombardo, C. Sissi, S. Polizzi, F. Mancin, U. Tonellato, P. Scrimin, *J. Am. Chem. Soc.* **2008**, *130*, 15744–15745.

[49] L. Deiana, L. Ghisu, S. Afewerki, O. Verho, E. V. Johnston, N. Hedin, Z. Bacsik, A. Córdova, *Adv. Synth. Catal.* **2014**, *356*, 2485–2492.

[50] H. Guo, L. Zhang, H. Zhou, W. Meng, Y. Ao, D. Wang, Q. Wang, *Angew. Chem. Int. Ed.* **2020**, *132*, 2645–2649.

[51] D. Y. Ma, H. Norouzi-Arasi, E. Sheibani, K. Wärnmark, *ChemCatChem* **2010**, *2*, 629–632.

[52] R. G. Konsler, J. Karl, E. N. Jacobsen, *J. Am. Chem. Soc.* **1998**, *120*, 10780–10781.

[53] J. Park, K. Lang, K. A. Abboud, S. Hong, *J. Am. Chem. Soc.* **2008**, *130*, 16484–16485.

[54] J. Park, K. Lang, K. A. Abboud, S. Hong, *Chem. Eur. J.* **2011**, *17*, 2236–2245.

[55] A. B. Xia, D. Q. Xu, S. P. Luo, J. R. Jiang, J. Tang, Y. F. Wang, Z. Y. Xu, *Chem. - A Eur. J.* **2010**, *16*, 801–804.

[56] J.-M. Lehn, *Angew. Chem.* **1988**, *100*, 91–116.

[57] J. Van Der Waals, *Nobel Lect. Phys.* **1910**, *254*.

[58] E. Fischer, *Nature* **1903**, *68*, 466.

[59] J. D. Watson, *The Double Helix: A Personal Account of the Discovery of the Structure of DNA.*, Atheneum Press, **1968**.

[60] C. J. Pedersen, *J. Am. Chem. Soc.* **1967**, *89*, 7017–7036.

[61] M. C. T. Fyfe, J. F. Stoddart, *Acc. Chem. Res.* **1997**, *30*, 393–401.

[62] C. Dietrich-Buchecker, M. C. Jimenez-Molero, V. Sartor, J. P. Sauvage, *Pure Appl. Chem.* **2003**, *75*, 1383–1393.

[63] S. P. Fletcher, F. Dumur, M. M. Pollard, B. L. Feringa, *Science.* **2005**, *310*, 80–82.

[64] J. A. Bravo, F. M. Raymo, J. F. Stoddart, A. J. P. White, D. J. Williams, *European J. Org. Chem.* **1998**, 2565–2571.

[65] T. van Leeuwen, A. S. Lubbe, P. Štacko, S. J. Wezenberg, B. L. Feringa, *Nat. Rev. Chem.* **2017**, *1*, 1–7.

[66] H. Hess, J. L. Ross, *Chem. Soc. Rev.* **2017**, *46*, 5570–5587.

[67] J. M. Lehn, *Angew. Chem. Int. Ed.* **2013**, *52*, 2836–2850.

[68] E. Mattia, S. Otto, *Nat. Nanotechnol.* **2015**, *10*, 111–119.

[69] G. Ragazzon, L. J. Prins, *Nat. Nanotechnol.* **2018**, *13*, 882–889.

[70] G. Monreal Santiago, K. Liu, W. R. Browne, S. Otto, *Nat. Chem.* **2020**, *12*, 603–607.

[71] J. Ottelé, A. S. Hussain, C. Mayer, S. Otto, *Nat. Catal.* **2020**, *3*, 547–553.

[72] P. Solís-Muñana, J. L.-Y. Chen, *Nat. Chem.* **2020**, *12*, 584–588.

[73] L. F. Lindoy, I. M. Atkinson, *Self-Assembly in Supramolecular Systems*, RSC, **2000**.

[74] E. E. Meyer, K. J. Rosenberg, J. Israelachvili, *Proc. Natl. Acad. Sci. U. S. A.* **2006**, *103*, 15739–15746.

[75] Ariga K.; Kunitake T., *Supramolecular Chemistry – Fundamentals and Applications*, Springer, **2006**.

[76] R. Breslow, L. E. Overman, *J. Am. Chem. Soc.* **1970**, *92*, 1075–1077.

[77] R. Salvio, S. Volpi, R. Cacciapaglia, A. Casnati, L. Mandolini, F. Sansone, *J. Org. Chem.* **2015**, *80*, 5887–5893.

[78] Y. Chao, D. J. Cram, *J. Am. Chem. Soc.* **1976**, *98*, 1015–1017.

[79] J. K. M. Sanders, *Chem. Eur. J.* **1998**, *4*, 1378–1383.

[80] P. Molenveld, S. Kapsabelis, J. F. J. Engbersen, D. N. Reinhoudt, *J. Am. Chem. Soc.* **1997**, *119*, 2948–2949.

[81] M. Diez-Castellnou, F. Mancin, P. Scrimin, *J. Am. Chem. Soc.* **2014**, *136*, 1158–1161.

[82] S. Maiti, I. Fortunati, C. Ferrante, P. Scrimin, L. J. Prins, *Nat. Chem.* **2016**, *8*, 725–731.

[83] F. della Sala, S. Neri, S. Maiti, J. L. Y. Chen, L. J. Prins, *Curr. Opin. Biotechnol.* **2017**, *46*, 27–33.

[84] R. Breslow, D. L. Huang, E. Anslyn, *Proc. Natl. Acad. Sci. U. S. A.* **1989**, *86*, 1746–1750.

[85] W. H. Chapman, R. Breslow, *J. Am. Chem. Soc.* **1995**, *117*, 5462–5469.

[86] C. Bazzicalupi, A. Bencini, A. Bianchi, V. Fusi, C. Giorgi, P. Paoletti, B. Valtancoli, D. Zanchi, *Inorg. Chem.* **1997**, 2784–2790.

[87] D. Desbouis, I. P. Troitsky, M. J. Belousoff, L. Spiccia, B. Graham, *Coord. Chem. Rev.* **2012**, *256*, 897–937.

[88] W. Jiang, B. Xu, Z. Xiang, F. Liu, Y. Zhang, *Colloid Polym. Sci.* **2014**, *292*, 1439–1447.

[89] A. Panja, T. Matsuo, S. Nagao, S. Hirota, *Inorg. Chem.* **2011**, *50*, 11437–11445.

[90] J. Qian, L. Wang, W. Gu, X. Liu, J. Tian, S. Yan, *Dalt. Trans.* **2011**, *40*, 5617–5624.

[91] C. T. Liu, A. A. Neverov, R. S. Brown, *Inorg. Chem.* **2007**, *46*, 1778–1788.

[92] G. Feng, D. Natale, R. Prabaharan, J. C. Mareque-Rivas, N. H. Williams, *Angew. Chem. Int. Ed.* **2006**, *45*, 7056–7059.

[93] J. Chin, *Curr. Opin. Chem. Biol.* **1997**, 514–521.

[94] R. Sasaki, S. Murata, *Langmuir* **2008**, *24*, 2387–2394.

[95] G. Li, S. Zhang, N. Wu, Y. Cheng, J. You, *Adv. Funct. Mater.* **2014**, *24*, 6204–6209.

[96] A. Nadler, C. Hain, U. Diederichsen, *European J. Org. Chem.* **2009**, 4593–4599.

[97] D. A. Brown, D.M.; Usher, *J. Chem. Soc.* **1965**, 6558–6564.

[98] M. C. A. Stuart, J. C. Van De Pas, J. B. F. N. Engberts, *J. Phys. Org. Chem.* **2005**, *18*, 929–934.

[99] J. F. Rathman, *Curr. Opin. Colloid Interface Sci. Opin. Colloid Interface Sci.* **1996**, *1*, 514–518.

[100] F. Rajabi, R. Luque, *RSC Adv.* **2014**, *4*, 5152–5155.

[101] D. Kumar, K. Seth, D. N. Kommi, S. Bhagat, A. K. Chakraborti, *RSC Adv.* **2013**, *3*, 15157–15168.

[102] M. Cortes-Clerget, N. Akporji, J. Zhou, F. Gao, P. Guo, M. Parmentier, F. Gallou, J. Y. Berthon, B. H. Lipshutz, *Nat. Commun.* **2019**, *10*, 1–10.

[103] B. H. Lipshutz, S. Ghorai, *Green Chem.* **2014**, *16*, 3660–3679.

[104] G. Zaupa, C. Mora, R. Bonomi, L. J. Prins, P. Scrimin, *Chem. Eur. J.* **2011**, *17*, 4879–4889.

[105] H. Hoffman, *Berichte der Bunsengesellschaft für Phys. Chemie* **1978**, *82*, 988–1001.

[106] D. L. Nelson, M. M. Cox, *Lehninger Principles of Biochemistry*, Springer, **2004**.

[107] P. Solís-Muñana, G. Ragazzon, J. Dupont, C. Z. J. Ren, L. J. Prins, J. L. Y. Chen, *Angew. Chem. Int. Ed.* **2018**, *57*, 16469–16474.

[108] F. Jiang, L. Huang, X. Meng, J. Du, X. Yu, Y. Zhao, X. Zeng, *J. Colloid Interface Sci.* **2006**, *303*, 236–242.

[109] C. Bazzicalupi, A. Bencini, E. Berni, A. Bianchi, V. Fedi, V. Fusi, C. Giorgi, P. Paoletti, B. Valtancoli, *Inorg. Chem.* **1999**, *38*, 4115–4122.

[110] D. Voet, J. G. Voet, *Biochemistry*, Wiley-VHC, **2011**.

[111] S. Bal, K. Das, S. Ahmed, D. Das, *Angew. Chem. Int. Ed.* **2019**, *58*, 244–247.

[112] E. Sheibani, K. Wärnmark, *Org. Biomol. Chem.* **2012**, *10*, 2059–2067.

[113] K. Lang, J. Park, S. Hong, *Angew. Chem. Int. Ed.* **2012**, *51*, 1620–1624.

[114] S. Jónsson, F. G. J. Odille, P. O. Norrby, K. Wärnmark, *Org. Biomol. Chem.* **2006**, *4*, 1927–1948.

[115] S. Jónsson, F. G. J. Odille, P. O. Norrby, K. Wärnmark, *Chem. Commun.* **2005**, 549–551.

[116] F. M. Menger, L. H. Gan, E. Johnson, D. H. Durst, *J. Am. Chem. Soc.* **1987**, *109*, 2800–2803.

[117] B. Gruber, E. Kataev, J. Aschenbrenner, S. Stadlbauer, B. König, *J. Am. Chem. Soc.* **2011**, *133*, 20704–20707.

[118] E. Kimura, H. Hashimoto, T. Koike, *J. Am. Chem. Soc.* **1996**, *118*, 10963–10970.

[119] C. Bazzicalupi, A. Bencini, C. Bonaccini, C. Giorgi, P. Gratteri, S. Moro, M. Palumbo, A. Simionato, J. Sgrignani, C. Sissi, B. Valtancoli, *Inorg. Chem.* **2008**, *47*, 5473–5484.

[120] S. C. Cheng, G. G. Chang, C. Y. Chou, *Biophys. J.* **2010**, *98*, 1327–1336.

[121] S. M. Kupchan, W. A. Court, R. G. Dailey, C. J. Gilmore, R. F. Bryan, *J. Am. Chem. Soc.* **1972**, *94*, 7194–7195.

[122] A. R. da Silva, D. A. dos Santos, M. W. Paixão, A. G. Corrêa, *Molecules* **2019**, *24*, 1–23.

[123] J. Larrow, P. Quigley, in *Compr. Chira.*, Elsevier Ltd., **2012**, pp. 129–146.

[124] M. Tokunaga, J. F. Larrow, F. Kakiuchi, E. N. Jacobsen, *Science.* **1997**, *277*, 936–938.

[125] S. E. Schaus, B. D. Brandes, J. F. Larrow, M. Tokunaga, K. B. Hansen, A. E. Gould, M. E. Furrow, E. N. Jacobsen, *J. Am. Chem. Soc.* **2002**, *124*, 1307–1315.

[126] J. M. Keith, J. F. Larrow, E. N. Jacobsen, *Adv. Synth. Catal.* **2001**, *343*, 5–26.

[127] L. P. C. Nielsen, C. P. Stevenson, D. G. Blackmond, E. N. Jacobsen, *J. Am. Chem. Soc.*

2004, *126*, 1360–1362.

[128] L. P. C. Nielsen, S. J. Zuend, D. D. Ford, E. N. Jacobsen, *J. Org. Chem.* **2012**, *77*, 2486–2495.

[129] R. G. Konsler, J. Karl, E. N. Jacobsen, *J. Am. Chem. Soc.* **1998**, *120*, 10780–10781.

[130] D. E. White, P. M. Tadross, Z. Lu, E. N. Jacobsen, *Tetrahedron* **2014**, *70*, 4165–4180.

[131] X. Zheng, C. W. Jones, M. Weck, *J. Am. Chem. Soc.* **2007**, *129*, 1105–1112.

[132] B. M. Rossbach, K. Leopold, R. Weberskirch, *Angew. Chem. Int. Ed.* **2006**, *45*, 1309–1312.

[133] B. Svensson, U. Olsson, P. Alexandridis, K. Mortensen, *Macromolecules* **1999**, *32*, 6725–6733.

[134] D. M. Rein, R. Khalfin, Y. Cohen, *J. Colloid Interface Sci.* **2012**, *386*, 456–463.

[135] S. Aerts, A. Buekenhoudt, H. Weyten, I. F. J. Vankelecom, P. A. Jacobs, *Tetrahedron Asymmetry* **2005**, *16*, 657–660.

[136] S. S. Thakur, W. Li, C. K. Shin, G. J. Kim, *Catal. Lett.* **2005**, *104*, 151–156.

[137] K. J. Neurohr, H. H. Mantsch, *Can. J. Chem.* **1979**, *57*, 1986–1994.

[138] D. E. Condon, S. D. Kennedy, B. C. Mort, R. Kierzek, I. Yildirim, D. H. Turner, *J. Chem. Theory Comput.* **2015**, *11*, 2729–2742.

[139] R. B. Martin, *Chem. Rev.* **1996**, *96*, 3043-3064.

[140] G. Dodson, A. Wlodawer, *Trends Biochem. Sci.* **1998**, *23*, 347–352.

[141] A. Rauwerdink, R. J. Kazlauskas, *ACS Catal.* **2015**, *5*, 6153–6176.

[142] C. Z.-J. Ren, P. Solís-Muñana, G. G. Warr, J. L.-Y. Chen, *ACS Catal.* **2020**, *10*, 8395–8401.

[143] R. Kowalczyk, P. Kwiatkowski, J. Skarzewski, J. Jurczak, *J. Org. Chem.* **2009**, *74*, 753–756.

[144] Y. Kogami, T. Nakajima, T. Ikeno, T. Yamada, *Synth.* **2004**, 1947–1950.

[145] M. H. Wu, K. B. Hansen, E. N. Jacobsen, *Angew. Chem. Int. Ed.* **1999**, *38*, 2012–2014.

[146] R. Chloe Z.-J., P. Solís-Muñana, J. Dupont, S. Zhou, J. L. Chen, *Angew. Chem. Int. Ed.* **2019**, *58*, 15254–15258.

[147] L. Tjioe, T. Joshi, B. Graham, L. Spiccia, *Inorg. Chem.* **2011**, 621–635.

[148] C. A. Johnson, S. Sharma, B. Subramaniam, A. S. Borovik, *J. Am. Chem. Soc.* **2005**, *127*, 9698–9699.